



# BRNO UNIVERSITY OF TECHNOLOGY

FACULTY OF ELECTRICAL ENGINEERING AND COMMUNICATION



ELECTRICAL ENGINEERING, INFORMATION SCIENCE, AND COMMUNICATION TECHNOLOGIES

PROCEEDINGS II OF THE 26<sup>TH</sup> STUDENT EEICT 2020  
SELECTED PAPERS

APRIL 23, 2020  
BRNO, CZECH REPUBLIC

<b>Title</b>	Proceedings II of the 26 <sup>th</sup> Conference STUDENT EEICT 2020
<b>Supervisor</b>	Prof. Vladimír Aubrecht
<b>Editor</b>	Assoc. Prof. Vítězslav Novák
<b>Publisher</b>	Brno University of Technology, Faculty of Electrical Engineering and Communication
<b>Year released</b>	2020
<b>1st Edition</b>	

Content and language issues are the responsibility of the authors.

ISBN 978-80-214-5868-0

## **Sponsors**

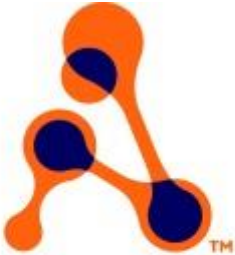
**Diamond tier**

# **Honeywell**

**Gold tier**

# **ThermoFisher** S C I E N T I F I C

Silver tier



**Adesto**



Honored tier



## Expert guidance



## Media



# Contents

## Foreword

<b>Martin Košút</b>	
MPPT CONTROLLER FOR UAV .....	1
<b>Radek Theumer</b>	
SYNTHESIS OF ELECTRONICALLY RECONFIGURABLE 3RD-ORDER FLF-OS FILTER IN SINGLE-ENDED AND FULLY-DIFERENTIAL DESIGN .....	5
<b>Jan Novotný</b>	
CONTROL SYSTEM FOR MICRO HYDROPOWER PLANT .....	8
<b>Khmil Denys</b>	
THE CRANE MANIPULATOR FOR THE 3D PRINTERS .....	12
<b>Martin Mikulka</b>	
DIGITAL CONTROLLED POWER SUPPLY .....	16
<b>Radim Kejzlar</b>	
REMOTE-CONTROLLED CROSS-COUNTRYFOUR-WHEELER .....	20
<b>Martin Balajka</b>	
MEASURING CARD FOR ELECTRICAL IMPEDANCE TOMOGRAPHY V2.0 .....	24
<b>Jakub Majerčík, Michal Špaček</b>	
PROSTATIC CELLS CLASSIFICATION USING DEEP LEARNING .....	28
<b>Kryštof Šara</b>	
APPLICATION FOR HEART RATE ESTIMATION USING SMARTPHONE .....	32
<b>Kateřina Širůčková</b>	
SPECTRAL COMPUTED TOMAGRAPHY: COMPARISON OF REAL AND VIRTUAL NATIVE IMAGES .....	36
<b>Jan Malucha</b>	
ADVANCED ESTIMATION OF SPEECH SIGNAL PERIODICITY .....	40
<b>Milan Bubniak</b>	
APPLICATION FOR AN EARLY DETECTION OF TRANSMISSION PARAMETERS DEGRADATION OF POINT-TO-POINT MICROWAVE LINKS .....	44
<b>Tadeáš Cvrček</b>	
ELLIPTIC CURVE CRYPTOGRAPHY FOR CONSTRAINED DEVICES IN INTERNET OF THINGS AND INDUSTRY 4.0 .....	48
<b>Daniel Petra-Kajňák</b>	
LED OPTIMISED CONTROL SYSTEMS .....	52
<b>Lukáš Jagla</b>	
ACQUISITION SYSTEM FOR ADAPTATION OF DIGITAL PREDISTORTER TO LINEARIZE AMPLIFIERS USING COMPARATOR .....	56
<b>Štěpán Brázdil</b>	
ACTIVE UPPER LIMB PROSTHESIS .....	60
<b>Marek Zemek</b>	
METHOD FOR EXTENDING THE FIELD OF VIEW FOR X-RAY COMPUTED TOMOGRAPHY WITH SUBMICRON RESOLUTION .....	64
<b>Cindy Veselá</b>	
REAL TIME EMG DETECTION IN THERAPEUTIC GAME .....	68
<b>Jakub Nemček</b>	
DETECTION OF INTRACRANIAL HAEMORRHAGES IN HEAD CT DATA BASED ON DEEP LEARNING .....	72
<b>Lujza Barilíková</b>	
MY_UMI_TOOL: PROCESSING OF UNIQUE MOLECULAR IDENTIFIERS WITHOUT MAPPING TO A REFERENCE GENOME .....	76
<b>Dominik Friml</b>	
QUALITY IMPROVEMENT OF LQG CONTROL USING $H_{\infty}$ OPTIMIZATION .....	80
<b>Matouš Hýbl</b>	
USING RYZE TELLO UAVS IN MULTI-ROBOT SYSTEMS .....	84

<b>Matouš Hýbl</b>	DESIGN AND DEVELOPMENT OF A HANDHELD ROBOT CONTROLLER WITH TELEPRESENCE CAPABILITIES .....	90
<b>Jakub Piska</b>	COMPARISON OF ARC EROSION COEFFICIENTS .....	95
<b>Jan Klusáček</b>	BMS SETTINGS ANALYSIS .....	99
<b>Ondřej Klvač</b>	THE DESIGN OF SAMPLE HOLDER FOR XRD MEASUREMENTS IN INERT ATMOSPHERE WITH DISPLACEMENT ERROR CORRECTION .....	103
<b>Vaclav Havlicek, Petr Vyroubal</b>	APPLICATION OF GRAPHITE IN THERMAL MANAGEMENT OF MICROELECTRONICS .....	108
<b>Radek Hanuš</b>	ADVANCED DRIVING SYSTEM OF THE THREE-PHASE DC MOTOR .....	112
<b>Jakub Kaderka</b>	PICOBALLOON PROBE .....	116
<b>Jan Spurek</b>	ENHANCEMENT OF AXIAL RATIO BANDWIDTH OF ANTENNA ARRAY BY PARASITIC PATCHES .....	121
<b>Miroslav Waldecker</b>	UNIVERSAL POWER SEQUENCER FOR RF POWER AMPLIFIERS .....	126
<b>Amirmohammad Shamaei</b>	DEEP LEARNING FOR MAGNETIC RESONANCE SPECTROSCOPY QUANTIFICATION: A TIME-FREQUENCY ANALYSIS APPROACH .....	131
<b>Ondřej Mihálik</b>	RECONSTRUCTION OF NON-UNIFORMLY SAMPLED SIGNALS USING GERCHBERG-PAPOULIS METHOD .....	136
<b>Eva Valterova</b>	AUTOMATED FOVEA CENTER ESTIMATION IN ADAPTIVE OPTICS IMAGES .....	141
<b>Jakub Krejčí</b>	SIMULATIONS AND MEASUREMENT OF ACOUSTIC EMISSION EFFECTS .....	146
<b>Ondřej Bartík</b>	THE TWO-MASS SYSTEM PARAMETER IDENTIFICATION WITH LEVENBERG-MARQUARDT ALGORITHM .....	151
<b>Jan Kunz</b>	FIR FILTER RESONANCE COMPENSATION FOR RANDOM VIBRATION GENERATION .....	156
<b>Vlastimil Mancl</b>	MEASUREMENT SYSTEM FOR DETERMINING FORCES ACTING ON LOOSE CONCRETE ROOF PAVER .....	161
<b>Ondřej Bostík</b>	SEMI-SUPERVISED DEEP LEARNING APPROACH FOR BREAKING GEOCACHING CAPTCHAS .....	166
<b>Lukas Kratochvila</b>	COMPUTING PLATFORMS FOR DEEP LEARNING TASK IN COMPUTER VISION .....	171
<b>Viktor Jurák</b>	INFLUENCE OF REACTIVE POWER COMPENSATION IN TRANSFORMER STATION ON VOLT-VAR REGULATION OF DISTRIBUTED ENERGY SOURCES .....	176
<b>Martin Folprecht</b>	POWER CONVERTERS FOR CELL ELECTROPORATION .....	181
<b>Radek Tománek</b>	ZERO CURRENT SWITCHING QUASI-RESONANT BUCK CONVERTERS .....	187
<b>Daniel Burda</b>	FIELD ELECTRON EMISSION PERFORMANCE AND ORTHODOXY TEST OF TUNGSTEN EMITTERS WITH AND WITHOUT THIN TUNGSTEN TRIOXIDE BARRIER .....	192
<b>Rashid Dallaev</b>	STRUCTURAL CHARACTERIZATION OF ALN THIN FILMS OBTAINED ON SILICON SURFACE BY PE-ALD .....	197

<b>Nikola Papež</b>	
STRUCTURAL ANALYSIS OF GAAS-BASED PV CELLS AFTER IONIZING IRRADIATION .....	203
<b>Jan Smejkal</b>	
EFFECT OF ORGANIC ADDITIVES ON ELECTROCHEMI-CAL PROCESSES INFLUENCING ZINC-AIR BATTERY PARAMETERS .....	209
<b>Tomáš Musil, Martin Andruška</b>	
VIBRATION AND IMPACT MEASUREMENT FOR COLLISION ANALYSIS .....	215
<b>Martin Mačák</b>	
NUMERICAL MODELLING OF Li-S CHEMISTRY .....	220
<b>Michal Látal</b>	
SIMULTANEOUS TRANSMISSION OF AMPLIFIED OPTICAL SIGNALS OF SELECTED PHOTONIC SERVICES .....	225
<b>Radek Možný</b>	
ON THE LIMITS OF THE LORAWAN TECHNOLOGY: EVALUATION OF SPREADING FACTORS’ PERFORMANCE .....	229
<b>Petr Musil</b>	
COMPARISON OF POWER QUALITY MONITOR DATA TRANSMISSION BETWEEN MODBUS TCP/IP AND IEC 60870-5-104 .....	234

In modern technology, exchanging information, experience, and contacts on a broad basis is the cornerstone of success. To promote this principal activity, the Faculty of Electrical Engineering and Communication, Brno University of Technology, has organized and hosted for a quarter of a century the **STUDENT EEICT**, a multifaceted symposium of young researchers in electrical engineering, information science, and communication technologies. This year's **26th annual conference** continues the fruitful tradition of joining together creative students and seasoned science or research specialists and industry-based experts. Supervised by the Electrical and Electronic Association of the Czech Republic, the event involves multiple corporate partners, collaborators, and evaluators, whose intensive support and advice embody an invaluable asset for the entire EEICT community.

Importantly, the conference is a competitive, motivating forum that, in addition to encouraging students to further develop their knowledge, interests, and employability potential, also directly offers career opportunities through the affiliated PerFEKT JobFair, a yearly job-related workshop and exhibition complementing the actual EEICT sessions. In this context, the organizers acknowledge the long-term assistance from the Ministry of Education, Youth and Sports of the Czech Republic, which has proved essential for refining the scope and impact of the symposium.

These Proceedings comprise 52 award winning full papers, all selected by the conference's evaluation boards, grouped in chapters according to relevant topics and subdisciplines. The contributed manuscripts were first peer-reviewed and then submitted to the authors for correction or rearrangement; at present, the articles are ready to be defended before examiners including corporate specialists and academics.

Considering all the efforts and work invested, I hope that the 26<sup>th</sup> **STUDENT EEICT (2020)** will be successful and beneficial for all the participants and would like to thank the sponsors, experts, students, and collaborators, whose relentless energy enabled us to make the conference happen. I believe that the inspiration gathered during the event will contribute towards further rise of open science and research, giving all the attendees a chance to freely discuss their achievements and views.

Prof Vladimír Aubrecht

*Dean of the Faculty of Electrical Engineering and Communication*

# MPPT CONTROLLER FOR UAV

**Martin Košút**

Bachelor Degree Programme (3), FEEC BUT

E-mail: xkosut02@stud.feec.vutbr.cz

Supervised by: Michal Kubíček

E-mail: kubicek@feec.vutbr.cz

**Abstract:** This paper describes a prototype design of a maximum power peak tracking controller for a solar cell array embedded on a wing of UAV. Solar cells are used to both cover part of the UAV power consumption and (at suitable conditions) to charge onboard battery. As the UAV changes its position and attitude to the sun relatively fast, the lighting conditions on the solar cells change rapidly. Thus, it is necessary to implement a fast maximum power peak tracking controller to ensure maximum efficiency of the system. The proposed design is based on commercial off-the-shelf components. The implemented DC/DC converter, which represents the core of the regulator, is a combination of a step-up and a step-down converter. Weight, dimensions and overall efficiency were the key optimization parameters of the design.

**Keywords:** MPPT controller, solar cells, H-bridge, UAV

## 1 INTRODUCTION

Goal of this paper is to design a prototype of a controller, that tracks Maximum Power Point (MPPT; Maximum Power Point Tracking) of solar cells for use in UAV (Unmanned Aerial Vehicle) to cover power consumption of onboard electronics, or at suitable conditions, for charging onboard batteries during flight. Due to relatively rapid changes in the UAV position, it is necessary to have a rapid tracking of maximum power point with response time less than 1 second. Maximum power point of solar cells changes its position depending on the current lightning conditions on the solar cell. Equally important is also the overall size, weight and efficiency of the final solution, because the available space in the UAV is quite limited.

## 2 SOLAR CELLS

The V-I characteristics is used to define the properties of solar cells. It is a graphical interpretation of the load characteristics of the solar cell. There are important points, which characterize each solar cell under certain working conditions. When the V-I characteristics is displayed with the V-P characteristics in one plot, it shows Maximum Power Point (MPP), at the point of breaking in the V-I curve [1].

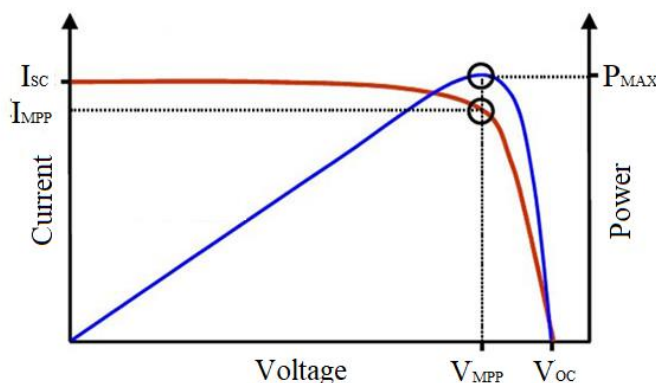


**Figure 1:** V-I and V-P characteristics of the solar cell

Characteristic points of the solar cell

$I_{SC}$	Short circuit current at zero output voltage
$I_{MPP}$	Current in MPP
$V_{MPP}$	Voltage in MPP
$V_{OC}$	Open circuit voltage at zero output current
$P_{MAX}$	Maximal output power in MPP

### 3 DESIGN OF MPPT CONTROLLER

Currently, Li-Ion SONY VTC6 onboard batteries in 4S5P configuration are used in the UAV. Those batteries comes in the 18650 size with maximum output voltage of 4.2 V/cell with maximum charging current of 4 A [2]. So maximum output voltage of 4-cell battery pack is 16.8 V. After implementation of solar cells into wing, the battery pack will shrink down to 4S3P configuration. This change saves 400 grams of weight, which will be divided into weight of solar cells in the wing, weight of cables and weight of the MPPT controller. Final weight of the MPPT controller is required to be lower than 50 g, with dimension limits 67x67x37 mm, which corresponds to the dimensions of saved Li-Ion battery pack in 4S1P configuration.

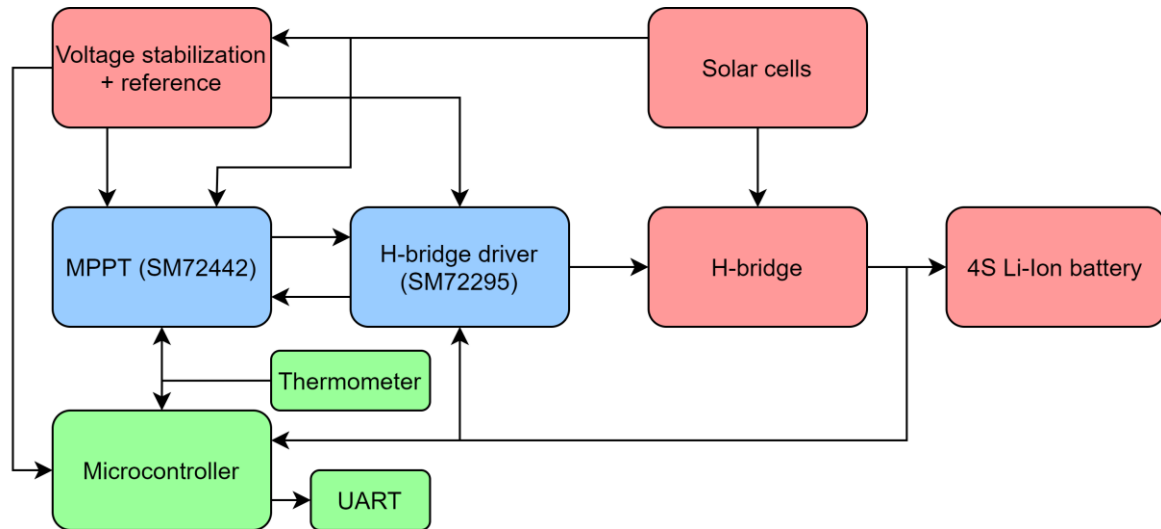


Figure 2: Block diagram of the MPPT controller

#### 3.1 MPPT CONTROLLER SM72442

This integrated circuit (IC) made by Texas Instruments controls switching of MOSFET transistors connected in H-bridge configuration via H-bridge driver through 4 PWM signals. Response time of its MPPT algorithm is 10 ms. This IC contains 8-channel 12-bits AD converter used for sensing input, output and configuration parameters. SM72442 also includes I<sup>2</sup>C communication interface to enable reading of current input and output currents and voltages and change its configured parameters [3].

#### 3.2 H-BRIDGE DRIVER SM72295

This IC is also made by Texas Instruments. Its main function is to drive 4 N-channel MOSFET transistors connected in the H-bridge configuration. It provides up to 3 A of peak gate drive current for fast switching of the transistors. It also contains 2 integrated amplifiers with configurable gain for sensing voltage drops on the current sense resistors. Amplifier outputs are connected to voltage buffers and then connected to the output pins, to provide information about input and output currents to the control IC SM72442 [4].

### 3.3 H-BRIDGE

Four N-channel MOSFET transistors in an H-bridge configuration of a DC-DC converter allows lower or higher output voltage than input voltage (buck-boost). The total ripple of the output voltage depends on the combination of the input and the output capacitances and the inductance of the inductor in the middle of the H-bridge [5].

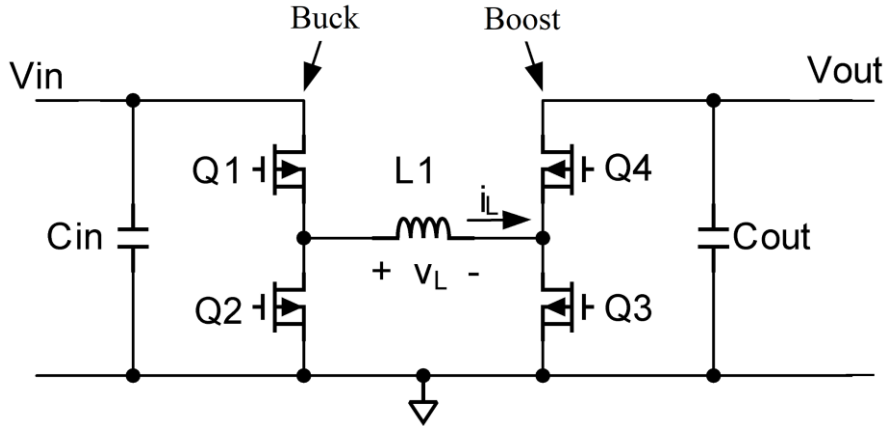


**Figure 3:** Basic H-bridge configuration

Overall efficiency of the whole controller depends mainly on the used inductor and switching transistors. Therefore, those components should feature the lowest possible resistance in the on-state and the transistors should feature the lowest possible total charge required to charge junction between gate and source ( $Q_G$ ). The total charge  $Q_G$  affects the dynamic losses during switching of the transistor. The selected inductor SRP1265-6R0 has a winding resistance of 10 m $\Omega$ , switching transistors NTMFS4955NT3G have a channel resistance of 5.6 m $\Omega$  and a total gate charge  $Q_G$  10.8 nC. The input and output capacitances are composed of ceramic capacitor banks, to reach very low equivalent series resistance (ESR). In total 26 discrete 22  $\mu$ F capacitor chips are used as the output capacitor to meet the required output voltage ripple of 50 mV. The large number of capacitors is required due to expected large DC-bias induced capacity drop typical for ceramic capacitors of this class.

### 3.4 MICROCONTROLLER

The AVR ATmega48A from Microchip in TQFP32 package was chosen as a monitoring microcontroller. It is based on 8-bit architecture with maximum internal oscillator frequency of 8 MHz. The required features for its selection were the master I<sup>2</sup>C communication interface, UART interface for easier communication with computer during firmware debugging and an internal AD converter. The microcontroller also reads temperature from TC74 digital thermometer made by Microchip via I<sup>2</sup>C. If MPPT controllers temperature or input voltage operating limits are exceeded, the microcontroller will limit maximum output current or suspend function of the MPPT controller via a reset signal. The input voltage is sensed by the microcontrollers internal AD converter.

### 3.5 POWER SUPPLY

Linear regulators are used to supply all the regulator components. Namely the LP2985 linear regulator with fixed output voltage of 10 V, which is required by the switching part of the H-bridge driver SM72295. Also, a 5 V variant of the same linear regulator is used for powering the MPPT controller SM72442, the logic part of the SM72295 and the microcontroller. Finally, there is also LT6654 0.1 % voltage reference which is shared between the MPPT controller and the microcontroller (as a reference for its internal AD converter).

## 4 DESIGN OF PROTOTYPE

Prototype printed circuit (PCB) board of the MPPT controller is designed in Autodesk Eagle with dimensions of 72x43 mm. To minimize area, a 4-layer PCB was selected, outer layers are used for signal traces while the inner ones are used for power distribution. The final version of the controller (with required dimensions of 67x37 mm) will be designed after functional tests of the prototype.

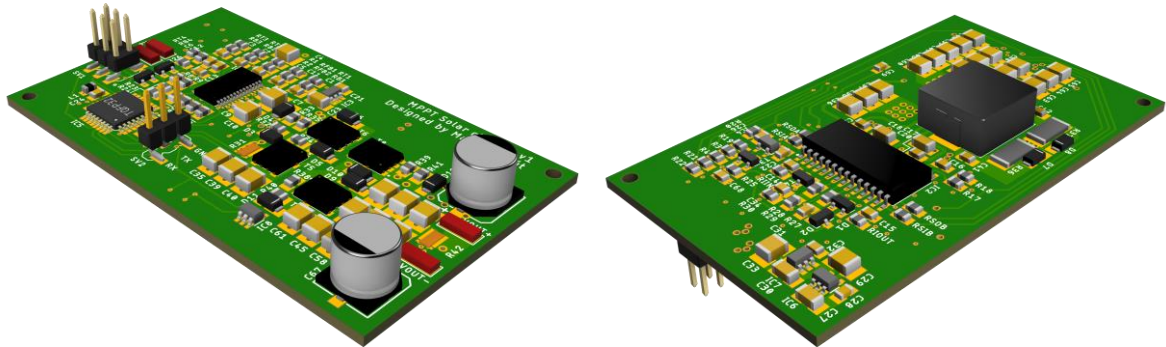


**Figure 4:** 3D visualization of the controller prototype

## 5 CONCLUSION

This paper deals with design of a fast MPPT controller prototype. The result is finalized schematic circuit and printed circuit board for the UAV meeting required functional parameters. The designed controller will operate in boost mode. The selected integrated circuit, which takes care of monitoring maximum power point of solar cells with latency of 10 ms, cooperates with the driver of H-bridge, which forms the power part of the entire controller. The selected microcontroller is used to monitor the operational parameters of the entire controller and in case of unfavorable conditions, it has ability to suspend the function of the entire device, which is important safety feature for installation in the UAV. After construction and functional validation of the prototype, a final miniaturized version of the controller will be designed.

## REFERENCES

- [1] DUNLOP, James P. Photovoltaic systems. 3rd ed. Orland Park, Illinois: American Technical Publishers, c2012. ISBN 978-1-935941-05-7.
- [2] IMRbatteries SONY VTC6 Datasheet: Product Specifications [online]. [cit. 2019-11-08]. Available at: [https://www.imrbatteries.com/content/sony\\_us18650vtc6-2.pdf](https://www.imrbatteries.com/content/sony_us18650vtc6-2.pdf)
- [3] SM72442 Programmable Maximum Power Point Tracking Controller for Photovoltaic Solar Panels: Datasheet [online]. [cit. 2019-11-29]. Available at: <http://www.ti.com/lit/ds/symlink/sm72442.pdf>
- [4] SM72295 Photovoltaic Full Bridge Driver: Datasheet [online]. [cit. 2019-12-01]. Available at: <https://www.ti.com/lit/ds/symlink/sm72295.pdf>
- [5] AN-2124 Power Circuit Design for SolarMagic™ SM3320: Application report [online]. 2013 [cit. 2019-12-06]. Available at: <http://www.ti.com/lit/an/snosb84c/snosb84c.pdf>

# SYNTHESIS OF ELECTRONICALLY RECONFIGURABLE 3RD-ORDER FLF-OS FILTER IN SINGLE-ENDED AND FULLY-DIFERENTIAL DESIGN

**Radek Theumer**

Bachelor Degree Programme (3), FEEC BUT

E-mail: xtheum00@stud.feec.vutbr.cz

Supervised by: Lukáš Langhammer

E-mail: langhammer@feec.vutbr.cz

**Abstract:** This paper deals with a proposal of 3rd-order single-ended and fully-differential frequency filters based on the follow-the-leader-feedback topology with the output summation (FLF-OS) working in the current mode. The main feature of both of these filtering structures is an ability of the electronic reconfiguration of their transfer functions. Active elements used for the filter design are implemented by transconductance amplifiers, current amplifiers and current followers. Simulation results of available transfer functions, their tunability and comparison of both circuits are presented.

**Keywords:** frequency filter, electronic reconfiguration, single-ended filter, fully-differential filter

## 1 INTRODUCTION

The electrical reconfiguration allows a synthesis of the multifunctional reconnection-less SISO circuits. Active elements with electronically controllable parameters, which allow a reconfiguration of the transfer function, are necessary parts of this type of active filters. Elimination of undesirable frequency components and distortions in the processed signal (switching distortion) and quick response are main advantages of this realization. [1][2] One of the many topologies which is suitable for synthesis of the high order filters is the follow-the-leader-feedback topology (FLF). It is one of the general multi-loop-structure (MLS) and it is well known for its easy modular synthesis. However, there is a problem when the processed signal is differential (for example differential amplifiers or differential AD converters). It is necessary to use the fully-differential filters in the mentioned applications. High common mode rejection ratio and dynamic range are advantages of fully-differential realizations. [3]

## 2 SYNTHESIS OF THE SINGLE-ENDED FILTER

There are two main types of FLF topology: with input distribution into nodes of the cascade and with output summation. [4] I chose realization of the FLF filter with output summation (FLF-OS). There is essential advantage due to the current mode realization – summation of the output current is realized only by the node. Unfortunately, a higher number of output pins of the active elements is needed to collect current for feedback, next block of the cascade and output independently. [5]

I determined a form of the denominator of the general transfer function (1) from Figure 1a) with help of SNAP software. Coefficients  $b$  for polynom I determined with help of program NAF. Parameters of filter zone tolerance are: characteristics frequency  $f_0 = 100$  kHz, maximal band-pass attenuation  $K_{\max} = -3$  dB, band-stop frequency  $f_{\text{att}} = 1$  MHz, band-stop attenuation  $K_{\min} = -57$  dB and Butterworth approximation. Coefficients  $b$  are given in (2).

$$D(s) = s^3 + s^2 \frac{g_{m1}}{C_1} + s \frac{g_{m1}g_{m2}}{C_1C_2} + \frac{g_{m1}g_{m2}g_{m3}}{C_1C_2C_3} = s^3b_3 + s^2b_2 + sb_1 + b_0 \quad (1)$$

$$b_0 = 2.4846 \cdot 10^{17} \quad b_1 = 7.9128 \cdot 10^{11} \quad b_2 = 1.2600 \cdot 10^6 \quad b_3 = 1 \quad (2)$$

The designed FLF structure consists of three lossless integrator OTA-C (1st-order) with transfer  $T_i = \frac{1}{s}$ . Therefore, only all-pole filters can be realized. All-pole filters has a constant in the numerator and polynomial in the denominator of the transfer function (without zeros), so the band-reject function is not available. Nominal value of all capacitors was chosen (with respect to the magnitude of the parasitic impedance)  $C = C_1 = C_2 = C_3 = 1$  nF.

### 3 TRANSFORMATION INTO FULLY-DIFFERENTIAL STRUCTURE

The easiest way how create a fully-differential structure is a transformation which consists in mirroring of the single-ended realization. After this transformation, active elements have twice the number of outputs and same transconductance  $g_m$  (Figure 1b). [3] Due to on-chip implementation each floating capacitor was replaced by a pair of the grounded capacitors (Figure 1b).

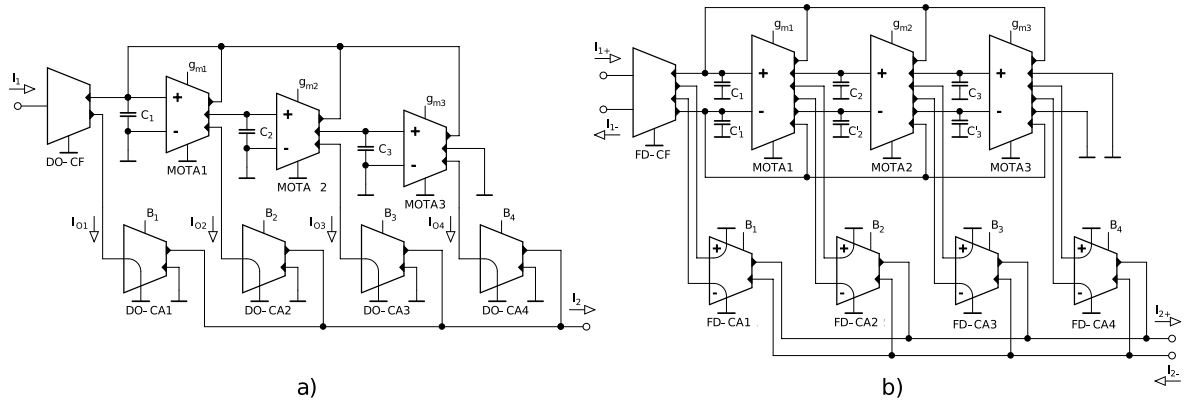


**Figure 1:** Designed FLF-OS 3rd-order filter in a) single-ended, b) fully-differential form

Multiple output operational transconductance amplifiers (MOTA), adjustable current amplifiers (ACA) and differential adjustable current amplifiers (FD-CA) were used in both filters. Electronic controllability of their parametrs (transconductances  $g_{m1} - g_{m3}$  of MOTA and current gains  $B_1 - B_4$  of ACA) is essential feature for implementation into the tunable filters. [1][2]

Both realizations are reciprocal, thus their transfer functions are identical. Tunability of characteristic frequency is possible by changing the transconductances of all MOTA elements simultaneously (must be in proportion). Control of the transfer function is realized by current gains  $B_1 - B_4$ , whereas for F-D version current gains are halved. The proposed 3rd-order S-E and F-D filter offers low-pass (LP), high-pass (HP), two asymmetric band-pass filters (BP) and 2nd-order symmetric band-pass.

**Table 1:** Available transfer functions and their controllability (for F-D realization in bracket)

filter	transfer function	$B_1$	$B_2$	$B_3$	$B_4$
LP 3rd-order	$K_{I(LP)} = (g_{m1}g_{m2}g_{m3})/D$	0	0	0	1 (0.5)
HP 3rd-order	$K_{I(HP)} = (s^3[C_1C_2C_3])/D$	1 (0.5)	1 (0.5)	1 (0.5)	1 (0.5)
BP 3rd-order A	$K_{I(BP-A)} = (s^2[g_{m1}C_2C_3])/D$	0	1 (0.5)	0	0
BP 3rd-order B	$K_{I(BP-B)} = (s[g_{m1}g_{m2}C_3])/D$	0	0	1 (0.5)	0
BP 2nd-order	$K_{I(BP)} = (s^2[g_{m1}C_2C_3] + s[g_{m1}g_{m2}C_3])/D$	0	1 (0.5)	1 (0.5)	0

### 4 SIMULATIONS

Designed filters were simulated in OrCAD Pspice. Transistor models of transconductor (MOTA), current follower (CF) and current amplifier (ACA) in CMOS TSMC 0.18  $\mu\text{m}$  technology were used.

Transconductances of appropriate MOTA ( $g_{m1} = 1.26 \text{ mS}$ ,  $g_{m2} = 628 \text{ }\mu\text{S}$  and  $g_{m3} = 314 \text{ }\mu\text{S}$ ), which are identical for both of this circuits, I calculated from denominator coefficients by expressing from (1). In default configuration, the characteristic frequency is  $f_0 = 100 \text{ kHz}$  and quality factor  $Q = 0.92$ .

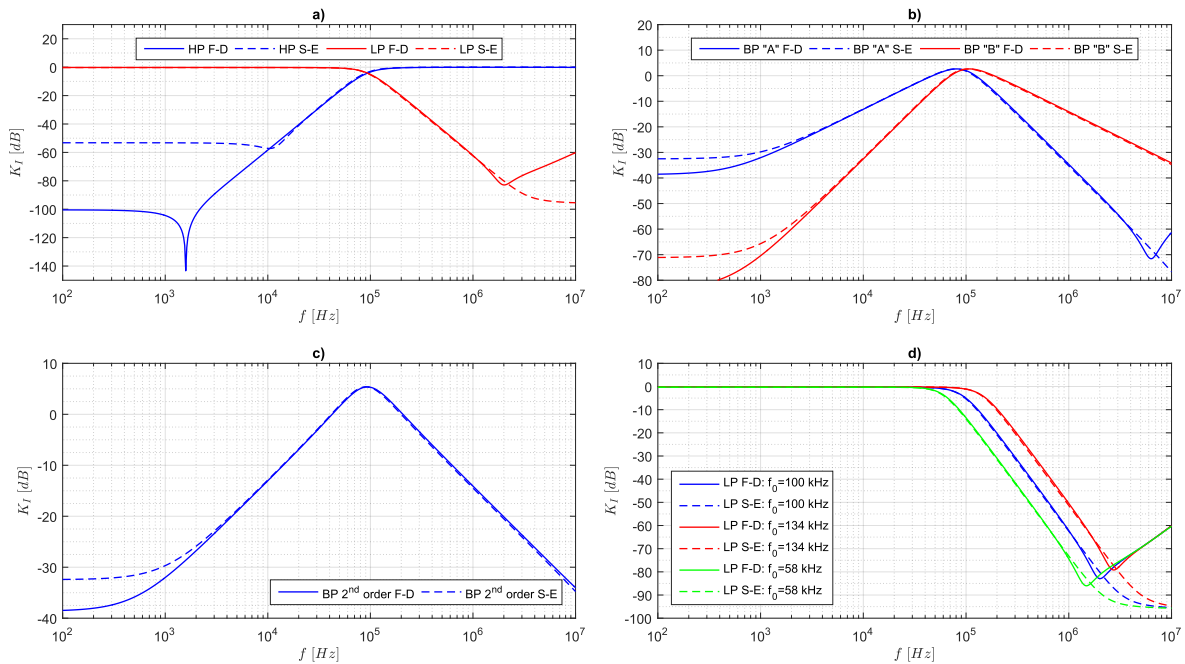


**Figure 2:** Module characteristics of available transfer functions FLF filter

## 5 CONCLUSION

In this paper, the electronically reconfigurable multifunctional 3rd-order FLF filter in single-ended and fully-differential form was proposed. Control of characteristics frequency is possible by changing the transconductances of all MOTA elements simultaneously. The proposed SISO filters have electronically controllable transfer function. It is clear, that fully-differential filter has better attenuation in band-stop area. Both circuits are suitable for on-chip implementation.

## REFERENCES

- [1] ŠOTNER, R.; PETRŽELA, J.; JEŘÁBEK, J.; VRBA, K. a DOSTÁL, T. [online] *Solutions of reconnection-less OTA-based biquads with electrical transfer response reconfiguration*. 25th International Conference Radioelektronika, Pardubice, 2015. ISBN: 978-1-4799-8119-9.
- [2] JEŘÁBEK, J.; ŠOTNER, R.; POLÁK, J.; VRBA, K.; DOSTÁL, T. *Reconnection-Less Electronically Reconfigurable Filter with Adjustable Gain Using Voltage Differencing Current Conveyor*. Elektronika Ir Elektrotechnika, 2016, Vol. 22, No. 6, p. 39-45. ISSN: 1392-1215.
- [3] JEŘÁBEK, J.; VRBA, K. *Design of Fully Differential Filters with Basic Active Elements Working in the Current Mode*. Elektrověue. 2010, Vol. 1, No. 1, p. 28-32. ISSN: 1213-1539.
- [4] CHEN, Wai-Kai. *The circuits and filters handbook*. 2nd ed. Boca Raton, FL: CRC Press, 2003. ISBN: 0-8493-0912-3.
- [5] DOSTÁL, T. *Filters with Multi-Loop Feedback Structure in Current Mode*. Radioengineering. 2003, Vol. 12, No. 3, p. 6-11. ISSN: 1805-9600.

# CONTROL SYSTEM FOR MICRO HYDROPOWER PLANT

**Jan Novotný**

Bachelor Degree Programme (3), FEEC BUT

E-mail: xnovot1i@vutbr.cz

Supervised by: Tomáš Beneš

E-mail: xbenes23@stud.feec.vutbr.cz

**Abstract:** This paper deals with design and realization of control system and power part in application for micro hydropower plant consisting of non-regulation turbine and asynchronous generator working in isolated network. The micro hydropower plant is intended to serve as a substitute for gasoline generators at appropriate locations, thus reducing environmental impact and increasing electricity coverage in remote locations. The main goal was to design its own control system, which will be more cost-effective than using a PLC. The next part deals with the design of the power part needed to control the water turbine. An integral part was also the assembly, commissioning and programming of its own control system.

**Keywords:** water microsupply, control system, PLC, asynchronous generator, isolated network, ARM

## 1 INTRODUCTION

Today, electricity is part of everyday life and we cannot imagine life without it. Few people also know what is behind the production of electricity and the only thing that is important for consumers is its final price (cost of technology, fuel price, maintenance and other factors). Less emphasis is then placed on the impact of the environment. The nation's goal is to strive to produce energy from renewable sources as much as possible so as to minimize the burden on the environment.

The main idea of the work is to replace the portable gasoline generator in places without access to the public network. Although these generators are affordable, they are expensive to operate and produce emissions.

This paper deals with the design and implementation of a control system and power part of the control for a water micro source consisting of a non-regulating turbine and an asynchronous generator operating in an isolated network. The project is developed in cooperation with the company ELZACO spol. s r.o..

## 2 REQUIREMENTS FOR IMPLEMENTATION

The aim was to design and implement a control system for a water micro source at an affordable price, as the final product should be exported to third world countries. Another requirement was the simplicity of operation due to the designation for operation without special qualifications. The task is to create the electrical part of the generator control, where in the development phase I will replace the turbine with the generator with a pair of directly mechanically connected asynchronous motors. One asynchronous motor will have the function of a turbine with a torque curve similar to a turbine, which will be realized by a frequency converter. The frequency converter will provide protection against possible conditions to which the turbine may enter and will be more resistant to control deficiencies during initial tests. The next phase will be testing the control at the site connected to the turbine.

The use of a self-excited asynchronous generator [1] [2] with one output phase was one requirement in order to reduce the purchase price. However, this requirement places increased demands on control.

## 2.1 PRINCIPLE OF IMPLEMENTATION

The control principle used is based on the fact that the turbine power is approximately constant around the rated speed at a constant flow and gradient (non-regulating turbine). Constant speed is achieved with the help of a constant load on the generator. Thus, the so-called ballast (artificial) load will be used, with the help of which it is possible to achieve a constant load of the generator even if no load is connected to the source output. When the payload changes (connection of an external device), the power balance is balanced and the speed is changed. However, for operational reasons, the turbine may change its power over time (change of slope and flow) and mere regulation to constant power is not sufficient to maintain the operating parameters of the isolated network. Another control factor is the output voltage, which in a self-excited asynchronous generator depends on the size of the excitation capacity and the load impedance. Improper design of excitation capacities will prevent speed control due to the behavior of the generator as a soft voltage source and the turbine can then reach continuous speed, which is not suitable for long life of the micro source.

The control parameters should meet the standard for petrol generators ČSN ISO 8528-5. For the transient and in terms of steady state, the output of the source will be compared with the parameters of the normal network specified in the standard ČSN EN 50160 ed. 3.

## 3 CABINET

The figure 1 shows a block diagram of the overall system connection. The connection for testing will be different for the turbine, which will be replaced by a motor-generator (described in the chapter 2.1) and the control system will be located in a different switchboard than the power section. The connection between the power switchboard and the control switchboard will be made using cables with heavy connectors. This solution was chosen due to the possibility of simple replacement of the control system. During the final design, the switchboard will be optimized to the most compact dimensions.

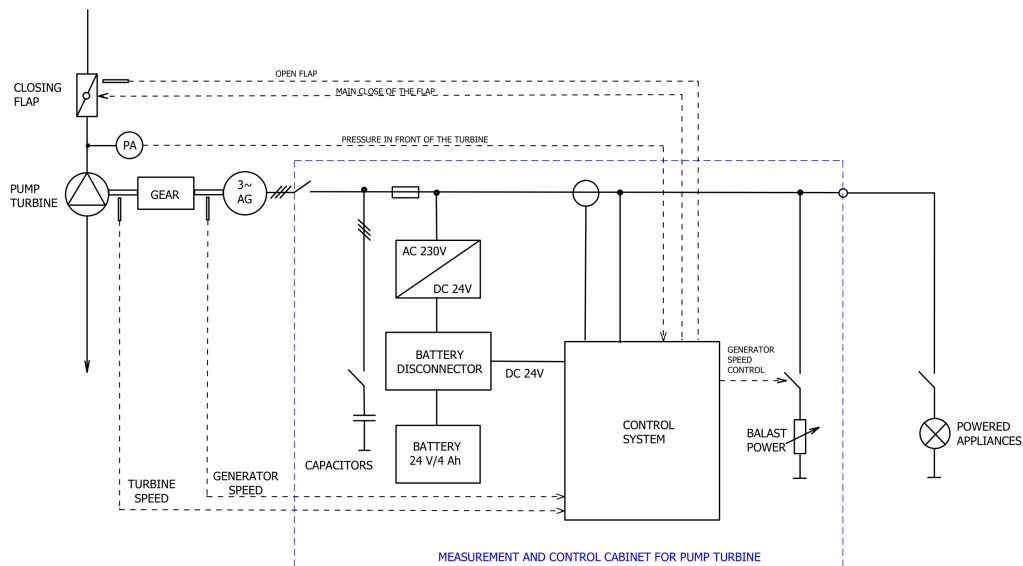


**Figure 1:** Block diagram of the switchboard of the power section of the water micro-source

## 4 CONTROL SYSTEM

Given the requirement to minimize cost, an alternative to a PLC control system was considered. The analysis revealed that with the proposed control system, the price could be a quarter compared to a solution with a PLC. The savings do not only lie in the price of the control system, but also in the implementation of the network analyzer as a peripheral into the control system itself.



(a) Assembled own control system



(b) Power control cabinet

**Figure 2:** Own control system and power control cabinet

### 4.1 PERIPHERALS OF THE CONTROL SYSTEM

I/O peripherals have been designed according to industrial requirements (similar to PLC). Thus, digital I/Os are designed with levels of 24 V and analog I/Os have ranges 0...10 V or 0...20 mA.

The control system contains the following peripherals:

- **16 digital inputs** with 24V V logic level, they are galvanically separated to 5 kV.
- **4 fast digital inputs** differ from normal digital inputs only in speed, higher impedance, comparator, the possibility of measuring time events and counter functions.
- **20 digital outputs**, which are solved as an open collector using the circuit VN340. Subsequently, the outputs are equipped with a fuse on the power input and are galvanically isolated to 2.5 kV.
- **4 analog inputs** are switchable between voltage and current. Voltage inputs are possible as 0...10 V and current inputs in the range 0...20 mA, where it is possible to set the range 4...20 mA.
- **4 analog outputs** are current in the range 0...20 mA with software option to select range 4...20 mA.
- **Display** displaying the measured data using a 4-digit alphanumeric display and in combination with an encoder allows setting of basic parameters.
- **USB** will allow setting advanced parameters using a PC application.
- **Memory** - the control system includes the possibility of inserting a micro-SD memory card. There is also an external EEPROM and RAM memory.
- **Power meter** supports voltage measurement in the range  $\pm 500$  V DC and current measurement 0...5 A AC, which requires a current measuring transformer, the conversion of which determines the maximum measured current.

## 4.2 REALIZATION

The control system (figure 2a) was designed as one four-layer printed circuit board. An ARM processor from Atmel ATSAM4E16 [3] was chosen as the main processor. The first implemented version of the control system showed shortcomings in the accuracy of current measurement. The cause of the inaccuracy was the circuit used using Hall probes. This circuit had a very unstable signal at its output, which led to unsatisfactory measurement accuracy. In another version of the prototype, the principle for measuring current was changed using a measuring current transformer, the output current of which causes a voltage drop across the measuring resistor. This voltage drop is then amplified and measured by an AD transducer.

The programming environment Atmel Studio 7 was used for the development of the SW. The control system contains a program for the operation of peripherals and currently only the implementation of the control algorithm for the micro source remains.

The HW was installed, revived, tested and SW equipment was created to operate all peripherals of the control system.

## 5 CONCLUSION

I managed to design, revive and test our own control system for a water micro source with other own peripherals. The implementation of a network analyzer proved to be particularly challenging. One of the advantages is the start-up time in terms of control and safety at start-up, as the battery for starting the control system does not have to be implemented before the water supply is opened and thus the control system will switch on when the generator starts.

It is estimated that the cost of the proposed control system could be a quarter compared to using a PLC solution. In the next phase of control system development, the design of the control system for industrial use will be reworked. The main change will be the partition into several sub-boards and their placement in a box on a DIN-rail to save space and pass EMC tests. The use of the control system does not have to be limited to a water micro source, as it has been designed universally.

## ACKNOWLEDGMENT

I would like to thank the company ELZACO spol. s r.o., which offered me the background for development and material support. I would also like to thank Ing. Tomáš Beneš and Ing. Jakub Streit for their valuable advice.

## REFERENCES

- [1] PETROV, G.N. Elektrické stroje 2: Asynchronní stroje-synchronní stroje. Praha: Academia, 1982, 728 s
- [2] HORNÍK, Vincenc. Problematika provozu asynchronních generátorů malých vodních elektráren v praxi a možnosti jejich využití pro napájení ostrovních sítí. Vysoké učení technické v Brně. Fakulta elektrotechniky a komunikačních technologií, 2013, 65 l. : il. + 1 CD-ROM.
- [3] Atmel. ATMEL AT03088: Getting Started with SAM4E [online]. 2013 [cit. 11. 3. 2020]. Dostupné z: [http://ww1.microchip.com/downloads/en/Appnotes/Atmel-42145-SAM-AT03088-Getting-Started-with-SAM4E\\_Application-Note.pdf](http://ww1.microchip.com/downloads/en/Appnotes/Atmel-42145-SAM-AT03088-Getting-Started-with-SAM4E_Application-Note.pdf)

# THE CRANE MANIPULATOR FOR THE 3D PRINTERS

**Khmil Denys**

Bachelor Degree Programme (3), FEEC BUT

E-mail: xkhmil00@stud.feec.vutbr.cz

Supervised by: Jakub Arm

E-mail: Jakub.Arm@vut.cz

**Abstract:** The aim of this work is to design the architecture of a manipulator that takes the finished product out of the 3D printer. This article deals with the whole concept of the machine, its design in the CAD program Siemens NX12, selection of parts, software development, and real prototype assembling. The manipulator is driven by LinuxCNC ecosystem installed on a single-board computer Beaglebone Black. To control the machine, a client PC application was developed. The manipulator movements are achieved using the tooth rail gearing and closed loop stepper motors Nema23.

**Keywords:** Manipulator, 3D Printer, CAD, LinuxCNC, Beaglebone Black.

## 1 INTRODUCTION

Nowadays 3D printers are commonly used for manufacturing, prototyping or hobby. The main disadvantage of traditional 3D printers is the impossibility of printing a large number of elements without human intervention. To start a new printing, it is necessary for the operator to pull out the printed part and start another print.

An analysis of the current situation in this area has revealed that there are several solutions to this problem. The first one is printing on a belt conveyor, which rotates after printing finishes. This frees space for further printing. The second solution is to use a 6-axis robotic manipulator for removing printed parts. Each of these solutions has its disadvantages. The disadvantage of the first solution is the unstable printing surface which can cause printing problems. For the second solution, it is the high cost and limited manipulating range. [1]

This work deals with the design of a machine that solves this problem in a different way. During the work, a manipulator will be designed. This manipulator removes the printing surface with the printed parts from the printer and places a new one for further printing. All the manipulations are based on the signals from the printers.

## 2 DESIGN OF THE MANIPULATOR

A prototype of the manipulator is designed to operate with up to four printers. This gives a working area of 1 x 1 m. In case of a larger number of printers, the design allows extension of the working area by another 1 m in each direction.

### 2.1 MECHANICS

The manipulator is designed as a 3-axis CNC machine, where X is a horizontal axis, Y - vertical, and Z axis is presented as the mechanism for taking the printing surface from the printer. The machine is mounted to the front side of the printers, so it has access to each one of them.

Figure 1 shows a model of the manipulator that was created in the program Siemens NX12. For the construction of the manipulator, modular aluminum profiles 30 x 30 mm are used. These profiles give good strength and simplicity of manipulator assembling.

Linear motion is provided by a Hiwin HGR15 linear guideway and rack and pinion. Using these components, it is possible to achieve high speed and accuracy of movement over long distances. Another advantage is the possibility of expanding the working area of the machine. [2]

The printing surface pick-up mechanism designed as a carriage which can move 100 mm in both directions from the zero position. This makes it possible to work with printers from both sides of the manipulator. The movement of the printing surface on the carriage is implemented using a belt conveyor which is designed as two belts, one on each side of the carriage. When the manipulator reaches the printer coordinates, Z axis carriage moves inside of the printer and uses a belt conveyor to remove or place the printing surface.

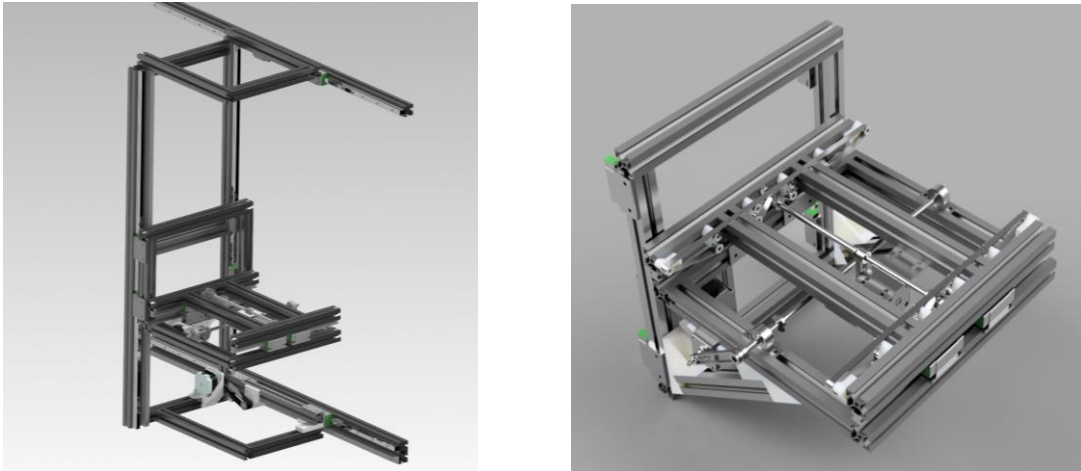


**Figure 1:** Manipulator and Z axis carriage

## 2.2 MOTORS

For the design of the manipulator, closed loop stepper motors with a torque of 0.9 N.m from the company Makerbase are used. These motors have drivers mounted on the back side of the motor and have a built-in position sensor to provide feedback.

In this case, the feedback is implemented using a magnet located on the shaft and magnetic angle sensors. Based on the output of these sensors, the driver evaluates whether the required movement has occurred. If it is not, driver will try to compensate the difference or change its state to an error.

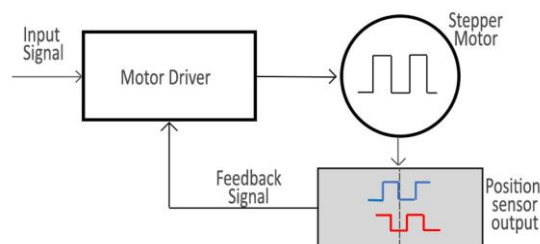


**Figure 2:** Closed loop stepper motor principle

The advantage of magnetic encoder against optical, that are typically installed on these motors, is smaller size, better reliability, and better accuracy (2048 pulses per revolution versus 1000 pulses per revolution) [3].

Communication between the control unit and this driver can be implemented using standard STEP / DIR signals or using the serial interface SPI or UART. Communication of this type makes it possible not only to control the movement of the motor, but also to read or change the settings of the driver.

## 2.3 ELECTRONICS

Figure 3 shows a schematic arrangement of the electronic components of the machine. The machine control is divided into main and secondary control components. The main component controls the movements in X and Y axes while the secondary controls Z-axis mechanism.

The main control component is Beaglebone Black. The single-board computer was chosen because of the possibility of implementing more complex service modules such as industrial I/O modules or a motor driver with industrial communication protocols support (EtherCAT, Powerlink etc.).

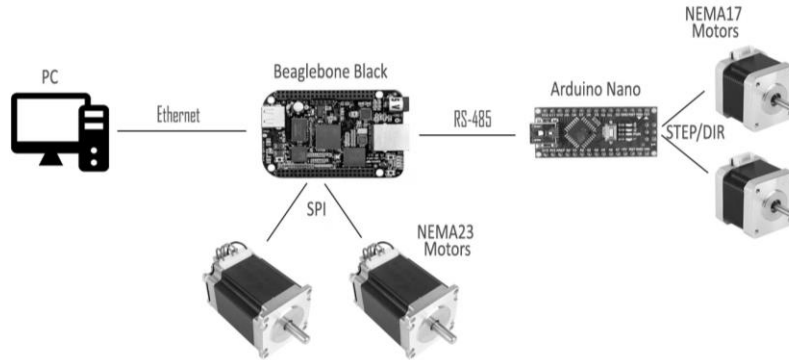


**Figure 3:** Electronic component arrangement

Arduino Nano was chosen as a secondary control component. Based on a command from the Beaglebone and the values from the sensors, Arduino will control the movements of the Z-axis carriage and the belt conveyor. Two inductive sensors are used for detection of the carriage limit positions. Capacitive sensors are used for detection of the printing surface on a belt conveyor, which allows using not only metal surfaces but also glass.

For the Arduino, a printed circuit board was designed, which makes it possible to connect up to 5 sensors using optocouplers and two stepper motors.

## 2.4 SOFTWARE

For controlling the manipulator, a client computer application was developed. Interface of this program is shown in Figure 4. The program is designed to work with four printers, each of which has preset coordinates. Using the buttons, we can choose whether the machine must remove the printed part, place a new printing surface or just move to the printer. From the client app, commands are sent to the Beaglebone Black single board computer using the TCP/IP protocol in a structure format (X, Y, direction), where X and Y are coordinates and the direction determines whether the printing surface will be removed or placed.

LinuxCNC was installed on the Beaglebone, which is controlled by a Python script. The script needs a few more files for proper functionality. The overall structure of the Beaglebone software is shown in Figure 4. The first file is a *.bbio* file. This file defines functions of the individual pins of the Beaglebone. Next one used is an *.ini* file, in this file the parameters for LinuxCNC are set, such as the number of machine axes, maximum speed and acceleration of movements, etc. The last one is the *.hal* file, which serves as a layer between software and hardware and allows the script to work with various hardware types.

After running the script, first of all, all the required settings are set and then LinuxCNC is started. At the beginning of each movement, the possibility of starting the machine is checked (the Estop button is not pressed and machine is not in fault state). If all conditions are good, the manipulator starts moving to the specified coordinates. After reaching the position, Beaglebone sends a command for Arduino subsystem using the RS-485 bus [4].

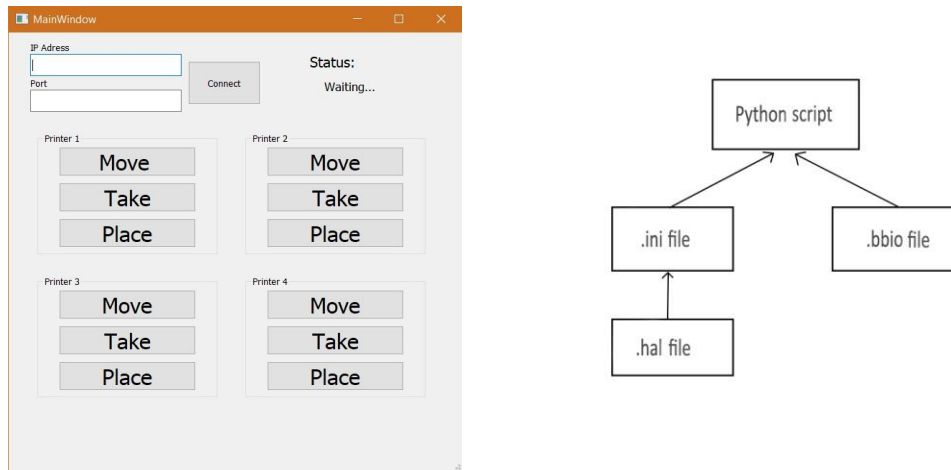


**Figure 4:** Client user interface and software structure

Based on the command from the Beaglebone, Arduino turns on the motor to move the carriage into the printer to a precise, predetermined location. Then it starts the sequence of removing the printing surface with the printed part, i.e. starts the movement of the belt conveyor and will wait until it receives a signal that the target position of the pad has been reached. When a pad is detected on the cart, the Arduino will send a confirmation to the Beaglebone that the command has been properly performed and the machine will continue to move. In case the pad is not detected within a certain time, an error message will be sent and the whole machine will be stopped.

### 3 CONCLUSION

During the work, the mechanical principle of the manipulator was designed. Based on the calculations, the necessary components were selected. Using selected components, a 3D model of the manipulator was created. According to this model a prototype of the machine will be assembled. As the next step, a client application for the computer, software for Beaglebone and Arduino, and communication between them were developed. The next step will be to build and test a physical prototype of the machine.

The developed machine makes it possible to automatically collect printed parts and start next printing. Using this machine instead of human operator, some benefits arises, such as time efficiency and cost reduction. Since the components are chosen from the hobby and semiprofessional domain, it is not yet possible to quantify the financial benefit. A distinct advantage of this manipulator is the possibility to extend a working area for more printers.

### REFERENCES

- [1] Turn Your 3D Printer Into a Factory: Automatically Remove Parts [online]. [Accessed 2020-03-09]. Available at: <https://www.instructables.com/id/Turn-Your-3D-Printer-Into-a-Factory-Automatically-/>
- [2] Hiwin Datasheet [online]. [Accessed 2020-03-09]. Available at: [https://www.hiwin.com/pdf/linear\\_guideways.pdf](https://www.hiwin.com/pdf/linear_guideways.pdf)
- [3] A1333LLETR-T Datasheet [online]. [Accessed 2020-03-09]. Available at: <https://pdf1.alldatasheet.com/datasheet-pdf/view/1148490/ALLEGRO/A1333LLETR-T.html>
- [4] Machinekit Documentation [online]. [Accessed 2020-03-12]. Available at: <http://www.machinekit.io/docs/>

# DIGITAL CONTROLLED POWER SUPPLY

**Martin Mikulka**

Bachelor Degree Programme (3), FEEC BUT

E-mail: xmikul64@stud.feec.vutbr.cz

Supervised by: Jiří Háze

E-mail: haze@feec.vutbr.cz

**Abstract:** This work deals with the design of a laboratory power supply with a modular number of additional modules for individual inputs, outputs or monitoring circuits. Design of individual parts of control circuits, circuits for monitoring of output parameters and their control by the user is solved. Furthermore, the design of the control module, which is in charge of managing the entire source, including the added modules, is solved.

**Keywords:** Power supply, modularity, digital control, STM32, regulation, control, communication

## 1 INTRODUCTION

Laboratory supply is integral part of every laboratory or home electrical workshop. Most of the experiments used with laboratory power supply is powered by single ended supply. There are also some special applications, like audio amplifiers, which needs symmetrical power supply. This type of power supply also needs quite solid accuracy and low output noise and adequate power. This work is about construction and hardware design of such a power supply. There is also a description of software, hardware design and realization. The power supply is a modular type, which means that is possible to connect up to 127 modules such as another power supplies, monitoring circuits or controlling circuits. Modules are galvanic isolated from themselves and from the mains. There is also variant of grounding them with build-in relays. All of the modules, of the power supply, can be controlled from any connected control module or remote device, such as computer. There are two build-in modules, which can operate in voltage range 0-24 V<sub>DC</sub> and with current range 0-5 A<sub>DC</sub>. These modules are easily changeable to voltage ranges up to 100 V<sub>DC</sub>. For the change, you only needed to change main transformer, voltage divider and software description (identification) of module. Regulators and other parts are already ready.

## 2 CONTROLL AND DEVICE DRIVE PART

The control part of the power supply is implemented as separate PCB (module). That module contains I2C [3] bus for communication with the individual modules of power supply, individual I2C bus for temperature sensors and other elements in basic part power supply. Whole power supply is divided into 2 modules of power supply and one control module. Control module also contains RS232 for communication with remote control such as PC. That external control part can be also connected with I2C. All of the functions are controlled by MCU STM32F103[1]. That microcontroller provide driving of cooling system, user input control of power part, communication with other modules / PC, etc.

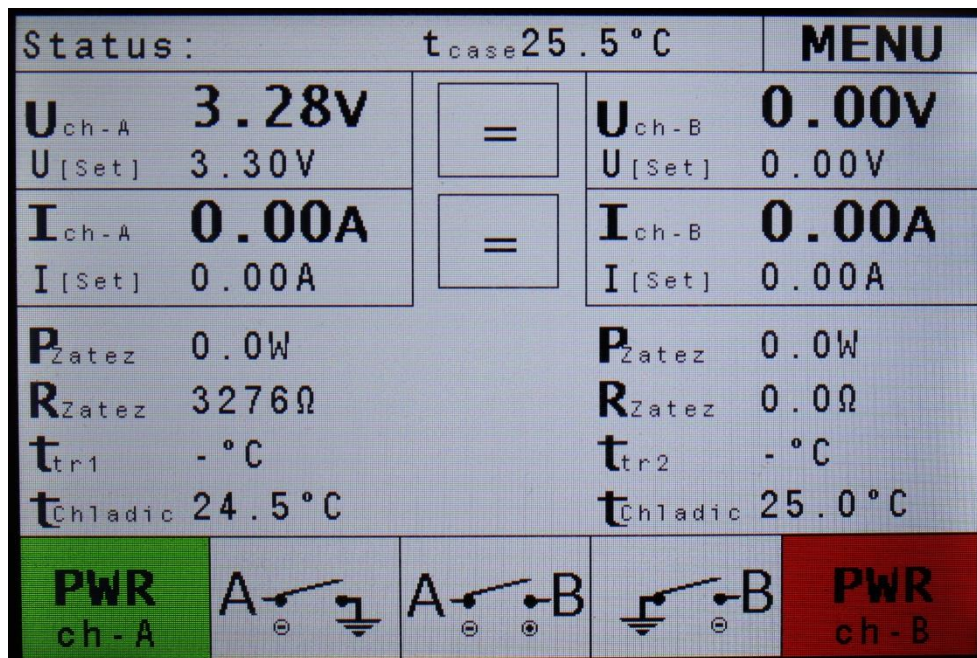
As a user interface is used LCD display about size 3,95", with resolution of 480x320 px. That resolution is enough for organized representation of individual parameters and simple control by using touch surface. On the LCD is displayed all of the necessary data of power supply.

Control module communicate with other modules on a frequency about 400 kHz. This frequency is enough fast for communication with all the 127 modules till 300 ms including elaboration accepted

or sent data. Because of this, most of the communication is performed by using DMA requirements and the core is taking care only about screen redrawing and user control interface.

User control of the power supply is mostly managed by using display by touchscreen. There is also rotary encoder for variable settings such as setting of voltage or current amplitude. This type of input, specifically for this type of data, is more comfortable. Main on/off the power supply to the stand-by regime is provided by using separate button on the main panel. The power supply is also possible to shut down by mains switch, which is placed on the back side of the device.

External modules are connected on the I2C bus, which work on 400 kHz frequency. The I2C bus has big limitations on load capacity and because of this is not possible to connect the external devices with the long power cord or connecting the external devices at all. Due to extension of the I2C bus and elimination the problem with capacity, there was used converter P82B96 [2]. This driver moves the voltage on the bus up to 12 V and ensure greater line-capacity loads.



Picture 1: Device home screen with shown main values

### 3 POWER SUPPLY MODULE

Module of the power supply is main part of the device. Its function is step regulation of output parameters (voltage, current or even frequency or signal shape) and their measurement. Each module has its own galvanically isolated power supply and own power input. The two main power supply modules have the possibility of regulating the output voltage in the range of 0-24 V and the current in the range of 0-5 A. These parameters are determined only by the used transformer. Transformers are the industrial older type with an output voltage of 24 V and a power of 120 VA. The basic modules do not have the possibility to regulate the output current waveform or its frequency. Connectable external power supply modules, which are not part of this work, could control these signal properties, respectively, the main control unit is ready for this control.

The power supply is starting the search for modules automatically every time the power supply is started. There is also an option of manual searching in the menu. This feature allows automatic mapping of external modules connected to the power supply. Each module (each I2C address) is asked for identification using a special data package. The power supply works with packages with a size of 28 bytes and for this reason this size has been preserved for the identification data package. If no response is received at the given address (NACK), the address is skipped. If the response arrives (ACK), an identification request is sent, the response is decoded and stored in the database in the

control module and then the module is accessible to the user for switching it in the menu or control from remote controller such as PC. The identification packet is described in Table 1. If the module has other options that did not fit into the basic identification packet, the appropriate value is set to the 24th byte ("Module status"), which the control module evaluates and sends a request for closer identification (e.g. signal output shape, shift control, etc.). The modules are then included in the memory. If they are selected by the user (the given module of the power supply is switched on), they are regularly asked for start of measuring values, as well as entering new values. The communication timestamp is set to 300 ms when an 8 bit address is used. Control module and basic power supply modules are software-ready to change to a 10-bit address for connecting up to 1023 devices, but this option is not preset in the user settings and must be activated in the software itself. During communication, each module has approximately 30 ms in response to the control module. The module must process the desired data into a communication protocol and calculate a checksum during that time. Full communication transfer takes about 80 ms. The measurement of individual values in the power supply modules takes place based on DMA transfer from peripheral to memory. Meanwhile software part only checks for possible errors when there isn't any calculation needed (checksum, temperature, etc.).

**Table 1:** Communication identification packet

Size	SLAVE action use	MASTER action use
32 bits	-	Maximal input voltage
32 bits	-	Input voltage $\frac{1}{2}$
32 bits	-	Input voltage $\frac{2}{2}$
32 bits	-	Maximal output current
32 bits	-	Maximal output frequency
8 bits	Identification command byte 1	DAC resolution [bit]
8 bits	Identification command byte 2	ADC resolution [bit]
8 bits	-	Additional module parts (relay etc.)
8 bits	-	Module state (Error, OK etc.)
32 bits	CRC	CRC



**Picture 2:** Two of basic modules on common heatsink

## 4 REMOTE CONTROL

Remote control of the power supply is possible via the RS232 bus or by connecting the control device to the external I2C bus. Control via the RS232 bus is provided using ASCII characters and it is therefore possible to control it clearly from any console that allows communication via RS232. The communication contains several commands listed after sending the character "?". When control module receives invalid command, that command table is also printed. Communication via the I2C interface is a bit more complicated. That I2C bus must follow special protocol described earlier. It's necessary to use special program or device for that reason. This communication has two control options, one is reading data from modules and writing data directly to the modules in the same form as the control module. The control module reads this data in the same way as the controlled module and writes the data to the display as if it were entered directly there.

The second possibility of communication via I2C is the connection as a slave device. When this variant is selected, that device appears as new slave device and need identical ID (address). When the control module selected this device, it is needed to transfer needed data such as new values of voltage amplitude etc. In the case of a request for reading rather than writing to these modules, the desired information is sent during the next communication cycle.

## 5 CONCLUSION

The result of the work is a fully functional adjustable power supply with two basic power supply modules, cooling, and other blocks necessary for full-fledged operation. The power supply is tested and gradually measured, which provides the necessary data for the design and development of other modules with higher quality. That new modules will be still connectable to this basic source, which can easily manage their work. The measured parameters of the power supply are sufficient for all the work that is expected from the power supply.

The first of the other modules is almost done. It is an AC power supply module with the possibility of sampling a signal with triangle, sine or rectangle shape. There will be also space for customized signal. Signal can be sampled with frequency up to 50 kHz with a resolution of 360 samples per period. The output range of this power supply module is still only in range of -50 V to +50 V with maximum current 2 A (current and voltage adjustable). Next version of that module is prepared for voltages up to 350 V to allow sampling fully separated output like island photovoltaic system.

## REFERENCE

- [1] *STM32 32-bit Arm Cortex MCUs* [online]. STMicroelectronics [cit. 2019-12-09]. Available at: <https://www.st.com/en/microcontrollers-microprocessors/stm32-32-bit-arm-cortex-mcus.html>
- [2] *P82B96: datasheet. NXP Semiconductors* [online]. [cit. 2019-09-12]. Available at: <https://www.nxp.com/docs/en/data-sheet/P82B96.pdf>
- [3] *I2C: SparkFun Electronics* [online]. 2013 [cit. 2019-12-09]. Available at: <https://learn.sparkfun.com/tutorials/i2c/all>

# REMOTE-CONTROLLED CROSS-COUNTRY FOUR-WHEELER

**Radim Kejzlar**

Bachelor Degree Programme (3.), FEEC BUT

E-mail: xkejzl00@stud.feec.vutbr.cz

Supervised by: Jiří Háze

E-mail: haze@vutbr.cz

**Abstract:** The thesis deals with a complete design of a remote controlled cross-country four-wheeler for FEEC BUT „Elektrikarium“. Vehicle can be controlled using the Android smart phone app. The vehicle uses a BLDC motor with a regulator and control unit in the form of a microcontroller from the AVR family. The thesis describes the selection of components and the actual solution of communication between the HC-05 module, application and microcontroller with regulator. Part of the thesis is also a practical demonstration of the model.

**Keywords:** RC vehicle, BLDC, Regulator, HC-05, AVR, ATMEGA, Bluetooth, MIT App Inventor 2

## 1 INTRODUCTION

RC vehicle models are an important part of hobbies and military and space technology today. This time allows construction of different types of RC models for specific applications. In this text, there is design of a remotely controlled cross-country four-wheeler suitable for the BUT FEKT interactive room with the ability to overcome larger obstacles with solid speed.

## 2 CHASSIS

Great demands were placed on the chassis, including space for electronics, good suspension and durability. The original variant has been a chassis printed on a 3D printer. Due to lack of time, this concept was rejected and a commercially available variant was decided. The most advantageous variants were damaged RC vehicles due to very low price. These broken RC vehicles usually have only damaged electronics and the chassis is intact. The RC Truggy in 1/16 scale in aluminum-plastic design with 4x4 drive was therefore chosen as the chassis. This chassis comes from the leading manufacturer of RC models HIMOTO with the possibility of replacing individual parts (Fig. 1).

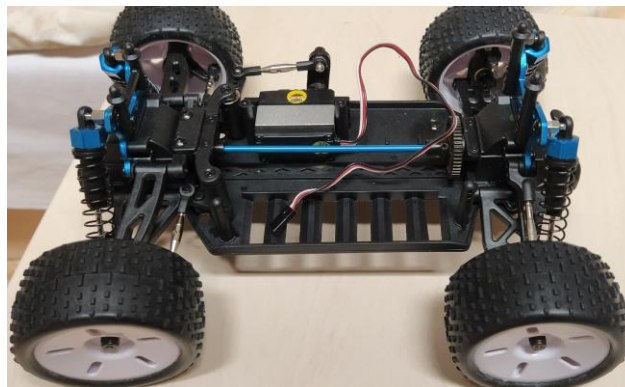


**Figure 1:** Chassis of RC Truggy 1/16 HIMOTO

### 3 CONCEPT OF CONTROL ELECTRONICS

The concept of the control electronics is shown in a functional block diagram (Fig. 2). The heart of the whole control is the AVR ATMEGA 328P microcontroller, which receives data from the Bluetooth module, processes it and sends it in the form of a PWM signal to the BLDC motor controller, turn servomotor and sets the lights switched on and off. The communication module takes information via Bluetooth from a mobile phone with the installed application. The controller is directly powered by the battery and disconnects these batteries in the event of a discharged battery. For this reason, all electronics are powered by the controller.

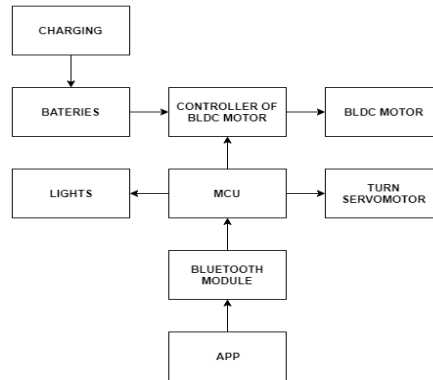


**Figure 2:** Block diagram of control Electronics

### 4 BLDC MOTOR, CONTROLLER AND SERVOMOTOR

In the past, DC motors were very often used. However, these motors do not have good efficiency and over time the commutator carbons wear out. The BLDC motor (Brushless DC) is a synchronous type of motor. Therefore, there is no slip. It means, that control frequency is synchronous with the speed. It is clear from the name that the motor does not contain a commutator. The problem of this commutation is solved in modern BLDC motors by electronic commutation. This is not a solution of classical commutation by electronic systems, but an integral part of the BLDC motor is an electronic unit, best integrated into the motor structure, which controls the supply of individual stator windings. [1] In this case, the electronic commutation is solved by a controller, which regulates the motor speed by PWM control signal with a changing duty between 1 and 2 ms (500 and 1000 Hz). The advantage of these motors is high endurance due to the absence of a commutator and the possibility of precise regulation. For the needs of a four-wheeled vehicle, a combo (combination of motor and controller) without sensors motor BH POWER 2430 and controller 25 A was chosen. This controller also includes a programming card for the initial settings of the speed control and braking. The already integrated servo in the chassis was chosen for turning. This servo is also from HIMOTO with a force of 6 Kg/cm for a sufficiently smooth turn.



**Figure 3:** Selected BLDC motor with regulator and servomotor

## 5 BATTERY SYSTEM AND CHARGING

The vehicle is powered by one two-cell battery of Li-Pol technology. The battery has a capacity of 5500 mAh. This ensures high endurance of the vehicle with time up to 30 minutes. Li-Pol batteries have very high discharge currents and very good capacity stability. The battery is protected against complete discharge by a protective function of the regulator, which disconnects it in case of low voltage. Charging is realized by an external Li-Pol charger, which ensures balancing of individual cells in real time. The user must interfere with the vehicle electronics to recharge the battery.

## 6 PROGRAM SECTION

The main part of the program section is the already mentioned ATMEGA 328P microcontroller. It ensures communication between the Bluetooth module HC-05 and the controller with the servomotor. The Bluetooth module is connected via the USART serial interface and always sends 8-bit application status information in series. The received data in the 8-bit register looks as shown in Table 1 (the individual sections are color-coded).

value of bit	128	64	32	16	8	4	2	1
significance of bit	LIGHTS ON/OFF	DRIVE ON/OFF	DRIVE DIRECTION	SPEED		TURN DIRECTION	TURN POSITION	

**Table 1:** 8-bit communication with significance of each bit

Four bits were reserved for the needs of smooth driving, where two bits show whether the car should go and where and the other two at what speed (4 speeds). The speed can be adjusted in the application described below. A space of a total size of three bits was reserved for turning. One bit determines the direction of turning and the other two determine how much the wheels should be turned. The bit with the highest value (128) is reserved for information on whether the user wishes to switch on the lights.

The microcontroller only functions as a serial data receiver. It converts 8-bit information and converts it into a PWM signal for the controller and servomotor. The PWM signal is implemented by a counter / timer integrated in the microcontroller. Microcontroller also switches transistors to turn on the lights as needed. The micro-controller also operates the function of checking the connection between the mobile device and the Bluetooth module. This is done by another counter / timer, where it is monitored in the interrupt loop if data is still coming. If no data arrives for a while. The microcontroller switches off all controlled devices (controller and servomotor) to prevent the vehicle from escaping spontaneously.

## 7 APP FOR ANDROID OS

The RC four-wheel drive control application was created in the MIT APP INVENTOR 2 development environment. This environment offers intuitive work with mobile device peripherals.

Using the application, turning was tilted by the device. A gyroscope is used for this and the application directly recalculates the tilt values for 2-bit information (Table 1). The layout of the application is shown in Fig. 4. The buttons for the direction of ride are located on the sides of the application screen. It is ensured that both buttons are not pressed at the same time. There are two buttons in the middle of the application. One opens a list of Bluetooth devices to connect to. The user selects the Bluetooth module and the application automatically connects it with a text message above the button: Connected. It is necessary to have the module already paired in settings of the device. With the second button, the user switches the lights of the RC vehicle on and off. In the lower part of the center of the application, there is a slider which can be used to set the already mentioned 4 speeds. This status will be shown in the text box above the slider. The application sends data every 0.5 s to detect microcontroller disconnection and for low power consumption. The whole application is created to dark mode. This ensures low power consumption for today's smart device displays without disturbing the brightness.

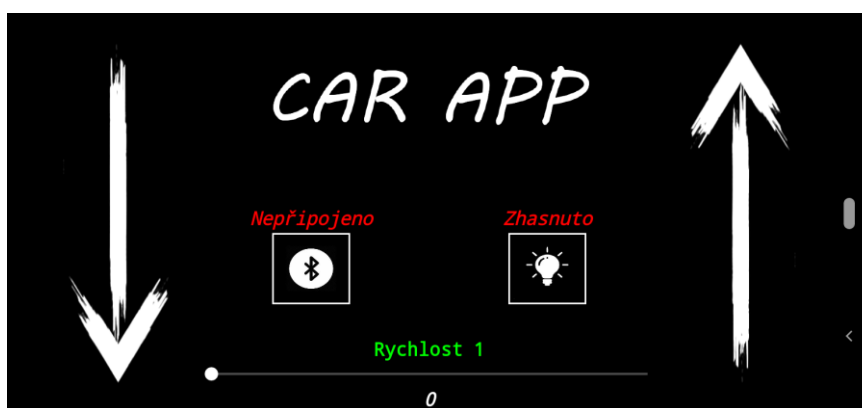


**Figure 4:** APP for Android OS

## 8 CONCLUSION

In this text, a remote-controlled cross-country four-wheeler was largely implemented for the needs of the BUT FEEC Elektrikarium. The model is in a state of complete completion now. As part of the assignment, all conditions for the completion of this work were met. A complete application for the Android OS with communication via Bluetooth was created, a sufficiently durable off-road chassis was ensured and high battery life compared to commercially available RC models. In the program part, all undesirable conditions (disconnection, etc.) were treated. In the future continuation of the work, it is necessary to optimize all parts (app, control electronics).

## REFERENCE

- [1] ŠIMON, Josef. *BLDC aneb DC motor s nulovými náklady na údržbu*. *ELEKTRO* [online]. *FCC PUBLIC*, 2011/10 [cit. 2020-03-09]. Dostupné z: <http://www.odbornecasopisy.cz/elektro/casopis/tema/bldc-aneb-dc-motor-s-nulovymi-naklady-na-udrzbu--10016>
- [2] Big Hobby. *Big Hobby* [online]. 2020 [cit. 2020-03-09]. Dostupné z: <https://www.bighobby.cz/>
- [3] DEJAN. *How Brushless Motor and ESC Work. How To Mechatronics* [online]. 2019 [cit. 2020-03-11]. Available from: <https://howtomechatronics.com/how-it-works/how-brushless-motor-and-esc-work/>
- [4] ATMEL CORPORATION. *ATmega 328P: datasheet* [online]. San Jose, 2015 [cit. 2020-03-09]. Available from: [http://ww1.microchip.com/downloads/en/DeviceDoc/Atmel-7810-Automotive-Microcontrollers-ATmega328P\\_Datasheet.pdf](http://ww1.microchip.com/downloads/en/DeviceDoc/Atmel-7810-Automotive-Microcontrollers-ATmega328P_Datasheet.pdf)

# MEASURING CARD FOR ELECTRICAL IMPEDANCE TOMOGRAPHY V2.0

**Martin Balajka**

Bachelor 2, FEEC BUT

E-mail: xbalaj04@stud.feec.vutbr.cz

Supervised by: Jan Dušek

E-mail: xdusek19@stud.feec.vutbr.cz

**Abstract:** This project aims to improve the first version of an electrical impedance tomography card. The main enhancement of this version is the replacement of Raspberry Pi with a better platform - STM32, implementation of voltage and phase shift measurements, and error correction in the first version. The main reason for moving from Raspberry Pi to STM32 is speed, power consumption and ease of use for the end user.

**Keywords:** Electrical impedance tomography, MOSFET, Shift register, STM32.

## 1 INTRODUCTION

EIT (Electrical Impedance Tomography) EIT is a noninvasive diagnostic method for the reconstruction of impedance distribution in the measured environment. This method is based on the switching current source and voltage measurement. At the same time, the phase shift between voltage and current is measured for the individual measuring combinations. Most EIT studies only deal with the measurement of the real part of the impedance, the resistance without measuring the phase shift - the imaginary part of the impedance. For certain materials, the phase shift itself can range from 1 to 600 mrad depending on the input frequency. For this reason, it was necessary to select the correct components and at the same time guarantee their calibration. The first version of the measurement card for the EIT only included the possibility to control the switching of the current source and the voltage measurement, while the remaining measurements had to be performed on external measuring devices. To limit errors due to cable lengths and subsequent interference it was necessary to design and implement a new version of EIT measuring card, which directly involves phase shift and voltage measurement as well as calibration. The main control board of the measuring card contains the STM32 microcontroller, which ensures communication with the PC via the USB interface. This microcontroller also contains precise 12 bit ADC converters and comparators.

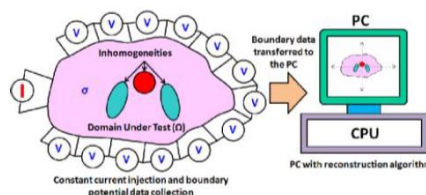


**Figure 1:** EIT [4]

## 2 REALISATION OF MEASURING CARD

The main control board provides communication with the PC, control of switching cards and measurement of voltage and phase shift. Each switching board contains 2 shift registers and 64 opto MOSFETs together with a signaling LED and 16. IO points. Individual switching boards can be chained - additional measuring layers can be added. The measuring card is powered by 12V due

to type of the shift registers used. The functionality of the measuring card is described in more detail in the following subchapters.

## 2.1 SWITCHING AC CURRENT WITH MOSFETS AND INTERNAL WIRING OF SSR

To switch AC current, it is necessary to use a combination of two MOSFETs of type N controlled optoelectronically - fig. no. 2. The TLP3545A was used in this solution, which proved to be successful in the first version of the measuring card, as its transition area was minimal, fully galvanically separated and did not distort the switched signal. To simplify the PCB design, 12V is applied to each anode via a resistor. The cathode is connected to the shift register.

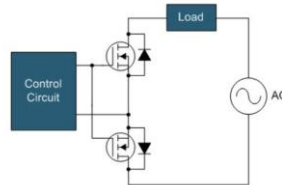


Figure 2: Solution of SSR[1]

## 2.2 SHIFT REGISTER AND SWITCHING OPTO MOSFETS

In order to switch a larger number of opto MOSFETs, it was necessary to select a shift register that allows chaining. In this solution, the HV5530 is used, which allows switching 32 outputs to ground. This shift register has proven successful in several projects. In total, it needs only 3 control signals for control (data in, latch enable and clock). It contains data IN and data OUT for chaining more shift registers. One of the other advantages is the low consumption of 15 mA and max. clock speed 8MHz. The block of the internal connection is shown in fig. no.3.

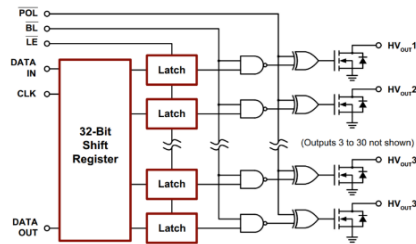


Figure 3: Internal wiring of HV5530. [3]

## 2.3 MEASURING PHASE SHIFT AND VOLTAGE.

This is important information for measurements in the EIT. This connection makes it possible to measure both the real and the imaginary part of the impedance. Fig. no. 4. For measuring real component of impedance are used 12bit ADC converters in combination with a digitally controlled amplifier with adjustable gain in the range of 45dB. Comparators are used to measure the imaginary part of the impedance. For measuring voltage, it is necessary to take into note the AC voltage and its large range. In fig. no. 5. voltage and phase measurements are shown in block form.

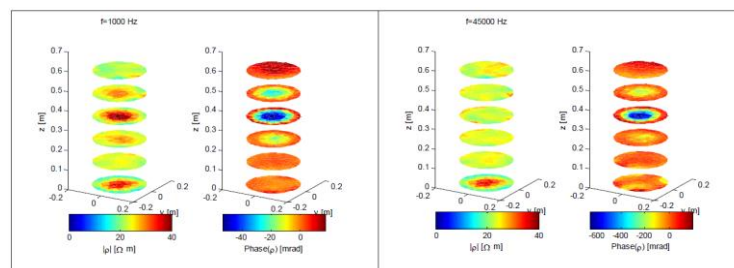
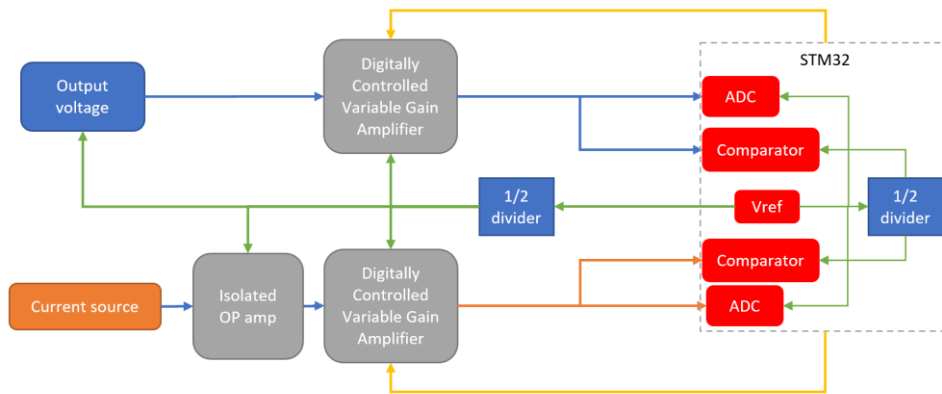


Figure 4: Display of measurement of imaginary and real part of impedance. [2]



**Figure 5:** Measuring of phase shift and voltage.

The connection consists of the measuring branch of the current source and the output voltage. The input from the current branch is isolated from the rest of the circuit using an isolated operational amplifier. Subsequently, an operational amplifier with adjustable gain is used. A  $\frac{1}{2}$  reference voltage divider connected to the non-inverted input, to the inverted input of the measured voltage and output to the input of the ADC and the comparator. This connection makes it possible to shift the transition point of the 0V measured voltage to half the value of the reference source. For more accurate voltage measurement and maintenance within the ADC range, the microcontroller adjusts the required voltage gain. To detect a zero crossing, the comparator compares the measured voltage with  $\frac{1}{2}$  of the reference source; if it exceeds this voltage, the comparator starts the trigger. To calculate the phase shift, the microcontroller records the time from the trigger at the output voltage and current source and at the same time from the start of the measurement of the given combination of IO points. The system allows automatic calibration - when connecting a current source and output voltage to one pair of IO points and connecting a calibration resistor.

## 2.4 CONTROL BOARD AND COMMUNICATION WITH PC

Unlike the original control board, the STM32 microcontroller with the ARM Cortex M7 core is used in this case. It allows communication via CAN, I2C, SPI, USART and USB. Serial communication via USB is used in this application. It allows to communicate in both directions with a PC. The control system application currently works on the principle that the user selects a layer and 2 out of 16 points, which will be used to connect the current power supply, and 2 out of 16 for voltage measurement. Subsequently, the user confirms the selection and the program on the PC sends the data to the control board, which sets the switching card to the user selected IO pins. The control board will measure the value of the measured voltage and the phase against the current source. This measured data is sent back via USB to a PC, where the user can read the values.

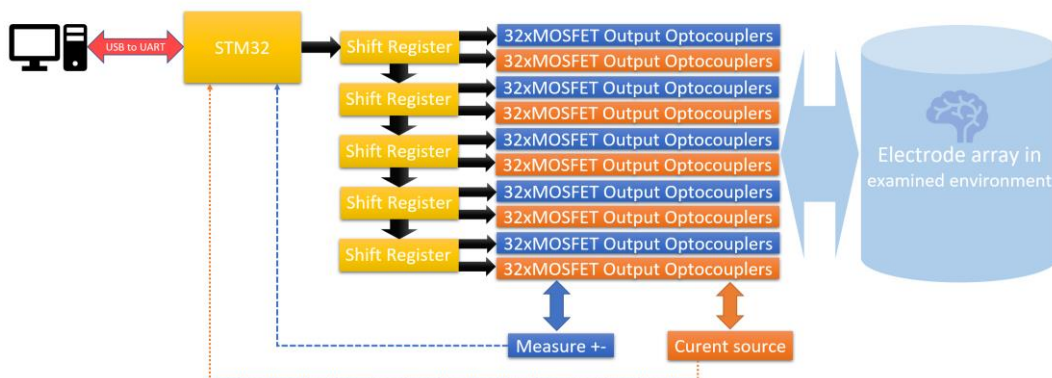


**Figure 6:** Block diagram of communication, control and measurement.

## 2.5 PARTIAL WIRING DIAGRAM.

This part of the diagram contains the connection of 16 opto MOSFETs, one shift register and 4 IO points. The overall scheme has 16 IO points, 64 opto MOSFETs and two shift registers with connections for cascading the boards and the input of the current source and voltage measurement.

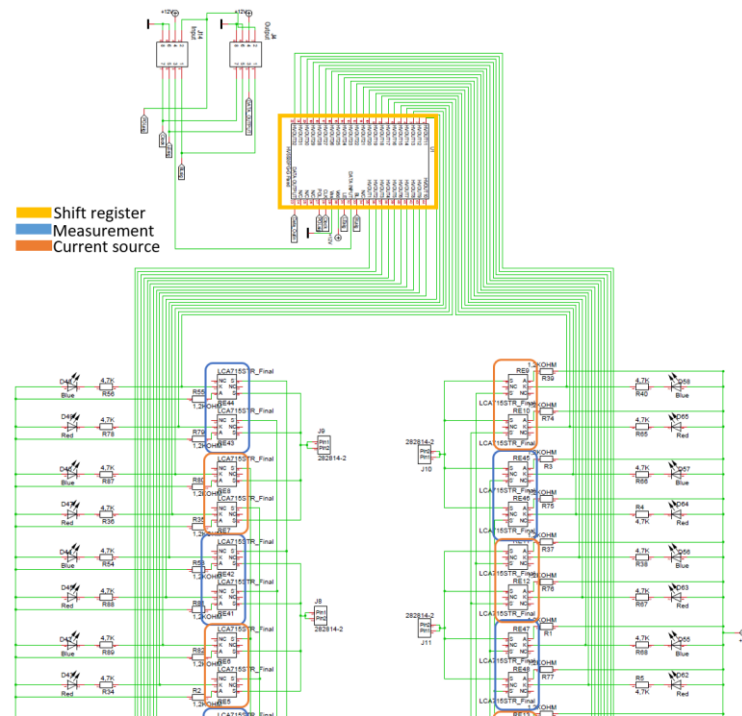


Figure 7: Partial diagram of the switching card.

## 3 CONCLUSION

The new version of the EIT measuring card adds the possibility to directly measure the real and imaginary part of the impedance in the measured environment, without the need to use external instruments and thus increase the comfort of measurement. At the same time, the device can be expanded as needed with additional layers - modularity.

## REFERENCES

- [1] A modern approach to solid-state relay design [online]. 2016 [cit. 2020-03-13]. Available from: [https://e2e.ti.com/blogs\\_/b/industrial\\_strength/archive/2016/07/26/a-modern-approach-to-solid-state-relay-design](https://e2e.ti.com/blogs_/b/industrial_strength/archive/2016/07/26/a-modern-approach-to-solid-state-relay-design)
- [2] Advanced electrical impedance tomography system with high phase accuracy [online]. 2019 [cit. 2020-03-29]. Available from: [https://www.researchgate.net/publication/257929367\\_Advanced\\_electrical\\_impedance\\_tomography\\_system\\_with\\_high\\_phase\\_accuracy](https://www.researchgate.net/publication/257929367_Advanced_electrical_impedance_tomography_system_with_high_phase_accuracy)
- [3] HV5530. Microchip.com [online]. 2017 [cit. 2020-03-13]. Available from: <http://ww1.microchip.com/downloads/en/DeviceDoc/20005851A.pdf>
- [4] BERA, Tushar Kanti, Atanu CHOWDHURY, Hiranmoy MANDAI, Kalyan KAR, Animesh HAIDER a Jampana NAGARAJU. Thin domain wide electrode (TDWE) phantoms for Electrical Impedance Tomography (EIT). Wwww.semanticscholar.org [online]. 2015 [cit. 2019-02-24]. Available from: [https://www.semanticscholar.org/paper/Thin-domain-wide-electrode-\(TDWE\)-phantoms-for-Bera-Chowdhury/43f20ea8802bf4dae40956a32b96d20ba5b46a93](https://www.semanticscholar.org/paper/Thin-domain-wide-electrode-(TDWE)-phantoms-for-Bera-Chowdhury/43f20ea8802bf4dae40956a32b96d20ba5b46a93)

# PROSTATIC CELLS CLASSIFICATION USING DEEP LEARNING

**Jakub Majerčík, Michal Špaček**

Bachelor Degree Programme (2), FEEC BUT

E-mail: xmajer19@stud.feec.vutbr.cz, xspace31@stud.feec.vutbr.cz

Supervised by: Tomáš Vičar, Jaromír Gumulec

E-mail: vicar@vutbr.cz, j.gumulec@med.muni.cz

**Abstract:** Human prostate cancer PC-3 cell line is widely used in cancer research. Previously, Zinc-Resistant variant was described characteristically by higher dry cellular mass determined by quantitative phase imaging. This work aims to classify these 2 cell types into corresponding categories using machine learning methods. We have achieved 97.5% accuracy with the correct preprocessing using Res-Net network.

**Keywords:** cell classification, deep learning, neural network, quantitative phase imaging, microscopy

## 1 INTRODUCTION

Classification of two variants of PC-3 metastatic prostate cancer cell line, being wild-type and Zinc resistant, plays a crucial role in correctly assessing possible diagnosis and afterward an eligible treatment. Additionally, a zinc resistant variant is characterized by increased migration rate, increased cell stiffness and increased cell dry mass, as shown by quantitative phase imaging. With this regard, the aim here was to classify the wild-type and zinc-resistant counterparts based on quantitative phase imaging [3]. During the past decade, we have seen a significant “boom” in the use of machine learning to take over originally human executed tasks. Many fields could start to take advantage of this possibility, such as medicine or many different applications. Our goal was to develop an algorithm that would distinguish between PC-3-WT and PC-3-Zinc-resistant correctly. We approached this task using deep learning methods.

## 2 METHODS

### 2.1 CELL CULTIVATION

PC-3 cells were cultivated at Department of Pathological Physiology, Faculty of Medicine, Masaryk University. Cells were cultured in Ham’s F12 medium with 10% FBS. This medium was supplemented with antibiotics (penicillin 100  $\mu$ /ml and streptomycin 0.1 mg/ml). Cells were maintained at 37°C in a humidified (60%) incubator with 5% CO<sub>2</sub> (Sanyo, Japan). The passages of the PC-3 cell line ranged from 15 to 25 [4].

### 2.2 CELL IMAGING AND DATA GATHERING

Here we performed microscopic acquisitions of the data and subsequent analysis. Imaging was performed using Nanolive holotomographic 3D Cell Explorer microscope with 60x/0.8 objective which provides quantitative information (refractive index tomography) of living cells. Refractive index of Ham’s F12 mounting medium was measured as 1.34. Both types of PC3 cells were cultivated in separate ibidi  $\mu$ -Slide Luer 0.8 chambers. Thus when imaging, 2 unique data-sets have been created. For both categories, there were 200 images taken. Every image consists of 96 slices and was labeled with a slice in which we could see the different cell structures the best. We made use of Steve, microscopy

software, provided by Nanolive. The size of FOV was  $94 \times 94 \times 35 \mu\text{m}$ . The result was 400 tiff-files in total, containing roughly 700 cells. For example images, please see Figure 1.

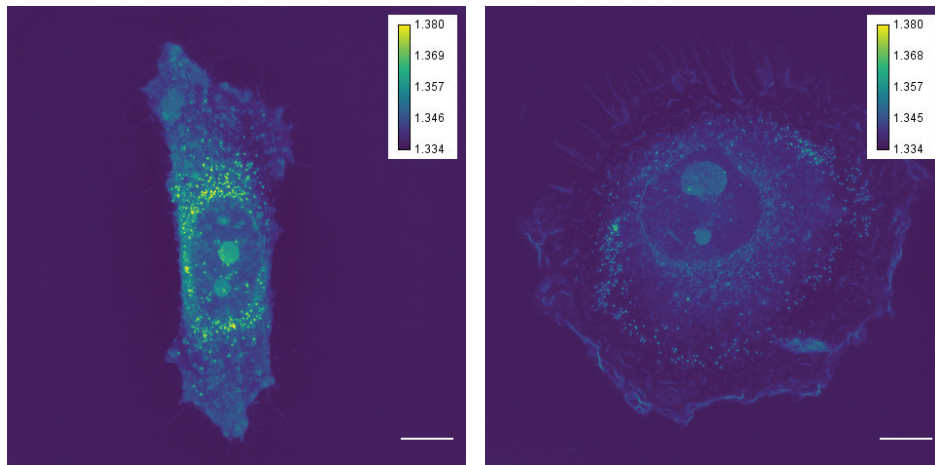


**Figure 1:** Example of typical PC-3 WT and PC-3 Zinc Resistant cells, quantitative phase imaging, max projection, scale bar indicates  $10 \mu\text{m}$ .

### 2.3 IMAGE ANNOTATION AND PREPROCESSING

Every image was labeled with a corresponding type and a number representing the slice, in which we could see the cellular structures the best. We needed to simplify the  $512 \times 512 \times 96$  3D tiff image to a 2D image so it could be used easier in a neural network. Three different types of 2D image formats were tested: (1) use of manually selected slices, (2) maximum intensity projection over all slices, (3) use of slices with the largest entropy values.

### 2.4 DEEP LEARNING, CELL CLASSIFICATION

Considering that our data-set is not large enough, developing our own neural network would not bear any success. We implemented image augmentation in a form of rotating and changing sizes of individual images to expand our data-set but still believed that using an algorithm that is already pretrained would be more beneficial. Hence, ResNet-50 neural network [2] pretrained on ImageNet database [1] was used for our purposes. This neural network was retrained on images of PC-3 cells. Figure 2 represents a neural network architecture diagram. We split our data in a 4:1 ratio, thus 80% was used for training and 20% for testing the network. While training on images acquired in 3 different ways, validation accuracies had been measured. Please see the Table 1 for the exact accuracy values. In our algorithm, we used a batch size of 32. Number of iterations was set to 2700. Data optimization was performed by SGD (stochastic gradient descent) optimizing algorithm with a learning rate of 0.001. Computational time was measured as approximately 31 minutes while running on following computer specifications: Intel Core i7-7700HQ CPU, 8GB DDR4 RAM, 6GB GDDR5 NVIDIA GeForce GTX 1060 GPU. Learning progress is shown in the Figure 3.

Detailed structure and functionals of ResNet-50 neural network can be found in article [2].

## 3 RESULTS

In this project, we managed to classify PC-3 cell cell types in 3 different ways. One of our goals was to find the classification with the best accuracy. All 3 approaches attained an accuracy greater than 90%, however, from 2D image format methods that were tested, the best accuracy of 97.5% was

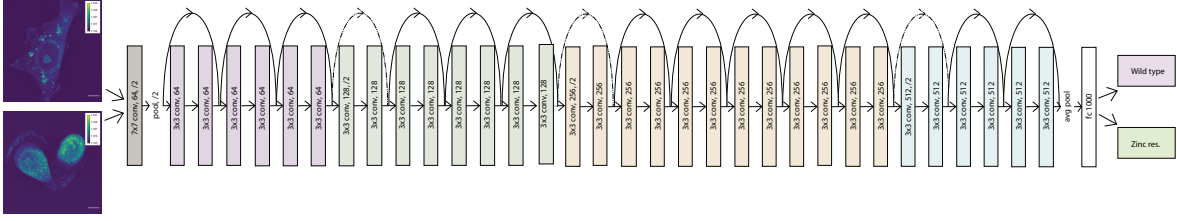


**Figure 2:** Scheme of a ResNet-50 neural network with our data. Arrows represent skip connections, where the value from previous layer. Every color change corresponds to pooling.

**Table 1:** Classification accuracy for different 2D image formation.

	Manually selected slice	Maximum intensity projection	Maximum entropy slice
Accuracy [%]	92.19	93.75	97.5

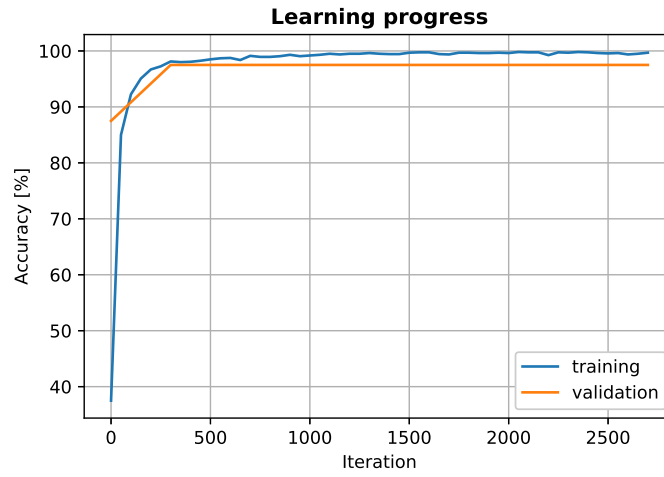


**Figure 3:** Learning progress while training on slices with the largest entropy value (best result achieved).

**Table 2:** Confusion matrix of network applied on slices with the largest entropy value.

	WT predicted	Zinc resistant predicted
True WT	78	2
True Zinc resistant	2	78

achieved by the method which made use of the largest entropy slice, see in Table 1. The performance of our algorithm was also measured through a confusion matrix displayed in Table 2.

#### 4 CONCLUSION

Our work was focused on automatic recognition of 2 variants of a PC-3 prostate cancer cell line. Results have shown that deep learning methods are able to recognize between these 2 types of cells, allowing for future experiments, such as measurement in a single sample. We hope that in the future, we will proceed and be able to quantify these differences. We would also like to test a 3D neural network, try analysis methods that would show how exactly are these cells different.

## REFERENCES

- [1] Deng, J.; Dong, W.; Socher, R.; aj.: ImageNet: A Large-Scale Hierarchical Image Database. In *CVPR09*, 2009.
- [2] He, K.; Zhang, X.; Ren, S.; aj.: Deep residual learning for image recognition. In *Proceedings of the IEEE conference on computer vision and pattern recognition*, 2016, s. 770–778.
- [3] Holubova, M.; Axmanova, M.; Gumulec, J.; aj.: KRAS NF- $\kappa$ B is involved in the development of zinc resistance and reduced curability in prostate cancer. *Metallomics*, ročník 6, č. 7, 2014: s. 1240–1253.
- [4] Kratochvilova, M.; Raudenska, M.; Heger, Z.; aj.: Amino Acid Profiling of Zinc Resistant Prostate Cancer Cell Lines: Associations With Cancer Progression. *The Prostate*, ročník 77, č. 6, 2017: s. 604–616, doi:10.1002/pros.23304.

# APPLICATION FOR HEART RATE ESTIMATION USING SMARTPHONE

**Kryštof Šara**

Bachelor Degree Programme (3rd), FEEC BUT

E-mail: xsarak00@stud.feec.vutbr.cz

Supervised by: Andrea Němcová

E-mail: nemcovaa@vutbr.cz

**Abstract:** This work deals with estimation of the human heart rate (HR) using a mobile phone camera. The goal was to create a functional application for a smartphone with a real-time HR detection. A preliminary functional algorithm was tested on a sample of 10 independent subjects and a mean deviation of 8.3 beats per minute (BPM), relative to an ECG reference record, was reached. Considering only visibly calm subjects, the mean deviation was 1.5 BPM.

**Keywords:** photoplethysmogram, PPG, heart rate, HR, mobile application, Swift, iOS, electrocardiogram, ECG, online detection of HR, Matlab, mHealth, telemedicine

## 1 INTRODUCTION

The modern age can be characterized by the rise of information technology, which is also related to the expansion of mobile devices usage. The daily use of smart devices is becoming more and more common. One often can no longer imagine everyday life without their help. Phones as personal helpers penetrate into many spheres of human life including healthcare. The problem with mobile applications, however, is that they are only minimally tested and their accuracy is often unknown. [1]

The estimation of heart rate (HR) can be performed in many ways. The main conventional techniques include palpation of the palpable arteries with stopwatches, or taking the electrocardiogram (ECG) record, which is the gold standard for other human HR measurement techniques. Using a mobile phone one can get an acoustic expression of heart activity (phonocardiogram, FCG), a video recording of blood flow in the fingertip using a flashlight and a camera (photoplethysmogram, PPG), or one can use an accelerometer to record chest movements (mechanical activity of the heart). [2, 3, 4]

## 2 ONLINE DETECTION ALGORITHM

Due to the computational complexity and nature of the detector itself (a real-time, online detector), the acquired PPG signal from the camera is processed in the time domain, and the algorithm is simplified to reduce computational and energy demands. Swift 5 programming language was used for the implementation; a block diagram of the algorithm is shown in the Figure 1.

The algorithm starts by acquiring a scene, which is provided by a built-in rear camera. By default, the camera sampling frequency is set to 30 Hz (Frames per second, *FPS*). After converting such scene into the Swift image class `UIImage`, the red channel is extracted, because it carries the largest amount of information necessary for HR estimation [4]. Then, the *PPG* signal sample is calculated as an average of one frame of the red channel, and the first difference signal *dPPG* sample can be obtained by (according to [5]):

$$dPPG(n) = \Delta PPG(n) = PPG(n) - PPG(n-1) \quad (1)$$

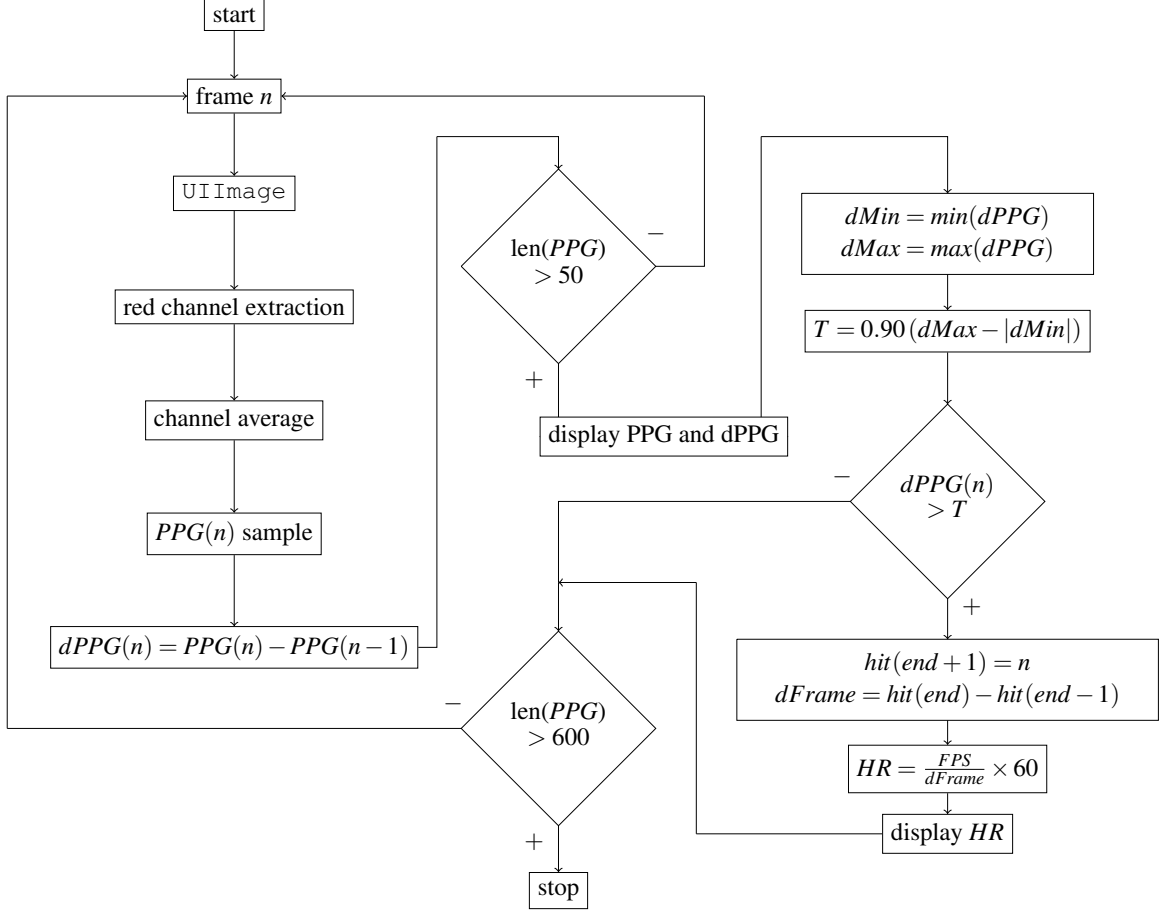


**Figure 1:** Block diagram of the algorithm for obtaining an instantaneous HR by proposed application, pseudocode.

Furthermore, the  $dPPG$  is used for the calculation of the instantaneous HR value. In the sliding window of 80 samples length the maximum and minimum are found and based on these two values, the threshold  $T$  is set. By thresholding the differential signal, a vector of passes ( $PPG$  peak positions)  $hit$  is created. The distance of  $PPG$  peaks  $dFrame$  is calculated and further used according to [4] to calculate the instantaneous HR value (in beats per minute, BPM):

$$HR = \frac{FPS}{dFrame} \times 60 \quad (2)$$

The instantaneous HR value is displayed in the lower left corner of the application prototype, and the average HR value is displayed after the acquisition (shown in Figure 2). The algorithm ends by pressing the *Stop* button, or after collecting 600 samples of the  $PPG$  signal (approximately 20 seconds).

### 3 MEASURING PROTOCOL AND DATA ACQUISITION

To determine accuracy of the algorithm and to test the functionality of the smartphone application, measurements were performed on ten human subjects. The Bittium Faros 360 ECG recorder with a 5-electrode lead system and silver chloride (Ag/AgCl) electrodes were used for the measurement together with Apple iPhone 5s and 6 and stopwatches.

Each subject was asked not to drink coffee and alcohol, and not to smoke or exercise 2 hours prior to the measurement. The person placed the index finger of the right hand on the rear camera of Apple

iPhone 6 and the index finger of the left hand on the rear camera of Apple iPhone 5s, ensuring that the fingers were also illuminated by the integrated LED flashlight. The electrodes of the ECG recorder were loaded on the person's chest. Then the 2-minute simultaneous acquisition was made. A note was taken, if any apparent restlessness (e.g. tremor, *Stress*) was present during.

The average HR values from the application prototype and measurement examples of the *PPG* and *dPPG* signals can be seen in the Figures 2a and 2b. A special case is the record No. 3 (Figure 2b), which was very weak. The subject was not compliant with the protocol (smoking). The vasoconstrictive effect of nicotine then probably caused a short-term poor blood flow to the fingertips [2].

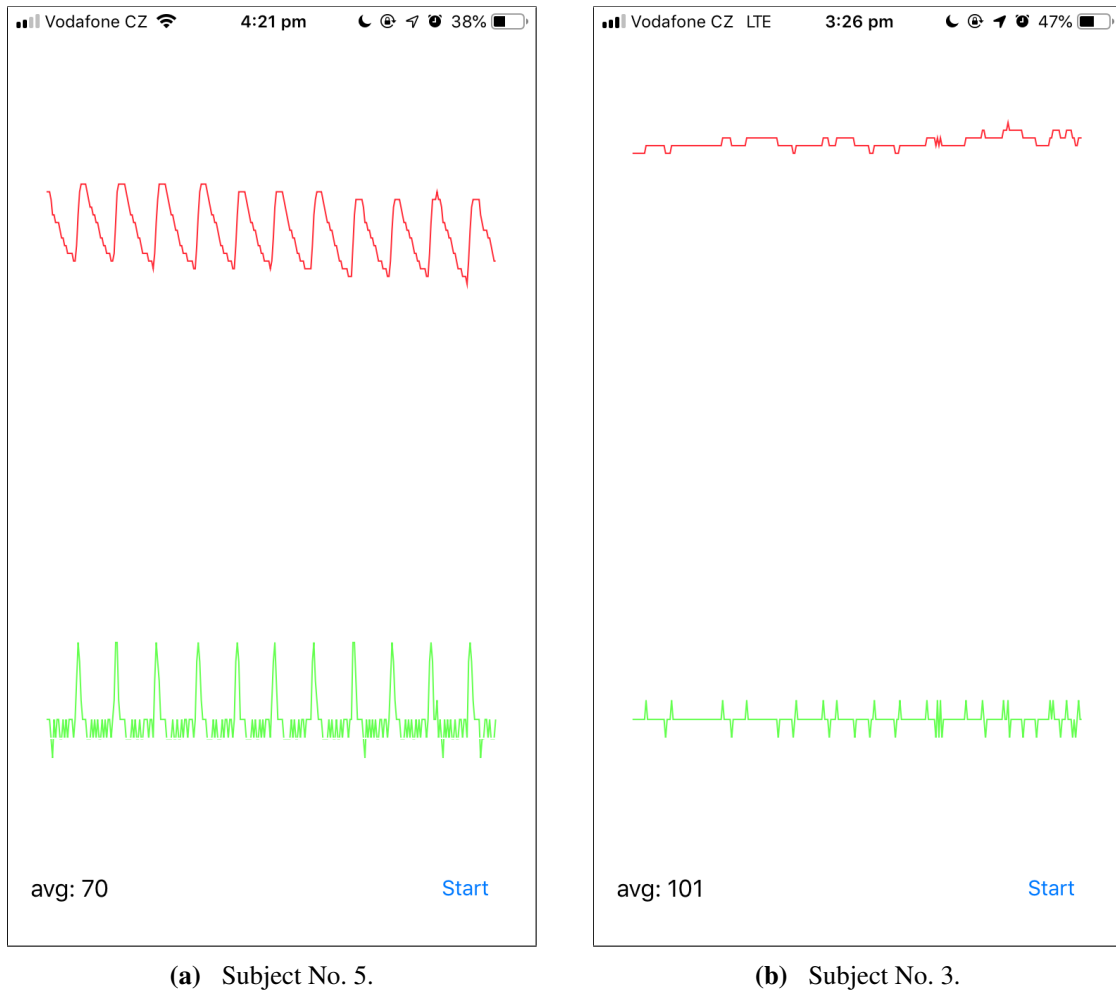


**Figure 2:** Examples of two waveforms – the *PPG* signal (red), and the differential signal *dPPG* (green) from the application prototype.

#### 4 RESULTS AND DISCUSSION

For each subject, the average HR values were estimated from the application, and from the reference ECG record, which was processed using the Matlab R2019b environment. The values, together with the assessed restlessness of the person, are shown in the Table 1. To determine the accuracy, the total average absolute deviation  $\delta$  (in BPM) was calculated:

$$\delta = \frac{1}{n} \sum_{i=1}^n |ECG_i - App_i| = \frac{1}{10} (|74 - 70| + |80 - 84| + \dots + |52 - 52|) \approx \pm 8.3 \quad (3)$$

**Table 1:** Average HR values from the application (*App*), and from the ECG recorder (*ECG*). Also, each subject is labeled with their stress level during the acquisition.

Subject No. [-]	<i>App</i> [BPM]	<i>ECG</i> [BPM]	<i>Stress</i> [-]
01	70	74	No
02	84	80	Yes
03	101	107	Yes
04	70	71	No
05	70	69	No
06	80	68	Yes
07	80	76	Yes
08	94	59	Yes
09	87	71	Yes
10	52	52	No

From the calculated total deviation of the measurement (Equation 3) one can easily tell that the currently proposed algorithm for getting the instantaneous, and the average human HR value using a smartphone is burdened with a big mistake. However, if the deviation is calculated over the restful subject only (*Stress* No), we obtain the following deviation (in BPM):

$$\delta_{No} = \frac{1}{4} (|74 - 70| + \dots + |52 - 52|) \approx \pm 1.5 \quad (4)$$

The difference between the Equations 3 and 4 shows a significant effect of false positive detections (motion artifacts) to the average HR value estimated by the app. Therefore, the addition of a motion detector prior to HR calculation, or the image color control using an RGB score are considered as optimization elements of the algorithm.

## 5 CONCLUSION

The presented application prototype was tested on a sample of ten independent human subjects with a simultaneous recording of ECG. The average deviation of the online detector, relative to the ECG record, was 8.5 BPM. Considering only stressless subjects, the deviation was only 1.5 BPM. The presented application prototype could be considered as usable for a quick on-the-spot HR estimation.

## REFERENCES

- [1] EUROPEAN COMMISSION. *Green Paper on mobile Health ("mHealth")* [online]. Brussels, 10. 4. 2014. <https://ec.europa.eu/digital-single-market/en/news/green-paper-mobile-health-mhealth>
- [2] NAVRÁTIL, Leoš. *Vnitřní lékařství pro nelékařské zdravotnické obory*. Prague: Grada Publishing, 2017. ISBN 978-80-271-0210-5.
- [3] KOLÁŘ, Radim. *Lékařská diagnostická technika*. Brno University of Technology, Faculty of Electrotechnical Engineering and Communications, Dept. of Biomedical Engineering, 2007.
- [4] SIDDIQUI, Sarah Ali, Yuan ZHANG, Zhiqian FENG, and Anton KOS. *A Pulse Rate Estimation Algorithm Using PPG and Smartphone Camera*. Journal of Medical Systems [online]. 2016, 40(5). DOI: 10.1007/s10916-016-0485-6. ISSN 0148-5598.
- [5] KOZUMPLÍK, Jiří. *Analýza biologických signálů*. Brno University of Technology, Faculty of Electrotechnical Engineering and Communications, Dept. of Biomedical Engineering, 2012.

# SPECTRAL COMPUTED TOMOGRAPHY: COMPARISON OF REAL AND VIRTUAL NATIVE IMAGES

**Kateřina Širůčková**

Bachelor degree Programme (3), FEEC BUT

E-mail: xsiruc03@stud.feec.vutbr.cz

Supervised by: Petr Marcoň

E-mail: marcon@feec.vutbr.cz

**Abstract:** This paper is based on the comparison of real and virtual native images obtained from spectral computed tomography (CT). Both types of images are compared by the signal-to-noise ratio (SNR), HU/HU\* ratio and in the relation of used contrast medium. Parametric and non-parametric tests were used for statistical analysis of the measurements. The main purpose of this study is to contribute on the wider issue which is radiation dose reduction on the patient. This problem has not been fully researched yet but it has been proposed that the virtual images could be computed mathematically from the images acquired by the conventional scanning protocol for spectral CT and used instead of the real images.

**Keywords:** Spectral CT, virtual non-contrast imaging, true non-contrast imaging, dual energy

## 1 INTRODUCTION

Considering heavy use of CT scanning in clinical medicine, it is necessary to reduce applied radiation dose on the patient during diagnostics or, therapy. Frequent scanning increases radiation dose that leads to a higher risk of malignant tumours and negative effects on gonads. Reduction of the radiation dose can be performed in several ways e.g. by using shielding technique, reducing scanning coverage or by the iterative reconstruction technique. The CT image reconstruction is fast-growing area of medical imaging. In general, there is an effort to develop accurate and effective methods for image reconstruction with a minimal dose of the x-ray on the patients [1].

Spectral CT uses dual energy (DECT) which improves accuracy and reduces the effects of metal artefacts. There are several types of images acquired by the spectral CT. One type is the true non-contrast images (TNC). TNC are created without contrast agent and weighted by HU. In multiphase imaging, TNC are always acquired before the application of contrast agent. The pathology can be detected by the difference in values before and after the administration of contrast agent. Another type of images from the spectral CT are virtual non-contrast images (VNC) quantified in HU\* units. VNC are computed by the deconvolution method from the first post-contrast image. The application of the deconvolution is further described in the reference [2]. The idea is to calculate the VNC that would be equal to the TNC, however, the effort has not been entirely successful. Therefore, the aim of this article is to compare TNC and VNC by determining their dependency. In the best scenario, it would be possible to save the patient from the first CT scan and the TNC would be replaced by the VNC.

## 2 METHODOLOGY

### 2.1 POPULATION

This is a retrospective study to determine the relation between TNC and VNC. The study included 10 men (36 - 75, mean 59.8 years  $\pm$  13.6) and 10 women (43 - 72, mean 58.7  $\pm$  10). All scans were

performed for diagnostic purposes only. It was a single center study at the University Hospital Brno at the Clinic of Radiology and Nuclear Medicine. The data were collected from May 2019 to November 2019.

## 2.2 IMAGE ACQUISITION

Philips IQon Spectral CT scanner was used for image acquisition. This CT scanner has two layers of detectors - the lower layer absorbs high-energy photons and the upper layer absorbs low-energy photons providing two different energies. Patients were scanned lying on their backs and during exhalation to prevent compression of the organs.

## 2.3 AIM OF STUDY AND IMAGE ANALYSIS

The main purpose of the research is to compare two types of images, TNC and VNC, obtained by spectral CT. The examined objects were the upper arch of the aorta, the left lung, the hepatic segment S7, and the right kidney at the entrance of the renal artery. Regions of interest (ROIs) were selected manually. To obtain valid data, there was an effort to place symmetric ROI in the TNC and VNC. The size of the ROI was set to 300 mm<sup>2</sup>, except for the fat where the ROI was represented by the size of 100 mm<sup>2</sup>. ROI of fat was used as a background. The total of 200 ROIs were defined (5 tissues, 2 reconstructions, 20 patients). The axial slice thickness was 1.5 mm and it was reconstructed from the available sections. Selected data were analysed statistically [3].

## 3 EVALUATION

Statistical analysis and evaluation of the results were performed in Statistica 13.5 and Microsoft Excel 2018.

The first evaluation focused on the *p-value* and confirmation or rejection of the null hypothesis, according to the statement in the reference [3]. The null hypothesis assumed zero difference of paired values. The *significance level*  $\alpha$  was set to  $\alpha = 0.05$  in all tested variables. Firstly, the data were tested for Gaussian distribution using histograms. A paired t-test was only used for the aorta and whose *p-value* resulted in  $p = 0.222$ . A non-parametric alternative to the paired t-test, the Wilcoxon test, was used for the remaining tissues; kidney tissue  $p = 0.5755$ , lung tissue  $p = 0.8227$ . The *p-value* in the liver was  $p = 0.0145$ , thus, in this single case, the null hypothesis for liver tissue was rejected.

Correlation analysis was used to compare the mean values of HU and HU\* numbers from the segmented areas of all the patients. Use of the correlation coefficients is described in the reference [3] and it represents the strength between two measured variables quantitatively. Pearson's correlation coefficient  $r$  for the aorta was  $r = 0.355$ . Spearman's correlation coefficient for data with nonparametric distribution reached the highest values in the lungs, where  $r = 0.788$ . Renal corresponds to  $r = 0.394$  and  $r = 0.304$  was for the liver. The next part of the evaluation examined the difference between HU and HU\* number. The ratio of these numbers was used to determine whether the VNC overestimated or underestimated. Despite some deviations, the average correlation value for lung tissue reached 1.0005 which can be considered as a very good result. The ratio of values for kidney tissue showed that VNC are often overestimated by 2.45%. Both, the aorta (0.955) and liver tissue (0.9455) achieved higher TNC values than VNC. **Chyba! Nenalezen zdroj odkazů.** interprets higher TNC values in the lung tissue than VNC values for the blue marked results. Yellow indicates the total equality of the TNC and VNC, green indicates the TNC underestimation.

Another method used to evaluate the signal-to-noise ratio is described in (1). This is obtained as the ratio of the power of the useful signal to the power of the useless signal:

$$SNR = \frac{mean_{tissue}}{SD_{tissue}}, \quad (1)$$

where: mean represents the average value of the CT number in the selected ROI and SD is the standard deviation of the same ROI.

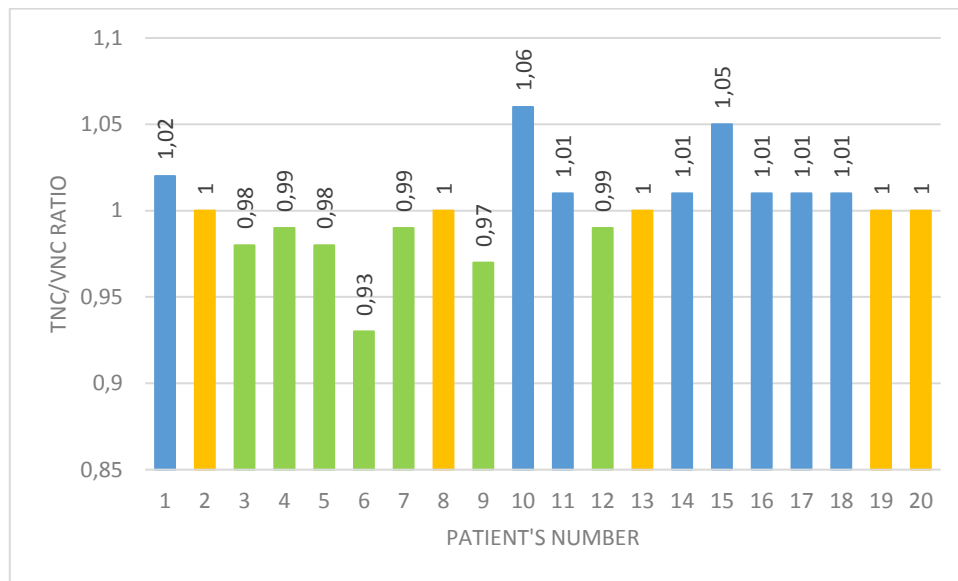


**Figure 1:** HU/HU\* ratio numbers for lung tissue.

Figure 2 shows that the VNC reaches higher values than the TNC. Contrast agent ULTR 370 allows radiographic visualization of internal structures. OMN 350, Omnipaque or Iohexol, is an iodine contrast agent used in radiological examinations.

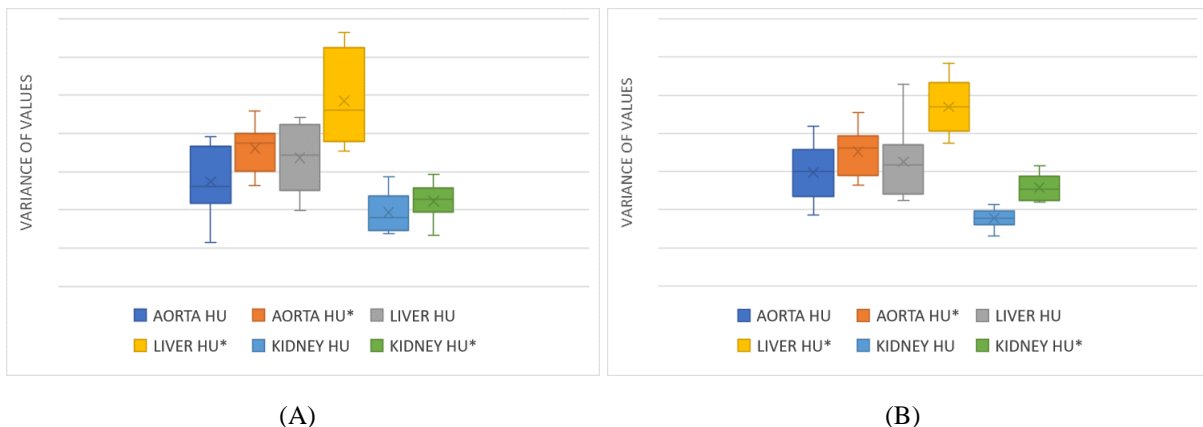


**Figure 1:** Comparison of SNR values in patients that were given either ULTR 370 (A) or OMN 350 (B).

The last analysed variable was the relative error of VNC determination depending on the selected tissues which was calculated from the formula (2):

$$\delta_{RNO} = \frac{mean_{VNO} - mean_{RNO}}{mean_{RNO}} \cdot 100, \quad (2)$$

where: mean represents the average value of the CT number for TNC and VNC.

**Chyba! Nenalezen zdroj odkazů.** represents the measurements of the three types of tissues. TNC values of fat (blue colour) were lower than VNC values in all cases. The mean underestimation value is  $9.5 \pm 6.09$ . Grey marked line for the liver tissue display the average value of the relative error ( $7.23 \pm 13.01$ ). Unfortunately, in 4 out of 20 patients (20%) the relative error becomes negative; therefore, this result is not reliable. The best values of the relative error were measured for the lung tissue

(pink); the average value was calculated by the relative errors ( $0.04 \pm 2.66$ ). Based on the statistical analysis, this measurement can be considered very precise.

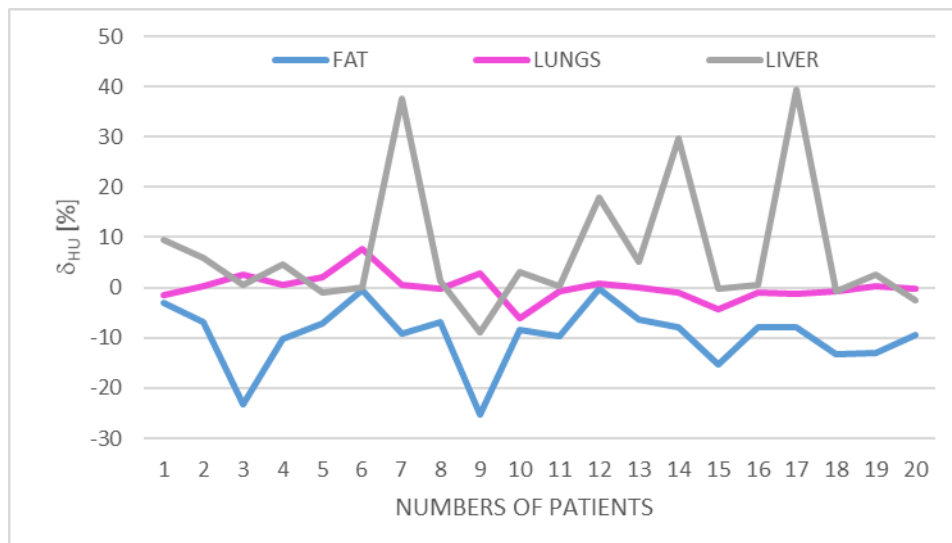


**Figure 3:** Behaviour of the relative error of VNC determination caused by image deconvolution for different patients.

#### 4 CONCLUSION

Measurements confirmed that VNC images are not equivalent to TNC images. Based on the analysed data, it can be determined that in most cases VNC are overestimated compared to TNC. The images were the most similar in the lung tissue when the lowest values of the relative measurement errors and the highest tightness in a relation of TNC and VNC with respect to the correlation analysis were measured. The relationship between the variable TNC and VNC can be characterized as a linear ascending line.

The evaluation of the results using correlation coefficients did not confirm our assumptions. Since the aorta ( $9.59 \pm 26.41$ ) is the most saturated, the differences between TNC and VNC should be the highest, which was not confirmed in this study. The liver showed the lowest value in the correlation analysis. In the contrary, the assumption of the relationship between the tissue saturation and the difference in values was confirmed for the lung tissue. The lungs were the least saturated tissue in this study due to the large volume of air in the lungs, therefore, the difference between TNC and VNC is the smallest.

These results are confirmed by 20 measurements from different patients. For statistically valid data, it is necessary to do research on a larger number of the patients to support or reject these results.

#### REFERENCE

- [1] SAUTER, Andreas P., Daniela MUENZEL, Julia DANGELMAIER, Rickmer BRAREN, Franz PFEIFFER, Ernest J. RUMMENY, Peter B. NOËL a Alexandr A. FINGERLE. *Dual-layer spectral computed tomography: Virtual non-contrast in comparison to true non-contrast images* [online]. European Journal of Radiology, Elsevier, 2018 [cit. 2020-02-02]. <https://doi.org/10.1016/j.ejrad.2018.05.007>Get rights and content.
- [2] JAN, Jiri. Digital filtering, signal analysis and restoration. 2<sup>nd</sup> add. ed. Academic Publishing House, VUTIUUM, 2002, 427 pp. ISBN 80-214-2911-9.
- [3] PROCHÁZKA, Bohumír. Brief biostatistics for physicians. Charles University in Prague: Karolinum, 2015, 125 pp. ISBN 978-80-246-2783-0.

# ADVANCED ESTIMATION OF SPEECH SIGNAL PERIODICITY

**Jan Malucha**

Bachelor Degree Programme (3), FEEC BUT

E-mail: xmaluc00@vutbr.cz

Supervised by: Milan Sigmund

E-mail: sigmund@feec.vutbr.cz

**Abstract:** This study examined the use of methods for advanced estimation of speech signal periodicity. The speech parameters of jitter, schimmer and short time period similarity were briefly explained as well as their estimation with appropriate methods, all of them integrated into a compact MATLAB program. The practical use of the program was demonstrated on the analysis of a stressed and neutral speech signal and achieved results were presented at the end of the study.

**Keywords:** speech signal, periodicity, stressed voice

## 1 INTRODUCTION

Speech signal is a very specific topic for signal data studies that can be applied to many subject fields such as robotization, security or health service. From the communication point of view, each language has a unique speech pattern which can be analysed. From the linguistic viewpoint, speech signal of the Czech language can be split into individual words that are separated from each other by intervals of silence. Furthermore, the words can be perceived as groups of letters.

If the signal is examined in the field of acoustics, we are able to study the attributes of each sound in a specific time interval. In such case, it is possible to divide individual phonemes (i.e. spoken letters) into two categories: voiced and unvoiced [1]. The unvoiced phonemes are not created by vocal cords vibrations but they are based on noise excitation (e.g. phoneme /s/). On the other hand, the voiced phonemes (e.g. phoneme /a/) are created by vocal cords vibrations in a quasiperiodic process. Quasiperiodicity is a non-ideal periodic process characteristic for the presence of deviations in time behaviour which is a typical phenomenon for a real-life environment. If analysed on the elemental level, we can split speech signal of voiced phonemes into short-time period microsegments.

## 2 PERIODICITY

Under ideal circumstances, the term *periodicity* has a binary characteristic – the signal is either periodic or not. However, we also need to consider all impacts affecting the excitation and signal transmission. These impacts cause deviations in signal periods - more specifically, they affect the duration of individual periods and their instantaneous values. We distinguish two types of deviations that can be quantified and measured: jitter and schimmer [1]. At this point, the term *periodicity* acquires a new meaning – rather than a binary attribute, it represents the amount of approaching the state of ideal periodicity. In order to be able to examine the quasiperiodic speech signal and its periodicity properly, we need to define physical quantities that would help us to express the properties of jitter and schimmer. Jitter relates to the variation of fundamental period duration measured from cycle to cycle. It is used for the description of speech intonation - sometimes referred to as a pitch. In spoken language, the fundamental frequency ranging between 50–600 Hz is comprehended as a melody. Conversely, schimmer - perceived as deviations in instantaneous values of individual periods - can be understood as a parameter for describing the similarity of two adjacent periods. We often perceive schimmer as a quivering voice during speech.

### 3 PROGRAM DESCRIPTION

For automatic estimation of speech signal periodicity, a new program was created in MATLAB environment. Its main functions use methods for signal processing (including pre-processing) in short-term analysis of speech signal. The input signal is split into short segments of an optional length from 20 ms to 40 ms that are examined further as shown in Fig. 1.

To determine whether a phoneme is voiced or unvoiced, low level methods are used as follows: short time energy (STE), zero crossing rate (ZCR) and harmonic-to-noise ratio (HNR). All these methods proceed from the previously mentioned fact that any unvoiced phoneme is naturally based on noise. STE algorithm checks different values of noise short-time energy and periodic signal [1], ZCR method is based on checking the different amounts of signal crossings of zero level [2] and HNR method considers the relation between harmonic and noise signal components [3].

The fundamental frequency is then estimated in voiced speech parts only using auto-correlation function (ACF), average magnitude difference function (AMDF) and normalized cross-correlation (NCC). ACF is a widely used function to determine similarity of the examined signals from its time lag based on multiplication of shifted signals [4]. The other two methods are ACF modifications; NCC is able to follow steep changes in the input signal more accurately due to normalization [5] and in ADMF is the multiplication substituted by subtraction [6].

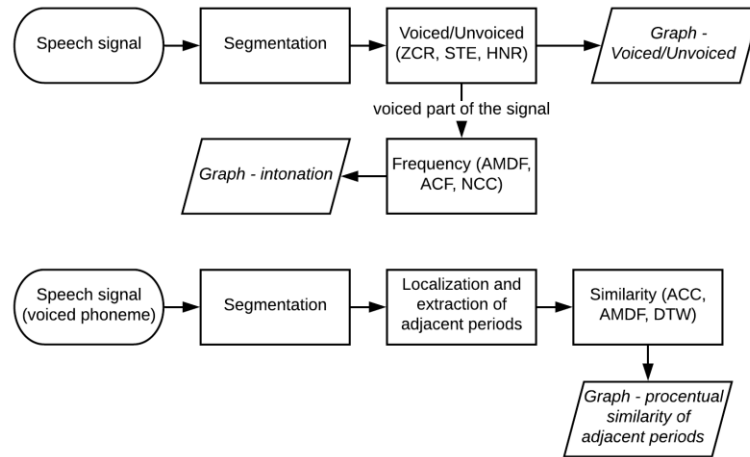


**Figure 1:** Block diagram of the MATLAB program

To be able to compare waves of adjacent periods with regard to deviations of period duration, we apply an algorithm for length adjustment that can either linearly or non-linearly reduce the length of the longer period to a length of the shorter one. The non-linear time alignment is based on dynamic time warping ACC algorithm [7]. After length adjustment, the similarity of adjacent periods is determined by ACC, AMDF or Dynamic Time Warping (DTW), which defines the similarity from the shortest Euclidean distance of compared signals.

### 4 PRACTICAL APPLICATION AND TESTING

The practical use of the developed program lies in a broad variety of new options when examining the speech periodicity. For example, we are able to study how much the speech signal is impacted by stress. The speech itself is created by controlling the vocal tract muscle tension. According [8], stress in speaker can affect this process and cause a loss of proper voice control by increasing the respiratory rate and vocal tract muscle tension. This is easily recognized as changes in voice fundamental frequency, speech intonation, quivering voice, speech rate and a number of pauses during the speech. We studied the stress effects via analysis of two kinds of Czech speech signals (22 kHz, 16 bits, mono, wav format). The first track was recorded during the final state examination at our

faculty and the recorded voice is strongly affected by stress. The other track was recorded with a neutral voice by the same speaker. The text is identical in both cases. One male person was selected for experiments. The stressed signal is 6:25 minutes long. That is two times longer than the neutral signal which lasts for 3:27 minutes. The neutral speech signal length is sufficient for the statistical reliability of experiments [9]. The difference in the length of tracks was caused by the speaker's frequent pausing and stuttering during the stressed speech.

The first parameter we analysed was voicing. It was expected that the unvoiced part of the speech affected by stress would be greater. The signals were split into frames of 20ms. The frames were sorted out as voiced or unvoiced by the STE algorithm and the obtained data were used to create histograms displayed in Fig. 2. As can be seen, the stressed speech track is slightly more voiced. Although the recorded track of the stressed speech is almost two times longer than the neutral speech track, it is noteworthy that the number of unvoiced segments is exactly twice as large but the number of voiced segments did not increase as much – approx. 1.38 times only. For this reason, it is possible to assume that pauses and stuttering appear far more often in stressed speech.

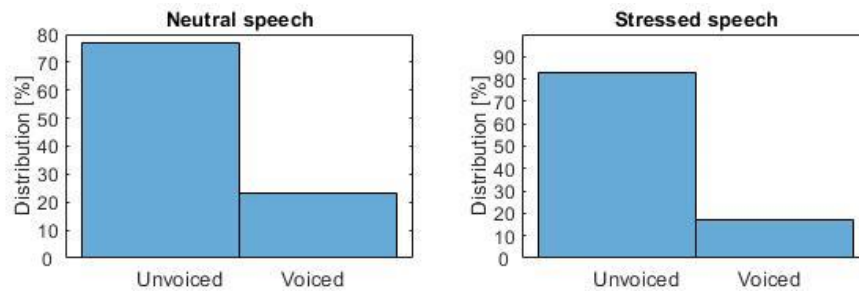


**Figure 2:** Histograms of voiced and unvoiced frames

The next analysed voice parameter was fundamental frequency. In general, vocal cords tension can increase due to stress and as a consequence the fundamental frequency may be raised. We examined this phenomenon using AMDF algorithm and the obtained total results are presented in the form of histograms in Fig. 3. It is apparent that fundamental frequency values of the neutral speech are concentrated mainly around 100 Hz and the higher frequencies influence the melodic accent. However, fundamental frequencies of the stressed speech are concentrated close to 127 Hz (not exceeding a total range of 70 Hz) and it completely lacks any melodic aspect. In other words, the voice pitch increased during the stressed speech and the voice became monotonic.

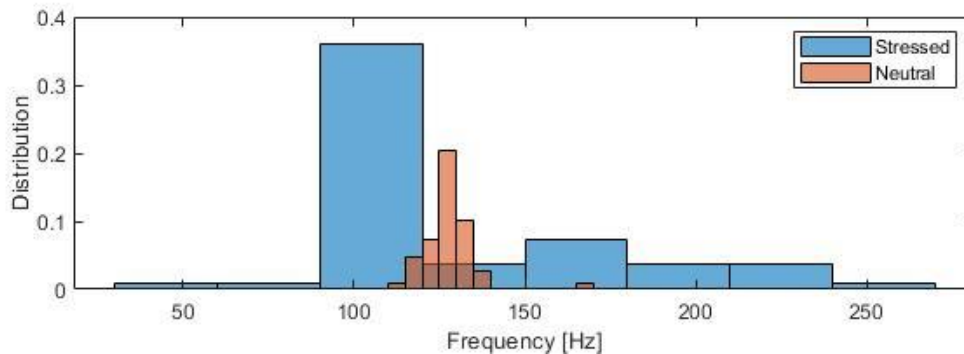


**Figure 3:** Histograms of voice fundamental frequencies

Schimmer was the last parameter investigated experimentally. We expected that acute stress may cause a quivering voice. In order to verify this hypothesis, several voiced phonemes /a/ of 10-period-length were extracted from the same parts of linguistic content in both speech signals. These phonemes were then examined by AMDF-based algorithm with a linear length adjustment. The similarity of all adjacent period was pairwise compared. Figure 4 illustrates that the periodicity of voiced phonemes extracted from the neutral speech is higher than the periodicity of phonemes extracted from the stressed speech.

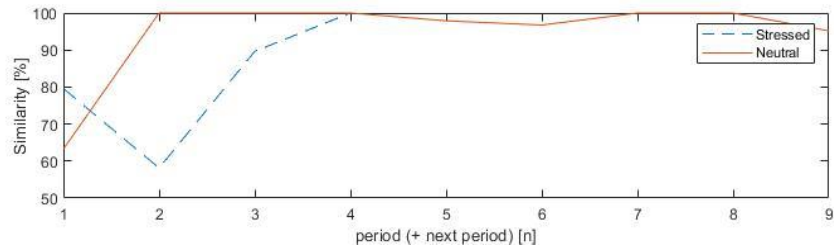


**Figure 4:** Diagram of adjacent period similarities for the phoneme /a/

## 5 CONCLUSIONS

To summarize the speech signal analysis provided by the developed program, the effect of acute stress on the speech signal were confirmed. Apart from the existing mathematical methods, the program disposes of a unique algorithm designed to split phonemes into separate periods, to adjust the length of individual periods in both linear and non-linear way as well as to create graphs of adjacent period similarities. Using the procedures, there is a variety of options for practical speech signal analysis and study of signal-impacting issues such as various voice dysfunctions or diseases. In future work, it will be useful to investigate the influence of nonstationary noise [10] and different vocal effort [11] on the accuracy of measured results.

## REFERENCES

- [1] L. R. Rabiner and R. W. Schafer, *Theory and Applications of Digital Speech Processing*. Prentice Hall, London, 2011.
- [2] R. G. Bachu, S. Kopparthi, B. Adapa, and B. D. Barkana, Voiced/unvoiced decision for speech signals based on zero-crossing rate and energy. In *Proc. Advanced Techniques in Computing Sciences and Software Engineering*. Springer, Dordrecht, 2010, pp. 279-282.
- [3] J. P. Teixeira, C. Oliveira, and C. Lopes, Vocal acoustic analysis-jitter, shimmer and HNR parameters, *Procedia Technology*, 2013, vol. 9, pp. 1112-1122.
- [4] L. R. Rabiner, On the use of autocorrelation analysis for pitch detection, *IEEE Trans. Acoust., Speech, and Signal Processing*, 1977, vol. 25, no. 1, pp. 24-33.
- [5] P. Motlíček, Estimation of fundamental frequency in speech. In *Proc. 1st Conference of Czech student AES*. 2000, FEEC BUT Brno, pp. 1-6.
- [6] L. Tan and M. Karnjanadecha, M. Pitch detection algorithm: autocorrelation method and AMDF. In *Proc. 3rd International Symposium on Communications and Information Technology*, 2003, vol. 2, pp. 551-556.
- [7] *Dynamic Time Warping* [online]. Available: <https://towardsdatascience.com/>
- [8] E. S. Jackson, M. Tiede, D. Beal, and D. H. Whalen, The impact of social-cognitive stress on speech variability, determinism, and stability in adults who do and do not stutter. *Journal of Speech, Language, and Hearing Research*, 2016, vol. 59, no. 6, pp. 1295-1314.
- [9] M. Sigmund, Statistical analysis of fundamental frequency based features in speech under stress. *Information Technology and Control*, 2013, vol. 42, no. 3, pp. 286-291.
- [10] P. Zelinka and M. Sigmund, Hierarchical classification tree modeling of nonstationary noise for robust speech recognition. *Information Technology and Control*, 2010, vol. 39, no. 3, pp. 202-210.
- [11] P. Zelinka and M. Sigmund, Automatic vocal effort detection for reliable speech recognition. In *Proc. International Workshop on Machine Learning for Signal Processing*, 2010, Kittila, pp. 349-354.

# APPLICATION FOR AN EARLY DETECTION OF TRANSMISSION PARAMETERS DEGRADATION OF POINT-TO-POINT MICROWAVE LINKS

**Milan Bubniak**

Bachelor Degree Programme (3), FEEC BUT

E-mail: xubuni03@stud.feec.vutbr.cz

Supervised by: Petr Musil

E-mail: xmusil56@stud.feec.vutbr.cz

**Abstract:** Radio equipment of microwave links operating in an outdoor environment under the influence of weather conditions is at risk of a link failure or device defect occurrence, as well as their indoor units. This paper aims to present the creation of a network monitoring application capable of timely detection of potential failures, based on analyzing trends in monitored device parameters. The architecture is being described, as well as a graphical user interface. Several failure detection methods are covered. Conclusion summarizes the development results and outlines a future of the application.

**Keywords:** microwave link, radio-relay, wireless, point-to-point, network monitoring, SLA, NOC, SNMP, .NET, WPF, InfluxDB, SQLite, OpenWeatherMap

## 1 INTRODUCTION

Microwave link is a widely used technology of long-range data transmission used in B2B as well as B2C telecommunication sectors. They are utilized by service providers either as last miles or in back-haul portion of the network [1, 2]. Customer contracts often include SLA (service-level agreement) specifying strict levels of link availability, packet loss, latency, jitter etc. [3]. Outages threaten the accomplishment of these levels on given data link which can be caused by defects of microwave units. This can be avoided, apart from various levels of redundancy, by effective monitoring of links.

This article deals with the creation of a monitoring tool in form of desktop application designed for specific characteristics of microwave links, periodically requesting status parameters of monitored devices by Simple Network Management Protocol. The application then analyzes gathered data and detects anomalies with several methods. A completed application should be ready for deployment in network operations centres of service providers, where it can improve reliability of their services in combination with timely replacement of the defective part of the link within preventive maintenance.

## 2 APPLICATION DESIGN

The application is designed as a compact executable, integrating the core of the application as well as a graphical user interface. It is assumed it will be run by small and medium service providers on a machine directly connected into the management sector of their network. The operator can access this machine directly or by remote desktop (e.g. in case of virtualized environment). Optionally with the use of VPN, the application can be run on any appropriate machine. Application core consists of components forming the SNMP manager, which gathers data from remote SNMP agents on monitored devices. Further components provide saving and reading data from the database environment, managing of the device definitions and analyzing of gathered data. Notification in an alarm form with various priority is created in case of positive anomaly detection. Graphical interface renders gathered data in realtime charts and shows lists of current and historical alarms.

### 3 APPLICATION DEVELOPMENT

.NET Framework is used as application basis with code written in C# language. The graphic interface utilizes WPF libraries and scheme. InfluxDB is chosen as a specialized NoSQL database for storing of gathered time series data due to its efficient compression and performance during their processing. [4]. Device and link definitions are stored in a compact SQLite database file of which database engine is embedded into the application in the form of a library. The application uses weather data provided by OpenWeatherMap API.

#### 3.1 CORE STRUCTURE

Fig. 1 shows a diagram of key components of application core with their relations.

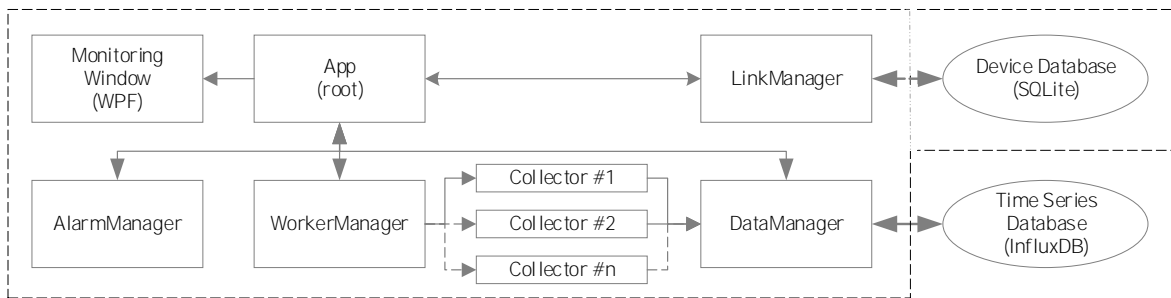


**Figure 1:** Diagram of application core components.

**App** – root object of a WPF application. Encapsulates *Manager* objects and WPF children objects.

**LinkManager** – ensures reading and writing data to local SQLite database files. These include *Device* table with device definitions and monitoring configuration and *Link* table with an assignment of devices into link groups.

**DataManager** – provides caching of data from collectors which are intended to write into database and sends them periodically via HTTP REST API to InfluxDB server. Also contains reading methods.

**WorkerManager** – initializes, starts and stops data collectors.

**AlarmManager** – periodically analyzes gathered data with several methods, contains device down and thresholds triggers, creates alarms when anomalies are detected and managing their collections.

**Collectors** – periodically collect values of monitored parameters from devices. Three types are currently implemented: SNMP collector sending *PDU GetRequest* with specific *OID*; Ping collector sending *ICMP datagrams Echo Request*; and Weather collector, sending HTTP requests to OpenWeatherMap API with geographical coordinates of a given device.

The application is built on asynchronous architecture because *Collectors* are highly input-output bound while *AlarmManager* is I/O bound as well and also slightly CPU bound. Waiting for an answer from a microwave unit to *SNMP PDU GetRequest* can take up to several hundreds of milliseconds, or it may not arrive at all (*SNMP PDUs* are encapsulated in *UDP datagrams* on transport layer). Therefore collectors must be run in separate threads or called via *Task<T>* objects.

#### 3.2 USER INTERFACE STRUCTURE

Fig. 2 shows the element layout of the application’s main window in the current development version. In the left part is located links list with a search box. The bottom part is also divided into two parts, on the left side notification area is located which lists information, alarm creation events, warnings and errors, while on the right alarm lists are situated. Alarms can be acknowledged and moved into the appropriate tab. Each alarm row consists of creation time, measure name, link name, etc.

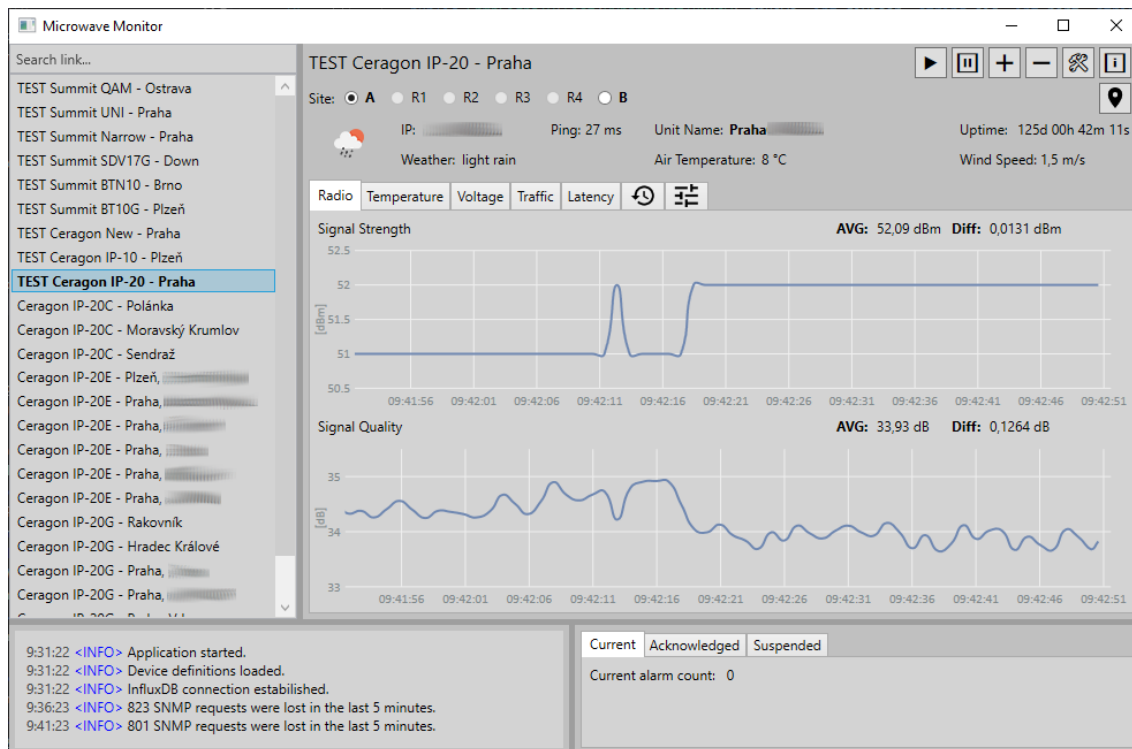


**Figure 2:** Screenshot of the running application (sensitive details are hidden).

A major part of main window area is populated by monitoring sector of selected link, with the header containing link name, site/device selection (up to six sites on a single link is supported), IP address of a selected device, control buttons and current site weather information. Parameters monitoring is divided into the tabs depending on the parameter type. Gathered values are displayed graphically in charts with realtime refreshing. Refresh interval is configurable for each parameter and device. In the current configuration, it is one second for most of the parameters. An important tab is Link Settings where the link monitoring configuration is being set. Also, the tab for historical reporting of parameters on the selected time window is included, but this function is not implemented yet.

#### 4 DATA ANALYZING METHODS

**Monitoring of the deviation from the long-term average** performs calculation of long-term mean from values which age corresponds with the set time interval. The deviation is calculated as a difference of the long-term mean and a short-term mean. The latter is computed of values from the upper limit of set time interval until the present moment. Currently, two analyzes of this type are tested. The first one has a time interval set to values up to the weekly age with the upper age limit of 30 minutes. The second one has a time interval set to values up to the age of 60 minutes, with the upper limit of one minute. The maximum percentage of deviation at which an alarm is generated is user-configurable in the application settings. In the default configuration, it is 10 % for the first analysis and 15 % for the second analysis. Deviations are recalculated with each newly obtained value.

**Long-term analysis by time** serves as a backup method in case of a long-term decline in the trend of any of the parameters, which the monitoring of the deviation from the average is not able to detect. This method compares the current value of a parameter with historical values in the past days at the same time. An alarm is generated when the user-configurable percentage deviation is exceeded. Currently, a comparison of the last read value with the corresponding values up to the age of the one week is being tested at an interval of one minute. The default maximum deviation is 10 %.

**Analysis of parameter periodicity** is an extension of the method of deviation from the long-term average. If any deviation exceeds the configurable percentage difference (3 % by default), the timestamp of this value is stored and then compared with the last stamps recorded in this way. If the time gaps between them have constant intervals (with a tolerance of 1 % of the time interval, but at least  $\pm 1$  s), which may indicate continuous external interference for example, an alarm is generated.

**Temperature correlation analysis** is one of the next methods suitable for future implementation. It compares the air temperature obtained using the Weather API with the temperature of radio of the outdoor microwave unit (ODU) considering current weather state and wind speed. Fig. 3 shows a sample of a linear relation between these temperatures. Safe temperature range will be determined for each type of ODU. Deviations from this range will then be considered as an impending radio failure.

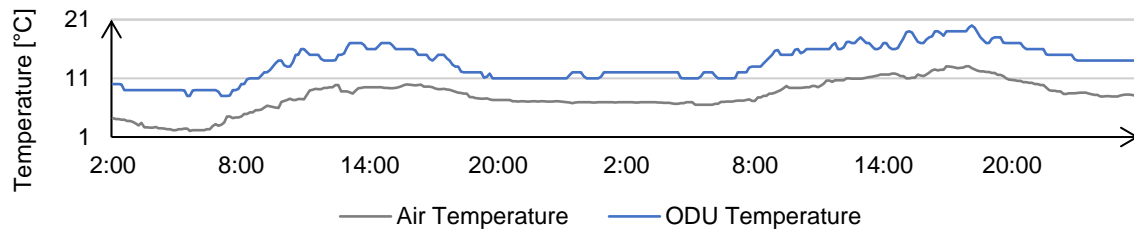


**Figure 3:** Sample of the linear relation between ODU temperature and outdoor ambient temperature. Data were obtained via the application during its continuous run.

## 5 CONCLUSION

The created application, although still in the development stage, can read parameters from remote devices using defined SNMP OIDs, measure latency and download weather information for each individual site. It performs effective monitoring, with the added value of user comfort thanks to an environment tailored to microwave links. In contrast to universal monitoring systems, it contains integrated methods of analysis, detecting sudden and long-term changes in parameters. The indication of total outages is included as a basic standard. By implementing other methods such as the above-mentioned temperature correlation and connecting basic methods with the evaluation of the atmospheric situation, the application can become a useful tool for NOC operators.

## 6 ACKNOWLEDGEMENT

This project was supported by company CBL Communication by light s.r.o. which provided the test range of real microwave units hardware with common traffic load for the purposes of this work.

## REFERENCES

- [1] KIZER, George. *Digital Microwave Communication: Engineering Point-to-Point Microwave Systems*. New Jersey: Wiley-IEEE Press, 2013. ISBN 978-0-470-12534-2.
- [2] LEHPAMER, Harvey. *Transmission Systems Design Handbook for Wireless Networks*. Norwood: Artech House, 2002. ISBN 1-58053-243-8.
- [3] HILES, Andrew. *E-Business Service Level Agreements*. Brookfield, CT: Rothstein Associates, 2002. ISBN 0-9641648-9-2.
- [4] RUDOLPH, Kevin. *A Comparison of NoSQL Time Series Databases*. Berlin: GRIN Publishing, 2015. ISBN 978-3656965763.
- [5] ALBAHARI, Joseph a Ben ALBAHARI. *C# 7.0 in a nutshell*. 7th edition. Sebastopol, CA: O'Reilly, 2018, 1070 s. ISBN 978-1-491-98765-0.

# ELLIPTIC CURVE CRYPTOGRAPHY FOR CONSTRAINED DEVICES IN INTERNET OF THINGS AND INDUSTRY 4.0

**Tadeáš Cvrček**

Bachelor Degree Programme, FEEC BUT

E-mail: tadeas.cvrcek@vutbr.cz

Supervised by: Petr Dzurenda

E-mail: dzurenda@feec.vutbr.cz

**Abstract:** The article summarizes the usability of devices (which are usually equipped with AVR and ARM Cortex-M microcontrollers) with low-power consumption in security solutions for IoT and Industrial 4.0 ecosystems. These devices have limited processing and storage capabilities and they often run on batteries. On the other hand, cryptographic algorithms are usually computationally demanding and, therefore, it is hard to implement them on constrained devices. This work studies the capabilities of current IoT devices to perform elliptic curve cryptographic protocols and the possibilities to design and implement own cryptographic protocols on constrained devices.

**Keywords:** Arduino, Cryptography, Low Performance Devices, Industry 4.0, Internet of Things

## 1 INTRODUCTION

Nowadays, there are many devices with low-power consumption which are part of various embedded systems and play an important role in our daily life. High growth of these devices is given mainly by the fast increasing market of IoT (Internet of Things) and Industry 4.0 [1]. The trend of IoT focuses on integration of real world devices into cyberspace. Embedded chips are almost in any device and these devices are connected to the Internet. All these connected (so-called smart devices) make our life easier and more comfortable. However, this connectivity brings a need of higher security, i.e. provide secure communication and access control, as well as economic aspects such as low price and operating costs.

The low power consumption is typical for many of IoT devices. These devices are usually based on ARM-Cortex-M (32-bit) or AVR (8-bit) processor families. Both processor families can be found on current Arduino single-board microcontrollers. For example, AVR processors are used on Arduino UNO and Arduino NANO (ATmega328 runs at 16 MHz) and ARM-Cortex-M powers Arduino DUE (Atmel SAM3X8E runs at 84 MHz).

Asymmetric cryptography is based on modular arithmetic operations (i.e., modular addition, multiplication, inversion and exponentiation) and operations over elliptic curve points (addition of two points and scalar multiplication of elliptic curve point). Furthermore, required modular arithmetic works with big numbers, e.g., RSA uses at least 2048 bits long keys by NIST (National Institute of Standards and Technology) recommendations. On the other hand, elliptic curve cryptography requires smaller keys (but still sufficiently big and secure) which are around 256 bits. However, Arduino natively supports only integer numbers up to 32 bits long.

## 2 LIBRARIES FOR ARDUINO PLATFORM

Currently, there are many available libraries for Arduino. These libraries extend Arduino capabilities such as network connection, cryptography and security support, and other. Many of these libraries

are freely available thanks to communities of developers that make them open source. First of all, we can use official Arduino repository, which can be accessed directly from Arduino IDE (Integrated Development Environment). In this repository, the libraries and their functionalities are well-tested and surely compatible with Arduino devices. The next great source of Arduino libraries and applications is GitHub, where many developers voluntarily and worldwide upload their source codes. It is difficult to find such libraries, that support modular arithmetic operations with big numbers (bigger than 512 bits) or elliptic curve operations in general. One option is to use *BigNumber* [2] library supporting modular arithmetic operations. Second option is to use *micro-ecc* [3] library, which implements ECDH (Elliptic Curve Diffie-Hellman) and ECDSA (Elliptic Curve Digital Signature Algorithm) protocols including underlying mathematical operations .

## 2.1 MODULAR ARITHMETIC OPERATIONS SUPPORT

*BigNumber* library supports all crucial modular operations: multiplication, addition and exponentiation. We provide benchmark tests of all operations on both Arduino UNO and Arduino DUE devices in order to see differences of their computational complexity based on used architecture, see Table 1 and Table 2 for more details.

**Table 1:** Benchmark results of modular arithmetic on AVR (BigNumber library)

Operation	16 bits	32 bits	64 bits	128 bits	256 bits	512 bits
Mod. addition	3 ms	4 ms	6 ms	8 ms	12 ms	-
Mod. multiplication	1 ms	5 ms	11 ms	35 ms	119 ms	-
Mod. exponentiation	45 ms	214 ms	1170 ms	7627 ms	-	-

**Table 2:** Benchmark results of modular arithmetic on ARM Cortex-M (BigNumber library)

Operation	16 bits	32 bits	64 bits	128 bits	256 bits	512 bits
Mod. addition	0 ms	0 ms	0 ms	0 ms	0 ms	1 ms
Mod. multiplication	0 ms	0 ms	0 ms	3 ms	8 ms	26 ms
Mod. exponentiation	5 ms	17 ms	78 ms	492 ms	3646 ms	25712 ms

Comparison of Table 1 and Table 2 shows that ARM Cortex-M offers 10 to 20 times faster operations processing than AVR architecture. Furthermore, these tests also discovered that AVR architecture is able to process only big numbers up to 256 bits length. Based on this fact, Arduino DUE and, therefore, ARM Cortex-M architecture is more suitable for cryptographic protocol implementation and integration to security solutions.

## 2.2 ELLIPTIC CURVE POINT OPERATIONS SUPPORT

The *micro-ecc* library offers a small and fast ECDH and ECDSA implementation for 8-bit, 32-bit, and 64-bit processors. Unfortunately, this library does not implement interface for modular and elliptic curve external calls. However, the existence of ECDH and ECDSA implementations means that there is already internal supports of modular and elliptic curve arithmetic operations. In our implementation we make these crucial operations available from outside to developers. The library implements by default the following elliptic curves: *secp160r1*, *secp192r1*, *secp224r1*, *secp256r1* a *secp256k1*.

Benchmark tests showed performance differences between AVR (Arduino UNO) and ARM (Arduino DUE), see Figure 1, where ARM architecture is ca. 12 to 20 times faster than AVR in executing ECDH protocol. In case of AVR, the time for ECDH key negotiation is between 5 to 18 seconds depending on the elliptic curve used. This time can be considered as very ineffective in real implementations.

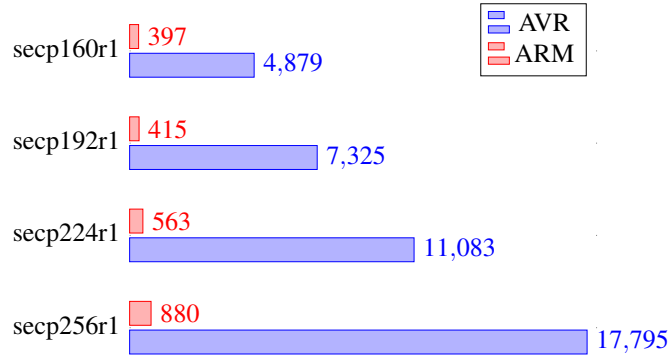


**Figure 1:** Performance comparison of AVR and ARM Cortex-M for ECDH protocol (Time [ms])

In order to make the *micro-ecc* library usable for implementation of our cryptographic protocols, the library functions needed to be modified. First of all, internal functions for modular arithmetic and point multiplication were made accessible from outside of library. Afterwards, a function for point addition was created.

Benchmark tests of modular arithmetic and elliptic curve point operations were performed only on Arduino DUE, due to its stability and fast processing even with big numbers. The results for all supported elliptic curves are depicted in Table 3. All results are in milliseconds and, therefore, they can be considered as negligible. The most crucial operation is scalar multiplication of elliptic curve point. This operation requires ca. from 60 to 160 ms to process.

**Table 3:** Benchmark results of micro-ecc on ARM Cortex-M

Operation	secp160r1	secp192r1	secp224r1	secp256r1	secp256k1
Mod. addition	0 ms				
Mod. multiplication	3 ms	2 ms	2 ms	3 ms	4 ms
Mod. inversion	2 ms	2 ms	3 ms	4 ms	3 ms
Point addition	0 ms				
Point multiplication	67 ms	79 ms	99 ms	189 ms	161 ms

### 3 ECDH PROTOCOL IMPLEMENTATION

We use standard *micro-ecc* library, the ECDH protocol was implemented and run between two Arduino NANO devices. Arduino NANO devices have same performance capabilities as Arduino UNO, but are significantly smaller. The final implementation uses I<sup>2</sup>C bus and it is controlled by *Wire* library. Communication itself took place over bridges of pins A4↔A4 and A5↔A5. Connection diagram of both devices is depicted in Figure 2. The final implementation was time consuming. In fact, the whole process of key negotiation took from 2 to 5 s depending on the selected elliptic curve.

### 4 PROOF OF KNOWLEDGE PROTOCOL IMPLEMENTATION

The implementation of proof of knowledge protocol of algebraic message authentication code  $MAC_{wBB}$  [4] was run on Arduino DUE. The authentication code  $MAC_{wBB}$  and the message  $m$  stay hidden during the proving phase. The prover only shows the possession of both these values. These kind of protocols are often used in privacy-enhancing protocols, such as anonymous credentials and group signatures). The protocol includes operations with elliptic curve points and modular arithmetic operations in the field of elliptic curve. Benchmark tests of the implementation are depicted in Figure 3. This protocol implementation is not compatible with AVR architecture.

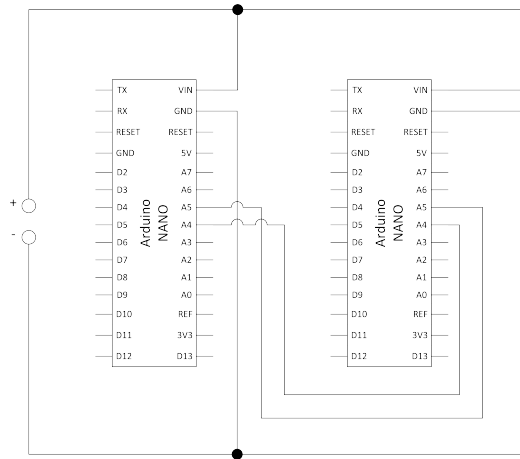


**Figure 2:** Basic connection of Arduino NANO devices through I<sup>2</sup>C bus

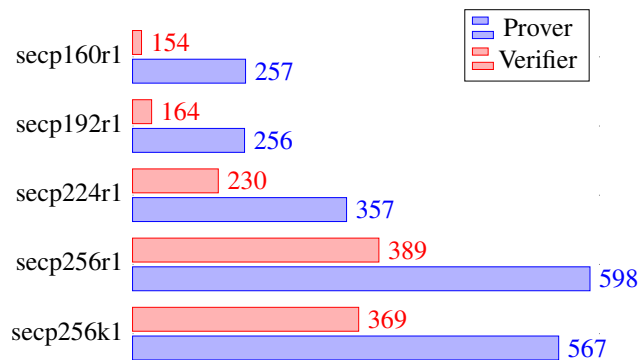


**Figure 3:** Performance comparison of Proof of Knowledge  $MAC_{wBB}$  on Arduino DUE (Time [ms])

## 5 CONCLUSION

Based on the provided benchmark tests, it is possible to come out with the conclusion that Arduino with ARM Cortex-M processors are the most suitable devices for the implementations of advanced cryptographic protocols with privacy protection features. In fact, the upcoming research follows this direction. Devices powered by AVR architecture are suitable only for less performance demanding projects. Moreover, Arduino DUE offers many possible ways how to develop a final application for a specific use case. In fact, Arduino DUE has sufficient processing power and memory resources, many I/O pins and interfaces for peripheral devices, such as smart cards (i.e., secure HW keystore) and wireless network modules.

## REFERENCES

- [1] Ministerstvo průmyslu a obchodu České republiky. [online]. [cit. 12. 03. 2020]. URL: <https://www.mpo.cz/assets/dokumenty/53723/64358/658713/priloha001.pdf>.
- [2] BigNumber. URL: <https://github.com/nickgammon/BigNumber>.
- [3] Ken MacKay. micro-ecc. URL: <http://kmackay.ca/micro-ecc/>.
- [4] Camenisch J., Drijvers M., Dzurenda P., Hajny J. (2019) Fast keyed-verification anonymous credentials on standard smart cards. In: ICFIS International Conference on ICT Systems Security and Privacy Protection 2019 Jun 25 (pp. 286-298). Springer, Cham.

# LED OPTIMISED CONTROL SYSTEMS

**Daniel Petra-Kajňák**

Master Degree Programme (5), FEEC BUT

E-mail: [xpetra17@vutbr.cz](mailto:xpetra17@vutbr.cz)

Supervised by: Lucie Hudcová

E-mail: [hudcova@feec.vutbr.cz](mailto:hudcova@feec.vutbr.cz)

**Abstract:** This work discusses the power supply and multiplexed LED display for the rear combination lamp. The benefit is improved communication between the vehicle and the environment, which increases safety. The paper presents a general overview of the solution developed under automotive specification. The paper also focuses on DC-DC converter, LED matrix thermal management and the software solution.

**Keywords:** DC-DC converters, automotive industry, matrix LED, power supply, display

## 1 INTRODUCTION

The increasing intensity of car traffic places higher demands on traffic safety. Better communication between vehicles can significantly increase traffic safety and smoothness. One of the possibilities is to use a part of the rear combination lamps of cars as LED matrix displays. The display allows to inform and warn the road users similar as in case of traffic signs, through displayed images and pictograms. Moreover, it will extend the already integrated Advanced Driver Assistance Systems (ADAS), which help the driver to control the vehicle with different level of autonomy. The added value of the given solution is also the design individualization of the rear headlight. For example, through the possibility to choose your own light design. The aim of this work is to design a prototype of the LED display integrated in rear combination lamp, which shows the future direction of development in car lighting. The practical goal is to create a prototype that will serve as a technological model for the development of serial light, for example in an autonomous vehicle. The prototype must be developed in accordance with the requirements of the automotive industry. An important part of this project is the design of the DC-DC converter that will power the LED matrix.

## 2 DEVICE CONCEPT

The display will consist of 528 LEDs connected in a matrix with a layout of 12 rows and 44 columns. DC-DC converter with constant voltage will power the display. This power supply will need to be completely designed for the application in order to regulate the battery supply voltage to the LED voltage. The control of the LED matrix will be divided into two levels. At the first level, the columns will be controlled by four 48 channel control circuits TLC5955 [1]. The lines will be controlled by transistors. At the second level, an ARM Cortex M4 microprocessor made by NXP will directly control the transistors and at the same time will control the multi-channel control circuits by sending values for each output via serial communication. This control provides multiplexing of the display. The microprocessor and control circuits will be powered by a linear Low dropout voltage regulator (LDO) inverter connected to the battery. Input protections will be connected in front of the power supply branch of both power supplies. The protection circuit will protect the device from unwanted voltage spikes or possible polarity reversal. Block diagram of the device is shown in Figure 1.

The integration of the LED matrix display into the rear combination lamp is a unique solution. The challenge is to design the prototype to meet the standards of the automotive industry. Therefore, all used components must be the subjects to the automotive qualification AEC (The Automotive Electronics Council). Components that meet this specification can be used in harsh automotive environments. Furthermore, the device will be developed according to Volkswagen group standards. VW 80000 is the standard [2] for the electrical requirements and the TL 81000 is the standard [3] for electromagnetic requirements. The standards also specify testing.

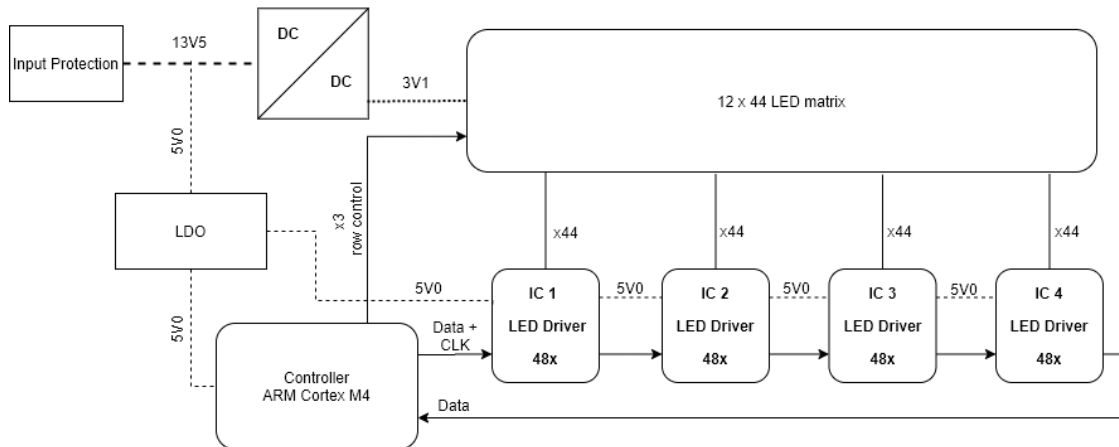


**Figure 1:** Block diagram describing hardware architecture of the device

### 3 DC-DC CONVERTER FOR THE POWER SUPPLY OF LED MATRIX

The power supply is provided by a switched-mode constant voltage source of the buck topology (step-down converter). It regulates the input voltage in the range of 8.7 - 17 V to the output voltage of 3.1 V with maximum current up to 5.5 A. The maximum ripple of the input voltage is 200 mV and only 50 mV of the output voltage. Despite the high supply current, the source is controlled by a controller with integrated MOSFET transistors. Converters for such a high power with integrated transistors are a novel solution in the automotive industry. Their main advantages are better EMC properties and simpler designing of the converter. The value 8.2  $\mu\text{H}$  of output coil was selected to limit the current ripple below 1 A, thus minimizing the coil losses. The combination of the capacitors at the output consists of the ceramic and electrolytic capacitors with the total capacity of 240  $\mu\text{F}$ . The high value of the output capacity should compensate for the dynamic load changes caused by the various animations on the display.

#### 3.1 PROTECTIONS CIRCUITS

Additional protective circuits were added to the input of the converter in order to meet the electrical requirements of the VW 80,000 standard. The protection consists of a cascade of three protective elements in a row. The first is the transil at the input. Its job is to cut over voltages or under voltages. The following is the protection against the reverse polarity, formed by the circuit with the PMOS transistor. The last one is the protection diode. These circuits protect the device against fluctuations and impulses generated in the vehicle's electrical network during operation (starting, the start of the alternator, etc.). Thanks to this protection the device can declare the functionality in tests. For example, when it is subjected to a pulse with a voltage of up to 100 V.

#### 3.2 ELEKTROMAGNETIC INTERFERENCE

The challenge in the design of the converter is to minimize electromagnetic interference. For this purpose, the LC filter is placed at the input, its task is to suppress interference (at the switching frequency of the converter) radiated to the supply line. The layout of the connections and components on the printed circuit board (PCB) is also designed with an effort to minimize interference. Adding additional components to the design allows additional tuning of the EMC features in the future. These will not be mounted on the first prototype, but will only serve as the mounting surfaces for the tuning components. To reduce the interference, the possibility of the symmetrical power supply to the input and output of the converter chip was used. The power supply lines and capacitors are from either side of the chip. These interrupt the current loops and reduce the interference (see Figure 2).

Moreover, to minimize the effects of the electromagnetic interference, all switched electrical components will be shielded by a metal case.

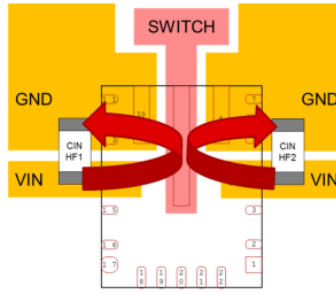


**Figure 2:** Symmetrical input power supply (Designing High-Performance, Low-EMI Automotive Power Supplies. In: Texas Instruments Incorporated, 2019 )

#### 4 THERMAL MANAGEMENT

In the automotive industry, electrical equipment must operate in the ambient temperature ranging from  $-40\text{ }^{\circ}\text{C}$  to  $85\text{ }^{\circ}\text{C}$ . Therefore, a necessary part of the design had to be the calculation of thermal management, which includes the calculation of power losses of all components as well as the sizing of cooling.

The most thermally sensitive part is the LED matrix. At a maximum load, the current of up to 5.5 A flows through matrix and power losses are approximately 17 W. In addition, a large number of diodes, which produce heat, are located on a small cooling surface. Their matrix arrangement does not allow the efficient heat dissipation through continuous layer of copper. Therefore, additional cooling will be provided by an aluminum heatsink on the bottom side of PCB under the LED matrix. The heat from the diodes is conducted to the opposite side of the PCB by thermal vias. The heatsink will be glued to the printed circuit board with an electrically non-conductive adhesive. Except for calculating the area of the cooler itself, it was necessary to verify if the pair of the thermal vias have a sufficiently low thermal resistance to dissipate heat from the top of the PCB.

The thermal resistance of the via was calculated from the volume of galvanically electroplated copper in the via and the known thermal conductivity of copper  $\alpha_{Cu} = 380\text{ W}\cdot\text{m}^{-1}\cdot\text{K}^{-1}$ . The area of copper is calculated as a circular section from the formula [4]

$$S = n \cdot \pi \cdot (r^2 - (r - t_{Cu})^2),$$

where  $n$  is the number of vias for heat dissipation from one LED,  $r$  is the radius of the hole in the PCB in meters,  $t_{Cu}$  denotes the thickness of the galvanically electroplated copper in meters. The thermal resistance of the via  $\theta_{Via}$  is calculated from the formula

$$\theta_{Via} = \frac{L}{\alpha_{Cu} \cdot S},$$

where  $L$  is the length of the material in the direction of heat propagation in m,  $\alpha_{Cu}$  is the thermal conductivity of copper  $\text{W}\cdot\text{m}^{-1}\cdot\text{K}^{-1}$  and  $S$  is the area through which heat passes [2].

#### 5 CONTROLS AND SOFTWARE

Microprocessor ARM Cortex M4 controls the whole device. Its task is to control the display, read the inputs for the buttons, the temperature of the LED matrix, and the correct operation of the switching power supply. The main task of the software is to reliably control transistors and communication with LED control circuits for multiplexing. The second task is calculating the data needed to display shapes or animations.

A refresh rate of 200 Hz is required to control the display. The multiplexing with ratio 1:3 increases this requirement to a minimum of 600 Hz. In practice, the microprocessor must map the data for the individual outputs of the multi-channel control circuits in about 1.5 ms, send approximately 3 Mbit/s of data via the Serial Peripheral Interface (SPI). Beside this, if necessary, MCU calculates the data for dynamic animations. To meet these requirements, SPI communication at speeds of up to 5 Mbit/s in eDMA (Direct Memory Access) mode is used, which allows to send the data in the background of processes. That creates a power reserve for the necessary calculations.

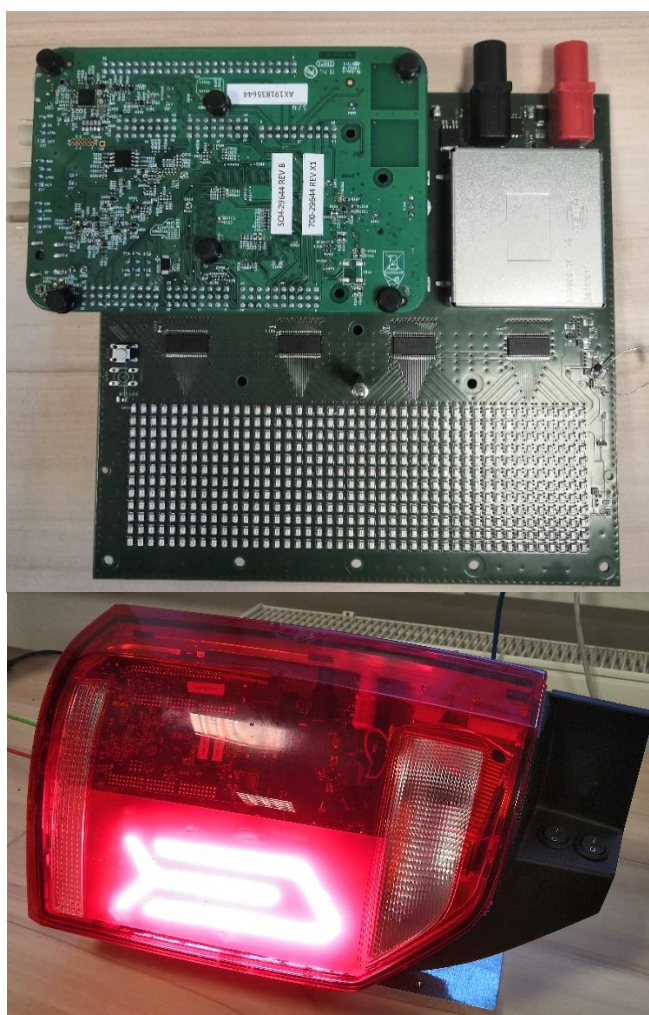


**Figure 3:** Fully assembled PCB (upper part of the picture) and the final prototype of rear combination lamp (lower part of the picture)

## 6 CONCLUSION

The paper deals with the introduction of an innovative concept of LED matrix display integrated into the rear combination lamp and the development pitfalls in the demanding automotive environment. The result is a fully functional prototype of the concept, including service software. The next steps are to verify the electromagnetic and electrical requirements as well as to design animations, which will demonstrate the capabilities of the device.

## REFERENCE

- [1] TLC5955 48-Channel, 16-Bit, PWM LED Driver with DC, BC, LED Open-Short Detection, and Internal Current Setting. In: *Texas Instruments Incorporated* [online]. ©1995-2020, 2014 [Accessed 2020-03-15]. Available at: <http://www.ti.com/lit/ds/symlink/tlc5955.pdf>
- [2] VW 80000. *Electric and Electronic Components in Motor Vehicles up to 3.5 t*. 2017-10. Germany: Volkswagen AG, 2017.
- [3] TL 81000. *Electromagnetic Compatibility of Automotive Electronic Components*. 2013-02. Germany: Volkswagen AG, 2013.
- [4] *OPTIMALIZACE DESKY PLOŠNÉHO SPOJE PRO VÝKONOVOU LED* [online]. Brno, 2013 [Accessed 2020-03-10]. Available at: [https://www.vutbr.cz/www\\_base/zav\\_prace\\_soubor\\_verejne.php?file\\_id=68151](https://www.vutbr.cz/www_base/zav_prace_soubor_verejne.php?file_id=68151). Diploma Thesis. BUT in Brno.

# ACQUISITION SYSTEM FOR ADAPTATION OF DIGITAL PREDISTORTER TO LINEARIZE AMPLIFIERS USING COMPARATOR

**Lukáš Jagla**

Master Degree Programme (2), FEEC BUT

E-mail: xjagla00@stud.feec.vutbr.cz

Supervised by: Jan Král, Tomáš Götthans

E-mail: jan.kral@vut.cz, gotthans@feec.vutbr.cz

**Abstract:** This paper presents a design of an acquisition system for adaptation of a digital predistorter implementing a comparator in the feedback path. The key parts of an acquisition chain are verified by simulations and suitable components are chosen for high-speed performance. Subsequently, a printed circuit board is designed, manufactured and prepared for further testing. Finally, an appropriate firmware is developed to evaluate the proposed hardware and to acquire data for digital predistorter adaptation.

**Keywords:** Digital predistortion, linearization, power amplifier, comparator, FPGA

## 1 INTRODUCTION

An essential part of the current wireless systems is a PA (Power Amplifier) enabling to transmit the RF (Radio Frequency) signal of the sufficient power through the environment. The best efficiency of the PA can be achieved when the PA operates as close as possible to its saturation region. Nevertheless, this is causing an undesired output signal distortion which is not acceptable in the current communication systems requiring a linear transmission and working with OFDM (Orthogonal Frequency Division Multiplexing) for instance. There are several methods for extending the linear region of the PA characteristics while achieving satisfactory efficiency, one of them is the DPD (Digital Predistortion) [1]. This work aims at a proposal of an acquisition module for adaptation of digital predistorter using comparator in the baseband. In specific terms, it focuses on hardware and firmware ensuring input data for further design evaluation in terms of deployment in the real DPD system.

## 2 COMPARATOR IN THE FEEDBACK PATH OF DPD SYSTEM

The proposed DPD system operates with signals in the baseband and enables to use of DSP (Digital Signal Processing) such as in the FPGA (Field Programmable Gate Array) or in a signal processor what makes a great advantage in terms of external components number mitigation. Moreover, it preserves temperature or aging stability [2]. A conventional digital predistorter includes the ADC (Analog-to-Digital Converter) in the feedback path which is the main bottleneck of the system, because in case of wideband signal operation it has to maintain high sample rate and resolution at the same time. These parameters make the ADC hardly available and very power hungry. A possible solution employs the comparator as a 1-bit ADC in the feedback path [3, 4].

## 3 PROPOSED DPD ARCHITECTURE USING COMPARATOR

The proposed architecture is depicted in Fig. 1 below. The IQ samples are converted to a continuous analog domain at the DPD output and modulated to the carrier frequency at first. Afterwards, the signal goes through the PA to the antenna and its small power is coupled back in the feedback

path. The feedback signal is demodulated and passed to the comparator input. One aspect of the proposed architecture is that the DPD coefficients estimation is based on just one signal component (in this case it is the in-phase component).

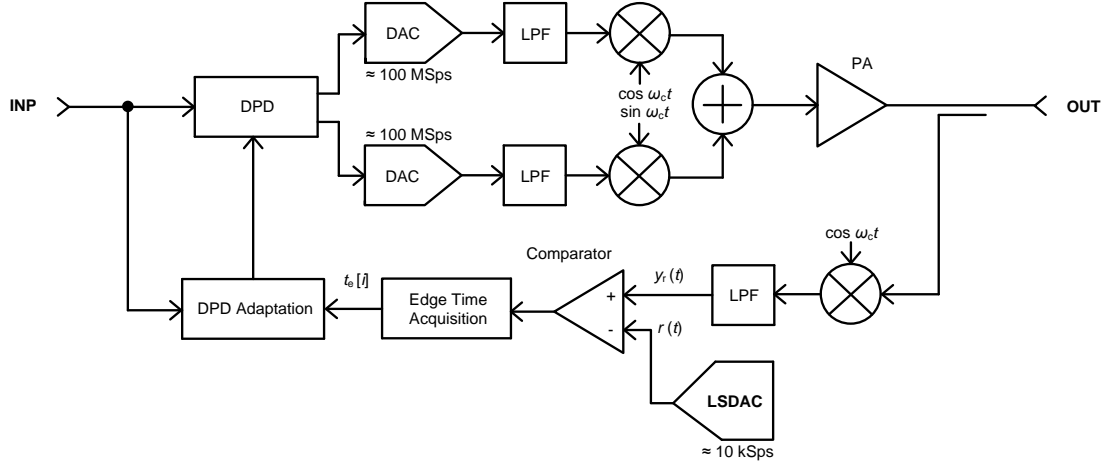


**Figure 1:** Proposed architecture using comparator in the feedback path.

The signal is compared with the output voltage level of the LSDAC (Low Speed Digital-to-Analog Converter). The comparator output edges indicate the input crossing the set voltage level at time instants  $t_e[i]$ , where  $i$  is the edge index. These time instants are acquired by the edge time acquisition circuit, which is described in the next paragraph. The output signal restoration can be described as follows:

$$y_r(t_e[i]) = r(t_e[i]), \quad (1)$$

where  $y_r(t_e[i])$  denotes a level of the demodulated signal and  $r(t_e[i])$  equals to a specific voltage level on the LSDAC output at appropriate time instant  $t_e[i]$ . The entire system is synchronized with single clock signal distributed all over the system the components ensuring the overall coherence between the transmitted and received samples.

### 3.1 EDGE TIME ACQUISITION CIRCUIT

The essential part of the feedback chain is the edge time acquisition circuit which is depicted in Fig. 2. This block consists of two D flip-flops with connected inputs in parallel but note that at the input of the first one there is a delay path. Subsequently, the comparator output signal edge is acquired at the rising edge of the clock signal. The acquisition precision depends on the set delay and timing properties of the D flip-flops and the clock signal distributor.

The acquisition of the time instants is not intended as the whole signal restoration at the certain sampling rate. It is sufficient to provide just several samples of the output signal at any time for the DPD coefficients estimation.

The time acquisition circuit has been simulated using OrCAD PSpice environment and the results can be seen in Fig. 2 on the right. On the upper side, there is depicted signal of the comparator input and on the following chart there are the inputs and outputs of D flip-flops. The simulation maintains the clock signal frequency of 100 MHz and the set delay equals to 6 ns.

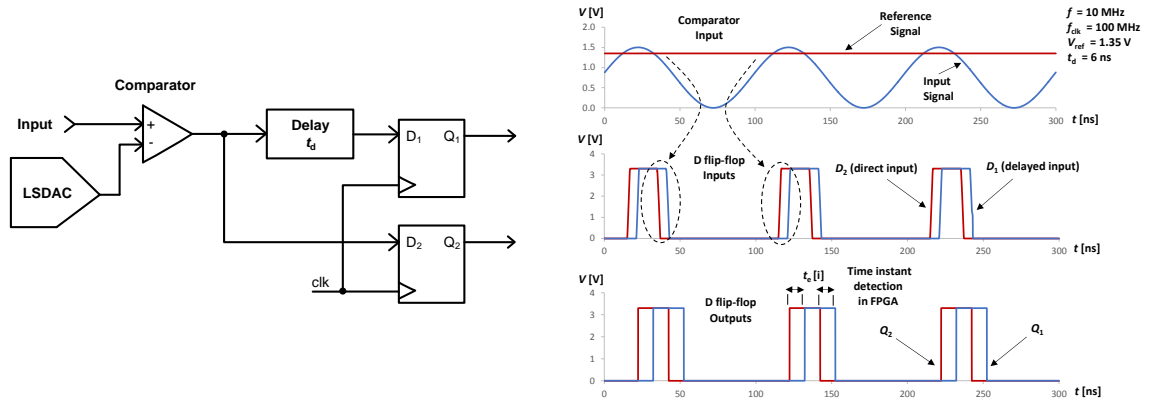


**Figure 2:** Edge time acquisition circuit (on the left), the simulation results (on the right).

#### 4 PROPOSED ARCHITECTURE EVALUATION CONCEPT

For the purpose of the architecture evaluation a concept depicted in Fig. 3 has been proposed. The core component of the system is the FPGA module Spartan-3A DSP 1800A containing a firmware and stored IQ data samples. These data are transmitted by the DAC Module. The output analog signal follows through the PA and attenuator and finally it is reaching the acquisition module which is the main objective of the development. The acquired edge time instants are sent back to the FPGA module afterwards. In the end, communication with PC (Personal Computer) is established and the data are transferred to the MATLAB software.

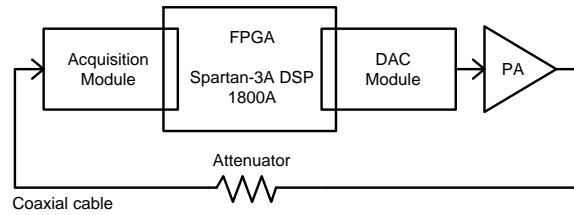


**Figure 3:** Evaluation concept of the proposed architecture.

##### 4.1 ACQUISITION MODULE DEVELOPMENT

The main objective of the development is the acquisition module containing demodulator, edge time detector circuit, clock signal distributor, and auxiliary components for communication with the FPGA module. The design has to fulfill the following requirements: the maximum working carrier frequency has to be 1600 MHz and the maximum frequency of the clock signal 500 MHz. In accordance with the required timing properties, the clock distributor and the D flip-flops have been selected to achieve the best performance.

The PCB (Printed Circuit Board) has been developed in KiCad environment. The description of the design steps is out of the scope of this paper, but the source files are available online [5]. The PCB is based on IS400 substrate of the 1.6 mm thickness. The manufactured and assembled PCB can be seen in Fig. 4 on the left side.

An appropriate firmware has been developed in VHDL (Very High Speed Integrated Circuit Hardware Description Language). The program flowchart is depicted in Fig. 4 on the right side. In the beginning, all the component registers have to be set up, subsequently, the transmission of the signal samples is started along with the data acquisition. After the last sample is sent, the stored data is transferred to PC (Personal Computer) for the further processing in MATLAB environment.

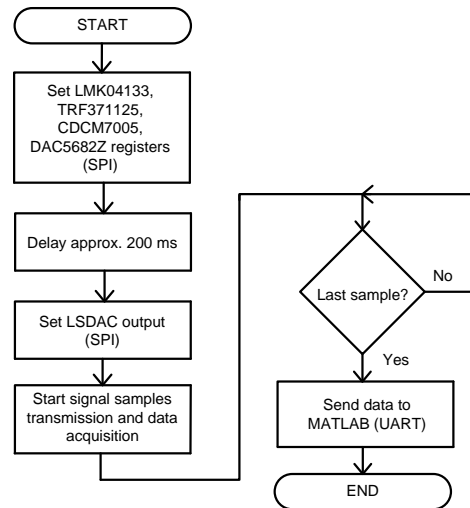
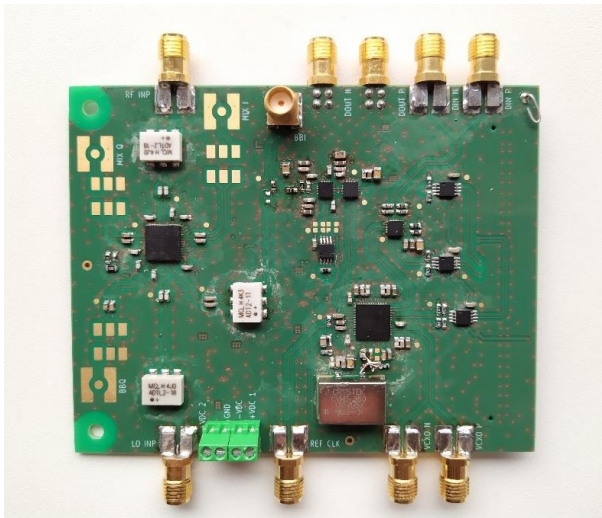


**Figure 4:** PCB design (on the left), flowchart of the proposed FW (on the right).

## 5 CONCLUSION

This paper presented the design of the acquisition module for the adaptation of a digital predistorter to linearize power amplifiers. The comparator deployment in the feedback path instead of ADC has been proposed. The PCB of the acquisition module has been developed along with an appropriate firmware in VHDL. The future steps are going to be focused on the hardware verification and the overall assessment of the architecture employment in real DPD systems.

## ACKNOWLEDGMENT

This work has been supported by the project of specific research FEKT-S-20-6325 „Mobilní komunikační systémy 5. a vyšších generací” and by the project InterReg AMOR ATCZ203 (Affordable Macro-Modeling Platform of Radio Frequency Systems and Devices).

## REFERENCES

- [1] GÖTTTHANS, Tomáš. *Advanced methods for analyzing non-linear dynamical systems* [online]. Université Paris-Est, 2014 [cit. 2020-05-05]. Available at: <https://tel.archives-ouvertes.fr/tel-01127560/file/2014PEST1020.pdf>
- [2] TEIKARI, Ilari. *Digital Predistortion Linearization Methods for RF Power Amplifiers* [online]. Helsinki University of Technology., 2008 [cit. 2020-05-05]. Available at: <https://pdfs.semanticscholar.org/e96b/cf6a9e14949b1ad82673b9149163fbd685ea.pdf>
- [3] WANG, H. et al. Forward modeling assisted 1-bit data acquisition based model extraction for digital predistortion of RF power amplifiers. *IEEE Topical Conference on RF/Microwave Power Amplifiers for Radio and Wireless Applications (PAWR)*. Phoenix: IEEE, 2017. pp. 59-62.
- [4] WANG, H. et al. 1-bit Observation for Direct-Learning-Based Digital Predistortion of RF Power Amplifiers. *IEEE Transactions on Microwave Theory and Techniques*, 2017, vol. 65, no. 7, pp. 2465-2475.
- [5] *PCB files repository* [online]. [cit. 2020-05-05]. Available at: <https://github.com/ljagla/kicad-masters-thesis>

# ACTIVE UPPER LIMB PROSTHESIS

Štěpán Brázdil

Master Degree Programme (2), FEEC BUT

E-mail: xbrazd18@stud.feec.vutbr.cz

Supervised by: Vratislav Harabiš

E-mail: harabis@feec.vutbr.cz

**Abstract:** This work focuses on the field of prosthetics, especially the issue of active prosthesis control. The goal is to perform a comprehensive analysis, design and construction of a mobile prosthetic system that, based on the analysis of sensory data (such as an EMG signal from multiple channels), can correctly classify a gesture and subsequent moving of the limb model. The measurements and test are executed on the real constructed system, which consists of the InMoov robotic hand, the Raspberry Pi controller and accessories. The results are critically evaluated, and future improvements are discussed.

**Keywords:** Active prosthesis, EMG, classification, Raspberry Pi, InMoov

## 1 INTRODUCTION

Currently there are rapid developments in the field of prosthetics, especially systems of actively controlled prostheses using advanced classification methods. Fast prototyping based on 3D printing allows to create high number of these solutions. This enables cheap development and implementation in comparison to commercial products. It is possible to consider using these systems in problematic areas of prosthetics – using it in developing countries and child prosthetics. This work focuses on the selection of a suitable open source model of the limb and the method of connection with the acquisition system. The main part is then aimed at the classification task. The selection of a suitable classifier, feature space and training procedure is one of the most significant fields which the success and applicability of active prostheses is based on. The importance of this work lies in the assessment of the functionality and real usability of a simple design solution of an active prosthesis, as well as in finding the optimal parameters and potential limits of EMG signal classification. Most of the scientific literature uses expensive immobile systems for testing, which in principle cannot be applied in practice.

## 2 DESIGNED SYSTEM

The designed active limb system is based on a relatively simple connection scheme shown in Figure 1. The robotic model InMoov is used [3]. Based on the application of 3D printing, a functional model of the upper limb is constructed. It allows 6 DOF using 6 rotation servomotors MG996R, which are controlled by PWM driver PCA9685. Acquisition of the EMG signal is enabled by connecting MyoWare amplifier with AD converter ADS1115 (16-bit, 860 Hz). Accelerometric and gyroscopic data are obtained by means of the MPU6050 module. The main control unit is the Raspberry Pi 2B (ARM Cortex-A7, 1.47 GFLOPS, I2C baudrate setting: 100 k Bd), which works on the official distribution of the Raspbian OS. All software codes were written in Python 3 language using several supporting libraries. The program enables controlling by a connected numeric keypad, execution of a script for passive prosthesis mode, learning mode (selection of SVM and LDA algorithms) and active prosthesis mode. Important information is displayed on the included 16x2 LCD. All hardware resources are selected in order to create a compact device that allows performing all functions without the need of a network adapter. Therefore, a standard 5V Li-Pol battery (power bank) can be used for power supply. Having regards to users' safety, this eliminates the possibility of getting a dangerous electric

shock. The mentioned parts are fully interconnected and functional, which allows subsequent data collection and analysis.

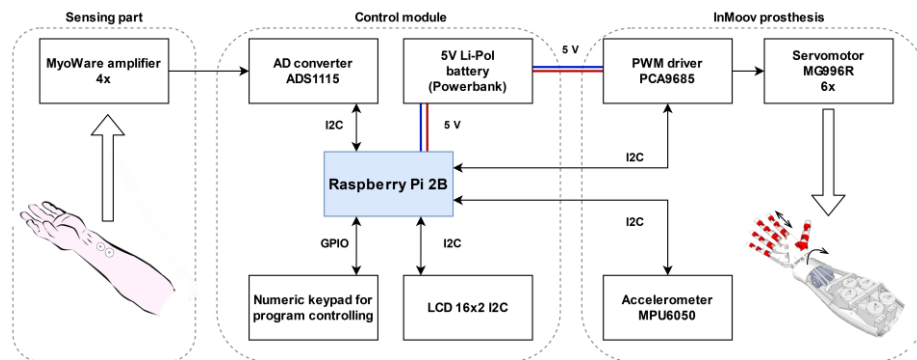


**Figure 1:** connection of main components of the active prosthesis



**Figure 2:** illustration of the active prosthesis prototype. Left: active prosthesis; right: control unit.

### 3 CLASSIFICATION

In the current phase of the development, only the sensing of EMG signals from four channels and subsequent classification into a specific class of gestures was implemented. In order to improve functionality of the prosthesis, future application of accelerometric data is already being considered. In order to increase the robustness of the system, information about the position can be used to create several classification subcategories. Learning a classifier to recognize a smaller number of gestures, in the case of the user's activity (walking, physical activity), could be an example. Subsequently, the automatic calm mode detection selects the other classifier with a greater number of gestures (typing, finer manipulation with objects). From a wide range of upper limb movements, only key gestures, which will facilitate the user's everyday life most, were selected. The analysis of these key gestures were performed on the basis of the work [1] [4], the graphical representation is shown in Figure 3

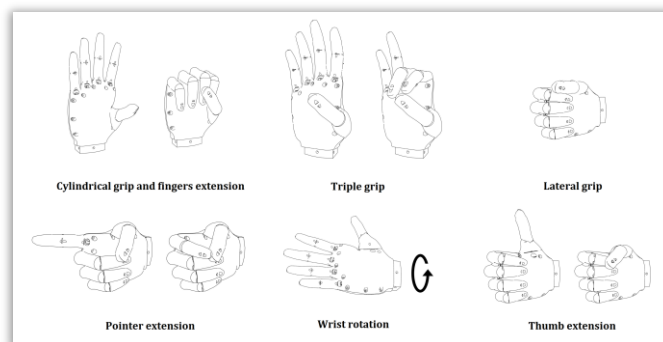


**Figure 3:** overview of key gestures

### 3.1 FEATURE SPACE

The selection of appropriate features belongs to one of the most discussed topics in the field of active prostheses. This work used the results of a series of testing [6], on the basis of which these features have been chosen: MAV, WL, ZC, WAMP, AR and SampEn. During the initial testing, a correlation between the features of MAV and WL was found. Therefore, it is recommended to delete one of these features from the dataset. If short-time windows for signal acquisition are selected, SampEn features do not contribute to improving the classification results.

### 3.2 CLASSIFIER

An analysis of the current trends in the application of gesture recognition was performed [2] [5]. Based on the evaluation of the average success rate and regarding the specific computing possibilities of the system, LDA and SVM classifiers were selected. The success of EMG signal classification is mainly influenced by the correct selection of the features and electrode placement. The very choice of the classifier has less impact on the success.

### 3.3 ELECTRODE PLACEMENT

At the present stage, a set of two adhesive electrode placement schemes has been developed, as shown in Figure 4. The individual schemes success rate will be compared in the following chapter. Scheme No. 1 allows the possible application of a prosthetic system for patients with trans carpal amputation and exarticulation of the wrist. Scheme No. 2 allows the application also for trans radial amputations of the upper limb.



**Figure 4:** electrode placement (MyoWare amplifiers)

## 4 TESTING AND RESULTS

Testing was performed on one healthy subject at rest position. The electrodes were applied to the right forearm according to the schemes above. SVM and LDA classifiers with the mentioned features were used. 4 measurements were performed for each scheme. Due to the low success of the rotation gesture classification and the inability of the prosthesis model to perform a lateral grip gesture, these gestures were excluded from testing. Proper classification of the rotation gesture will be a part of subsequent intensive research. 600 samples were obtained from individual measurements. 180 of them were randomly selected in order to evaluate the success of the classification. Due to the large quantities of the available results, a detailed overview will be given only for the more successful SVM classifier. The success of the LDA classifier was several percent lower. The results of the SVM classifier for the worst case of the 4 measurements available for a given scheme, including the confusion matrix and the t-SNE graph, are shown in Figure 5 and Figure 6. The t-SNE graph was selected due to the use of many features (40) projected into 2D space. This makes it easy to observe and compare the classifier's ability to create clusters into individual categories. The measurement was

validated on the basis of real-time gesture classification with subjective evaluation. In this case success drop in the range of 10-15% can be observed. The decrease can be caused by rapid changes in the gestures performing.

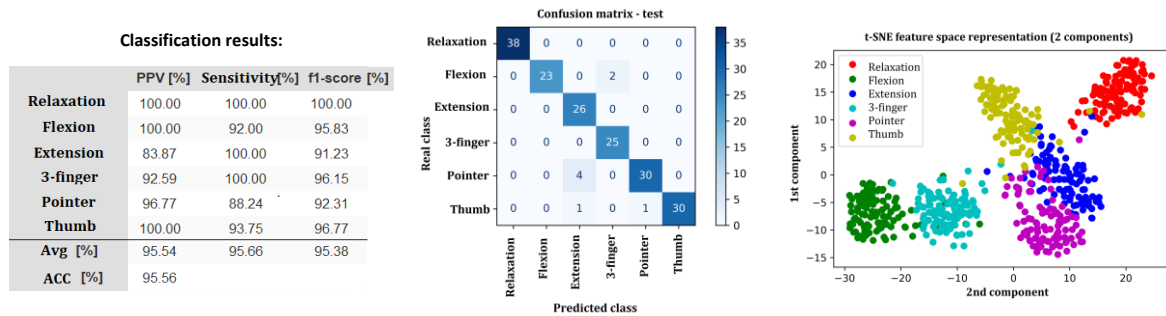


**Figure 5:** results of the SVM classifier, electrode placement: scheme 1

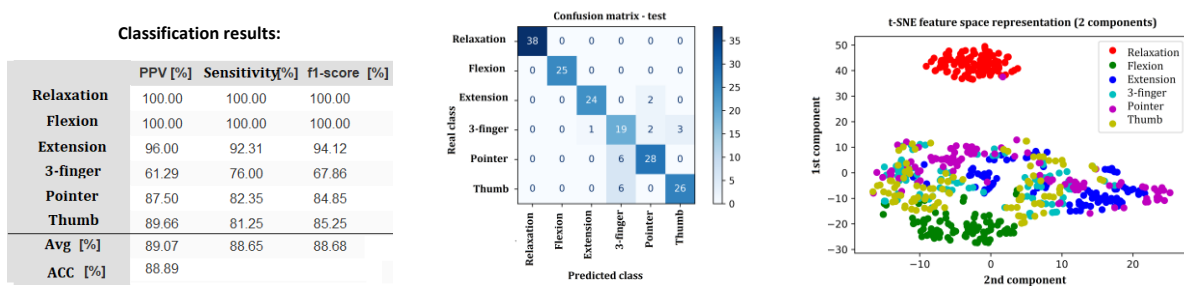


**Figure 6:** results of the SVM classifier, electrode placement: scheme 2

## 5 CONCLUSION

According to the achieved results, it can be stated that with the correct localization of the electrodes and selection of suitable classification features, satisfactory results of recognition of basic gestures can be achieved (90% success rate). The assembled active prosthesis is fully functional and allows displaying the learned gestures in real time after being connected to the main unit. The typical algorithm delay is in the range of 300-500 ms. The designed system works completely independently, miniaturization of the assembly can achieve the desired mobility.

## REFERENCE

- [1] CORDELLA, Francesca et al. Literature Review on Needs of Upper Limb Prosthesis Users. *Frontiers in Neuroscience*. 2016, **10**. DOI: 10.3389/fnins.2016.00209
- [2] HAKONEN, Maria et al. Current state of digital signal processing in myoelectric interfaces and related applications. *Biomedical Signal Processing and Control*. 2015, **18**, 334-359. DOI: 10.1016/j.bspc.2015.02.009.
- [3] Hand and Forarm. InMoov open source 3D printed life size robot [online]. InMoov [cit. 2020-03-07]. Available from: <http://inmoov.fr/hand-and-forarm/>
- [4] JANG, Chul Ho et al. A Survey on Activities of Daily Living and Occupations of Upper Extremity Amputees. *Annals of Rehabilitation Medicine*. 2011, **35**(6). DOI: 10.5535/arm.2011.35.6.907
- [5] NAZMI, Nurhazimah et al. A Review of Classification Techniques of EMG Signals during Isotonic and Isometric Contractions. *Sensors*. 2016, **16**(8). DOI: 10.3390/s16081304.
- [6] PHINYOMARK, Angkoon et al. EMG feature evaluation for improving myoelectric pattern recognition robustness. *Expert Systems with Applications*. 2013, **40**(12), 4832-4840. DOI: 10.1016/j.eswa.2013.02.023

# METHOD FOR EXTENDING THE FIELD OF VIEW FOR X-RAY COMPUTED TOMOGRAPHY WITH SUBMICRON RESOLUTION

**Marek Zemek**

Biomedical Engineering and Bioinformatics (2), FEEC BUT

E-mail: xzemek05@stud.feec.vutbr.cz

Supervised by: Martin Mézl, Jakub Šalplachta

E-mail: mezl@feec.vutbr.cz, Jakub.Salplachta@ceitec.vutbr.cz

**Abstract:** Computed tomography allows for nondestructive evaluation of samples. It is commonly used for many industrial and scientific applications. Some devices are capable of submicron resolutions, but this often comes at the cost of a limited field of view. Techniques that extend the field of view can greatly enhance the versatility of these scanners. One such technique is presented here. It is implemented on the Rigaku Nano3DX, almost doubling its lateral field of view. The method utilizes a standard reconstruction algorithm, and yields faithful reconstructions of scanned samples without the need for a larger detector.

**Keywords:** X-ray, computed tomography, field-of-view extension, offset scan

## 1 INTRODUCTION

Transmission X-ray computed tomography (CT) is an imaging modality used for non-destructive visualization of internal structures of objects. It is commonly used in medicine, various industrial fields, and scientific research. [1] Some specialized submicron CT scanners are capable of producing high-resolution images, with resolutions below a micrometer. [2]

The field of view (FoV) of standard CT scanners is limited mainly by the size of a scanner's detector array. For submicron CT scanners, the widths of FoVs are often in the range of single millimeters or smaller, which is a major restriction. Increasing the FoV by using a larger detector is straightforward in principle, but often impractical or not feasible in reality. An alternative approach, which uses the original detector, can greatly increase the versatility of these devices without requiring complicated hardware modifications.

This work presents an FoV extension method that allows for a nearly two-fold increase of the FoV. It is based on offsetting the sample, and its axis of rotation (AoR), to one side. The approach is implemented using the Rigaku Nano3DX X-ray microscope. Trials on simulated data show the method faithfully reconstructs cross-sections of large samples and yields images comparable in quality to ones created using a larger detector array. The method is referred to as an offset scan from this point.

## 2 MATERIALS AND METHODS

### 2.1 RIGAKU NANO3DX

The Rigaku Nano3DX [3] is an X-ray microscope capable of high-resolution CT measurements. The sample is placed close to the detector, and at a much greater distance from the X-ray source, leading to greater measurement stability, higher X-ray flux, and a low amount of beam divergence. The Nano3DX offers five degrees of freedom: 3-D translation, rotation around an axis parallel to the detector plane, and translation of the AoR in the T-stage, which is parallel to the detector plane, and perpendicular to the AoR. This T-stage enables the presented FoV extension approach. [3]

## 2.2 TEST DATA

The offset-scan approach was tested on four synthetic images, listed in table 1. Two projection datasets were formed for each image, simulating the geometry of the Nano3DX, and with the same amount of views across a  $2\pi$  angular range. The first, offset-scan dataset simulated an AoR offset and 1.8-fold FoV extension. The second, full-detector dataset had no offset, and the detector used was 1.8 times wider than in the first case. The presented method was used for the offset-scan dataset, and the Feldkamp-Davis-Kress algorithm (FDK) was used for reconstruction of both sets, using the same settings each time. Images were assessed both subjectively by comparing both reconstructions for each image, and objectively through peak signal-to-noise ratio (PSNR) and feature similarity index (FSIM). [9] Additionally, a sample of a tablet was scanned using the standard and extended FoVs to validate the practical merit of the offset-scan method. The presented method was implemented using Matlab R2018b, and the ASTRA toolbox was used for reconstruction. [4, 5]

## 3 FIELD-OF-VIEW EXTENSION METHOD

The presented FoV extension method depends on offsetting the AoR of the sample. It is based on approaches such as the one described by Chen et al. [6] Projections are acquired over an angular range of  $2\pi$ . The next steps of the method are estimation of the AoR's position, a transform onto a virtual detector, weighting of redundant data, padding, and finally reconstruction using an appropriate algorithm, such as FDK (fig. 1).

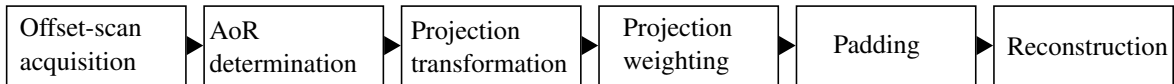


**Figure 1:** Flowchart of the presented method.

### 3.1 AXIS-OF-ROTATION POSITION ESTIMATION

Upon acquisition, offset-scan data are analyzed to determine where the AoR projects onto the detector. This is crucial, as an incorrect AoR position results in double edges or tuning-fork artifacts in the reconstruction. A reasonable compromise is to apply an automatic method for a rapid first estimate, and follow this by a manual check to ensure good accuracy.

Donath et al. [7] propose an AoR estimation method based on evaluating reconstructions for different AoR estimates. Three metrics are suggested in [7], but a different one has been applied here: the mean gradient magnitude of the reconstructed image. A curve formed by mean gradient magnitudes of reconstructions at a range of AoR estimates is detrended, its envelope is calculated, and the AoR at the maximum of the envelope is taken as the final AoR estimate.

### 3.2 VIRTUAL DETECTOR TRANSFORM

Reconstruction algorithms based on filtered backprojection (FBP) assume the central ray of the X-ray beam intersects the AoR at a right angle, and is orthogonal to the detector plane. [1] This is not the case when the AoR is offset relative to a stationary source and detector. Therefore, projections are transformed onto a slightly rotated virtual detector. Cone angles in the Nano3DX are relatively small, so the applied transform is subtle.

### 3.3 PROJECTION WEIGHTING

In the offset-scan approach, there is an overlap in the data around the AoR. Rays in this region are recorded twice over a  $2\pi$  scan, whereas outer regions of the sample are scanned only once. The central

region needs to be weighted to account for data redundancy. [6]

Simply removing redundant parts of projections would result in streak artifacts in FBP-based reconstructions. [8] Such artifacts are avoided when a smooth, typically sine-based weighting function is applied. Such a function must also ensure that it assigns a weight of 1 to non-redundant data, and that weights for two corresponding redundant datapoints add up to one. [6, 8]

### 3.4 PADDING AND TOMOGRAPHIC RECONSTRUCTION

After AoR determination, projection transform, and weighting of redundant data, the dataset is padded by zeroes to move the AoR to the middle of projections. The cone-beam reconstruction algorithm FDK is then applied. [6] For one-dimensional projections, this reduces to a fan-beam weighted FBP.

## 4 RESULTS AND DISCUSSION

Objective metrics for the two sets of synthetic images (Table 1) show that both reconstructions in each set are close in quality. Values of metrics for offset-scan data are slightly lower than full-detector values, most likely because every ray in full-detector data was measured twice across a  $2\pi$  range, leading to lower noise. This is not the case for most of the FoV in offset-scan data.

Apart from the marginally higher amount of noise in offset-scan data, there is no significant difference between the two types of images. There is no difference in scale between offset-scan data and full-detector reconstructions, and any loss of resolution caused by interpolation during the detector transform step is negligible for this particular scan geometry.

Reconstructed cross-sections in fig. 2 show the amount of FoV extension enabled by the presented method. The offset-scan method also helps reduce artifacts caused by truncated data, which are apparent in fig. 2A. This may be crucial in applications that benefit from undistorted gray values in the reconstruction, such as segmentation.

**Table 1:** Objective image quality metrics for simulated data (FD - full detector, OS - offset scan).

Dataset	PSNR (FD) [dB]	PSNR (OS) [dB]	FSIM (FD) [-]	FSIM (OS) [-]
Concentric rings	22.8400	22.1467	0.9994	0.9993
Grid	14.3180	13.9362	0.9987	0.9983
Siemens star	16.2160	14.4491	0.9975	0.9950
Shepp-Logan	28.2391	27.2125	0.9898	0.9888

## 5 CONCLUSION

An FoV extension approach for CT was presented, based on offsetting the AoR of a sample while scanning. The method was tested on synthetic data and yielded images on par with datasets that used a 1.8-times wider detector. Using the described approach, the Nano3DX is capable of performing scans of larger samples at very high resolutions, expanding the range of applications of this machine. Further testing on real datasets is planned in order to verify the functionality of the offset-scan method.

## ACKNOWLEDGEMENT

This work was supported by MEYS CR under the projects CEITEC 2020 (project No. LQ1601), CEITEC Nano Research Infrastructure (project No. LM2018110) and CEITEC Nano+ (project ID CZ.02.1.01/0.0/0.0/16\_013/0001728).

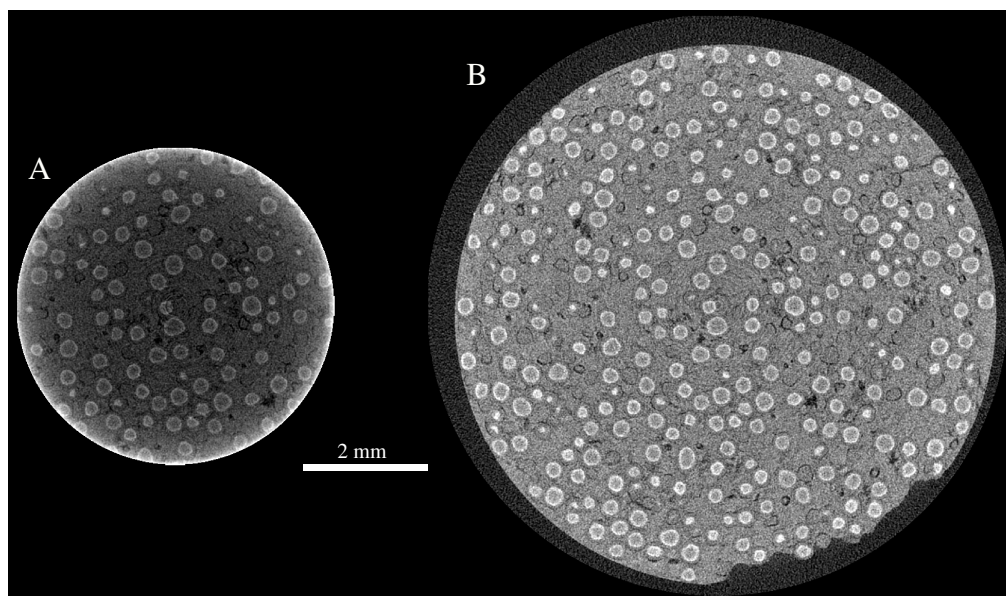


**Figure 2:** Reconstructed cross-sections of a tablet (original FoV in A, extended in B).

## REFERENCES

- [1] MARTZ JR., Harry E., Clint M. LOGAN, Daniel J. SCHNEBERK and Peter J. SHULL. *X-ray imaging: fundamentals, industrial techniques, and applications*. Boca Raton: Taylor & Francis, CRC Press, 2017. ISBN 978-0-8493-9772-1.
- [2] GELB, Jeff, Michael FESER, Andrei TKACHUK, et al. Sub-micron X-ray Computed Tomography for Non-Destructive 3D Visualization and Analysis. *Microscopy and Microanalysis*. 2009, **15**(S2), 618-619. DOI: 10.1017/S1431927609093623. ISSN 1431-9276.
- [3] TAKEDA, Yoshihiro and Kensaku HAMADA. A primer on the use of the nano3DX high-resolution X-ray microscope. *Rigaku Journal*. 2015, **31**(1), 10-15.
- [4] VAN AARLE, Wim, Willem Jan PALENSTIJN, Jan DE BEENHOUWER, et al. The ASTRA Toolbox: A platform for advanced algorithm development in electron tomography. *Ultramicroscopy*. 2015, **2015**(157), 35-47. DOI: 10.1016/j.ultramicro.2015.05.002. ISSN 03043991.
- [5] VAN AARLE, Wim, Willem Jan PALENSTIJN, Jeroen CANT, et al. Fast and flexible X-ray tomography using the ASTRA toolbox. *Optics Express*. 2016, **24**(22), 25129-25147. DOI: 10.1364/OE.24.025129. ISSN 1094-4087.
- [6] CHEN, Yunbin, Hao CHEN, Shoutao LI and Yuan WANG. An ICT Reconstruction Algorithm for Rotation Off-Centered Scan. In: *DIR 2015*. Ghent: NDT.net, 2015, s. 1-10. ISSN 1435-4934. Available from: [pdfs.semanticscholar.org/c1e6/65f144a4b05e60d199f188e8787668446929.pdf](https://pdfs.semanticscholar.org/c1e6/65f144a4b05e60d199f188e8787668446929.pdf)
- [7] DONATH, Tilman, Felix BECKMANN and Andreas SCHREYER. Automated determination of the center of rotation in tomography data. *Journal of the Optical Society of America A*. 2006, **23**(5), 1048-1057. DOI: 10.1364/JOSAA.23.001048. ISSN 1084-7529.
- [8] WESARG, Stefan, Matthias EBERT and Thomas BORTFELD. Parker weights revisited. *Medical Physics*. 2002, **29**(3), 372-378. DOI: 10.1118/1.1450132. ISSN 00942405.
- [9] ATHAR, Shahrukh a Zhou WANG. A Comprehensive Performance Evaluation of Image Quality Assessment Algorithms. *IEEE Access*. 2019, **7**(1), 140030-140070. DOI: 10.1109/ACCESS.2019.2943319. ISSN 2169-3536.

# REAL TIME EMG DETECTION IN THERAPEUTIC GAME

**Cindy Veselá**

Master Degree Programme (2), FEEC BUT

E-mail: xvesel75@stud.feec.vutbr.cz

Supervised by: Bronislav Hesko

E-mail: hesko@feec.vutbr.cz

**Abstract:** This article focuses on real-time detection of activity in electromyographical signal. The study is based on controlling the therapeutic game through the muscle activity, called myofeedback. Many different algorithms can be used to detect EMG signal. Nowadays there is rapid development of artificial intelligence not only in biomedical engineering. In this paper there is implemented convolutional neural network for signal segmentation with accuracy 97,13%.

**Keywords:** EMG, UNET, game, signal, biofeedback

## 1 INTRODUCTION

This work deals with sensing the electromyographic signal (EMG) and detecting muscle activity in real time. Electromyography is used in the diagnosis and therapy of the musculoskeletal or nervous system. To increase the motivation of the proband, a therapeutic game based on myofeedback was designed and implemented. The game is used to measure and possibly improve the user's reaction time.

There are a large number of methods that can be used to detect activity in an EMG signal. These can be based, for example, on thresholding, wavelet transform, empirical signal decomposition or artificial intelligence. [1] In order to calculate the reaction time, it is desirable that the chosen method of activity detection in the EMG record be as accurate as possible and at the same time the data processing time is minimal.

In recent years, there has been a rapid development of artificial intelligence, which also increases the popularity of these methods in solving segmentation problems. In most cases, however, these are two-dimensional signals (images), not one-dimensional signals. Equipping already learned networks is very fast. In this work, a convolutional neural network with U-Net structure was designed and programmed for signal classification. The network classifies individual samples of the EMG signal into two categories - resting sections and sections representing muscle activity, which then allows the calculation of the proband's reaction time.

## 2 BIOFEEDBACK

Biofeedback, or biological feedback, is used for therapeutic purposes in various medical disciplines. This technique is based on real-time recording of a biological signal. Feedback is most often communicated to the patient in audio or visual form. The patient's task is to achieve a predefined goal. For greater motivation, a game is very often implemented, which is controlled based on signal evaluation. [2]

This work focuses on myofeedback, which is feedback using an electromyographic signal. Myofeedback finds application in both diagnostics and therapy. Using myofeedback, it is possible to determine the proband's reactions to stimuli from the environment. It is a very widespread clinical technique in rehabilitation, intended for patients with disorders of the central nervous system (CNS) and patients with diseases or spinal cord injuries. The probe may not be able

to function the limbs, but still has the ability to activate the muscles and it is possible to sense the EMG signal, which extends the field of application to robotic limbs controlled by the signal. [2]

### 3 THERAPEUTIC GAME

In the work, a therapeutic racing game controlled by muscle activity was implemented. The task of the proband is to control the game of contractions and expansion of the muscle and to react as quickly as possible to the surrounding stimuli. The aim of the game is to avoid obstacles, react quickly enough to the relevant stimuli and thus achieve the highest possible score. The development of the game is outlined in Figure 1. During the game, the color of the traffic light changes at random time, to which the player must respond within three seconds by moving the limb (pedal simulation), otherwise the game ends. At the same time, they must avoid oncoming vehicles. If the oncoming vehicle is an ambulance, it will sound and the same reaction is required as when the traffic light changes color and the car disappears. During the game there is a gradual acceleration, which increases the difficulty. At the end of the game, the reaction times of the probands are displayed - the average and the best reaction time.



Figure 1: Therapeutic game

### 4 EMG SIGNAL RECORDING AND PROCESSING

The BITalino platform is used to record the EMG signal. It is hardware designed to record biological signals. An important parameter is the sampling frequency, which was selected as the maximum possible - 1000 Hz. The signal is stored in the BITalina tank and then loaded into the computer in the window. The window must be long enough to be informative, but it cannot be too long due to the long response time. The signal from BITalina is transmitted to the computer via Bluetooth 2.0, which causes a transmission delay in the range of 90-130 ms. The total delay is therefore given by the sum of the delay caused by the transmission (90-130 ms), the size of the loaded window (100 ms), the signal processing time (max. 5 ms) and the displaying of the corresponding response in the game (max. 3 ms).

In 20 probands, lower limb movement was recorded when the pedal was depressed. During the recording, the patient can sit or even stand. The electrodes for sensing the signal are placed on the lower limb according to the SENIAM recommendation, where to measure the activity of the gastrocnemius lateralis muscle, the active electrode should be placed in one third between the head of the fibula and the heel. [3]

#### 4.1 U-NET NEURAL NETWORK

It is very important for myofeedback that the signal processing is realized in a very short time, ideally real-time. However, for the purpose of calculating reaction times, the accuracy of detection cannot be reduced. For these reasons, the convolutional neural network U-Net was selected and implemented, the calculation of which can be performed on a computer graphics card.

U-Net is a fully connected convolutional network, its structure is shown in Figure 2 on the left. It consists of two sections - an encoder and a decoder. The dimensions of a feature map are shown at the bottom left corner of the element. The value above the rectangle indicates the number of channels. The arrows represent the individual operations according to the legend in the picture. [4]

The input of the designed neural network is the raw signal, so no signal preprocessing is required. In the descending part (encoder) the signal size decreases. Convolution operations create feature maps, these data are normalized and are an input to the activation function ReLU, the course of which is outlined in Figure 2 at the top right. The "max pool" operation performs data subsampling. From a window the size of two samples, only the sample with the higher value is always left, which halves the signal. This operation is described in Figure 2 at the bottom right. In the ascending part (decoder) the signal is resampled.

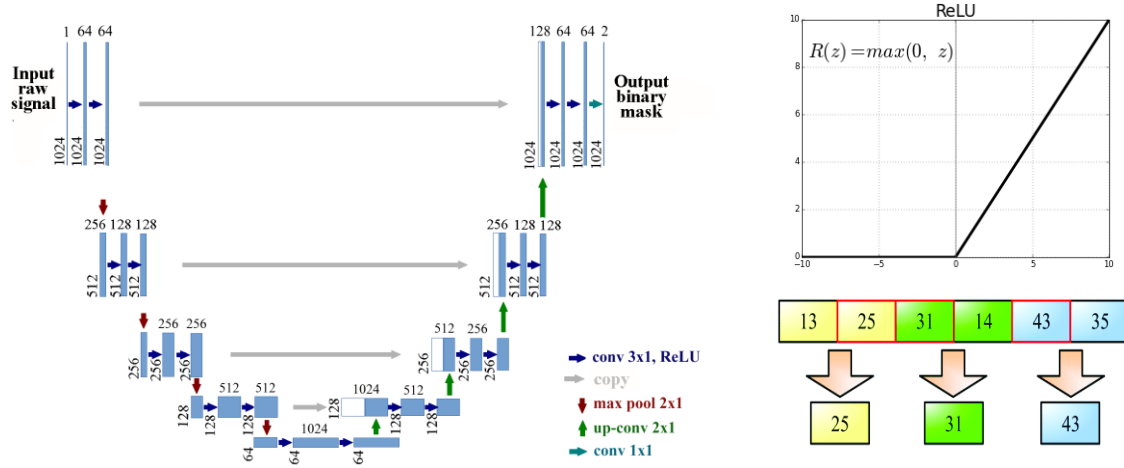


**Figure 2:** Hierarchy of convolutional neural network U-Net [4]

For network training, a database of manually annotated signals was created, which were marked at the site of apparent muscle activity. The annotation takes the form of assigning a binary value to each signal sample: 0 for calm EMG, 1 for activity. An example of annotated signals is shown in Figure 3. The database is divided into a training and test set, with the training set containing 544 signals and a test set of 42 signals.

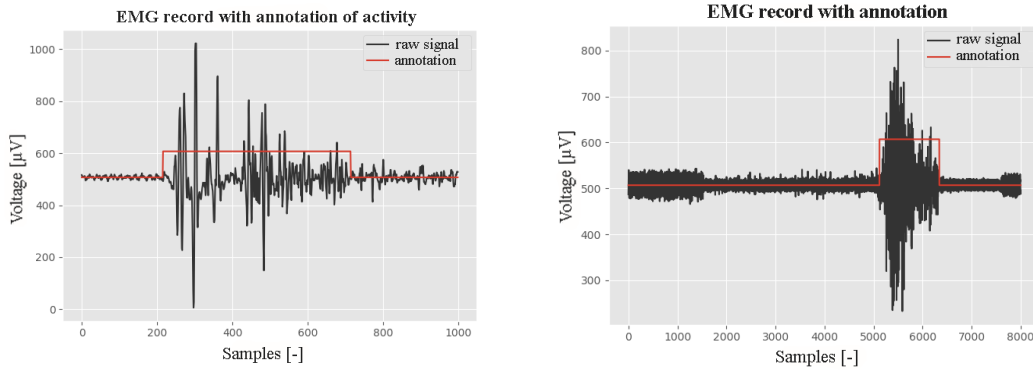


**Figure 3:** Manually annotated signals

When learning the network, the Adam optimization algorithm is used, which is very efficient. Adam uses adaptive learning speeds for various parameters. The difference between the network output and the reference data is described by the "Cross-Entropy" error function. When training a network, a "dropout" is included in the output layer, which helps reduce the interdependencies between neurons, thereby reducing the likelihood of re-learning and making the neural network more robust. The output of the network is a signal in which all samples are classified into two categories (calm / activity), as shown in Figure 4 on the right. Figure 4 on the left shows the output of the designed U-Net.

#### 4.2 REAL-TIME DETECTION AND RESULTS

The signal from BITalina is read in windows with a size of 100 samples. A signal length of 1024 samples is required at the input of the neural network. Since immediate processing of the current

section of the signal is required, this section is connected to the previous, already recorded, signal so as to produce a signal of the desired length - 1024 samples.

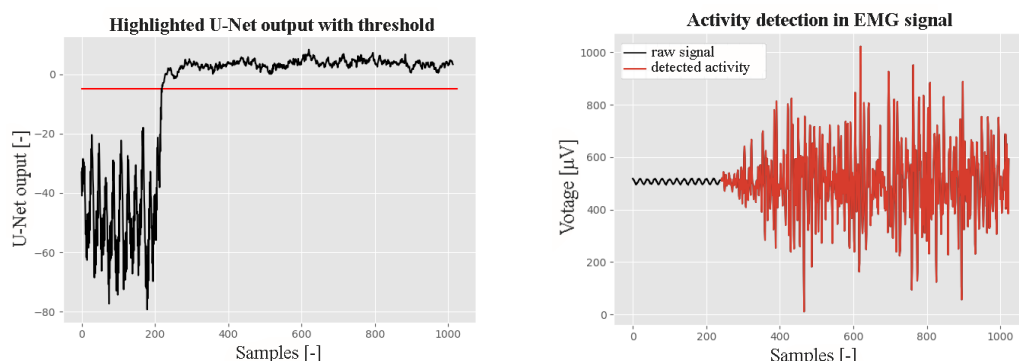


**Figure 4:** Neural network output, detection of EMG activity

The signal was processed by three different algorithms - the U-Net neural network, the Support Vector Machine (SVM) and the thresholding of the signal modified by the TKEO operator. The calculation was performed on a computer with an Intel i5 processor and an NVIDIA GeForce 940MX graphics card. The results of the methods are compared in Table 1.

Method	Accuracy [%]	Sensitivty [%]	Specificity [%]	Time [ms]
U-Net	<b>97,13</b>	<b>96,50</b>	<b>97,30</b>	4,61
SVM	95,36	94,82	95,47	2,03
TKEO	94,71	90,54	96,19	<b>1,45</b>

**Table 1:** Comparison of detection results by different methods

## 5 CONCLUSION

An approach for EMG signal processing was designed and implemented in the work, the output of which are signal samples classified into two categories: muscle activity or calm. Compared to other implemented methods, U-Net achieves the highest accuracy (97.13 %). The accuracy of the detection is important especially for the subsequent calculation of the reaction time. The processing of one section of the signal by the U-Net method takes an average of 4.61 ms, but a maximum of 5 ms, which is sufficient for the proposed game. The implemented therapeutic game is used to measure the reaction time, and possible to improve it.

## REFERENCE

- [1] REAZ, M. B. I., M. S. HUSSAIN a F. MOHD-YASIN. Techniques of EMG signal analysis: detection, processing, classification and applications. Biological Procedures Online. 2006, 8(1), 11-35. DOI: 10.1251/bpo115. ISSN 1480-9222
- [2] CONVERSE, Hayes, Teresa FERRARO, Daniel JEAN, et al. An EMG biofeedback device for video game use in forearm physiotherapy. In: 2013 IEEE SENSORS. IEEE, 2013, 2013, s. 1-4 [cit. 2020-03-22]. DOI: 10.1109/ICSENS.2013.6688474. ISBN 978-1-4673-4642-9.
- [3] HERMENS, Hermie J., Bart FRERIKS, Roberto MERLETTI, Dick Stegeman, Joleen Blok, Günter Rau, Cathy DISSELHORST-KLUG a Göran HÄGG. European Recommendations for Surface ElectroMyoGraphy: Results of the SENIAM project. SENIAM. ISBN 90-75452-15-2.
- [4] YUAN, LI, JIANG, et al. MU R-CNN: A Two-Dimensional Code Instance Segmentation Network Based on Deep Learning. Future Internet. 2019, 11(9). DOI: 10.3390/fi11090197. ISSN 1999-5903.

# DETECTION OF INTRACRANIAL HAEMORRHAGES IN HEAD CT DATA BASED ON DEEP LEARNING

**Jakub Nemček**

Master's degree Programme (5), FEEC BUT

E-mail: xnemce04@stud.feec.vutbr.cz

Supervised by: Roman Jakubíček

E-mail: jakubicek@feec.vutbr.cz

**Abstract:** In this paper, we present a method for detection of intracranial haemorrhages in the head CT data using convolutional neural networks. We introduce three 2D image classifiers that perform in three perpendicular anatomical planes and classify the CT slices into healthy or pathological, whereby they provide the information about the position of the haemorrhage in the 3D CT image. The accuracies of the three models are 90.19%, 88.15%, and 80.90% for the axial, sagittal and coronal plane.

**Keywords:** Intracranial haemorrhage, CT, classification, detection, convolutional neural network

## 1 INTRODUCTION

Intracranial haemorrhage is a common disease, which can affect various intracranial structures. This diagnosis represents a significant problem because of causing severe disabilities, and due to its high mortality risk. [1] Even a delay of a few minutes can cause death; therefore, the early determination of the diagnosis is of great importance. Computed tomography (CT) is the most common imaging modality used for examination of patients suspected of having a haemorrhage. However, traditional visual CT scan inspection done by radiologists is time-consuming. It demands the presence of an expert and requires a high level of concentration. False results can be easily caused by tiredness, focus on other diseases, or other human errors. Therefore, automated systems capable of detecting haemorrhages have been developed, which provide fast diagnosis estimation. Such a system helps the radiologist to make correct diagnostic conclusions. Nowadays, automated diagnostic systems are based on the machine learning methods thanks to their fast inference capability and the ability to perform complex tasks. [2]

Recently, many papers about machine learning-based automated detection of intracranial haemorrhages have been published. Chilamkurthy et al. (2018) [3] have described an approach to detection of all five types of haemorrhages (intraparenchymal, intraventricular, subdural, epidural, and sub-arachnoid) in 2D CT slices based on a combination of convolutional neural network (CNN) architecture ResNet18 and random forests. Two datasets are described: training dataset Qure25k, which includes 21 095 3D scans, and publicly available test dataset CQ500, which contains 491 scans. The authors have achieved an area under the receiver operating characteristics curve (AUC) 0.9419. Grewal et al. (2018) [2] have proposed slice-level CNN classification architecture DenseNet and a recurrent neural network for incorporating the 3D context. Training and testing datasets with 185 and 77 CT scans respectively are described, and the authors have demonstrated the accuracy of 81.82%. Cho et al. (2019) [4] have described a method for haemorrhage and its five types detection, which consists of several cascaded CNN models. The authors have achieved a sensitivity of 97.91% and specificity 98.76 % with a dataset with more than a hundred thousand CT scans.

This paper describes an approach of the detection of intracranial haemorrhages based on CNN due to their excellent performance potential without the need of relevant feature extraction. The de-

scribed detection method is based on series of three CNN classifiers performing in axial, sagittal and coronal anatomical planes.

## 2 AVAILABLE DATASET

The authors of [3] (2018) collected a head CT dataset CQ500 containing 491 scans, that is made available for public access and is used in our method. The anonymized scans were obtained from different CT scanners from various radiology centers. Every scan fulfils the conditions that the subject is more than seven years old and does not have any post-operative defects, and in addition, there should be at least one non-contrast CT series with a soft reconstruction kernel.

In addition, the annotations based on evaluations by three independent radiologists are available in the form of patient’s diagnosis. The CT data include scans of healthy subjects as well as scans with all types of intracranial haemorrhages together with the information about affected hemisphere, age (chronic or not) and about the presence or absence of a midline shift, mass effect, and fractures. [3] For our purposes, mentioned annotations need to be extended in the way of labelling the presence or absence of the haemorrhage in each 2D image. We created expert slice-level annotations of the presence of the haemorrhages and their types for individual slices in the axial, sagittal and coronal plane. However, for slices of the 3D scan to be annotated, the pathology must be observed by the majority of the radiologists [3]. Some of the slices may show more than one type of haemorrhage.

## 3 METHODS

The proposed method of the haemorrhages detection in a head 3D CT scan is based on a consecutive classification of 2D slices in mutually perpendicular anatomical planes: axial, sagittal and coronal. Three classification subsystems based on CNN are trained for the determination of the findings in the slices. Together, these three subsystems form a system that provides the final 3D bounding box via the classification of the individual slices.

### 3.1 EXPERIMENTAL DATA

Non-contrast scans from the CQ500 dataset (194 with and 221 without a finding) are used. The dataset is randomly divided into mutually disjunct subsets for training and testing in the ratio of 7:3. An approximate number of 2D images in the individual subsets are shown in Table 1.

All of the used slices are subjected to a pre-processing in the form of resampling to the size  $224 \times 224$ .

	Training subset			Testing subset		
	Axial	Sagital	Coronal	Axial	Sagital	Coronal
Pathological	6k	10k	15k	3k	5k	8k
Healthy	8k	19k	20k	3k	8k	8k
Total	14k	29k	35k	6k	13k	16k

**Table 1:** An approximate number of images in the training and testing subsets for the anatomical planes.

### 3.2 CNN

The CNN architecture ResNet50 [5] pre-trained on the ImageNet dataset [6] is chosen as the classifier of the slices in the three planes. The architecture is modified to be able to classify images into two categories (pathological or healthy slice). The networks for the three planes are fine-tuned with the images of the training subset with an augmentation in the form of a random reflection, slight translation and rotation in every epoch, together with a random data shuffle. In the case of each

network, the Adam optimisation method [7] was used. Other training parameters are listed in Table 2.

	Mini-Batch	Epochs	Init. LR	L2 reg.
Axial	30	5	$10^{-4}$	$10^{-8}$
Sagittal	24	3	$10^{-4}$	0.005
Coronal	24	4	$10^{-4}$	$10^{-8}$

**Table 2:** Training parameters of the classification networks for the three anatomical planes.

#### 4 RESULTS AND DISCUSSION

Three trained classifiers are validated on the prepared testing sets. The accuracy which is defined as the ratio of true positive detections to the number of tested images was chosen to evaluate the performance. The fine-tuned classification models achieve 90.19%, 88.15%, and 80.90% accuracy for the axial, sagittal and coronal planes respectively. The examples of true positive axial slices are shown in Figure 1, which points out the ability of the classifier to distinguish various types of haemorrhages despite their large size and shape variability.

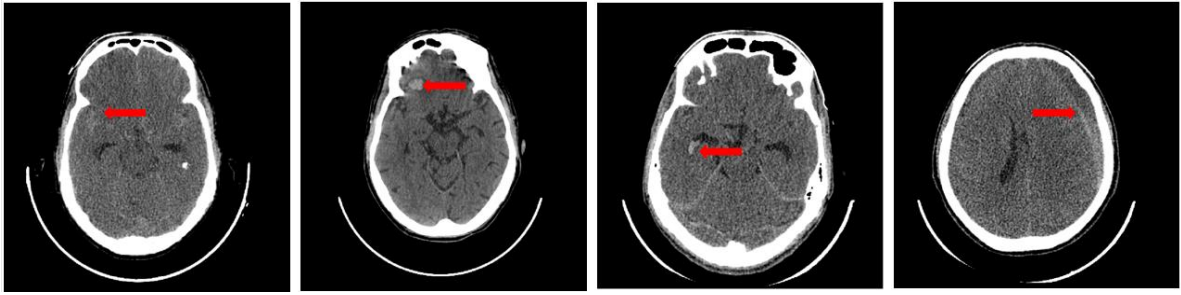


**Figure 1:** True positive axial slice classification results (the arrow denotes the haemorrhages).

In most cases the classifiers perform well and predict correct labels. False classification might appear; however, such a situation might occur while processing some hardly noticeable haemorrhages or marginal slices (see Figure 2). This minority misclassifications may be caused by the hardly distinguishable bleeding of small size.

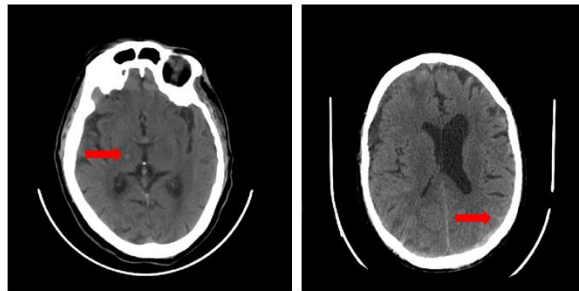


**Figure 2:** False negative axial slice classification results (the arrow denotes the haemorrhages).

The proposed method of the haemorrhage detection has great potential for computer aid diagnostic systems, forasmuch as it can warn a radiologist of the suspicion of a finding. It can roughly demark the affected region, which may minimize the chances for missing the haemorrhage by an oversight. Besides, the algorithm may reduce the time needed for diagnosis identification. The incorporation of such an algorithm into CT systems may help to prevent permanent disability or even death.

## 5 CONCLUSION

The automated detection of intracranial haemorrhages in CT scans has great medical potential, as a functioning algorithm incorporated into a CT system may prevent even patient's death. We introduce a detection approach based on three classification CNN-based models working in three mutually perpendicular anatomical planes. The nets have been fine-tuned for detection and localisation of intracranial haemorrhages as classification task. The paper describes the preparation of the training and testing dataset, the process of networks training, and their validation. The proposed classifiers achieve 90.19%, 88.15%, and 80.90% accuracy for the axial, sagittal and coronal planes respectively. These results point out the great potential of the algorithm as a tool for acceleration and refinement of the final diagnosis.

## REFERENCES

- [1] HEIT, Jeremy J, Michael IV a Max WINTERMARK. Imaging of Intracranial Hemorrhage. *Journal of Stroke* [online]. 2017, 19(1), 11–27. Dostupné z: doi:10.5853/jos.2016.00563
- [2] GREWAL, Monika, Muktabh Mayank SRIVASTAVA, Pulkit KUMAR a Srikrishna VARADARAJAN. RADnet: Radiologist level accuracy using deep learning for hemorrhage detection in CT scans. *Proceedings - International Symposium on Biomedical Imaging* [online]. 2018, 2018-April, 281–284. ISSN 19458452. Dostupné z: doi:10.1109/ISBI.2018.8363574
- [3] CHILAMKURTHY, Sasank, Rohit GHOSH, Swetha TANAMALA, Mustafa BIVJI, Norbert G. CAMPEAU, Vasantha Kumar VENUGOPAL, Vidur MAHAJAN, Pooja RAO a Prashant WARIER. Development and Validation of Deep Learning Algorithms for Detection of Critical Findings in Head CT Scans [online]. 2018, 1–18. Dostupné z: <http://arxiv.org/abs/1803.05854>
- [4] CHO, Junghwan, Ki Su PARK, Manohar KARKI, Eunmi LEE, Seokhwan KO, Jong Kun KIM, Dongeun LEE, Jaeyoung CHO, Jeongwoo SON, Myungsoo KIM, Sukhee LEE, Jeongho LEE, Changhyo YOON a Sinyoul PARK. Improving Sensitivity on Identification and Delineation of Intracranial Hemorrhage Lesion Using Cascaded Deep Learning Models. *Journal of Digital Imaging* [online]. 2019, 32(3), 450–461. ISSN 1618727X. Dostupné z: doi:10.1007/s10278-018-00172-1
- [5] HE, Kaiming, Xiangyu ZHANG, Shaoqing REN a Jian SUN. Deep residual learning for image recognition. *Proceedings of the IEEE Computer Society Conference on Computer Vision and Pattern Recognition* [online]. 2016, 2016-Decem, 770–778. ISSN 10636919. Dostupné z: doi:10.1109/CVPR.2016.90
- [6] RUSSAKOVSKY, Olga, Jia DENG, Hao SU, Jonathan KRAUSE, Sanjeev SATHEESH, Sean MA, Zhiheng HUANG, Andrej KARPATY, Aditya KHOSLA, Michael BERNSTEIN, Alexander C. BERG a Li FEI-FEI. ImageNet Large Scale Visual Recognition Challenge. *International Journal of Computer Vision* [online]. 2015, 115(3), 211–252. ISSN 15731405. Dostupné z: doi:10.1007/s11263-015-0816-y
- [7] KINGMA, Diederik P. a Jimmy BA. Adam: A Method for Stochastic Optimization [online]. 2014, 1–15. Dostupné z: <http://arxiv.org/abs/1412.6980>

# MY\_UMI\_TOOL: PROCESSING OF UNIQUE MOLECULAR IDENTIFIERS WITHOUT MAPPING TO A REFERENCE GENOME

**Lujza Barilíková**

Master Degree Programme (2), FEEC BUT

E-mail: xbaril02@stud.feec.vutbr.cz

Supervised by: Karel Sedlář

E-mail: sedlar@feec.vutbr.cz

**Abstract:** The presented paper describes a novel algorithm for processing unique molecular identifiers (UMIs) without mapping to a reference genome. For the past few years, there has been a rapid rise in the use of sequencing technologies and progress in bioinformatics tools. However, available tools for processing UMIs are usually relative computationally demanding and time-consuming which led us to design and develop a new algorithm as well as to implement some available software to provide an effective estimation of the total number of unique molecules. My\_UMI\_tool performs four major steps: preprocessing of an input file, clustering by UMIs, clustering by sequence similarity, and marking duplicates to generate final file.

**Keywords:** unique molecular identifiers (UMIs), next-generation sequencing (NGS), PCR error

## 1 INTRODUCTION

As each individual and organism has a specific nucleotide sequence, DNA sequencing can provide insights into diversity and evolution of organisms that cannot be grown in cultures in the laboratory and therefore are not easy to study. With the availability of sequencing technologies, study and analysis of nucleic acid composition for specific applications is accomplished and will be helpful in the area of basic science as well as translational research areas. Many high-throughput sequencing platforms require PCR amplification to be performed before sequencing [1]. Nevertheless, different molecules are amplified with unequal probabilities so this step can easily lead to certain sequences becoming excessively presented in the final library. Therefore, random oligonucleotide barcodes, otherwise referred to as UMIs, are added to DNA fragments before PCR amplification to distinguish between identical copies arising from distinct molecules and PCR duplicates arising from the same molecule [2]. Duplicate sequencing reads produced by PCR amplification may lead to mentioned biases which reduce quantitative accuracy and cause misleading interpretation of sequencing results [3].

## 2 MATERIALS AND METHODS

### 2.1 ANALYSED DATA

In this paper, samples prepared by two different protocols from Chronic Lymphocytic Leukemia (CLL) patients are studied. Data generated from Formalin-Fixation and Paraffin-Embedding (FFPE) sample have some advantages over data from Freshly Frozen (FF) sample including abundance and availability [4]. On the other hand, the sample is highly degraded and chemically modified, which could affect the final accuracy. However, as shown in Figure 1, there is a strong correlation of 0.841 (Pearson) of gene expression between FFPE and FF sample pair. Library of sequences was subsequently generated by all-in-one library preparation protocol QuantSeq 3' mRNA-Seq Library Prep Kit [5] with an additional module with UMIs.

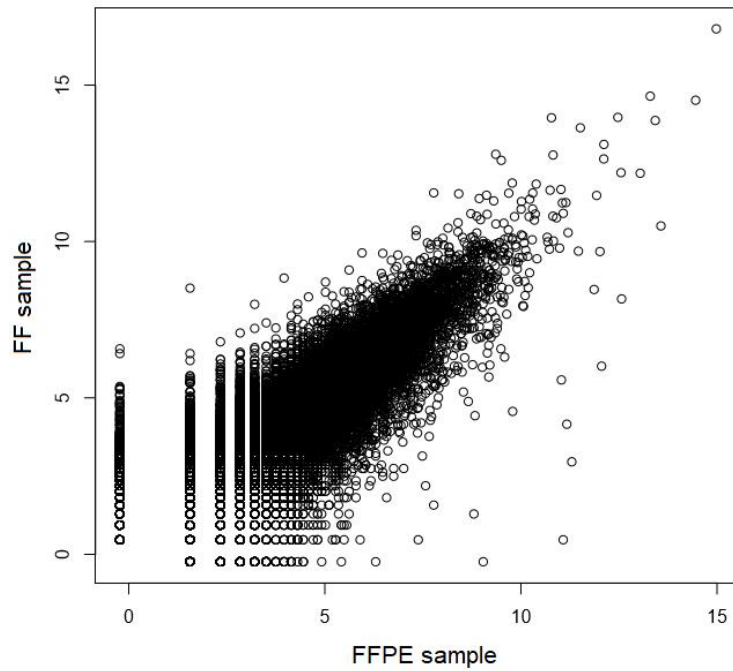


**Figure 1:** Correlation plot of gene expression in FFPE and FF sample pair

## 2.2 NOVEL ALGORITHM

The presented tool avoids time consuming alignment before deduplication in order to design fast algorithm that can efficiently determine the absolute number of unique molecules by identifying duplicate reads. Firstly, as shown in Figure 2, the novel algorithm requires FASTA or FASTQ file as an input. In preprocessing stage, UMIs are extracted from read sequences, afterwards added to the read name and with corresponding sequences stored to a separate file. According to UMIs, sequences are clustered to generate read groups only with the same UMI. Using versatile open-source tool VSEARCH [6], reads of each group are clustered by sequence similarity using global pairwise sequence comparison. Grouped sequences are additionally filtered by using a cutoff alignment score to identify reads originated from the same fragment. As an output, FASTA or FASTQ file with marked duplicates is generated.

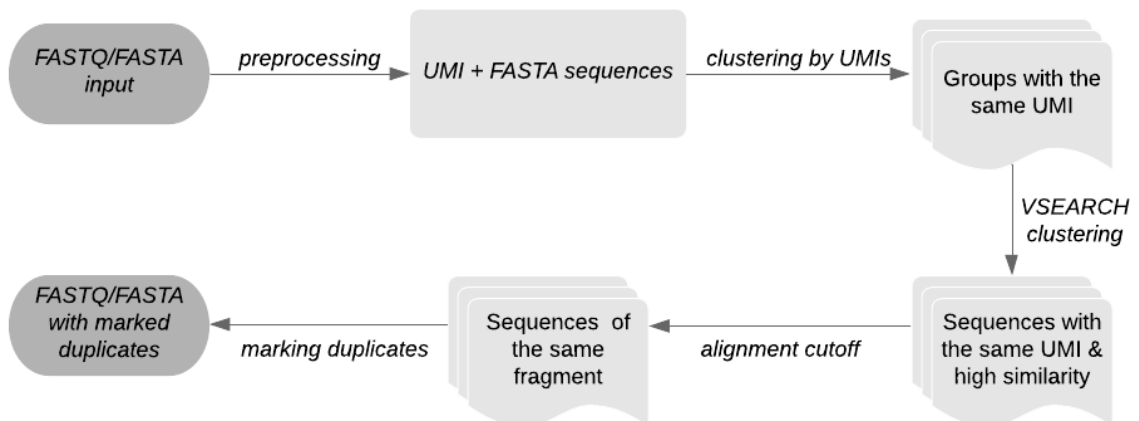


**Figure 2:** Schematic diagram of the proposed algorithm

### 2.3 RESULTS

As shown in Table 1, when comparing results from the proposed My\_UMI\_tool method to those obtained by available tool UMI-tools [1] for handling UMIs in NGS data sets, it must be pointed out that a high percentage of sequences in both samples are clustered and mapped identically in both tools. From this standpoint, it can be considered that these sequences are mapped correctly.

In this samples, UMIs are six bases long and it is important to highlight the fact that even UMIs with three error bases were grouped by UMI-tools together and this could be considered as very exaggerative. In line with the ideas of UMI-tools and its acceptance of UMI errors, it can be concluded that 5.7 % of sequences in FFPE sample and 14.5 % of sequences in FF sample are therefore clustered by My\_UMI\_tool more complexly in smaller groups.

In contrast, My\_UMI\_tool expects UMIs to be without any error bases and corresponding 2.1 % of sequences in FFPE sample and 2.2 % of sequences in FF sample, more complexly grouped by UMI-tools, could be the result of mentioned alignment before deduplication. After the alignment, reads aligned to the genome with the same mapping position are grouped together and then, by examining all UMIs at the single locus, clustered by different methods to resolve UMI errors.

	FFPE sample	FF sample
	[%]	[%]
<b>Clustered in both tools</b>	92.2	83.3
<b>Clustered in My_UMI_tool</b>	5.7	14.5
<b>Clustered in UMI-tools</b>	2.1	2.2

**Table 1:** Comparison results between the proposed My\_UMI\_tool and UMI-tools method

### 3 CONCLUSIONS

As stated at the beginning of this paper, the main purpose was to design fast and memory-efficient algorithm to determine the absolute number of unique molecules by identifying duplicate reads. The results show that avoiding time-consuming alignment before deduplication does not seem to impact the final determination of the absolute number of unique molecules and are equal to or better than results that are currently accepted. One limitation of our implementation is that we expect UMIs to be without any error base and this could be slightly considered in the future. The problem is that during PCR or sequencing, UMI errors, such as nucleotide deletion insertions or substitutions, could occur. However, there are reasons to doubt how UMI-tools take UMI errors into account. As we stated before, it is very debatable and final clusters are considered ambiguous. Furthermore, we believe that the option with the same UMI and some errors in sequences is still more possible than errors in mapped positions and at the same time error in UMIs. Under certain assumptions, our tool can be therefore construed as more probable.

In summary, this paper argued that My\_UMI\_tool is a valuable tool for deduplicating next-generation sequencing data using UMIs, where duplicate reads are removed from the sample to prepare data for downstream analysis. Apart from existing tools, My\_UMI\_tool is designed to avoid alignment before deduplication and therefore will fill the gap in the currently available tools. Consequently, we believe that this tool will be useful in a variety of applications that use UMIs to improve the accuracy of NGS assays. In conclusion, My\_UMI\_tool is provided as an open-source and is freely available online at [https://github.com/lujbarilikova/My\\_UMI\\_tool.git](https://github.com/lujbarilikova/My_UMI_tool.git).

## ACKNOWLEDGEMENT

This paper has been supported by the Bioinformatics Core Facility - CEITEC MU.

## REFERENCES

- [1] KULSKI, Jerzy K. Next-generation sequencing—an overview of the history, tools, and “Omic” applications. *Next Generation Sequencing—Advances, Applications and Challenges*, 2016, 3-60.
- [2] SMITH, Tom; HEGER, Andreas; SUDBERY, Ian. UMI-tools: modeling sequencing errors in Unique Molecular Identifiers to improve quantification accuracy. *Genome research*, 2017, 27.3: 491-499.
- [3] ISLAM, Saiful, et al. Quantitative single-cell RNA-seq with unique molecular identifiers. *Nature methods*, 2014, 11.2: 163.
- [4] PENNOCK, Nathan D., et al. RNA-seq from archival FFPE breast cancer samples: molecular pathway fidelity and novel discovery. *BMC Medical Genomics*, 2019, 12.1: 1-18.
- [5] MOLL, Pamela, et al. QuantSeq 3' mRNA sequencing for RNA quantification. *Nature methods*, 2014, 11.12: 972.
- [6] ROGNES, Torbjørn, et al. VSEARCH: a versatile open source tool for meta-genomics. *PeerJ*, 2016, 4: e2584.

# QUALITY IMPROVEMENT OF LQG CONTROL USING $\mathcal{H}_\infty$ OPTIMIZATION

**Dominik Friml**

Master Degree Programme (2), FEEC BUT

E-mail: xfriml02@stud.feec.vutbr.cz

Supervised by: Lukáš Pohl

E-mail: pohl@feec.vutbr.cz

**Abstract:** This paper describes the method of using  $\mathcal{H}_\infty$  optimization for tweaking of the existing structured controller. This method is presented on an example of LQG controller for the classical problem of the inverted pendulum on a cart. This means, that it is applicable not only on controller problems, but also on observer problems.

**Keywords:** H-infinity, optimization, H-2, norm, control, LQG, hinfstruct, inverted pendulum

## 1 DESCRIPTION OF CONTROLLED SYSTEM AND USED CONTROLLER

Assumed model of the inverted pendulum on a cart is shown in figure 1. This model has one input, force  $F$ , and four states. Those are cart position  $x$ , cart acceleration  $\dot{x}$ , pendulum angle  $\theta$  and angular acceleration  $\dot{\theta}$ . Further assume, that the only directly measured states are  $x$  and  $\theta$ . This assumption corresponds to reality, since the acceleration measurement is usually substituted with a differential approximation using measured data of  $x$  and  $\theta$ .

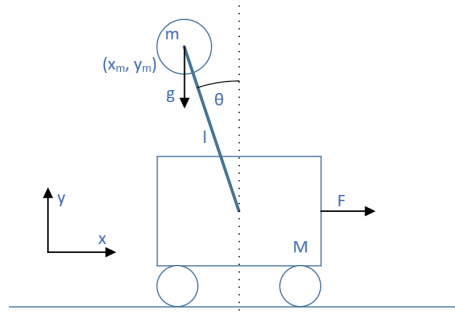


**Figure 1:** Inverted pendulum scheme

The problem of keeping the pendulum in an upright position has been solved using an LQG control. Details of this design are not concern of this article. As seen in the figure 5, the LQG solution successfully stabilizes the pendulum in the upright position. The cart position  $x$  control quality is poor, so it needs to be improved.

## 2 USING $\mathcal{H}_\infty$ OPTIMIZATION FOR CONTROL QUALITY IMPROVEMENT

Since the LQG control is a special case of  $\mathcal{H}_2$  controller synthesis problem [1], the LQG controller tuning using  $\mathcal{H}_2$  norm optimization seems to be an obvious solution, but similarity of the LQG and  $\mathcal{H}_2$  synthesis is shown to be rather obstruction. Using  $\mathcal{H}_2$  synthesis, even using a dynamic weights,

weight matrix that is not constant over all frequencies, does not offer any direct advantage over the classical LQG design using weight matrices  $\mathbf{W}$ ,  $\mathbf{V}$ ,  $\mathbf{R}$  and  $\mathbf{Q}$ .

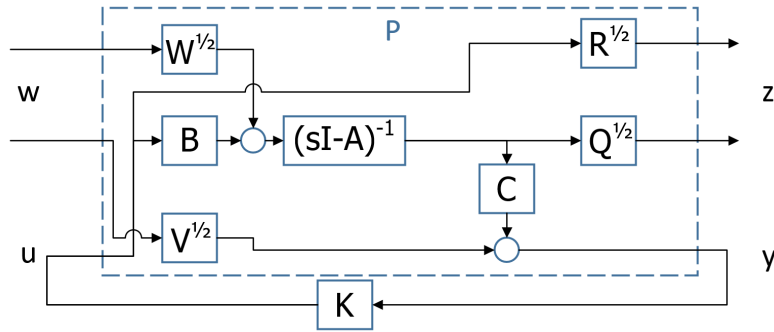


**Figure 2:** LQG problem defined as  $\mathcal{H}_2$  optimization problem [1]

$\mathcal{H}_\infty$  synthesis on the other hand, optimizes peaks of optimized frequency characteristics, and so definition of the desired control characteristics using dynamic weights is simpler. To adjust an existing controller, or observer, the LQG problem first needs to be reformulated to the standard  $\mathcal{H}_\infty$  state controller synthesis problem. As a next step, weights that will differ most at the adjustment target frequencies from the original design, to achieve the desired adjusted frequency characteristics, has to be designed. Example of this weights design is to be seen in next chapter.[1], [2]

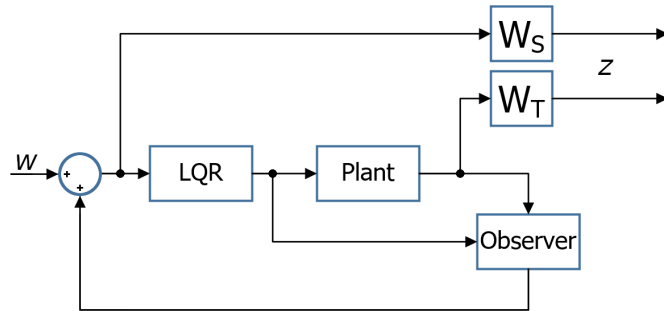


**Figure 3:** LQG problem reformulated as  $\mathcal{H}_\infty$  state controller synthesis problem with sensitivity and complementary sensitivity weights,  $\mathbf{W}_S$  and  $\mathbf{W}_T$  respectively.

### 3 EXAMPLE OF USING $\mathcal{H}_\infty$ SYNTHESIS FOR LQG CONTROLLER ADJUSTMENT

In the figure 4, there are frequency characteristics of the original and the adjusted LQG controller. It is obvious, that singular values of the original position sensitivity function  $\sigma(S_x)$  is inappropriately shaped, because the shape should be similar to low pass filter, and therefore control error should consist of noise only.

At first, the weights were selected such that they differ as little as possible from original singular characteristics, despite being first order dynamic weights. Target of this is to design as similar to the original controller as possible. Then, weight  $W_{S_x}$  has been adjusted so that a low frequency gain of  $\sigma(S_x)$  was suppressed. That should lead to suppressing the control error.

Synthesis has been done in MATLAB, utilizing command `hinfstruct` from robust control toolbox, that allows  $\mathcal{H}_\infty$  synthesis of controllers with predefined structure. Since  $\mathcal{H}_\infty$  optimization of

such systems is not generally convex problem, the optimization ran repeatedly with random initial conditions to avoid local minimum solution. Controller and observer matrices  $\mathbf{L}$  and  $\mathbf{K}$  has been resynthesized using  $\mathcal{H}_\infty$  optimization.[3], [4]

Low frequency gain of  $\sigma(S_x)$  is indeed suppressed in  $\mathcal{H}_\infty$  solution, which caused shifting of all other singular characteristics to higher frequencies. Also, spike has been created in  $\sigma(S_\theta)$  and  $\sigma(S_{\dot{\theta}})$ . This could lead to increased noise sensitivity of design. Results can be compared in the figure 4.

Note, that the weights does not bound state observer, nor controller output, which means, that singular characteristics of these signals could be affected by  $\mathcal{H}_\infty$  optimization.

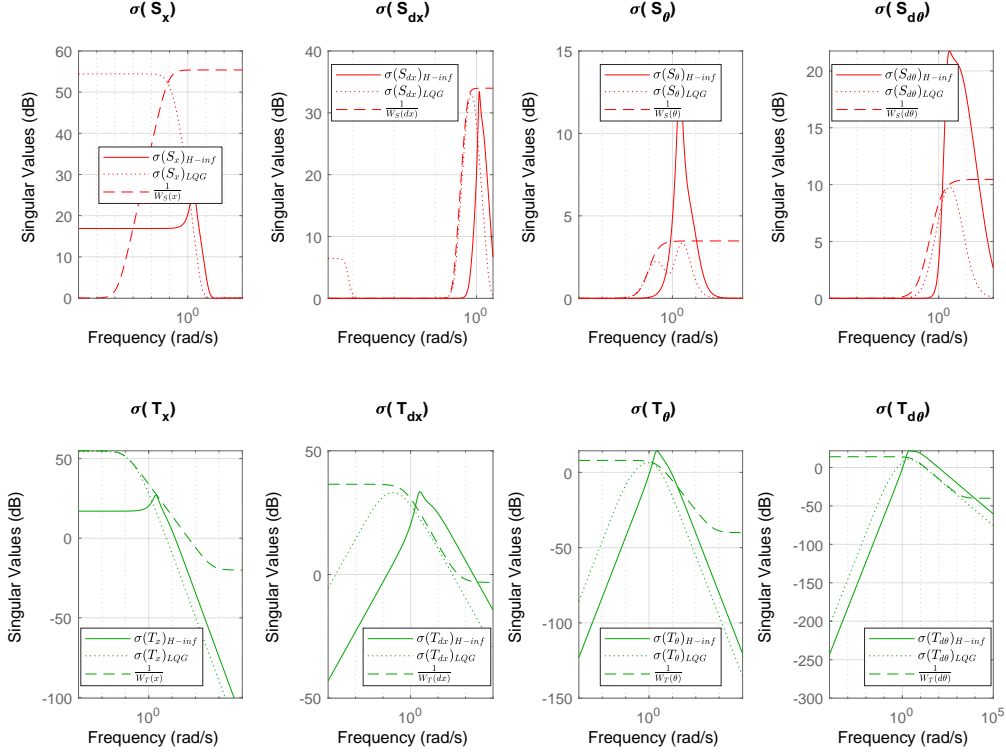


**Figure 4:** Singular characteristics of individual signals of sensitivity and complementary sensitivity functions compared to weights  $\mathbf{W}_S$  and  $\mathbf{W}_T$ .

#### 4 RESULTS OF USING $\mathcal{H}_\infty$ SYNTHESIS FOR LQG CONTROLLER ADJUSTMENT

The method is demonstrated on the inverted pendulum on a cart example. Results can be observed in the figure 5, that displays a simulation of original and adjusted controllers. The simulation consists of two parts. First part shows simulation of state controller part only, assuming that all states are measured. In this period, the state observers are stabilized. For second part of the simulation, only states  $x$  and  $\theta$  are measured and the system is controlled by using the LQG controller.

The cart position control quality has been increased compared to the original controller, as visible from figure 5. Since the controller output has not been bounded, it is generally bigger in the adjusted control. Also, the noise sensitivity of the adjusted LQG is visible, which was expected.

Results show, that by using this method the user is capable of adjusting an existing LQG controller.

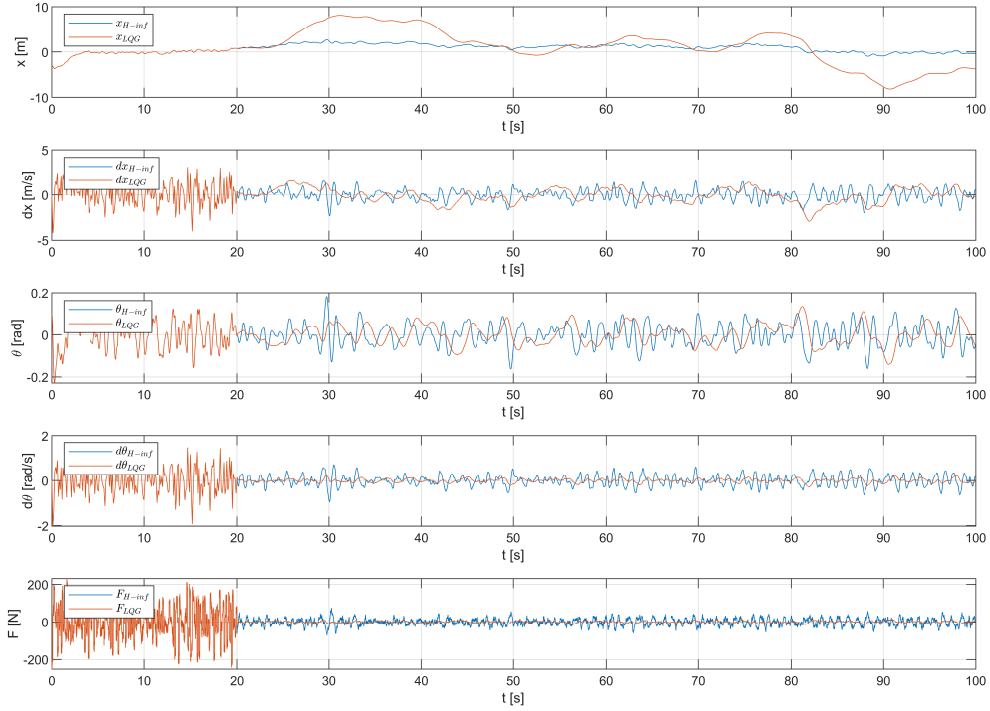


**Figure 5:** The original and  $\mathcal{H}_\infty$  adjusted LQG control comparison. For all the state variables, setpoints are set to zero.

## 5 CONCLUSION

The main target of this article is to demonstrate the possibility of using  $\mathcal{H}_\infty$  optimization to adjust an existing LQG controller. This method is now simple to implement, thanks to `hinfstruct` [4] command in robust control toolbox in MATLAB. The method consists of a few steps. The first step is reformulation to the standard  $\mathcal{H}_\infty$  state controller synthesis problem. The optimization weights needs to be designed, so that spikes appear where the singular characteristics needs to be attenuated and valley appears where it needs to be amplified. In order to attenuate all spikes,  $\mathcal{H}_\infty$  optimization leads to the desired adjustment. This method has been successfully demonstrated on the inverted pendulum on a cart example. Using this method, cart position control quality has been increased compared to the original controller.

## REFERENCES

- [1] S. Skogestad and I. Postlethwaite. *Multivariable Feedback Control: Analysis and Design*. John Wiley & Sons, Inc., Hoboken, NJ, USA, 2005.
- [2] H. T. Toivonen. Robust control methods, 2020-02-22. URL: <http://users.abo.fi/htoivone/courses/robust/>.
- [3] P. Apkarian and D. Noll. Nonsmooth  $h_\infty$  synthesis. *IEEE Transactions on Automatic Control*, 51(1):71–86, Jan 2006.
- [4] MATLAB. H-infinity tuning of fixed-structure controllers, 2020-02-22. URL: <https://www.mathworks.com/help/robust/ref/hinfstruct.html>.

# USING RYZE TELLO UAVS IN MULTI-ROBOT SYSTEMS

**Matouš Hýbl**

Master Degree Programme (2nd year), FEEC BUT

E-mail: xhyblm00@stud.feec.vutbr.cz

Supervised by: Petr Gábrlík

E-mail: xgabrl00@stud.feec.vutbr.cz

**Abstract:** This paper describes ways of integrating Ryze Tello UAVs (Unmanned Aerial Vehicles) with existing robotic systems. The main focus of this paper is the creation of bridging software and hardware that allows connecting of multiple drones to the robotic system while allowing for both video feed streaming and UAV control. The secondary focus of this paper is a proof of usability of the Rust programming language in robotic applications.

**Keywords:** unmanned aerial vehicle, multi-robot system, UAV, ROS, Rust

## 1 INTRODUCTION AND MOTIVATION

Ryze Tello UAVs (Unmanned Aerial Vehicles) (shown in the figure 1) are cheap and small UAVs that are originally aimed at students to study programming or being simply a toy. On the other hand the manufacturer provides a simple API (Application Programming Interface) based on UDP (User Datagram Protocol) datagrams that can be used to control the behavior of the UAV as well as reading some status information from it. Alongside with an on-board camera with video streaming capabilities, this makes the drone a good candidate for a research device, especially for UAV swarm research (an example of such swarm is shown in the figure 2) or research in UAV-UGV (Unmanned Ground Vehicle) cooperation.

There are two versions of the UAV - the Tello and Tello EDU, the latter one being more suitable for introduction to programming as it features a kit that can be used for simple visual robot navigation. The Tello can be controlled wirelessly using a mobile device via Wi-Fi, where it acts as an access point [1]. On the other hand, the Tello EDU allows for being connected to an external access point as a standard Wi-Fi station. This seems promising as it would allow for connecting multiple UAVs to a single access point, therefore allowing for easy implementation of robotic swarms. The problem with this configuration is that the video feed is not accessible in station mode, which disables one of the main advantages of the UAV - the real-time video stream. That means that then it cannot be used for visual navigation or SLAM (Simultaneous Localization and Mapping) and for example for reconnaissance with UGV-cooperation.

This paper aims at removing this problem by creating bridging hardware and software which doesn't require the drone to be switched to the station mode, therefore also eliminating the need to buy the more expensive EDU version.



**Figure 1:** Ryze Tello UAV [2].



**Figure 2:** An example of an UAV swarm equipped with lights [3].

## 2 METHODOLOGY

This section describes the hardware and software used and developed as well as different approaches of doing so, as the bridging software can be implemented using at least three different ways.

### 2.1 HARDWARE

Hardware used for the software bridge needs to meet following conditions:

- have a working Wi-Fi and ethernet network interface,
- have enough computing power to allow for video encoding and streaming.

For simplicity of implementation, a Raspberry Pi single-board computer was used, more specifically version 3B which was the first one to have a Wi-Fi interface and also enough computing power.

During development, it was also discovered that the UAV is not designed to withstand prolonged periods of being placed on a table with no airflow which results in overheating leading to frequent shutdowns. A simple PC case fan can be placed below the UAV, therefore mitigating the problem. In the future development integrated charging could also be implemented.

### 2.2 SOFTWARE

There are at least three approaches to developing the bridging software. These approaches differ only in the ways of controlling the UAV, video streaming implementation remains the same for all of them. The approaches are:

- direct retransmission of control and status datagrams,
- control and status datagram translation,
- using the ROS node to control the UAV.

#### 2.2.1 DIRECT RETRANSMISSION OF CONTROL AND STATUS DATAGRAMS

Direct retransmission of control and status datagrams is the most straightforward way of controlling the UAV. The principle is simple, the bridging computer opens the same ports on its ethernet interface as the ports that are opened on the UAV, where it receives the control data originally meant for the

UAV and sends them to it. Then it opens a port on which the UAV sends its status data to and sends the status data back to the control computer. With this configuration, the program on the bridging computer sends whatever data is received from the control computer directly to the UAV and when there are status data available from the UAV, they are sent to the control computer. The whole process is schematically shown in the figure 3. And an example of code in the Rust programming language is shown in the listing 1.

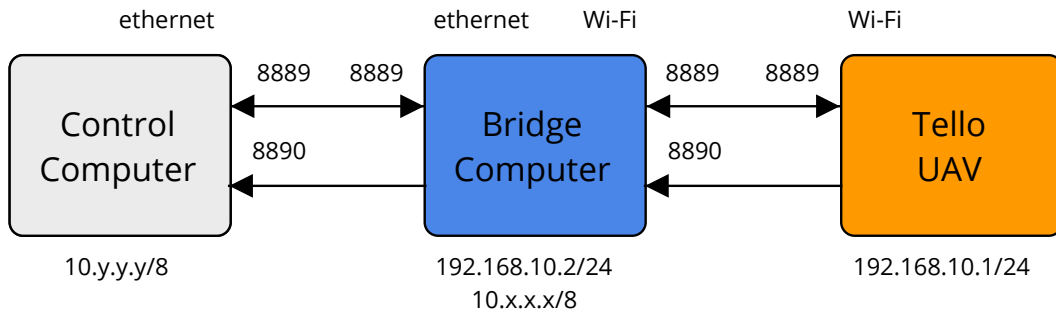


**Figure 3:** A simple schematic diagram depicting direct retransmission bridge.

```

1 let tello_control_socket = UdpSocket::bind("192.168.10.2:9009").unwrap();
2 let tello_state_socket = UdpSocket::bind("192.168.10.2:8890").unwrap();
3 let control_socket = UdpSocket::bind("0.0.0.0:8889").unwrap();
4 loop {
5     let mut buffer: [u8; 1500] = [0; 1500];
6     match control_socket.recv_from(&mut buffer) {
7         Ok((size, address)) => {
8             controller_address = address.ip().to_string();
9             tello_control_socket.send_to(&buffer[0..size], "192.168.10.1:8889");
10        }
11        Err(_) => {}
12    }
13    match tello_control_socket.recv_from(&mut buffer) {
14        Ok((size, address)) => {
15            control_socket.send_to(&buffer[0..size], format!("{}",:8889", &
16                controller_address));
17        }
18        Err(_) => {}
19    }
20    match tello_state_socket.recv_from(&mut buffer) {
21        Ok((size, address)) => {
22            control_socket.send_to(&buffer[0..size], format!("{}",:8890", &
23                controller_address));
24        }
25        Err(_) => {}
26    }
27    std::thread::sleep(Duration::from_millis(10));
28 }
  
```

**Listing 1:** Implementation of the direct retransmission approach.

This approach was tested and seemed to work quite well. The advantage of this approach is that the existing libraries and tools developed to control the UAV can be used, just by changing the IP addresses and the way video is streamed. The disadvantage is that this approach still requires the maintenance of custom software and changes to video streaming.

### 2.2.2 CONTROL AND STATUS DATAGRAM TRANSLATION

The second approach is similar to the first one, but with the difference that a custom control and status data model is employed. This means that the designer of the robotic system has complete control over the data being sent to the bridging computer the UAV. There is also room for adding, for example, some control logic to the bridge, such as autoland safety features that are not dependent on the control program. This approach was tested and seemed to work quite well. The advantages of this approach are clear - custom functions can be implemented and a standardized communication interface can be used. The disadvantages remain the same as with the previous approach - maintenance of custom software is required.

### 2.2.3 USING ROS NODE TO CONTROL THE UAV

The last approach is especially suitable for ROS (Robot Operating System) based robotic systems. As ROS is a distributed system a ROS node used to control the UAV can be run on the bridging computer. This is the easiest approach for all ROS enabled robotic systems as nodes for the Tello UAV are already prepared and ready for immediate use [4, 5, 6]. These nodes could also publish images which result in handling the live video stream in a very clean way.

### 2.2.4 VIDEO STREAMING

Retransmission of the video can be implemented using various audio/video streaming utilities, such as FFmpeg or GStreamer. In this case, GStreamer was used. The goal was to set-up an RTSP (Real-Time Streaming Protocol) streaming server serving the UAV video stream. The GStreamer pipeline was adopted and modified from a tutorial [7], while the RTSP server code in Rust was adopted from GStreamer-rs repository [8]. Based on some experiments, the server should be launched only after the UAV is commanded to begin streaming and with some delay.

## 3 RESULTS

### 3.1 BRIDGING DRONE CONTROL, STATUS, AND VIDEO STREAM

In the last section, three different approaches to implement bridging algorithms were described. The first two were tested as a part of this paper and the preliminary testing showed that they work reasonably well. The ROS based approach was not directly tested, however it is believed to be thoroughly tested by other ROS users as well as students of the DCI FECC Robotics and AI research group [6].

### 3.2 DEVELOPING BRIDGING SOFTWARE IN RUST

Another part of this paper was testing the suitability of the Rust programming language for robotic applications. During the work on this paper, an implementation of the Tello SDK (Software Development Kit) in Rust was developed as well as both of the bridge implementations. The area where Rust language stood out was memory safety in multi-threaded applications - the controller was checking for data races, etc. Another strong suit of the language is interoperability with C which allowed the use of the GStreamer Rust bindings, therefore allowing us to use an existing high-level library instead of developing a custom one. A feature of the language that was also used was its fully-featured standard library which conveniently out of the box supports, for example, UDP sockets. The disadvantage of the language was lack of remote development tooling which meant that the bridging code couldn't be run and debugged directly in the bridging computer.

## 4 CONCLUSIONS & FUTURE WORK

The aim of this paper was to explore approaches of integrating Tello UAVs into various multi-robot systems and to test suitability of Rust programming language for robotic applications.

The paper describes three approaches of integration of the UAVs with their advantages and disadvantages. For easy testing, the first one seems to be an optimal solution as it simply retransmits all communication. The other two approaches are suitable for integrating into an existing robotic system - whether it uses ROS or a custom communication protocol.

As for the suitability of using Rust for robotic applications, so far the safety features have proven useful in avoiding data races. C language interoperability was also successfully demonstrated and tested by integrating GStreamer bindings library. Rust language's standard library which already contains prepared implementations of many useful features such as UDP sockets etc. is extremely useful for jumpstarting software development.

In the future, the UAV will be implemented into the ATEROS robotic system and used for experimenting with indoor navigation and robotic swarms. As for the Rust programming language, it will be further evaluated - more specifically in areas such as direct hardware interfaces, tools, and ROS nodes.

## 5 ACKNOWLEDGEMENTS

The completion of this paper was made possible by the grant No. FEKT-S-20-6205 - "Research in Automation, Cybernetics and Artificial Intelligence within Industry 4.0" financially supported by the Internal science fund of Brno University of Technology.

## REFERENCES

- [1] Tello SDK Documentation EN 1.3 1122. In: *DJI CDN* [online]. Shenzhen, China: SZ DJI Technology Co., 2018 [ref. 2020-03-02]. Available at: [https://terra-1-g.djicdn.com/2d4dce68897a46b19fc717f3576b7c6a/Tello%E7%BC%96%E7%A8%8B%E7%9B%B8%E5%85%B3/For%20Tello/Tello%20SDK%20Documentation%20EN\\_1.3\\_1122.pdf](https://terra-1-g.djicdn.com/2d4dce68897a46b19fc717f3576b7c6a/Tello%E7%BC%96%E7%A8%8B%E7%9B%B8%E5%85%B3/For%20Tello/Tello%20SDK%20Documentation%20EN_1.3_1122.pdf)
- [2] DJI RYZE Tello. In: *Robot Advance* [online]. Mornant, France: Robot Advance, 2019 [cit. 2020-03-02]. Available at: <https://www.robot-advance.com/EN/ori-drone-dji-ryze-tello-2609.jpg>
- [3] A Swarm of 800 Drones Create a Giant Airplane in the Sky. In: *Interesting Engineering* [online]. San Francisco, California, USA: Interesting Engineering, 2019 [ref. 2020-03-02]. Available at: <https://interestingengineering.com/a-swarm-of-800-drones-create-a-giant-airplane-in-the-sky>
- [4] Tello\_driver. In: *ROS Wiki* [online]. Mountain View, California, USA: Open Robotics Foundation, 2019 [ref. 2020-03-02]. Available at: [http://wiki.ros.org/tello\\_driver](http://wiki.ros.org/tello_driver)
- [5] Flock: ROS driver for DJI Tello drones. In: *Github* [online]. San Francisco, California, USA: Github, 2018 [ref. 2020-03-02]. Available at: <https://github.com/clydemcqueen/flock>
- [6] PANSKÝ, Michal. *Autonomous Unmanned Aircraft Tello*. Brno, 2020. Semestral thesis. Brno University of Technology. Thesis supervisor Ing. Petr Gábrlík.

- [7] YOUNG, Neil. How to make a Raspberry Pi an RTSP streamer and how to consume this? In: *Github Gist* [online]. San Francisco, California, USA: Github, 2020 [ref. 2020-03-02]. Available at: <https://gist.github.com/neilyoung/8216c6cf0c7b69e25a152fde1c022a5d>
- [8] Rtsp-server.rs. In: *Gitlab Freedesktop.org* [online]. Freedesktop.org, 2019 [ref. 2020-03-02]. Available at: <https://gitlab.freedesktop.org/gstreamer/gstreamer-rs/-/blob/master/examples/src/bin/rtsp-server.rs>

# DESIGN AND DEVELOPMENT OF A HANDHELD ROBOT CONTROLLER WITH TELEPRESENCE CAPABILITIES

**Matouš Hýbl**

Master Degree Programme (2nd year), FEEC BUT

E-mail: xhyblm00@stud.feec.vutbr.cz

Supervised by: Luděk Žalud

E-mail: zalud@feec.vutbr.cz

**Abstract:** This paper describes the design and development of a prototype of a handheld controller that should be used to remotely control a robot during a field/service robotics mission. The controller is equipped with a touch screen display, that shows a video feed from robot's cameras and its status information, joysticks and buttons for controlling the robot and also an ethernet port for connecting external communication interfaces. Broken out HDMI and USB ports are used to connect an AR (Augmented Reality)/VR(Virtual Reality) headset with a head movement sensor, thus allowing for telepresence in the field . The secondary aim of the paper is to evaluate the Rust programming language in terms of directly interfacing hardware.

**Keywords:** handheld controller, field robotics, service robotics, telepresence

## 1 INTRODUCTION MOTIVATION

In the DCI FEEC robotics group, there is quite a long history of attempts to make a handheld controller usable for their robots [1]. One of the earliest attempts consisted of a backpack with a PC as shown in the figure 1, which was controlled via a gamepad and equipped with a telepresence enabled headset [2]. Furthermore, a truly handheld controller was developed, as shown in the picture 2. Such a controller used a Raspberry Pi single-board computer, a touchscreen display and built-in joysticks and buttons, thus it was a direct predecessor of the controller being described in this article. The problem with this design was bad ergonomics, as the placement of the controls was not optimal and there was a bag containing the computer and the battery on the back of the controller that was two times higher than the controller itself. Furthermore, there was never any universal controlling software developed and it lacked telepresence capabilities, as the Raspberry Pi version used doesn't have enough computing power. The controller which is described in this paper aims to solve the problems that were present in the previous versions - in the end being truly a handheld controller with good ergonomics, being telepresence capable and serving as a good platform for running robot control software.



**Figure 1:** Backpack based telepresence robot controller.



**Figure 2:** First version of a handheld robot computer developed by the robotic group.

## 2 METHODOLOGY

This section describes requirements that need to be met by the final product, as well as how these requirements were met in hardware and software.

### 2.1 HANDHELD OPERATION

In order to allow for handheld operation, the controller needs to be wireless both for power and for data transmission (it must not require permanent wired LAN (Local Area Network) connection). It was therefore designed to have a built-in battery. The battery is a custom welded 4S2P (4 cells in series and 2 of those series in parallel) battery pack made out of 18650 Li-ion cells. This configuration means that the nominal voltage of the pack is 14.8 V and its capacity is roughly 6 Ah. The battery pack was equipped with a BMS (Battery Management System) for balancing the pack and for overcurrent and undervoltage protection. A step-down converter was utilized to convert the input voltage to the 5 V suitable for the control computer. There is a switch on top of the case as well as a barrel connector suitable for charging.

The controller needs to somehow display data and video feed and also provide controls. Data and video feed are shown on a 7" LCD (Liquid Crystal Display) with a touch screen. Apart from the touchscreen, it is important to also have some controls with tactile feedback - such as joysticks and buttons, therefore the controller is built with two joysticks and eight buttons, where there are a joystick and four buttons on each side. The aforementioned buttons are connected directly to the control computer, while the joysticks are connected via an MCP3008 ADC (Analog-Digital Converter) using SPI (Serial Peripheral Interface).

### 2.2 COMPUTING POWER AND CONNECTIVITY

In order to allow for telepresence operation and running control software, a control computer with sufficient computing power needed to be used. In this case, a Raspberry Pi 4B was chosen as it features 4 GB of on-board RAM (Random Access Memory), 4 core ARM processor and two micro HDMI outputs capable of displaying 4K video [3]. These features alongside multiple GPIO (General Purpose Input Output), gigabit ethernet and four USBs (Universal Serial Bus) make it extremely suitable for our needs. The telepresence system can be connected to the micro HDMI connector using an HDMI/micro HDMI adapter integrated in the controller, while the head tracking unit can be connected via one of the USB ports, that are available on the bottom of the controller. When compared to other computers and SBCs (Single Board Computers), the Raspberry Pi provides a very good price/performance ratio, can drive up to two 4K displays and has an excellent software support.

The robots can be connected to the controller in various ways. If the robot isn't equipped with a wireless interface, it can be connected via an ethernet or USB cable. If the robot connects using a standard 802.11 Wi-Fi, the onboard Wi-fi interface of the Raspberry Pi can be utilized. As for robots that use non-standard wireless links, additional communication interfaces can be connected using the ethernet port, the USB or in special cases even using the on-board GPIOs. For those potential external interfaces, the charging barrel connector may be used as a power source.

### 2.3 ROBOT CONTROL SOFTWARE COMPATIBILITY

The robot control software running on the controller should not be dependent on the hardware, which means that there shouldn't be any hardware (interface) dependant code, meaning that there is a need for some kind of hardware abstraction. In this case, the whole hardware implementation was abstracted using networking - a UDP API (User Datagram Protocol, Application Programming Interface) was defined in the control software. The control software then binds a specific port on the localhost and listens for incoming datagrams containing state of the control buttons and joystick. This way the control software can stay hardware independent.

The program interfacing with the hardware was developed in the Rust programming language using their embedded HAL (Hardware Abstraction Layer) that allows for using the same code for device interfacing on Linux as on embedded MCUs [4]. This way an open-source library for MCP3008 could be used from Rust's crate ecosystem. There is also a library crate that was used for interfacing with Raspberry Pi's GPIO and SPI. The program periodically sends datagrams with the structure shown in the table 1.

left buttons	right buttons	left joystick x	left joystick y	right joystick x	right joystick y
1 B	1 B	4 B	4 B	4 B	4 B

**Table 1:** Structure of a datagram sent from the program interfacing with joysticks and buttons

## 3 RESULTS

### 3.1 DESIGNING HANDHELD ROBOT CONTROLLER

The aim of this paper was to describe the design and development of a handheld robot controller that should allow remote control of robots in field robotics missions. Such a controller was developed and certain aspects of its development were described here. The most important aspect of the development was certainly extensibility of use in the future, which is enabled by the computing power of the used computer, its many connectivity options, and also allowing for the control software to be hardware-agnostic by using a simple UDP based hardware abstraction. A working prototype of the controller can be seen in the figure 3, while a demonstration of the controller with a connected telepresence headset is shown in the figure 4.

### 3.2 INTERFACING HARDWARE WITH RUST

The secondary aim of this paper was to test how well the Rust programming language could be used when directly interfacing with hardware - in this case manipulating with GPIO of the control computer and accessing MCP3008 ADC using SPI. Rust's hardware support ecosystem seems vast and the community around it seems to be developing a lot of drivers and language support even for embedded ARM processors. They leveraged one important feature of the language - traits, which allowed to develop platform agnostic drivers for many peripherals, meaning that the same code could run on Linux as well as embedded microcontrollers. The problem, however, seems to be the lack of tooling, which means that there is no option of remote development, that would allow running and

debugging of the software directly on the control computer, while the code is developed on a standard PC.



**Figure 3:** New handheld controller being used to control Orpheus X3.



**Figure 4:** New handheld controller with telepresence headset enabled.

#### 4 CONCLUSIONS FUTURE WORK

This paper described the development of a prototype robot controller that should be useful for field robotics missions and is capable of telepresence. It was tested with the Orpheus X3 robot during the RegionTour fair, where it experienced some problems with wireless communication, but thanks to its architecture, it was possible to control the robot using a direct ethernet connection.

The Rust programming language seems to be quite suitable for directly interfacing hardware as apart from its standard safety features, a wide range of libraries (crates) are being developed to speed up development and there seems to be a quite large community working on bringing the language closer to bare metal devices.

More development will be done on the controller in the future software-wise, as full support for telepresence is yet to be developed because only a basic support is developed as of now. Hardware-wise, there will be many changes as this current design is still a prototype that is for example too thick. The thickness issue will be addressed by replacing the 18650 cells with flat Li-poly cells. The display will also be replaced using a bigger one with better resolution. In order to provide more ergonomics to the operator, the tactile switches will be replaced with rubber-dome ones.

#### 5 ACKNOWLEDGEMENTS

The completion of this paper was made possible by the grant No. FEKT-S-20-6205 - "Research in Automation, Cybernetics and Artificial Intelligence within Industry 4.0" financially supported by the Internal science fund of Brno University of Technology.

#### REFERENCES

- [1] ZALUD, L, L KOPECNY a F BURIAN. Orpheus Reconnaissance Robots. In: *2008 IEEE International Workshop on Safety, Security and Rescue Robotics* [online]. IEEE, 2008, s. 31-34 [ref. 2020-03-12]. DOI: 10.1109/SSRR.2008.4745873. ISBN 9781424420315.
- [2] ZALUD, L, L KOPECNY, F BURIAN a T FLORIAN. CASSANDRA - heterogeneous reconnaissance robotic system for dangerous environments. In: *2011 IEEE/SICE International Symposium on System Integration (SII)* [online]. IEEE, 2011, s. 1275-1280 [ref. 2020-03-12]. DOI: 10.1109/SII.2011.6147632. ISBN 9781457715235.

- [3] Raspberry Pi 4. *Raspberry Pi* [online]. Cambridge, UK: Raspberry Pi Foundation, 2020 [ref. 2020-03-12]. Available at: <https://www.raspberrypi.org/products/raspberry-pi-4-model-b/>
- [4] Embedded-hal: A Hardware Abstraction Layer (HAL) for embedded systems. In: *Github* [online]. San Francisco, California, USA: Github, 2018 [ref. 2020-03-02]. Available at: <https://github.com/rust-embedded/embedded-hal>

# COMPARISON OF ARC EROSION COEFFICIENTS

**Jakub Piska**

Master Degree Programme (2), FEEC BUT

E-mail: xpiska02@stud.feec.vutbr.cz

Supervised by: Jiri Valenta

E-mail: valentaj@feec.vutbr.cz

**Abstract:** The problem of nonunified approaches to giving arc erosion ratios is addressed for the application of molded case circuit breakers (MCCBs) in the range 6.5-10 kA. Charge, Joule's integral and arc energy are compared as possible quantities to use for ratios of mass loss. The linearity of the relationship of mass loss to those quantities was used as the main metric.

By this metric the ratio to charge was chosen as the most reliable one. But this relation was constant only for fixed contacts with arcrunners. For the moving contact, the mass loss ratio was a linear function of the effective value of the passing current.

**Keywords:** arc erosion, MCCB, mass loss, erosion ratios

## 1 INTRODUCTION

The design process of a switching device contact system needs to address a number of things, ranging from delivering low enough contact resistance to prevent softening and welding of the contacts to providing suitable environment for arc root movement.

To accomplish all of these functions, the contacts should ideally remain the same during the whole life cycle of the device. Alas, this is not achievable due to several factors. Namely corrosion, fretting and arc erosion. All of these need to be taken into consideration when designing a new product.

In circuit breakers, the main stress on a contact material occurs during breaking of high short circuit currents and therefore, is mainly influenced by arc erosion. And as such, there is a high demand for ways to calculate or estimate the mass loss during the life time of the device.

However, the rate of erosion still has not been described even approximately close to provide enough support in designing a contact system without previous experience with a similar construction.

To provide comparable data from measurements for different breaking operations, different ratios of mass loss to a quantity corresponding to energy absorbed by the electrode are used. The most commonly used ones are: charge passed during the switching time  $\int idt$ , Joule's integral  $\int i^2 dt$  or total power losses in arc  $\int iu_a dt$ .

The reasoning behind using different ratios is that different device heat up the contacts via different mechanisms. For example, the Joule's integral is being used when the predominant power losses are in the contacts themselves. The total power losses are used when radiation heat transfer from the arc causes the greatest part of contacts heating up. But there are yet no clear distinctions to which are to be used when. [1]

In order to tackle this problem, several tests were carried out on MCCBs in current range 6.5-10 kA. The measured mass losses were compared in different ratios with the quantities mentioned above. These ratios were determined for future development of the contact dimensions and contact overtravel of the particular MCCB used for testing.

## 2 EXPERIMENTAL SETUP

The tests were carried out as one phase shortcircuit tests on a MCCB in current range 6.5-10 kA, power factor 0.5, frequency 50 Hz, switching angle 60°, voltage 731 V and the instantaneous tripping current was set to 1.25 kA. Current and voltage were measured. Before and after each test, all contacts were removed from the breaker and weighed.

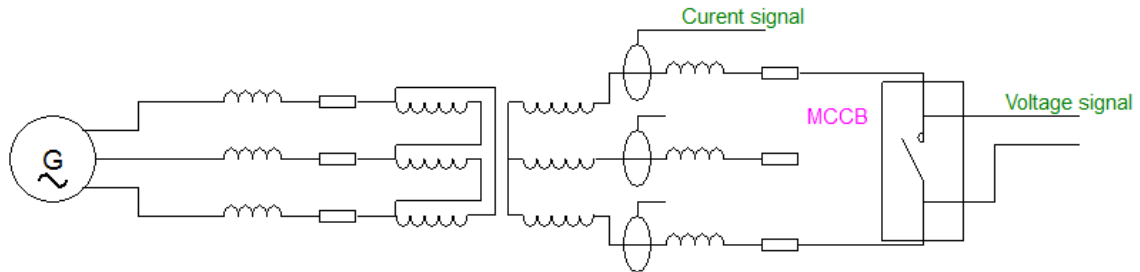


**Figure 1:** Experimental setup

The contact system of the MCCB consisted of one moving contact (2) and two fixed contact (1) pieces as shown in fig. 2. The upper fixed contact was further labeled as cathode and the lower one as anode. All test were carried out with the same polarity and all occurrences of arcs burning for more than one half-period were removed from the data.

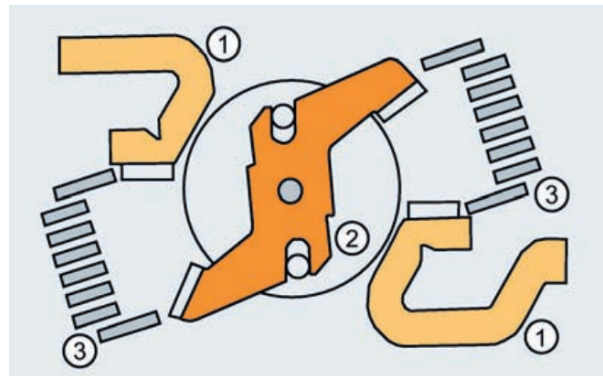


**Figure 2:** Contact system [2]

The moving contacts had area 5x5 mm and were made of Ag-W. Both fixed contacts were made of Ag-C and had area 7x7 mm. And both fixed contacts had additional 7x7 arcrunners situated towards the arc chute.

## 3 RESULTS AND DISCUSSION

The first three graphs plot mass losses as functions of  $\int i dt$ ,  $\int i^2 dt$  and  $\int i u_a dt$ . The used current was not taken into consideration in these graphs.

Most authors [4] were trying to express the mass loss as a function in the following form:

$$\Delta m = K \cdot \int i^n \cdot u_a^m dt \quad (1)$$

Where  $K$  is a parameter given for the design of the contact system.

To validate if there is this linear relationship, linear regression was used, Pearson correlation coefficient was calculated and compared with the critical value for significance level 0.05, the value being 0.514 for the number of measurements. [3]

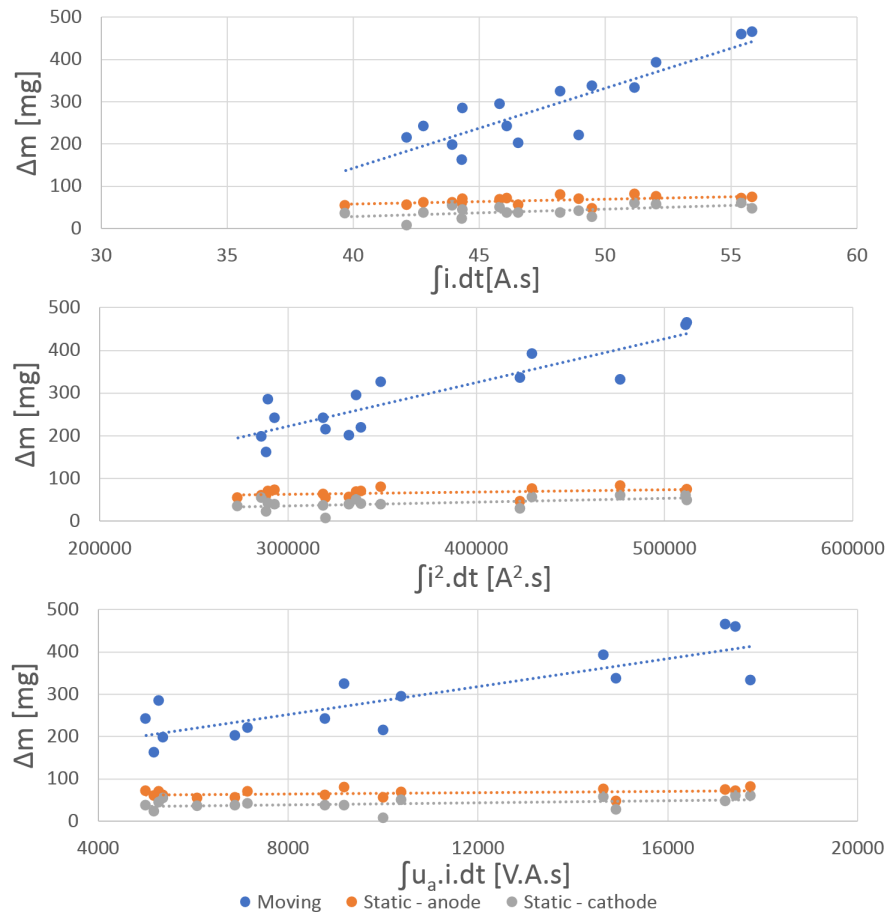


**Figure 3:** Comparison of used quantities

	$\int i . dt$	$\int i^2 . dt$	$\int u_a . i . dt$
Moving contact	0.875	0.890	0.852
Fixed contact - anode	0.548	0.413	0.331
Fixed contact - cathode	0.576	0.501	0.420

**Table 1:** Correlation coefficients

Only when plotted as a function of passed charge, the data give a reliable linear relationship. But this still does not check fully if the mass loss behaves as stated in (1). This is due to the fact that (1) does not account for the constant coefficient  $b$  in the general linear function  $y = ax + b$ . This was checked by plotting the ratio of mass loss and  $\int i dt$  as a function of effective value of the switching current.

The presumable reasons for overall lower correlation coefficients for fixed contacts is lower mass loss in comparison to the moving contact. Therefore any phenomena like re-deposition of metal from contacts or splitter plates, creation of metal oxides or deposition of carbon from the plastic casing will have higher impact on the total mass loss. Additionally the arc is partially transferred onto the first plate of the splitter plate array (see (3) fig. 2) and thus is not exposed to the arc for the full duration.

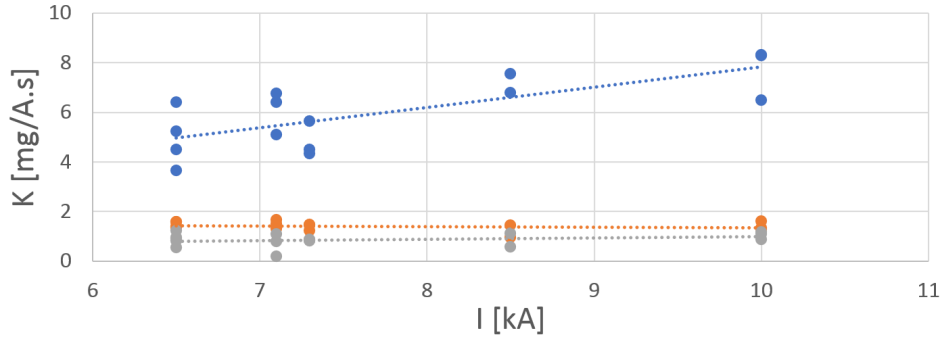


**Figure 4:** Ratio of passed charge as a function of current

For the fixed contacts, the value of ratio over the whole interval 6.5-10 kA is close to constant. For anode the change between value at 6.5 kA and 10 kA is 6.2 % with variation coefficient of 12.0 % and for the cathode the change is 22.5 % with variation coefficient of 30.0 %. However, the moving contact ratio still exhibits linear behaviour. For this, the equation (1) was altered to:

$$\Delta m = K_f \cdot I \cdot \int i \cdot dt \quad (2)$$

With this, coefficient  $K_f$  as a function of current yields a function with the change of 2.4 % and variation coefficient of 16.4 % over the whole interval.

The difference between fixed and moving contacts is most probably caused by the presence of arcrunners at the fixed contacts. Thus the arc root not burning in only one place but moving along the whole contact. This points to a bigger role of evaporation in the moving contact erosion than in the case of fixed contacts.

#### 4 CONCLUSION

It has been shown that for MCCBs the ratio of mass loss to  $\int idt$  is the most suitable for the range of currents 6.5-10 kA. But before these ratios can be used for future development of switching devices, it needs to be discerned what their relationships to other circuit parameters and construction changes are.

#### REFERENCES

- [1] SLADE, Paul G. *Electrical contacts: principles and applications*. Second edition. Boca Raton: CRC Press, Taylor Francis Group, [2014]. ISBN 1439881308.
- [2] 3VA molded case circuit breakers with IEC certificate [online]. 2019 [cit. 2020-03-01]. Available from: [https://publikacje.siemens-info.com/pdf/575/3VA\\_manual\\_molded\\_case\\_circuit\\_breakers\\_en\\_en-US.pdf](https://publikacje.siemens-info.com/pdf/575/3VA_manual_molded_case_circuit_breakers_en_en-US.pdf)
- [3] Table of Critical Values: Pearson Correlation [online]. 2019 [cit. 2020-03-04]. Available from: <https://www.statisticssolutions.com/table-of-critical-values-pearson-correlation/>
- [4] SHEA, J.J. Erosion and resistance characteristics of AgW and AgC contacts. *IEEE Transactions on Components and Packaging Technologies* [online]. **22**(2), 331-336 [cit. 2020-03-15]. DOI: 10.1109/6144.774755. ISSN 15213331. Available from: <http://ieeexplore.ieee.org/document/774755/>

# BMS SETTINGS ANALYSIS

**Jan Klusáček**

Master Programme (2.), FEEC BUT

E-mail: xklusa11@stud.feec.vutbr.cz

Supervised by: Jan Morávek

E-mail: moravek@feec.vutbr.cz

**Abstract:** Operation and performance of lithium-ion batteries strongly depend on configuration of Battery Management System (BMS). Set parameters must ensure both safe and efficient operation of the battery and it must be coordinated with specific operation profile of connected power converter. Whereas safe operation should be provided by safety assembly controlled by BMS, the efficient operation is mainly provided by superior system through connected converter. The configuration profile of battery is presented, its communication with energy system by Victron via CAN bus is evaluated, resulting performance of the system is examined and potential limitations are highlighted. A battery safety assembly for educational purposes is presented.

**Keywords:** BMS, CANBUS, Victron, Orion Jr., Lithium-ion, battery, Power system

## 1 INTRODUCTION

Distributed electrical power generation with renewable sources such as solar energy reduces carbon footprint of electrical power. From grid operation point of view, it is also beneficial to match the generation and consumption locally. This may be achieved either by demand response or accumulation. One of the suitable accumulators are lithium-ion batteries.

Correct settings of battery parameters in BMS is essential for safe and effective battery operation. Wrong settings may result in serious damage, e.g. thermal runaway, as described in [1] and [2]. The fundamental protection is provided by BMS and supporting assembly. The assembly design is described further in the work. Furthermore, coordination of individual cells settings in BMS and whole battery settings in the inverter is important for faultless operation. Another important aspect is to be familiar with behavior of the device systems and content of communication protocol. An observation and detailed specification of the protocol is necessary if the manufacturers don't support each other's products explicitly. In case of inverter by Victron and BMS by Orion, the communication protocol description must have been examined and it is part of this paper. Finally, the battery was cycled and the system setup was validated with comments on specific behavior of the battery.

## 2 BATTERY ASSEMBLY

The Lithium-ion battery with BMS are main parts of safety assembly which is responsible for disconnection when the operational limits are exceeded. The operational limits are Charge Current Limit (CCL) and Discharge Current Limit (DCL), which are calculated in BMS and are functions of battery temperature, State of Charge (SOC), individual cells voltages and cells internal resistance. Another event leading to battery disconnection might be faults (poor wiring, general BMS fault, etc.).

The battery assembly consists of battery made of 14 cells connected in serial, while each cell is a parallel connection of two LiNiMnCoO<sub>2</sub> (NMC) cells, cells contactor panel, current shunt, disconnection relay, BMS by Orion and fuse box. The electrical scheme of the assembly is in **Figure 1**.

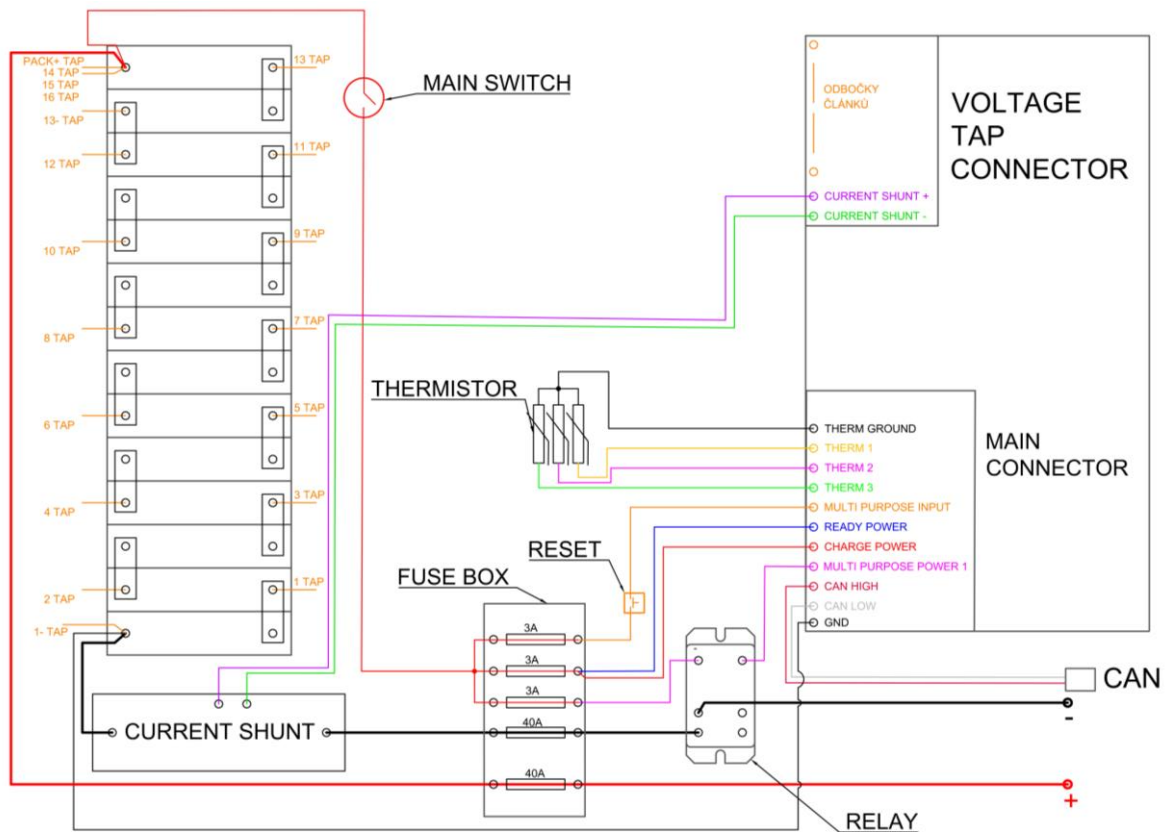


**Figure 1:** Battery assembly for safety disconnection.

### 3 DESCRIPTION OF BMS AND INVERTER COMMUNICATION

The CCL and DCL values are together with other battery parameters being sent to inverter control system through CAN bus. Although the CAN protocol is standardized, the interpretation of messages content and identification differs among manufacturers in real applications. Therefore, it is beneficial to enable the frame customization, especially in BMS's for general purpose. The BMS is also intended to operate in laboratory where inverters by various manufactures are tested and where practical workshops about different hybrid system behavior with various electrochemical accumulators are held. BMS Orion Junior has been chosen due to its ability of customization.

The best way how to obtain the communication protocol of a device is to find it in the operational manual. If the communication protocol is not included, it is necessary to examine the frame stream from communication busbar and derive the content. This is how the protocol can be specified alternatively. Inspection of the communication between inverter and one of the explicitly compatible battery (in this case BYD) must have been done. Obtained frames together with

Frame ID	Byte	Data	Length	Res./Unit
0x351 / 849	Data 0	Battery charge voltage	UINT16	0.1V
	Data 1	Battery charge voltage	UINT16	0.1V
	Data 2	Dc charge current limitation	SINT16	0.1A
	Data 3	Dc discharge current limitation	SINT16	0.1A
	Data 4	Dc discharge current limitation	SINT16	0.1A
	Data 5	Dc discharge cut voltage	SINT16	0.1V
	Data 6	Dc discharge cut voltage	UINT16	0.1V
0x355 / 853	Data 0	SOC value	UINT16	1%
	Data 1	SOC value	UINT16	1%
	Data 2	SOH value	UINT16	1%
0x356 / 854	Data 0	Battery voltage	SINT16	0.1V
	Data 1	Battery voltage	SINT16	0.1V
	Data 2	Battery current	SINT16	0.1A
	Data 3	Battery current	SINT16	0.1A
	Data 4	Battery highest temperature	SINT16	0.1C

**Table 1:** CAN bus protocol frames derived from inverter by Victron and BMS by Orion.

parameters are listed in **Table 1**. After this protocol was implemented into BMS by Orion, the battery appeared as a clone of the compatible battery in the inverter control system.

#### 4 BMS SETTINGS

Cell voltage settings in BMS must be set in accordance with limiting voltage parameters defined by both cell and inverter operational limits. The asymmetrical distribution of voltage among cells during charging must be taken into consideration to avoid undesired disconnection. To avoid inverter disconnection due to low voltage, the minimal voltage limit of the cell in BMS is set above the inverter cut-off voltage limit. It is also possible to set SOC correction as a function of cell voltage to compensate the SOC estimation error due to cell temperature and voltage disbalance. The voltage settings per one cell are listed in **Table 2**. The capacity of the battery has been set to 5.5 Ah according to cell datasheet.

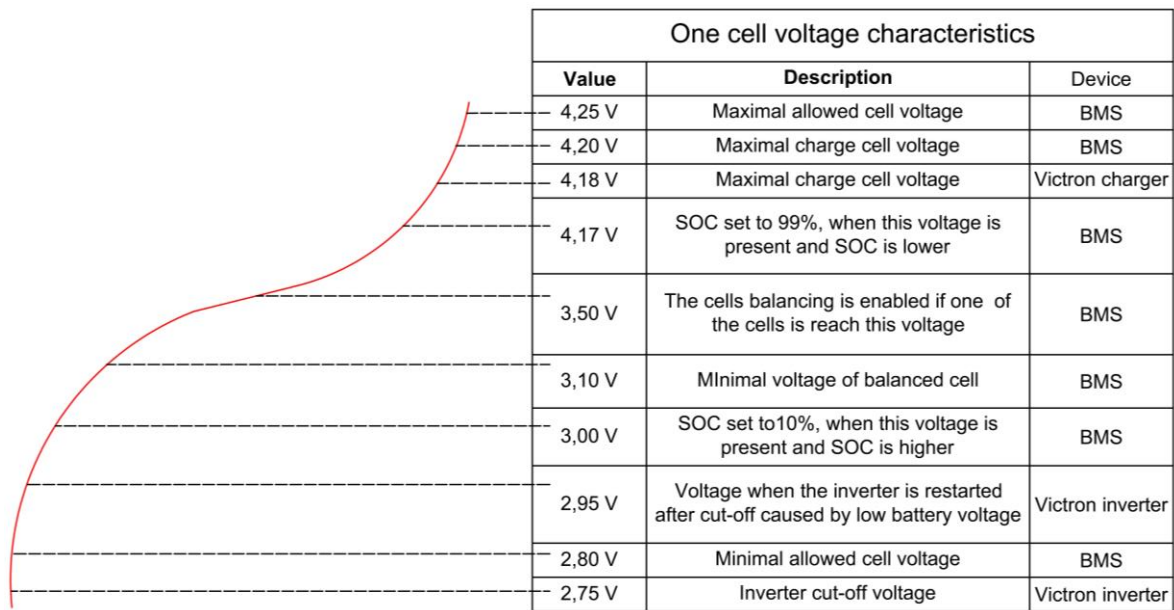


**Table 2:** Voltage parameters per one cell, values set in inverter are divided by 14 (number of cells in serial).

The DCL and CCL derating as a function of temperature and SOC is depicted in **Figure 2**. To ensure the battery disconnection before inverter disconnection, the DCL is derated to 0A at 10% of SOC.

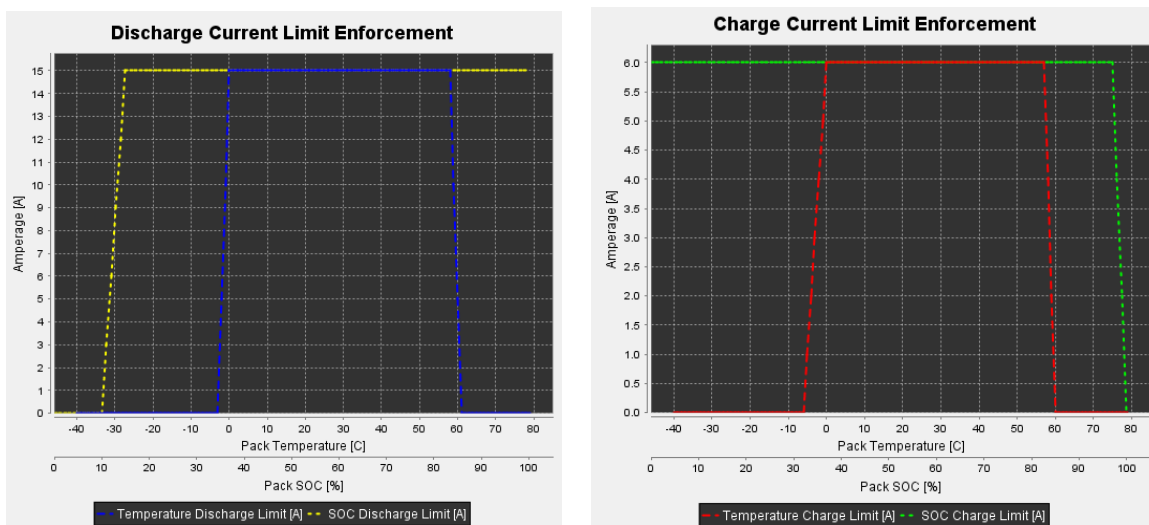


**Figure 2:** DCL and CCL derating as a function of temperature and SOC.

## 5 BMS SETTING VALIDATION

To validate the battery settings in both devices, charge and discharge curves has been recorded. The depicted curves show specific BMS and battery behaviour. In order to analyse the battery behaviour in whole operation range, the end of the measurement is considered as the moment of battery disconnection triggered by BMS.

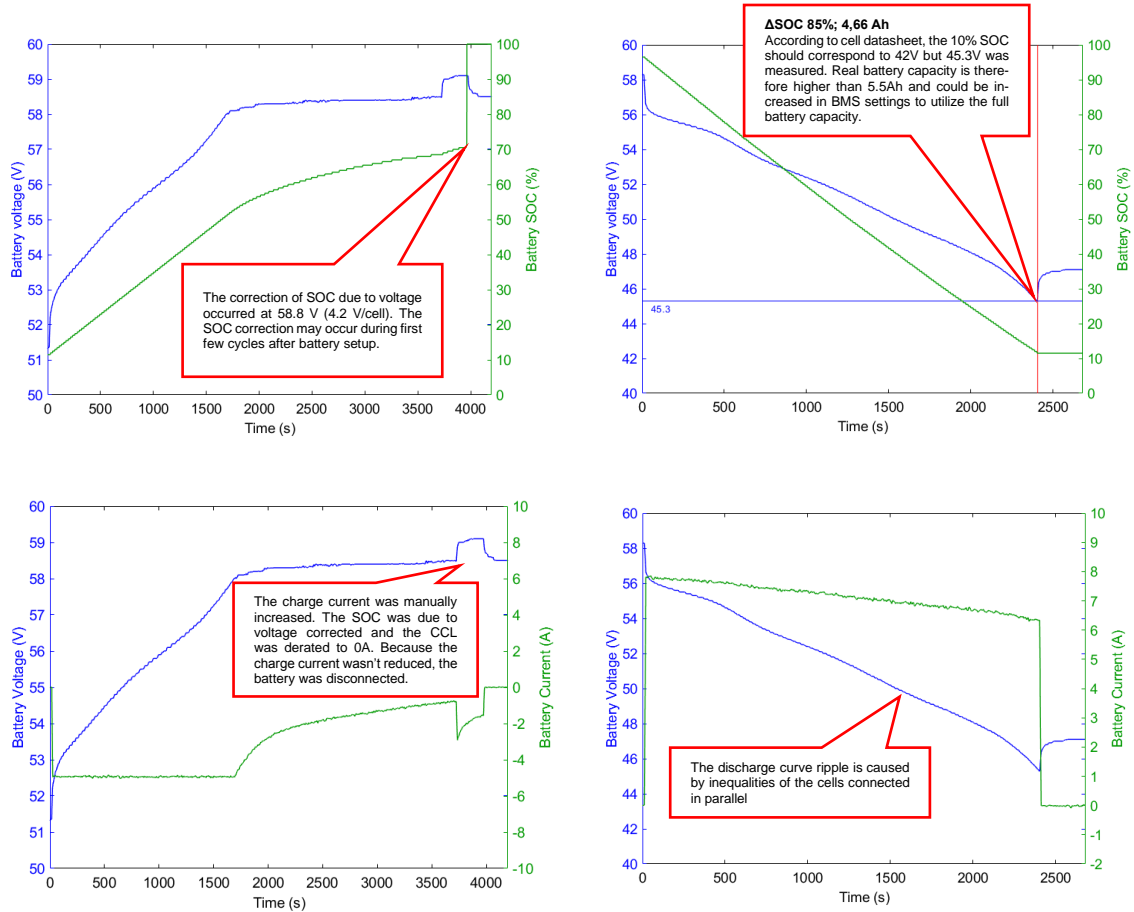


**Figure 3:** Battery charge using DC power source CC 5A, CV 58.5 (58.8)V (left). Battery discharge using resistor 7.5  $\Omega$  (right).

## 6 CONCLUSION

The paper describes design of autonomous assembly, which is responsible for safe operation of Lithium-ion batteries with BMS. The design was also validated and examples of charge and discharge curves, which led to settings adjustment, were described. Nevertheless, the battery should be cycled in full range of SOC several times after every setup to ensure correct BMS operation. During the cycling, the BMS adapts the SOC estimation algorithm to the battery parameters and thus the system works effectively.

## REFERENCES

- [1] MARQUES, José Miguel Branco. Battery Management Systems (BMS) for Li-Ion Batteries. Coimbra, 2014. Master thesis. Universidade de Coimbra.
- [2] ZHU, Xiaoqing, a kol. Overcharge investigation of large format lithium-ion pouch cells with Li(Ni<sub>0.6</sub>Co<sub>0.2</sub>Mn<sub>0.2</sub>)O<sub>2</sub> cathode for electric vehicles: Thermal runaway features and safety management method: Thermal runaway features and safety management method, 169, 868-880. DOI: <https://doi.org/10.1016/j.energy.2018.12.041>.
- [3] Orion Jr. BMS Operation Manual. In: Orion Jr. BMS (Original) [online]. [cit. 2020-03-15]. Available from: [https://www.orionbms.com/manuals/pdf/jr\\_operational\\_manual.pdf](https://www.orionbms.com/manuals/pdf/jr_operational_manual.pdf)

# THE DESIGN OF SAMPLE HOLDER FOR XRD MEASUREMENTS IN INERT ATMOSPHERE WITH DISPLACEMENT ERROR CORRECTION

Ondřej Klvač

Master Degree Programme (2), FEEC BUT

E-mail: xklvac02@stud.feec.vutbr.cz

Supervised by: Ondřej Čech

E-mail: cechondrej@feec.vutbr.cz

**Abstract:** This article describes a designed of a holder for post-mortem XRD measurements of Li-ion, Na-ion and Li-S electrodes, which need to be performed in the inert atmosphere. The first part describes the measurement method and problems arising during the measurements of the samples. Subsequently, the design and construction of a new cell with hermetic insulation and sample displacement error correction possible during the operation of the diffractometer is described. Finally, the inert gas attenuation within the cell is theoretically calculated. The calculation is verified by practical measurements, and alternatives are proposed to improve the signal-to-noise ratio.

**Keywords:** XRD, ex-situ, post-mortem, sample displacement, attenuation, SNR

## 1 INTRODUCTION

In recent years, increasing demands have been placed on the capacity and service life of electrochemical cells. For this reason, research into the electrode materials used is ongoing. One of the possible and accurate methods for their characterization is X-ray diffraction spectroscopy (XRD) [1].

During measuring by XRD, there is a problem with intercalated samples, as they are extremely sensitive to atmospheric influences due to the presence of alkali metals. Therefore, their hermetic isolation into a suitable cell is necessary [2, 3]. This presents several complications that can distort the obtained data.

The work describes a test accessory designed for the Rigaku device, which solves current problems and allows to achieve accurate results.

## 2 PROBLEM

A Rigaku Miniflex diffractometer is used for the measurement. It measures in the theta-2theta arrangement (tilts the sample and the detector). The schematic drawing is in Fig.1

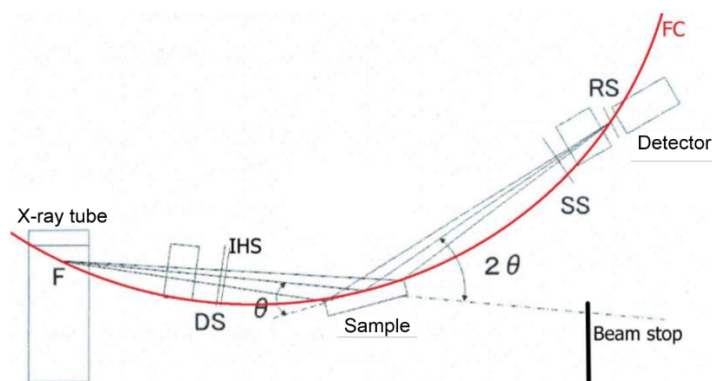


**Figure 1:** Schematic drawing of theta-2theta arrangement

The source of radiation is an X-ray tube; the X-ray beam is limited by a horizontal and divergence slit (IHS, DS) and falls on the sample. Depending on the structure of the material, it is reflected and scanned by an energy-selective detector according to Bragg's equation (only the Cu-K $\alpha$  spectral line is detected). The Soller slit (SS) is composed of parallel plates that shield radiation from directions outside the sample.

For the correct measurement, the focal spot in the X-ray tube, the surface of the sample, and the detector must lie on an imaginary focus circle (FC). In the case of electrodes, where it is necessary to close them to the cell, it is not possible to precisely adjust the height. This results in a shift of the diffraction peaks. However, the studied structural changes after intercalation can have the same effect. Therefore, the data may be incorrect, and the analysis cannot be performed.

Even the insulation of the sample itself is problematic. The used material must have good insulating properties, but also low attenuation for X-rays because the used energy is low (approx. 8 keV). Kapton foil is often used, which can be glued directly to the sample in a standard holder [4]. However, our experiments show that the insulation is not sufficient because the samples became moisten. Better insulating properties has, for example, a "coffee bag" foil (CBF), in which a thin aluminum layer is applied to a polymeric carrier. On the other hand, it results in higher attenuation and significantly distorts the data by its own contribution to the diffractogram.

### 3 SOLUTION

Negative properties of the CBF can be reduced by placing it in a circle, where it lies outside the FC (limits the distortion) and the penetrated thickness of the material is the lowest (limits the attenuation). For this purpose, various variants of accessories were created using additive technologies, see Fig.2 and 3.

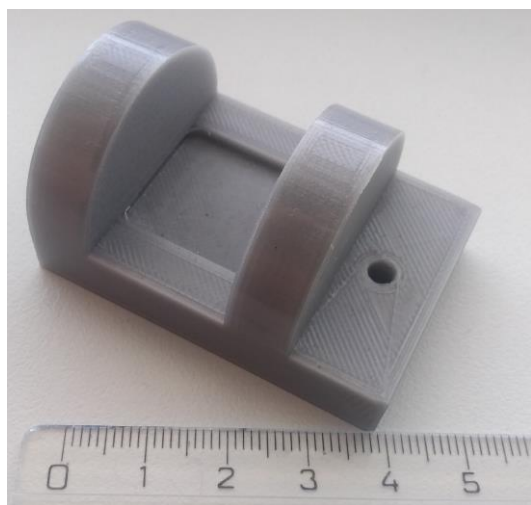


**Figure 2:** Printed ABS cell (3D print)

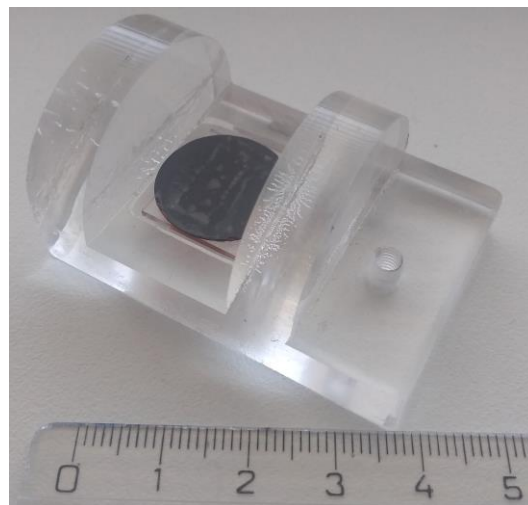


**Figure 3:** Glued PMMA cell with sample

A comparison of the unwanted contribution of the CBF film depending on its location is shown in Fig. 4. It can be seen the contribution is negligible in case of circular placement.

In both cases, the use of plastic causes moisture to penetrate despite prolonged drying before use. Assembly is difficult, the foil must be glued to the polished semicircles with a suitable tape in the glove box, and if the height of the sample is set inappropriately, no adjustment can take place. Despite these complications, these cells represent progress towards more successful results.

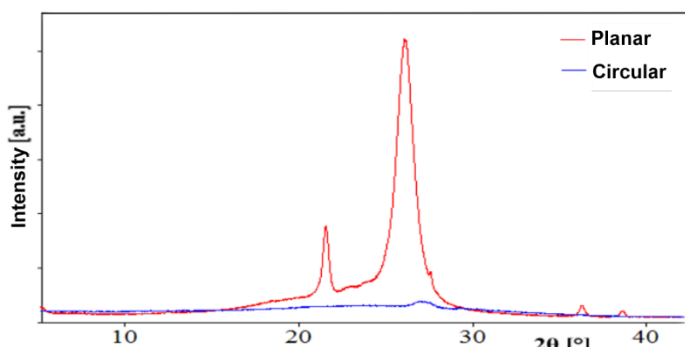


**Figure 4:** Comparison of unwanted CBF contribution

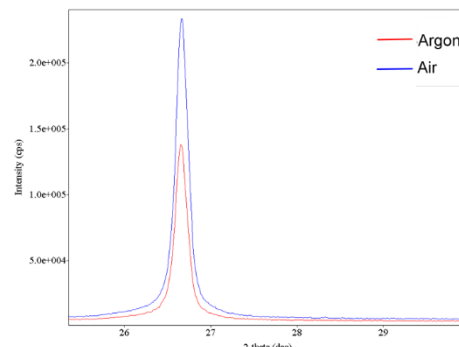


**Figure 5:** Comparison of peaks according to the gas in the cell

Using the above findings, a new cell with better insulation was designed, facilitating handling in the glove box. The design also includes a positioning system that allows the electronic movement of the sample inside the diffractometer during operation. Fig. 6 is a design with labels, which will be further discussed, the photograph in Fig. 7 represents the current appearance of the real accessory.

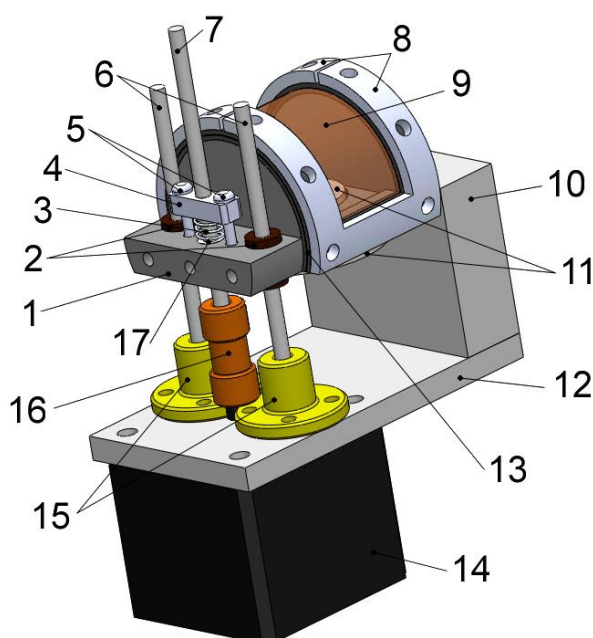


**Figure 6:** Design of a new cell with a positioning system

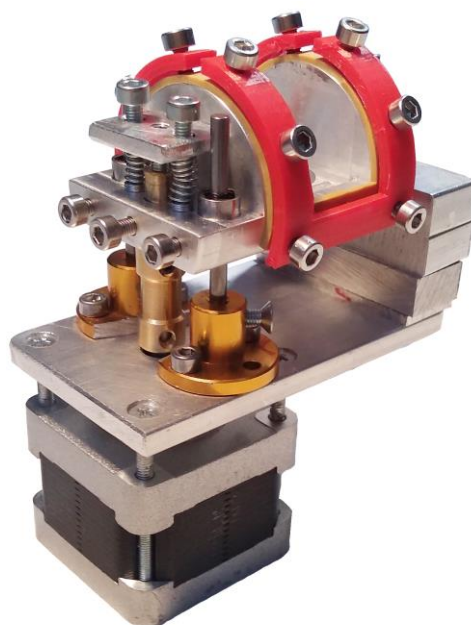


**Figure 7:** Photo of the assembled product

Holder (1) is made of duralumin rod. This material is light, sufficiently resistant to damage short threads, and, compared to iron, causes less distortion by the photoelectric effect. The foil (9) is fixed to a circular profile (for clarity it is not placed in the photo), which continues below the plane of the sample to facilitate manufacturing and allow polishing already on the lathe. The foil is held by pressing the seal (13) with round "U" profiles (8) screwed to the holder. The profiles in Fig. 7 are printed, the optimal inner diameter for the future turning of metal parts will be determined on them. The foil can be fixed outside the glove box and used indefinitely, as the sample is inserted from the bottom, glued to the sealing 'stopper' (11). Assembly is very simple compared to the previously mentioned variants. The cell is made so that it is possible to attach it to the goniometer of diffractometer even without a positioning system.

The active component of the positioning system is the stepper motor (14). The control is provided by the driver Pololu A4983, which is controlled via a serial terminal by the ATmega 8 microcontroller. When turning it (200 steps/revolution) a movement of 2.5  $\mu\text{m}$  per step can be achieved. Smooth chromed rods (6) anchored in coupling shafts (12) passing through linear ball bearings (2) serve to define the vertical movement. The backlash caused by the screw imprecisions is limited by a second nut (4), fixed by rivets (5), pressed by a spring (3) against the holder. In practice, this system consists of two springs on the screws, which setting the preload.

The whole device is attached to the goniometer of the device by a base (12) through a spacer block (10). In reality, it was created by a system of small blocks, which allow rough adjustment of the height for cases of significantly different samples.

#### 4 DISCUSSION

Measurements showed that the signal intensity decreased by 1.1% when using Kapton foil, and by 3.6% with CBF. This data came from test measurements when there was air inside the cell. When measuring the electrodes, the interior is filled with argon from the glove box. The attenuation then increases with respect to the air by another 41% (see Fig. 7, where the intensity of the diffraction maximum of the graphite plane (002) is shown). When taking into account the standard value of atmospheric pressure (and the corresponding density  $\rho$ ) and the diameter of the cell  $l$ , the attenuation can also be calculated theoretically (values of the mass attenuation coefficient  $\mu$  obtained from tables [5]):

$$1 - \frac{e^{\mu_{mass,Ar} \cdot \rho_{Ar} \cdot l}}{e^{\mu_{mass,air} \cdot \rho_{air} \cdot l}} = 1 - \frac{e^{-84,84 \cdot 1,67 \cdot 10^{-3} \cdot 3,5}}{e^{-6,93 \cdot 1,21 \cdot 10^{-3} \cdot 3,5}} \cong 0,37 = 37 \%. \quad (1)$$

The theoretical calculation is useful for the design of alternative accessories. It is obvious that the main component of the attenuation is argon. The calculation can lead to the conclusion that if helium, for example, is used instead, the radiation intensity will be almost 3% higher than in the case of measurements without any "obstacle", despite the presence of the foil. The intensity of the useful signal can also be increased by decreasing pressure.

It is also possible to experiment with the type of used foil. The ability of the detector to select the energy corresponding to the spectral line  $K\alpha$  ( $\cong 8.0$  keV) is limited. Typically, it also records the  $K\beta$  line ( $\cong 8.9$  keV), which may result in two diffraction maxima for one crystallographic plane (results are confusing). Therefore, the so-called  $K\beta$  filter is used. It is a nickel plate (typically tens of micrometres) inserted in front of the detector. Its energy levels are arranged so that just behind the energy  $K\alpha$  the attenuation increases sharply due to the photoelectric effect and  $K\beta$  is significantly attenuated. The use of a nickel foil for sealing the cell and removing it in front of the detector will have the same effect and will not increase the attenuation as in the case of using the filter and the foil separately.

#### 5 CONCLUSION

An accessory enabling post-mortem measurement by X-ray diffraction spectroscopy was designed and manufactured. The product allows hermetic isolation of samples in inert gas or vacuum environment. There is an insulating foil at the passage of the X-rays, which can be practically changed as needed outside the glove box. Inside the box, only the sample from the bottom is inserted, which closes the cell. This option significantly simplifies the work.

The accessory includes a positioning system for sample displacement correction with a step of 2.5  $\mu\text{m}$ . The adjustment takes place electronically via the serial terminal during the operation of the diffractometer. If the sample contains an element with known crystallographic parameters, it is possible to adjust the height according to it, thus eliminating the sample displacement error and more

accurately evaluating the structural changes of the investigated material. The cell can also be used without a positioning system by clamping it directly into the goniometer of the Rigaku device.

It has been calculated that by using suitable inert gases or decreasing the pressure, a higher signal-to-noise ratio can be obtained than with conventional measurements, despite the presence of insulating foils. The theoretical calculation of attenuation is verified by practical measurements. The used foil can also be used as a  $K\beta$  filter.

## ACKNOWLEDGEMENTS

This work was supported by the project of specific research: Materialy a technologie pro elektrotechniku III, reg. no. FEKT-S-17-4595. CzechNanoLab project LM2018110 funded by MEYS CR is gratefully acknowledged for the financial support of the measurements at CEITEC Nano Research Infrastructure.

## REFERENCE

- [1] ČECH, Ondrej, Jorge E. THOMAS, Arnaldo VISINTIN, Marie SEDLARIKOVA, Jiri VONDRÁK a Sergio MORENO. Cobalt Doped LiFePO [online]. In: . 2012, s. 93-98 [cit. 2020-13-03]. DOI: 10.1149/1.4729091. Available at: <http://link.aip.org/link/EC-STF8/v40/i1/p93/s1&Agg=doi>
- [2] KAZDA, T., P. ČUDEK, J. VONDRÁK, M. SEDLAŘÍKOVÁ, J. TICHÝ, M. SLÁVIK, G. FAFILEK a O. ČECH. Lithium-sulphur batteries based on biological 3D structures. Journal of Solid State Electrochemistry [online]. 2018, 22(2), 537-546 [cit. 2020-13-03]. DOI: 10.1007/s10008-017-3791-0. ISSN 1432-8488. Available at: <http://link.springer.com/10.1007/s10008-017-3791-0>
- [3] CECH, O., J.E. THOMAS, M.S. MORENO, Arnaldo VISINTIN, Marie SEDLARIKOVA a Jiri VONDRAK. Synthesis of LiFePO<sub>4</sub>/C Composite Cathode for Lithium-Ion Batteries [online]. In: . 2011, s. 23-31 [cit. 2020-13-03]. DOI: 10.1149/1.3641834. Available at: <http://ecst.ecsdl.org/cgi/doi/10.1149/1.3641834>
- [4] Experimental Setup. SEECK, Oliver H. a Bridget M. MURPHY. X-Ray Diffraction: Modern Experimental Techniques. 1. Boca Raton, Florida: CRC Press, 2014, s. 93 [cit. 2020-03-14]. ISBN 9789814303606.
- [5] X-Ray Mass Attenuation Coefficients. *NIST* [online]. USA: National Institute of Standards and Technology, December 11, 2019 [cit. 2020-13-03]. Available at: <https://physics.nist.gov/PhysRefData/XrayMassCoef/chap2.html>

# APPLICATION OF GRAPHITE IN THERMAL MANAGEMENT OF MICROELECTRONICS

**Vaclav Havlicek, Petr Vyroubal**

Department of Electrical and Electronic Technology, Faculty of Electrical Engineering and Communication,  
Brno University of Technology, CZ-61600 Brno, Czech Republic

vhavlicekv@gmail.com, vyroubal@feec.vutbr.cz

**Abstract:** This paper is shortly describing the possibility to improve the thermal management of microelectronics by implementing carbon-based materials, more exactly graphite foils. It explains current thermal challenges in the field of microelectronics and moves to commonly used materials, where it adds carbon allotropes into the scope, with a special focus on graphite foils. In the last part, this paper contains a use case of the pyrolytic graphite sheet in thermal management.

**Keywords:** thermal management, thermal architecture, carbon, graphite, PGS, heat

## 1 INTRODUCTION

We live in times where our pocket computers are way more powerful than our desktop computers were a decade ago, and the techniques that were once a standard cannot achieve the required cooling. Despite all of the development in the field of thermal management, there are still cases where devices have poor architecture and their chips have to be throttled down not to overheat. But still, two main materials being used in this field - aluminum and copper. In this paper, the option of using pyrolytic graphite foil is introduced, followed by an example of the use, demonstrated using finite volume method simulation in SolidWorks Flow Simulation.

## 2 THERMAL MANAGEMENT IN MICROELECTRONICS

Thermal management in microelectronics can be divided into parts, as the heat travels. In the cooling applications, heat from the heat source must at first travel by thermal conduction of some kind to a surface exposed to the cooling fluid. The system as a whole can be improved simply by reducing the amount of heat produced by the heat source. The second way is by improving the thermal conduction, the path through the heat travels to the surface area. The next option is making the contact area where heat can be exchanged between parts and systems the largest possible. Adjusting the cooling fluid itself - its composition, density and heat transfer properties can also help.

### 2.1 CHALLENGES

The architecture of the electronics is creating non-uniform heat dissipation across the die surface, with localized functional areas - so-called power-dense regions, where the density of power can be five to ten times higher than the average of the die. Also, the number of metal layers interconnecting the microprocessors technology had increased from seven in 2001 to thirteen in 2014. [1] At the same time, these "System on a Chip" (SoC) are changing its structure from the 2D planar chip into a 3D structure with nanowires connecting different levels of the system creating a thermal architecture maze with more attention needed. The packaging itself is also becoming more of a thermal challenge, as the single flip-chip can be cooled down by classic techniques, but as the architecture is getting more and more complicated, the layers are stacked one on top of another. And as the field of flexible

electronics is becoming stronger and grows it brings questions about its thermal management and cooling.

## 2.2 MATERIALS USED FOR THERMAL MANAGEMENT

Materials that are used have a high range of thermal conductivity, starting at  $0.2 \text{ Wm}^{-1}\text{K}^{-1}$  for polymers and going all the way up to  $3450 \text{ Wm}^{-1}\text{K}^{-1}$  for diamond. [1] Aluminium is commonly used for heat sinks in thermal management of microelectronics, because of the thermal conductivity of  $220 \text{ Wm}^{-1}\text{K}^{-1}$  and low cost. [2] Copper has desirable properties for the use in thermal management, starting with high thermal conductivity - around  $400 \text{ Wm}^{-1}\text{K}^{-1}$ , corrosion resistance, high allowable stress, and internal pressure. Pure copper slug is the most common copper heat sink material and it is also often used as heat spreader on the chips, as a cold plate for liquid cooling or heat pipe material. [2]

### ALLOTROPES OF CARBON, HIGHLY ORIENTED PYROLYTIC GRAPHITE - HOPG

Carbon occurs in two natural allotropes, diamond, and graphite. Both forms have different, but unique physical properties like hardness, thermal and electric conductivity and lubrication behavior. For a long time, these were the only two allotropes known, but that changed in 1985, with the discovery of fullerenes, followed by carbon nanotubes in 1991 and then graphene in 2004. The youngest from the carbon allotropes family is two-dimensional graphene, basically a single graphite sheet. Graphite can be found and made into various forms, like crystalline - which are small flakes of graphite, amorphous graphite, lump graphite, graphite fiber and highly oriented pyrolytic graphite (HOPG), which is highly pure synthetic graphite.[3]

HOPG is based on pyrolytic carbon, which is produced by heating hydrocarbon to a temperature near its decomposition, thus allowing the graphite to crystallize - pyrolysis. [4] HOPG has exceptionally high thermal conductivity along the layer plane - as much as  $1600 \text{ Wm}^{-1}\text{K}^{-1}$ , and very small conductivity at the plane perpendicular to the layer, where it can go as low as  $7 \text{ Wm}^{-1}\text{K}^{-1}$ . So it can conduct heat one way but insulate the other. This anisotropy is caused by the structure, where layers do have strong  $\sigma$  bonds, but parallel stacking of these layers are bonded by the van der Waals forces caused by the interactions between  $\pi$ -electron clouds on the neighboring layers. [5] There are several graphite products - foils and membranes - for the use in the field of microelectronics, with very high heat conductivity. Based on pyrolytic carbon there is Pyroid-HT from MINTEQ, based on graphite and Kapton it is PGS line from Panasonic. Based on natural graphite it is Grafoil from Graf Tech.[5] Heat conductivity of these foils vary, depending both on thickness and manufacturer, but they do provide highly different heat conductivity in the layer plane and the plane perpendicular to the layer, with differences as big as  $1800 \text{ Wm}^{-1}\text{K}^{-1}$ . [6]

## 3 USE CASES OF PYROLYTIC GRAPHITE SHEET

This simulation was made with a commercially available product - Pyrolytic Graphite Sheet (PGS) from Panasonic. They have both catalog [7] and datasheet [8] available online, so the product information from these sources was be used for the simulation, computed in SolidWorks Flow Simulation. In this example, the use of PGS for transferring the temperature across the material with a bad heat conductivity - poly-carbonate - will be demonstrated. This material was chosen as it is commonly used for making various cases and boxes for electronics, so the example will simulate a possible use case.

The design is simple: PCB board with IC chip with 0,5 W volume heat source on in, covered by silicon and by  $0,3 \mu\text{m}$  of material - poly-carbonate, aluminum, copper, or PGS - and covered by a poly-carbonate desk. The dimensions can be seen in Table 1, and the cut through the model itself can

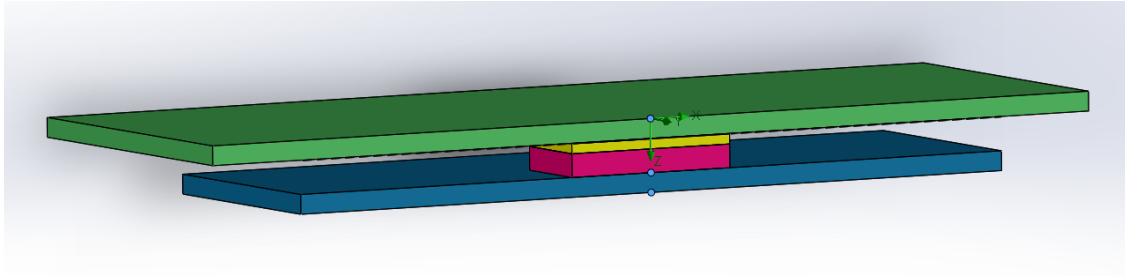


**Figure 1:** Cut through the design with layers described bottom up - blue is PCB, pink is the IC, yellow silicon, barely visible black layer is the thin added material, that is variable for each iteration and the top green layer is the poly-carbonate.

be seen at Figure 1. On the same figure, you can see three control points, where the temperature is measured. On the top and the sides of the poly-carbonate desk on the top of the design, there is a heat transfer coefficient  $\alpha = 10 \text{ Wm}^{-2}\text{K}^{-1}$ , simulating air running over the plate.

**Table 1:** Dimensions of the design.

material	dimensions [mm]
PCB	25 x 40 x 1
IC	9 x 9 x 1,2
Silicon	9 x 9 x 0,5
“material”	25 x 40 x 0,03
Poly-carbonate	35 x 50 x 1

Points are distributed subsequently: First one is at the bottom of the PCB, the second one is between the PCB and the IC, and the third is on the poly-carbonate. All of these three points are aligned along the z-axis.

In the Table 2, there are temperatures for the point mentioned above, for different materials, showing that PGS can distribute the heat equally to the poly-carbonate plate, preceding the IC to overheat. (The fourth material here - poly-carbonate - is in the simulation to show how would the temperature spreading look like without anything added - but to show that the better heat spreading is not provided only by extra volume, there is the  $0,03 \mu\text{m}$  layer added.)

**Table 2:** Converged temperatures in three different points for four types of material.

material	PCB [°C]	IC [°C]	poly-carbonate [°C]
poly-carbonate	193,98	194,18	184,99
aluminium	58,18	58,38	56,12
copper	54,96	55,15	53,06
PGS	51,05	51,18	49,32

To even more understand the heat spreading, it can be demonstrated using maximal and minimal temperatures on the top plate. In all four cases, the maximal and minimal temperatures are located at the same spots - maximum in the middle of the plate, where the center of the IC lays underneath. The minimum is then located in the corners. As can be seen in the Table 3, the PGS actually have the lowest maximal temperature, but the highest minimal. That is a clear example of its heat conductivity, as it leads the heat beneath the material to the most distant corner more effectively than any other material used in this simulation.

**Table 3:** Minimal and maximal temperatures of the top plate for different underlaid materials.

material	minimum [°C]	maximum [°C]
poly-carbonate	21,47	184,99
aluminium	25,70	56,12
copper	26,02	53,06
PGS	26,42	49,32

#### 4 CONCLUSION

Thermal management of microelectronics has problems, such as the creation of hot spots, complicated designs with 3D stacking of individual chips and flexible electronics and touchscreen devices. These three challenges can be solved by using not only aluminum and copper but also a Pyrolytic Graphite Sheet (PGS), which has great heat conductivity and it can be very thin and flexible. In the paper, there was a demonstration comparing the PGS with traditional aluminum and copper, revealing that PGS had 7% lower temperature than copper and 12% lower temperature than aluminum. This is showing the possibility of use of PGS, especially considering its flexibility, ability to be layered with PET (thus behaving as electric isolation) and because of the thickness of only 30  $\mu\text{m}$  it can be used both between components and inside of packages.

#### ACKNOWLEDGEMENT

This work was supported by the BUT specific research programme (project No. FEKT-S-20-6206).

#### REFERENCES

- [1] MOORE, Arden L.; SHI, Li. *Emerging challenges and materials for thermal management of electronics. Materials today*, 2014, 17.4: 163-174.
- [2] EKPU, Mathias, et al. *Advanced thermal management materials for heat sinks used in microelectronics. In: 18th European Microelectronics and Packaging Conference. IEEE, 2011. p. 1-8.*
- [3] ANTHONY, John W., Richard A. BIDEAUX, Kenneth W. BLADH and Monte C. NICHOLS. 1990. *Handbook of Mineralogy. I (Elements, Sulfides, Sulfosalts). Chantilly, VA, US: Mineralogical Society of America.*
- [4] L. C. F. Blackman, A. R. Ubbelohde (1962). "Stress Recrystallization of Graphite". *Proceedings of the Royal Society of London. A266 (1324): 20–32.*
- [5] Inagaki, M., Kaburagi, Y., Hishiyama, Y. (2014). *Thermal Management Material: Graphite. Advanced Engineering Materials*, 16(5), 494–506.
- [6] *Pyrolytic Graphite Sheet Evolves to Meet Tough Thermal Demands. 2015. In: ElectronicDesign [online]. Available at: <https://www.electronicdesign.com/circuit-protection/pyrolytic-graphite-sheet-evolves-meet-tough-thermal-demands>*
- [7] *Pyrolytic Graphite Sheet: The Advanced Thermal Management Solution For Today's Designs. In: Panasonic [online]. Available at: [https://b2b-api.panasonic.eu/file\\_stream/pids/fileversion/910](https://b2b-api.panasonic.eu/file_stream/pids/fileversion/910)*
- [8] *PGS Graphite Sheets: Datasheet. 2019. In: Panasonic [online]. Available at: [https://b2b-api.panasonic.eu/file\\_stream/pids/fileversion/1652](https://b2b-api.panasonic.eu/file_stream/pids/fileversion/1652)*

# ADVANCED DRIVING SYSTEM OF THE THREE-PHASE DC MOTOR

**Radek Hanuš**

Master Degree Programme (2), FEEC BUT

E-mail: xhanus12@stud.feec.vutbr.cz

Supervised by: Jiří Háze

E-mail: haze@feec.vutbr.cz

**Abstract:** The presented article briefly outlines a field-oriented control algorithm used to drive a permanent magnet three-phase DC motor with efficiency maximization and its modification to reduce overall computational complexity. This enables the utilization of the algorithm in computer constrained devices, for example in a self-balancing vehicle, which the algorithm and electronics were previously designed for.

**Keywords:** BLDC motor, PMSM motor, field-oriented control, Park transformation, Clarke transformation, look-up table.

## 1 INTRODUCTION

The discovery of the alternating current initiated following widespread usage of three-phase motors, known for almost no need of any maintenance. In these days they can be found in the industrial sector on the one hand, but on the other hand they are also becoming more and more popular in consumer electronics, where they act as a replacement of traditional brushed motors. Some examples of this case represent blenders, vacuum cleaners, white goods and other household appliances. Three-phase motors can be found also in transportation vehicles, including electric bikes, electric cars, trains, trams, etc. Especially in vehicles that carry accumulators as a source of energy along with them, it is essential to convert this energy into suitable voltages to drive each phase of the motor and reduce any power losses to maximize overall efficiency and range.

This article focuses on the solution of energy maximization which will be used as a part of the self-balancing vehicle [1].

## 2 ROOT OF THE PROBLEM

The previous solution of driving the permanent magnet motor in the self-balancing vehicle was based on a six-step commutation. It means that according to the rotor position sensed with Hall sensors, each phase was connected to the positive or negative pole of a power supply. The speed of the rotation was controlled by a pulse-width modulation duty. This method is simple and easy to implement, but its inefficiency rises with the rotational speed. The reason of this is the inductance of the stator winding, which causes a lag of the current, as a force-creating element, behind the driving voltage. The situation is shown in figure 1. The left side of the figure belongs to a simplified sketch of the rotor. The maximum force and efficiency could be obtained by pushing the magnet with an electromagnetic force perpendicular to the magnet longitudinal axis. In that case, the quadrature component, marked with letter Q, will be the highest, and the direct component, marked with letter D, will be eliminated.

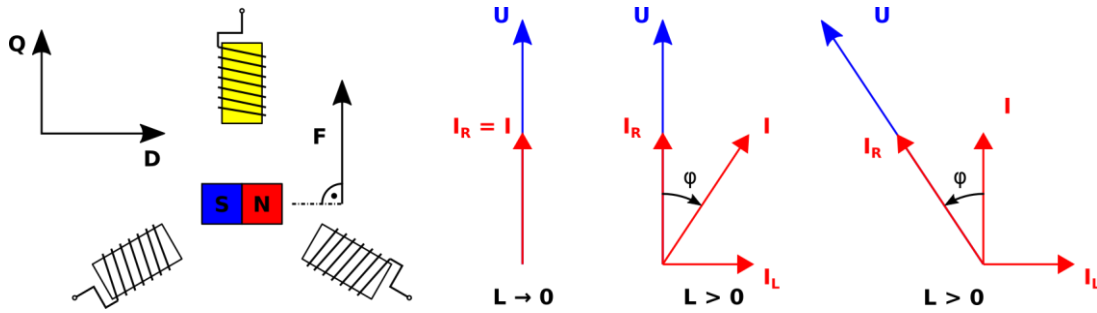


**Figure 1:** The impact of the winding inductance while driving the motor

The right side of the figure shows three situations. The first one assumes only the resistance of winding and no inductance, which implies that the voltage and current vector share the same orientation. However, the situation in practice is much more like the second part, where the current vector lags behind the voltage vector, due to the previously mentioned and not negligible inductance. It is necessary to move the voltage vector ahead of the direction of the rotation to compensate this effect, which increases the impact of Q component, cancels impact of D component and maximizes the motor efficiency and performance.

### 3 GENERAL SOLUTION

The traditional solution to this problem is an implementation of a so-called field-oriented control, shown in figure 2. The currents flowing through each phase are measured and converted from a three-component representation into two components of a complex plane by using Edith Clarke's transformation. However, both of these complex plane components named  $I_\alpha$  and  $I_\beta$  always change in accordance with the rotor position. Robert Park's transformation is used to simplify subsequent mathematical calculations and to synchronize both components to the current rotor angle, resulting in creation of two almost static current components  $I_d$  and  $I_q$ . These are fed into PI controllers, to minimize  $I_d$  and keep  $I_q$  in the compliance with an external requirement.

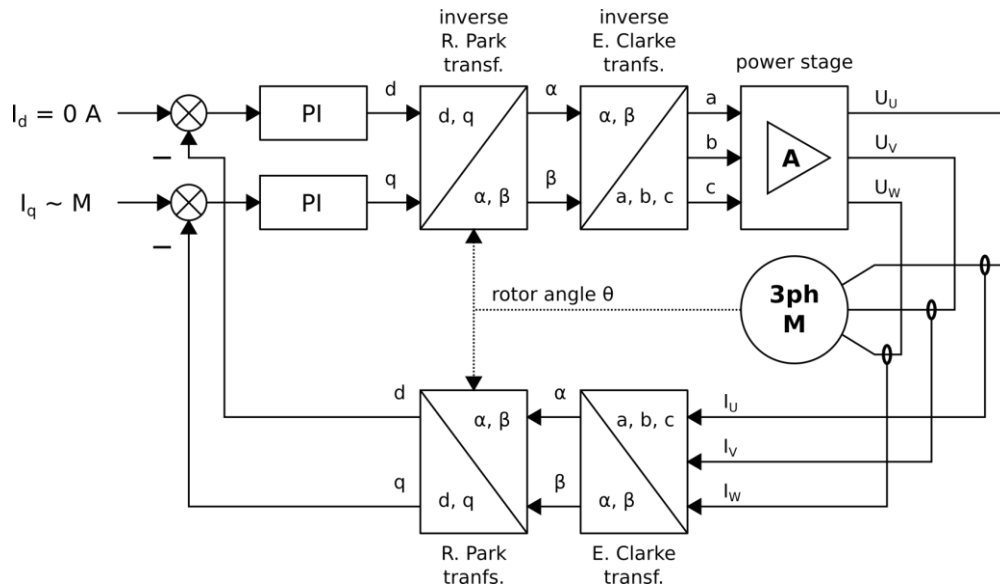


**Figure 2:** Field-oriented control scheme

The next part of the control scheme consists of inverse transformations. Robert Park's inverse transformation changes PI controllers outputs in terms of voltages  $U_d$  and  $U_q$  to the right value, depending on the position of the rotor. Edith Clarke's inverse transformation creates three components again to drive each phase. The main disadvantage of this solution is its computational complexity and the fact that the maximal voltage each phase can be driven with is 87 % of the nominal

power supply voltage. An advanced driving method should be employed to utilize the full magnitude of power supply voltage, for example Space Vector Pulse-Width Modulation (SVPWM), the third harmonic injection or the use of saddle-shaped profiles, resembling letter M, stored in the look-up table in microcontroller programme memory, as described in [2].

#### 4 THE SOLUTION

The stored driving waveforms and the inspiration taken from [3] serve as the main basis of the solution shown in figure 3. The initial part of the control scheme is the same as in the previous example. The phase currents are measured and gradually transformed into  $I_d$  and  $I_q$  components. They act as a feedback to PI controllers simultaneously with current commands. The D part needs to be eliminated and Q part should be set accordingly to the output of a balancing algorithm, described in author's previous article [1]. The principle of the balancing algorithm will not be analysed here, but for the purpose of the control algorithm it is essential to mention that it uses the arctan function to estimate the position of the driver from the data provided by the integrated accelerometer. The same function can be used to determine the angle of the voltage vector, given by  $U_d$  and  $U_q$  components, and to advance the current position, given by the rotor angle, in the look-up table containing suitable driving waveforms. These waveforms are subsequently multiplied by a modulus of the voltage vector and in the form of a pulse-width modulation duty amplified in a power stage.

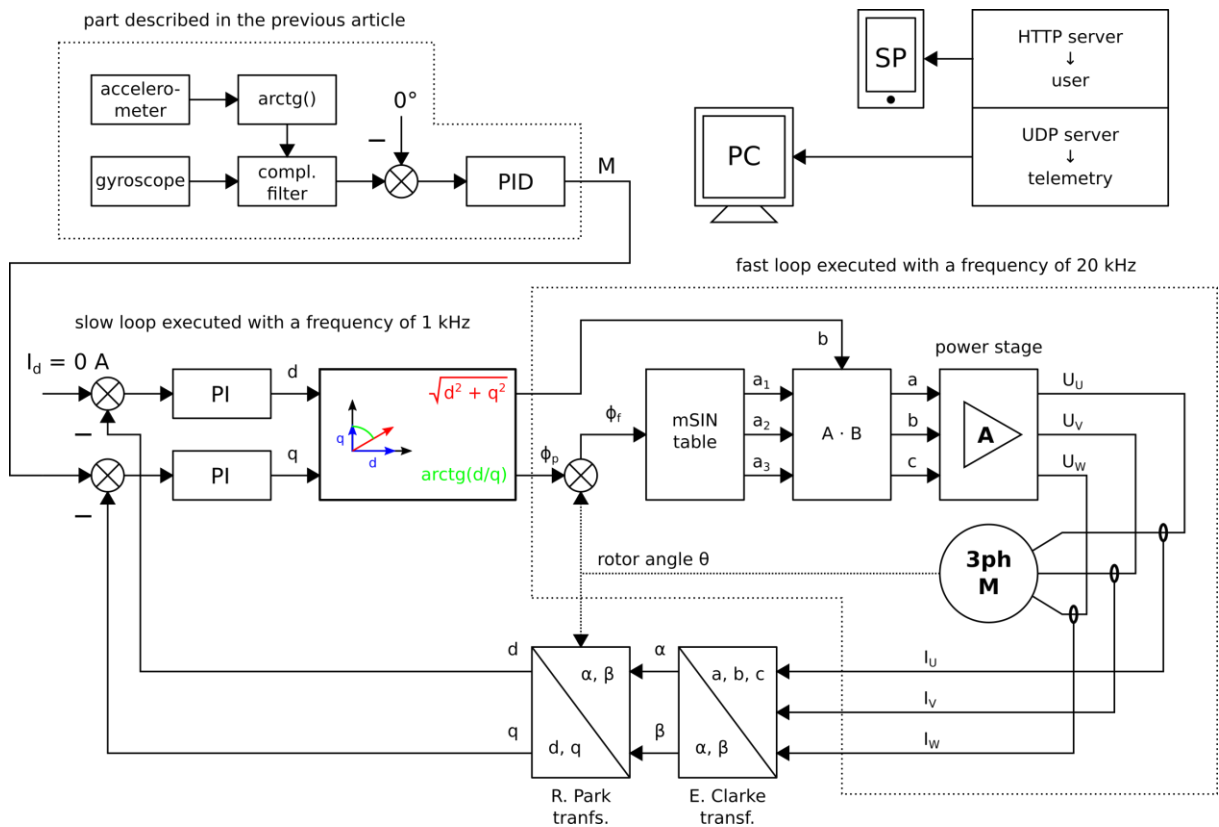


**Figure 3:** Modified field-oriented control scheme

There is no need to do backward transformations with the solution described above and whole control algorithm can be divided into two separate loops with a different speed of execution. The slow loop calculates all necessary quantities, while the fast one only reads the data from the look-up table and scales them as necessary. There is also a possibility to see selected waveforms and set algorithm coefficients in real time through PC application and to communicate with a smartphone, for example in order to check the battery voltage.

## 5 ELECTRONIC DESIGN

The key part of the whole electronics, which is shown in figure 4, is the 32-bit Cortex-M3 microcontroller STM32F103C8T6, clocked with a frequency of 32 MHz, performing all calculations described above and providing the communication with external peripherals. These include the three-axis accelerometer and gyroscope LSM6DS3 in a package and the UART to Wi-Fi bridge ESP-01 containing the integrated circuit ESP8266. The power stage consists of three half-bridges, each one containing two N-MOS transistors YJG85G06A and a driver IRS21867. The current sensing in all three phases is done by three Hall effect based sensors ACS712 with a sensing range  $\pm 30$  A. The power supply stage contains a buck converter AOZ1282CI and a pair of AMS1117 voltage regulators. The three-phase BLDC motor with the voltage and power rating 24 V and 500 W respectively stays the same from the previous version of the self-balancing vehicle, as well as the six-cell lithium-polymer accumulator with a capacity of 12 Ah.

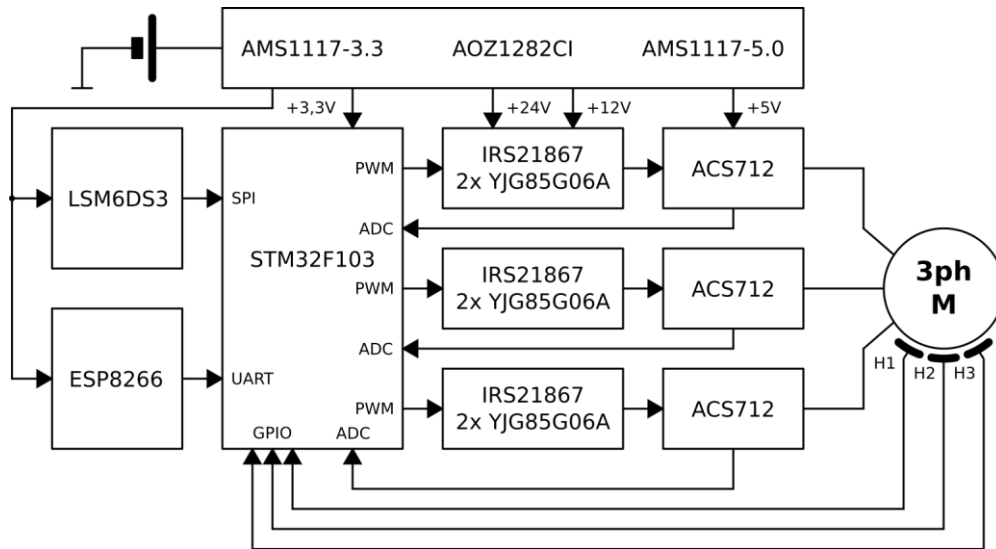


Figure 4: Block scheme of the electronics

## 6 CONCLUSION

The main purpose of this article is to describe a fast, simple and in term of computational complexity modest implementation of a field-oriented control algorithm used in order to maximize the efficiency of a three-phase BLDC motor. The reason for this was the integration of the algorithm in the self-balancing vehicle, where a part of the computational power already belongs to estimate the rider's position. Another reason can be the utilization in similar personal electric vehicles with low-cost and low-power microcontrollers.

## REFERENCES

- [1] HANUŠ, Radek. Single Wheel Vehicle. In: *Proceedings of the 24th Conference STUDENT EEICT 2018* [online]. Brno University of Technology, Faculty of Electrical Engineering and Communications, 2018, s. 66-68 [cited 2020-02-27]. ISBN 978-80-214-5614-3. Available at: <http://hdl.handle.net/11012/138170>
- [2] \* Atmel. AVR447: *Sinusoidal driving of three-phase permanent magnet motor using ATmega48/88/168* [online]. 12th October 2016, [cited 2019-11-10]. Available at: <http://ww1.microchip.com/downloads/en/Appnotes/doc8010.pdf>
- [3] 3ph Duo Wrap-Up Part 2. *Shane Colton* [online]. 13th January 2010, [cited 2019-11-22]. Available at: <http://scolton.blogspot.com/2010/01/3ph-duo-wrap-up-part-2-control.html>

# PICOBALLOON PROBE

**Jakub Kaderka**

Doctoral Degree Programme (first year), FEEC BUT

E-mail: [xkader12@stud.feec.vutbr.cz](mailto:xkader12@stud.feec.vutbr.cz)

Supervised by: Tomáš Urbanec

E-mail: [urbanec@feec.vutbr.cz](mailto:urbanec@feec.vutbr.cz)

**Abstract:** The Brno Observatory and Planetarium organised an international competition of PicoBalloon probes in March 2020. This article describes a technologies used in designing such probe. The probe is powered by a lithium battery which limits runtime to several days, but in comparison with the solar powered solutions it allows data transmission during the night. The probe is equipped with a pressure sensor and a GPS receiver. The telemetry is sent over an Internet of Things network. The probe was launched on 2nd of March and travelled over 1800 km in temperatures reaching -40 degrees Celsius.

**Keywords:** picoballoon, probe, LoRaWan, low-power, IoT

## 1 INTRODUCTION

In March 2020 the Brno Observatory and Planetarium in cooperation with Slovak Organisation for Space Activities organised a PicoBalloon Challenge [1] for a second year in a row. The goal of this challenge was to build a probe that would weight below 20 grams and could send it's altitude periodically. This probe would be launched on a helium filled balloon into altitudes between approximately 5 to 10 km above the ground. The probe that sends it's altitude as the last one wins the competition, probes that are silent for more than 7 days are considered dead.

The probe will be exposed to a rough weather, the temperatures during night can fall down to -50 degrees Celsius, also a humidity can condensate on the probe surface when flying though a cloud. In a good weather conditions a balloon can circle the Earth several times before the helium leaks [2].

## 2 TELEMETRY TRANSMISSION

Licensed HAM radio operators usually use an APRS (Automatic Packet Reporting System) protocol on 2 m or 70 cm amateur radio band together with ground station networks as `aprs.fi`. There's even a network called `habhub.org` devoted to tracking high altitude balloons.

With a rise of a Internet of Things (IoT) there are multiple networks designed for communication with low power devices. The IoT network are usually country based, but there's an open LoRaWan network called The Things Network (TTN) that has over ten thousands active gateways (base stations) spread over almost 150 countries forming a perfect solution for a telemetry transmission [3].

The LoRaWan provides two modes of node authentication, the OTAA (Over The Air Activation) and ABP (Activation by Personalization). The OTAA requires bidirectional link and the node has to request session keys from network after every power up. The ABP requires session keys to be hardcoded in the device, but unidirectional (uplink only) communication can be used afterwards, reducing the air time and increasing link reliability over long distances [4].

## 2.1 TRANSMITTER DESIGN

A commonly used RF module RFM95 working at 868 MHz was selected as a RF fronted. It's compatible with a SX127x family of transceivers and comes with a sleep mode current consumption below 1  $\mu$ A. It contains a 20 dBm amplifier which allows to generate 100 mW of output power.

The antenna is made from a piece of cooper wire cut to 1/4 of the wavelength (82 mm for 868 MHz band) forming a ground plane antenna. No radials were used and the ground plane on the PCB is very small due to the weight limitations, but the antenna proved to be working satisfactory. The SWR was not measured due to the lack of time before the launch (the PCBs arrived from the manufacturer three days before the launch).

## 3 POWER SUBSYSTEM

The weight limit severely reduces an amount of possible power sources to solar and battery power. The probe was designed in a way both methods could be used. The solar cells come with almost unlimited probe runtime. On the other side a battery powered probe can transmit even during nights, however the battery capacity drops severely with a dropping temperature [5].

The solar cells are charging a supercapacitor, initially directly through a low drop Schottky diode, once the voltage rises above 0.65 V the step-up converted MCP1640 starts to operate boosting the voltage to 3 V. A MPPT (Maximum Power Point tracking) capable charger would achieve a higher efficiency, but for the intended usage the solution described above is acceptable. Once the voltage on the supercapacitor reaches 2.7 V a power supervisor circuit MCP101 triggers a second MCP1640 that boosts the supercapacitor voltage to stable 3.3 V for powering a rest of the circuit.

If the probe is powered directly from a battery, the solar power related part of the PCB can be snapped off to reduce weight and a battery can be fitted instead of the supercapacitor.

This year the probe was equipped with a CR2 lithium battery with estimated runtime of two weeks with 30 minutes telemetry sending period. The finished probe with the battery connected is show on Figure 1.



**Figure 1:** The finished probe

## 4 SENSORS

The probe is equipped with a low-power air pressure and ambient temperature sensor MS5607, optional humidity sensor and a GPS receiver SIM28ML. A small passive 16x6 mm GPS ceramic antenna without any amplifier was used.

To minimize a power consumption, the GPS receiver power is gated by a MOSFET transistor. To reduce a time-to-fix a backup power input of the receiver is connected directly to the battery, this way the content of the receiver's RAM is preserved during the power off state avoiding cold-start condition after power on.

## 5 ENVIRONMENTAL PROTECTION

The assembled PCB was painted with a transparent nail polish to protect the probe from a humidity. Most of the components are designed to work down to -40 degrees Celsius, except the RF module which is supposed to work down to -20 degrees. However it proved to work well below this limit in the last year competition.

Due to a lack of time before the launch, the probe was not tested under low temperatures.

## 6 SOFTWARE

A firmware for the probe is written in a pure C language. To reduce a firmware size a libopenm3 - lightweight opensource library for STM32 microcontrollers - was used instead of the official ST library. To speed up the development and debugging, the unit tests were written for most of the non-hardware related code.

After the probe is powered on, the code initializes all the peripherals (RFM95, pressure and humidity sensors, GPS receiver), measures the air pressure, temperature and humidity and waits for a GPS fix. After the position fix is obtained or 30 seconds since boot elapsed the data are sent over LoRaWan (in ABP mode) and the MCU powers off all the peripherals, setups a wake up timer to 30 minutes and goes to a low power mode.

As the LoRaWan is using different frequencies across the world a simple georeferencing algorithm is used to determine a correct LoRaWan frequency from a current GPS position. Only 3 frequency regions were implemented - Europe (868 MHz), America (902 to 928 MHz) and Asia ( 920 to 923 MHz). A selection of the correct region is based on comparing current position with pre-programmed latitude and longitude ranges. In future versions a list of regions where LoRaWan usage is illegal (North Korea for example) should be made and taken into the consideration.

The whole design (all source codes and hardware design files) was released under a copyleft license GNU GPL 3 at [6].

### 6.1 PROBE TRACKING

The telemetry data received by the TTN are encoded as JSON and sent to a custom web server for further processing.

The code running on the server was written in PHP. The JSON data from TTN are parsed and stored in a SQLite database. To avoid tampering with the server a basic HTTP authorization is required. The data transferred between the TTN and the server are encrypted using an HTTPS protocol.

Additionally the server provides a simple tracking web page written in PHP. The probe position is drawn on map using `mapy.cz` and a javascript that processes the location data and draws lines and

points on the map. The tracking webpage is shown on Figure 2 and can be directly accessed at [bal.deadbadger.cz](http://bal.deadbadger.cz).

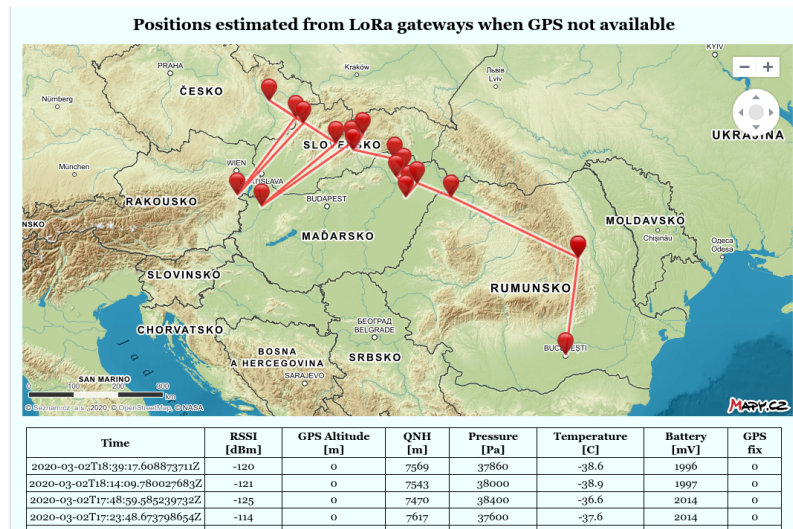


**Figure 2:** The probe tracking website

In case the GPS data are not valid the probe position can be estimated from metadata about the gateways that received the packet. Due to a lack of time only a simple averaging of latitudes and longitudes was implemented. For the next year a more precise localization based on received signal strength shall be developed.

## 7 THE COMPETITION

The final take off weight of the probe is 15.3 grams. It was launched on Monday 2nd of March 2020 at 10:15 UTC from Brno. The first few telemetry packets were lost due to issues with internet connection on the tracking server side. The first packet was captured at 11:49 at approximately 7 km above the ground with ambient temperature at -20 degrees Celsius. During the night the ambient temperature dropped to -41 degrees Celsius and the probe descended to the 5.5 km. The ambient air temperature is tightly coupled to the time of the day as can be seen on Figure 3.

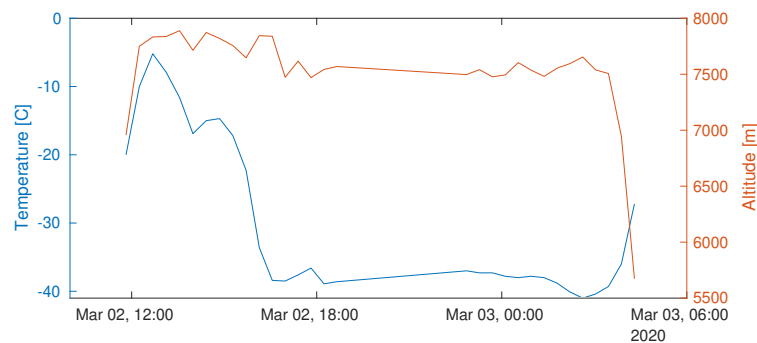


**Figure 3:** Temperature and altitude changes in time

The last packet was received at 4:18 UTC on 3rd of March 2020 after 18 hours of flight by station located in a Russian city Rostov on Don, over 1800 km from the launch site. Unfortunately due to a bug in the GPS code the georeferencing algorithm could not be used and the probe continued to transmit on the European frequencies instead of retuning to the Asian ones.

The battery was expected to last for about two weeks for estimated 5 seconds intervals needed to get a GPS fix. Due to the GPS issues prolonging the MCU power on period the runtime was severely reduced to approximately 2 and half days. Therefore even if the probe was still airborne it won't be alive when it flies over the Europe in reach of ground stations again.

Other probes using LoRaWan went silent similarly after leaving Europe (the gateways coverage over Russia is almost non-existent). To the date of writing this article (13th of March) the only probe alive is the one constructed by SP9UOB, the latest position known was above the Canada.

## 8 CONCLUSION

A probe weighting 15.3 g was built, it was sending telemetry for over 18 hours since the launch and it crossed distance over 1800 km before leaving a range of available ground stations. Due to a bug in the software the GPS module was not able to obtain any valid data, but the probe position was estimated from the ground stations that received the telemetry. At the time of writing this article the competition results were still not final, but the probes using the APRS were still responding after my probe went silent.

The battery powered probe proved to be working well. As the probe position can be estimated from the IoT network metadata, the battery powered probe with only a pressure sensor to fulfill the competition rules (approximate information about altitude required) can be used. Without a power hungry GPS receiver a runtime in range of several months should be achievable.

The LoRaWan IoT network proved to be a reliable solution for sending the telemetry. The longest distance on which the telemetry was successfully received was over 200 km.

## ACKNOWLEDGEMENT

The presented research was supported by the Internal Grant Agency of Brno University of Technology project no. FEKT-S-20-6526.

## REFERENCES

- [1] *PicoBalloon Challenge 2020* [online]. [cit. 2020-03-06]. Available from: <https://www.hvezdarna.cz/wp-content/uploads/picoBalloon-Challenge-2020.pdf>
- [2] *Master of High-Altitude Balloon Projects*, Bill Brown, WB8ELK [online]. [cit. 2020-03-06]. Available from: <http://www.arrl.org/files/file/QST/This\%20Month\%20in\%20QST/May2017/GLIFORT.pdf>
- [3] *The Things Network* [online]. [cit. 2020-03-13]. Available from: <https://www.thethingsnetwork.org/>
- [4] *Addressing and Activation: The Things Network* [online]. [cit. 2020-03-13]. Available from: <https://www.thethingsnetwork.org/docs/lorawan/addressing.html>
- [5] ZHU, Gaolong, Kechun WEN, Weiqiang LV, et al. Materials insights into low-temperature performances of lithium-ion batteries. *Journal of Power Sources* [online]. Elsevier B.V, 2015, 300, 29-40 [cit. 2020-03-13]. DOI: 10.1016/j.jpowsour.2015.09.056. ISSN 0378-7753.
- [6] *Picoballoon2020: Probe for Observatory and Planetarium Brno Picoballoon Challenge 2020* [online]. [cit. 2020-03-13]. Available from: <https://github.com/kajusK/Picoballoon2020>

# ENHANCEMENT OF AXIAL RATIO BANDWIDTH OF ANTENNA ARRAY BY PARASITIC PATCHES

**Jan Spurek**

Doctoral Degree Programme (4), FEEC BUT

E-mail: xspure01@stud.feec.vutbr.cz

Supervised by: Zbynek Raida

E-mail: raida@feec.vutbr.cz

**Abstract:** This paper summarizes the concept of a circularly polarized antenna array fitted with parasitic patches to increase its axial ratio bandwidth and compares the results of simulations and measurements taken on a reference antenna array. The measurements show a good agreement with the simulations and confirm validity of the proposed technique.

**Keywords:** circular polarization, axial ratio bandwidth, parasitic patches, antenna array

## 1 INTRODUCTION

Today's communication technologies are characterized by increasing data rates, which brings higher demands on bandwidth of systems and the antennas. Their bandwidth is a limiting factor, especially in case of circularly polarized antennas, which often do not offer very high axial ratio bandwidth since the required conditions to generate a circularly polarized wave are typically met only in a narrow interval of wavelengths. To address the needs, we propose to utilize parasitic patches to enhance this property of circularly polarized antennas [2], [3].

Parasitic patches are typically planar structures that are placed in the vicinity of the radiating elements of the antenna. In our proposal, the patches are placed above the radiating elements of an antenna array, in a defined distance (see Figure 1). A dielectric substrate is used as the carrier material for the parasitic patches. Phase shift and coupling between the parasitic patches and the radiating elements help to equalize the magnitude of the rotating electric field intensity vector and thus improve the axial ratio bandwidth.

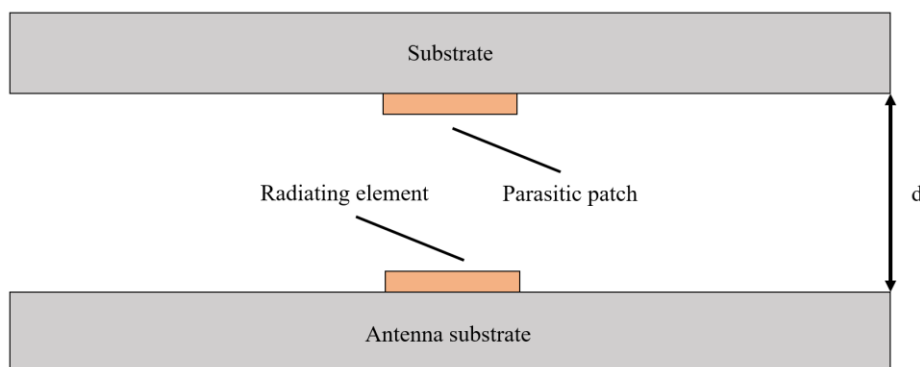


**Figure 1:** Parasitic patch placed above the radiating element in a defined distance

## 2 REFERENCE ANTENNA ARRAY

A reference circularly polarized antenna array with known and verified properties was used to validate the concept [1] (see Figure 2). It consists of four rectangular patches that are organized into a 2x2 matrix to which the power is provided by substrate integrated waveguide network embedded in

two layers of ARLON Cuclad 217LX substrate with the thickness of 1.54 mm [4]. Coupling slots are used as transitions between the layers. The array is designed to work at the center frequency of 17 GHz. In the design there are already applied the existing techniques to extend axial ratio bandwidth [5], [6].

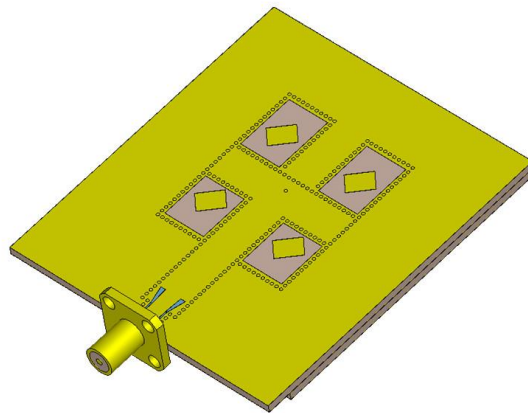


**Figure 2:** Reference antenna array

### 3 ADDITION OF THE PARASITIC PATCHES

The reference antenna array was extended with a 2x2 matrix of parasitic patches that have the same shape, orientation and horizontal placement as the radiating patches (see Figure 3). Since the substrate on which the parasitic patches are placed serves only as the carrier, air-like properties are desired. Due to this reason ARLON FoamClad of 1.88 mm height with the dielectric constant  $\epsilon_r = 1.25$  was chosen. Optimizations indicated that the structure has the best performance if the carrier substrate is 5.65 mm thick (three stacked layers) and the distance between the parasitic and radiating patches is 3 mm. The distance between the patches was identified as the main parameter to influence the axial ratio properties of the array.

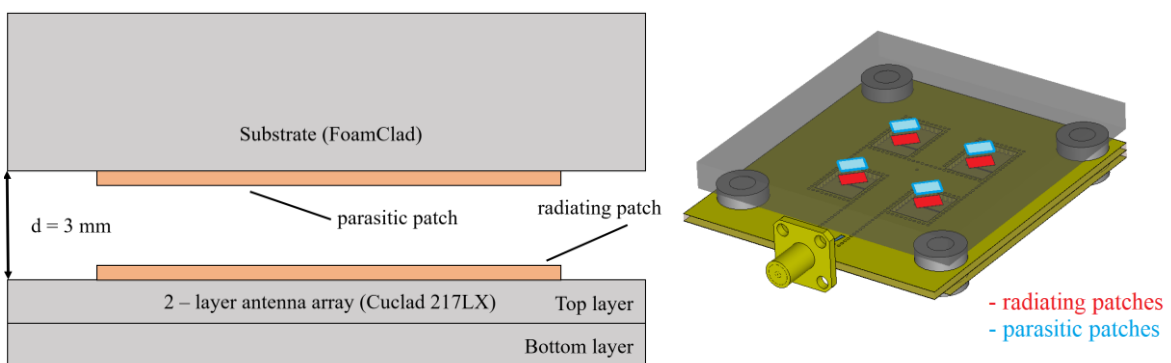


**Figure 3:** Side view (left) and complete view (right) on the organization of the antenna array fitted with the parasitic patches

### 4 SIMULATION RESULTS

The numerical models were simulated in CST Microwave Studio. Figure 4 depicts the comparison of axial ratio frequency responses taken in the main lobe direction. Considering the condition  $|AR| < 3\text{dB}$ , the axial ratio bandwidth is 16.45 GHz to 17.59 GHz (1.14 GHz, 6.7% relatively) in case of the reference antenna array and 16.56 GHz to 19.40 GHz (2.84 GHz, 16.7% relatively) in case of

the reference antenna array fitted with the parasitic patches. Addition of the parasitic structure therefore improves the axial bandwidth by approximately 1.7 GHz (10% relatively).

In Figure 5 are shown E-field distributions in the vicinity of the radiating and parasitic patch at 17 GHz that illustrate the phase shift between them.

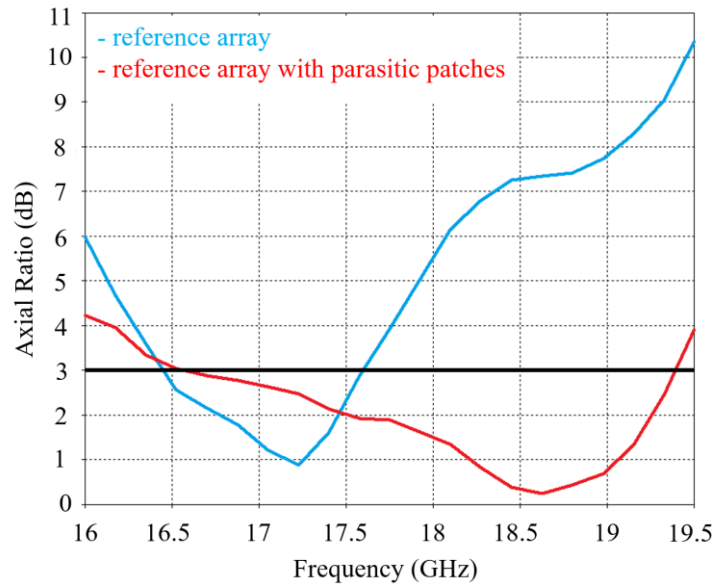


**Figure 4:** Comparison of frequency responses of axial ratio for the original array and array fitted with the parasitic patches

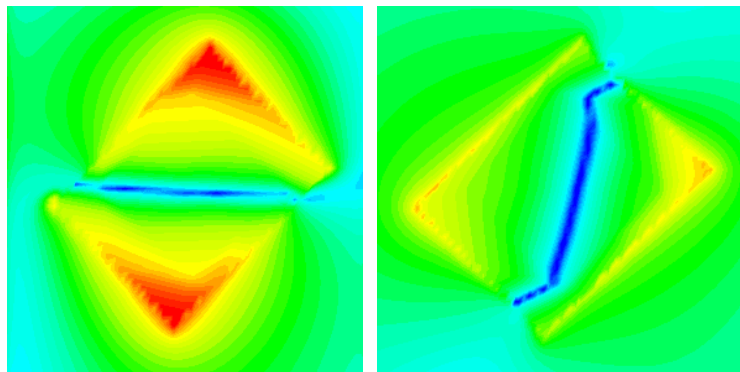


**Figure 5:** E-field distributions in the vicinity of the radiating (left) and parasitic (right) patch at 17 GHz

## 5 MEASURED RESULTS

In the next step, the structure was manufactured so the properties could be verified by measurements. In contrast to the numerical model, the manufactured array has imperfections. The SMA connector is not optimally soldered and the parasitic structure is prone to deformation due to pliable carrier substrate, resulting in creation of airgaps between the stacked layers of the carrier substrate. The distance between the parasitic and radiating patches is not constant – by simulations indicated as critical for the performance of the array (see Figure 6 and Figure 7). It is therefore expected that the measured properties will show certain degradation in comparison to the simulated results.



**Figure 6:** Manufactured antenna array fitted with the parasitic structure – top view



**Figure 7:** Manufactured antenna array fitted with the parasitic structure – side view

Figure 8 depicts comparison of axial ratio frequency responses of the simulated and measured antenna array with the parasitic patches. The results show a good match. There is an offset added to the measured line, a degradation caused by manufacturing imperfections. As an attempt to remove the airgaps between the stacked layers of the carrier substrate, the layers were glued together using 3M 467MP 200MP adhesive. Partial improvement has been achieved by this modification.

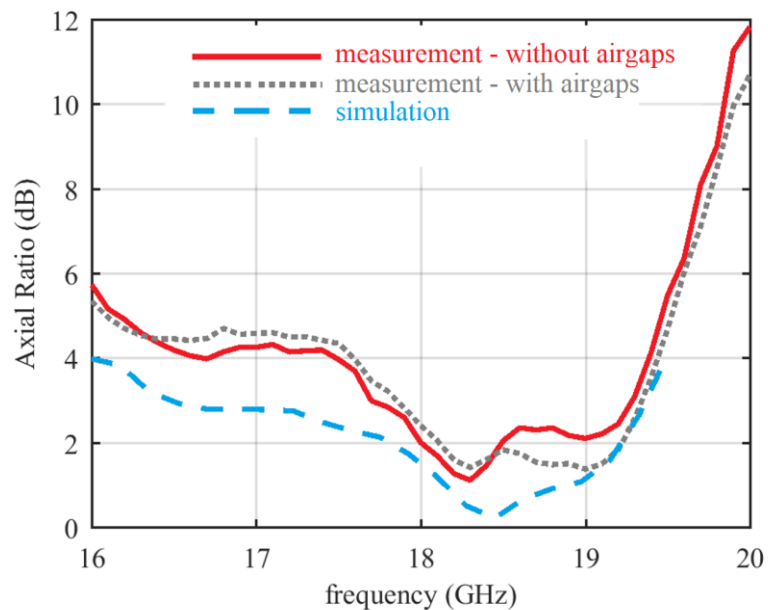


**Figure 8:** Comparison of axial ratio frequency responses of the simulated and measured array

## 6 CONCLUSION

The paper summarizes the concept of parasitic patches as a structure that can be used to increase the axial ratio bandwidth of circularly polarized antenna arrays. A reference antenna array was used to verify the proposed technique where the simulations show increase in axial ratio bandwidth from 6.7% to 16.7% relatively when the parasitic structure is added. The simulations and measurements show an agreement.

Research indicates that improvement of the manufacturing technique is needed to provide better precision and prevent degradation of the antenna performance, focusing mainly on maintaining constant distance between the radiating and parasitic elements.

## ACKNOWLEDGEMENT

The presented research was supported by the Internal Grant Agency of Brno University of Technology project no. FEKT-S-20-6526.

## REFERENCES

- [1] SPUREK, Jan and Zbynek RAIDA. Circularly polarized modular patch antenna array fed by substrate integrated waveguide. *Microwave and Optical Technology Letters* [online]. 2018, 60(6), 1398-1403 [cit. 2020-03-10]. DOI: 10.1002/mop.31173. ISSN 08952477. Available at: <http://doi.wiley.com/10.1002/mop.31173>
- [2] SPUREK, Jan and Zbynek RAIDA. Realization of circularly polarized antenna array with parasitic patches. In: 2019 IEEE-APS Topical Conference on Antennas and Propagation in Wireless Communications (APWC) [online]. IEEE, 2019, 2019, pp. 239-242 [cit. 2020-03-24]. DOI: 10.1109/APWC.2019.8870419. ISBN 978-1-7281-0566-6. Available at: <https://ieeexplore.ieee.org/document/8870419/>
- [3] SPUREK, Jan and Zbynek RAIDA. Extending axial ratio bandwidth of antenna array by parasitic patches. In: 2018 22nd International Microwave and Radar Conference (MIKON) [online]. IEEE, 2018, 2018, pp. 357-359 [cit. 2020-03-24]. DOI: 10.23919/MIKON.2018.8405224. ISBN 978-83-949421-1-3. Available at: <https://ieeexplore.ieee.org/document/8405224>
- [4] POZAR, David M. *Microwave engineering*. 4th ed. Hoboken, NJ: Wiley, c2012. ISBN 978-0470631553.
- [5] LI, Yue, Zhi Ning CHEN, Xianming QING, Zhijun ZHANG, Junfeng XU and Zhenghe FENG. Axial Ratio Bandwidth Enhancement of 60-GHz Substrate Integrated Waveguide-Fed Circularly Polarized LTCC Antenna Array. *IEEE Transactions on Antennas and Propagation* [online]. 2012, 60(10), 4619-4626 [cit. 2020-03-10]. DOI: 10.1109/TAP.2012.2207343. ISSN 0018-926X. Available at: <http://ieeexplore.ieee.org/document/6236079/>
- [6] SPUREK, Jan, Jan VELIM, Miroslav CUPAL, Zbynek RAIDA, Jan PRASEK and Jaromir HUBALEK. Slot loop antennas printed on 3D textile substrate. In: 2016 21st International Conference on Microwave, Radar and Wireless Communications (MIKON) [online]. IEEE, 2016, 2016, s. 1-3 [cit. 2020-03-10]. DOI: 10.1109/MIKON.2016.7492085. ISBN 978-1-5090-2214-4. Available at: <http://ieeexplore.ieee.org/document/7492085/>

# UNIVERSAL POWER SEQUENCER FOR RF POWER AMPLIFIERS

**Miroslav Waldecker**

Doctoral Degree Programme (2), FEEC BUT

E-mail: xwalde01@stud.feec.vutbr.cz

Supervised by: Roman Maršálek

E-mail: marsaler@feec.vutbr.cz

**Abstract:** More often used Gallium Nitride (GaN) based Radio-Frequency high power transistors in the various RF PA configurations e.g. Doherty is by their nature easily destroyed, great care must be taken, when powering-up and shutting down this circuits. That means, proper power biasing and sequencing is necessary. The Doherty type RF PA with RF drivers four different gate, drain voltages and time when the individual voltages are turned on or off must be controled. Universal power sequencer and biasing device, which meets this requirements is described in this article.

**Keywords:** GaN, RF PA, Biasing, Power Sequencing

## 1 INTRODUCTION

Emerging 5G technologies promising greener, environmentaly friendly technologies with demand for higher bandwidths by introducing massive multiple - input - multiple output (MIMO), beamforming, small cells techniques, while network should be as much energy efficient as possible. To achieve this goals special care must be taken for radiofrequency power amplifiers (RF PA). Nowadays, promissing technology for RF PAs power transistors are Gallium Nitride types - an effiecient, wide band-gap transistors, offering supperior properties e.g. power density, power added efficiency (PAE), gain, impedance matching and so on. Common techniques to achieve higher efficiency is to push bias point closer to saturation region in combination with some kind of predistorting technique due to non-linear behavior of the transistor in this region. This require intensive measurements and tests of the power amplifiers and predistorters, with many on-off cycles. Power transistors in the RF PAs are very sensitive devices and require special care, particularly GaN devices are very sensitive, because they are opend, when  $V_{GATE}$  is equal zero.

Recommended power sequence for correct turn on sequence is shown in fig. 1 a), where is very important to turn on drain voltage ( $V_{drain}$ ) after gate voltage ( $V_{pinch}$ ) is applied and stable. Than is bias gate voltafe set. Power sequence for correct turn off sequence is shown in fig. 1 b).

Commercial solution is either using of several power supplies with triggering option or using multichannel programmable power supply with possibility of the power sequencing e.g Keysight [2] or Rohde & Schwarz [1]. This solutions are expensive for such problem, so cheaper alternative with use of the shelf power supply is introduced, which is able to automatically and correctly cycle thru this sequencing is introduced. Commercial product of this type is not known in the time of writing this paper. Nowadays are often used and investigated various structures for RF PA and one of them is Doherty structure consisting pair of output the power transistors and often pair of the driver transistors and therefor four channel sequencer is necessary, with need of synchronized outputs. Brief simplified schematic is schown in fig. 2.

Proposed RF PA power sequencer should have this properties.

- Four channel output

- Gate voltages generated internally, it is highly recommended to set pinch off voltage, and after drain voltage set, bias gate voltage
- Possibility to set up all parameters, e.g. pinch off voltage, gate voltage, drain on-off time, gate time directly on the sequencer
- Able to switch drain voltage up to 60V with current at least 10A.
- Internally generated gate voltage  $\pm 10V$
- Basic fault sensing
- As compact as possible
- Cheaper than commercial programmable power supplies

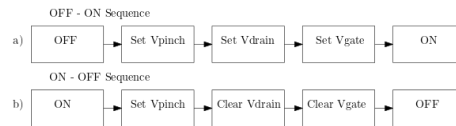


**Figure 1:** a) Recommended turn on sequence b) Recommended turn off sequence

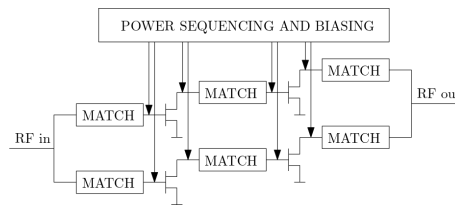


**Figure 2:** Connecting sequencer to RF Power Amplifier

## 2 IMPLEMENTATION

Block diagram of the proposed fig. 2 consist main microcontroller, in this case ARM Cortex M4 by NXP semiconductor, MK64FN1, which is controlling whole system, to which is connected rotary encoder for data input and setup sequence according to requirements, TFT display with internal driver for displaying status of the sequencer, setted values e.g. pinch off voltage, gate voltage, time delays and which channel is enabled or disabled, and realtime measured voltages of the gate, drain in voltage and drain out voltage. Next, microcontroller is responsible for correctly controlling quad channel modules CH1 - CH4. Signal  $V_{drainON}$  is turning in P-MOSFET transistor for drain voltage. This is supplied from external source and is only monitored by internal analog to digital converted (ADC), where are connected monitoring signals  $V_{DinMonitor}$  and  $V_{DoutMonitor}$ . Gate and pinch-off voltage is generated internally, because pinch-off and gate biasing voltages are generally different. Digital to analog converter (DAC) in the channel modules is used for this purpose and is controlled via SPI bus from microcontroller. Gate voltage is enabled with signal  $V_{GateON}$  and is monitored by ADC measuring signal  $V_{GateMonitor}$ . Start and Stop sequence are triggered by separated push buttons located at the front panel of the power sequencer.

More detailed block diagram of the circuitry if one of the channels, which is the same for all of them, is shown in fig. 4. Drain voltage is switched by P-MOSFET power transistor. Parameters of this transistor are crucial for this operation. On behalf of required switching current, transistor should be able to swith at least 10A current and have as low  $R_{DSON}$  as possible. Firstly due to minimizing termal loss and secondly for keep voltage drop between  $V_{Din}$  and  $V_{Dout}$  as low as possible. Gate driver for this transistor is causing correct switching characteristics of the transistor and level shift from 3.3V

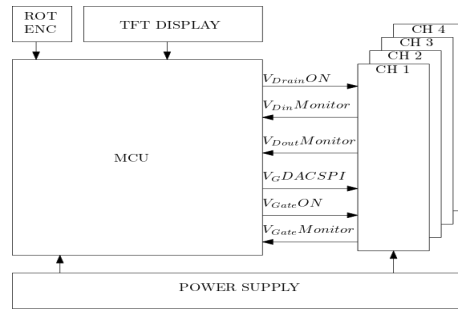


**Figure 3:** Block diagram of the sequencer

logic of the microcontroller. Sensing drain voltages are done by attenuation, filtering, buffering by operational amplifiers, filtered by anti-aliasing filters and then fed into internal ADC channels of the microcontroller. Gate voltage is generated by digital to analog converter located as close as possible to output terminals, driven by SPI interface from microcontroller. Used DAC is Texas Instruments DAC8811, one channel DAC with resolution of 16bit and current output, which is transformed into bipolar voltage  $\pm 10V$ , then filtered and fed into high power operational amplifier OPA453, with shutdown option. Generated gate voltage is monitored and fed back after attenuation, buffering and filtering to microcontroller's ADC. Channel modules are implemented on the separated printed circuit boards (PCB) and are located as close as possible to output terminals. Prototype realization is shown in fig. 5, where is visible channel terminals on the bottom, START, STOP push-buttons on the right, rotary encoder between push-buttons and TFT display, and TFT display. Display is showing current state of the sequencer (idle state on the picture), parameters legend, values set by user and realtime measured voltages on the sequencer terminals. Output set voltages error is shown in fig. 6. Accuracy of the output voltage is well within range of  $\pm 0.0001\%$

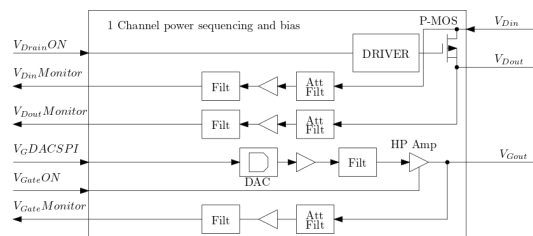


**Figure 4:** Block diagram of one channel of the sequencer

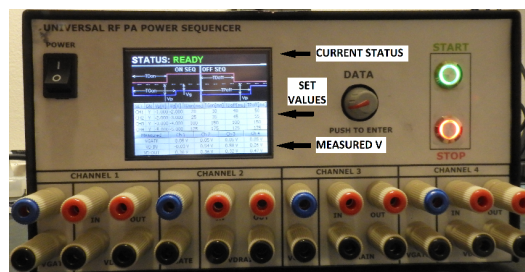


**Figure 5:** RF Power sequencer prototype

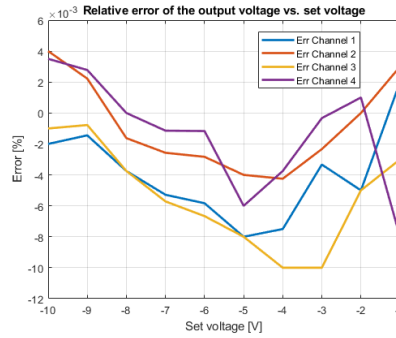


**Figure 6:** Output voltage relative error vs. set voltage

### 3 SOFTWARE IMPLEMENTATION

There are two main parts implemented in the software of the power sequencer. First part is setup parameters. By holding encoders push-button for at least 3 seconds, sequencer enters setup device, where is possible to set these parameters:

- Active channel - enables - disables current channel. Necessary for operation with fewer channels.
- Pinch-off voltage  $V_p$
- Biasing gate voltage  $V_g$
- Time to switch on drain voltage  $T_{Don}$
- Time to switch gate bias voltage  $T_{Gon}$
- Time to switch drain voltage off  $T_{Doff}$
- Tme to switch pinch-off gate voltage  $T_{Poff}$

Second part of the software is main control loop, which is best described by flow-diagram in fig. 7. After power up, sequencer immediately enter idle mode, when gate and drain voltages are turned off, which is shown on the display as STATUS: READY and is waiting for triggering start sequence by START button or activating setup menu by pressing and holding down rotary encoder knob. Firstly are checked all voltages on the enabled channels. If exist voltage failure there, e.g. drain voltage not present, this cause fault message and it is restricted to continue in the sequence. After correct voltage check, pinch-off voltage is set by DAC which is also monitored (in case there is no voltage in the gate terminals, fault is generated and sequence is interrupted) and sequencer is waiting  $T_d$  ms to turn on, which follows setting up biasing gate voltage after  $T_g$  ms. Correct operation and successful sequence is shown on the display as STATUS: RUNNING. Now, sequencer constantly checking voltages on the terminals and in case, there is problem e.g. difference between set and measured gate voltage, drain voltage missing, immediatelly is state interrupted. This means as soon as possible is switched off drain voltage and after  $T_{goff}$  gate voltage. Other way, sequencer is waiting for stop sequence trigger caused by STOP button. After STOP button is hitted gate voltage is set to pinch-off voltage, than waits  $T_{Doff}$  ms to switch off drain voltage and after  $T_{pinch}$  ms is switched off gate voltage also. Then sequencer enters IDLE mode.

Output voltage waveforms of the start sequence and stop sequence are shown in fig. 8 for two channels, where yellow trace is gate voltage, green trace is drain voltage of channel 1, blue trace gate voltage and magenta drain voltage of the channel 2.

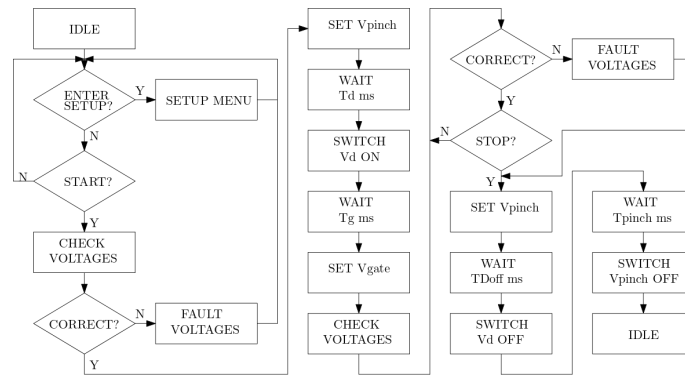


**Figure 7:** Flow diagram of the sequencer



**Figure 8:** Measured start (left) and stop (right) sequence

## 4 CONCLUSION

Prototype of the power sequencer was built and it turn out, that it is very valuable device during designing and testing of the various kind of RF power amplifiers and predistorters, mostly for ease of the GaN transistors to be destroyed and ability to set various biasing parameters during development.

## ACKNOWLEDGEMENT

I would like to thank prof. Roman Maršálek for valuable comments and advices. The research was financially supported by the FEKT-S-20-6325.

## REFERENCES

- [1] Keysight.com. 2020. [online] Available at: <[https://scdn.rohde-schwarz.com/ur/pws/dl\\_downloads/dl\\_common\\_library/dl\\_brochures\\_and\\_datasheets/pdf\\_1/NGP800\\_dat\\_en\\_3609-1927-32\\_v0100.pdf](https://scdn.rohde-schwarz.com/ur/pws/dl_downloads/dl_common_library/dl_brochures_and_datasheets/pdf_1/NGP800_dat_en_3609-1927-32_v0100.pdf)> [Accessed 12 January 2020].
- [2] Keysight.com. 2020. [online] Available at: <<https://www.keysight.com/zz/en/assets/7018-05460/data-sheets/5992-1880.pdf>> [Accessed 12 January 2020].

# DEEP LEARNING FOR MAGNETIC RESONANCE SPECTROSCOPY QUANTIFICATION: A TIME-FREQUENCY ANALYSIS APPROACH

**Amirmohammad Shamaei**

Doctoral Degree Programme (1st year at FEEC BUT), Czech Academy of Sciences, Institute of Scientific Instruments

E-mail: [amirshamaei@isibrno.cz](mailto:amirshamaei@isibrno.cz)

Supervised by: Radovan Jiřík, Jana Starčuková

E-mail: [jirik@feec.vutbr.cz](mailto:jirik@feec.vutbr.cz); [jana@isibrno.cz](mailto:jana@isibrno.cz)

**Abstract:** Magnetic resonance spectroscopy (MRS) is a technique capable of detecting chemical compounds from localized volumes in living tissues. Quantification of MRS signals is required for obtaining the metabolite concentrations of the tissue under investigation. However, reliable quantification of MRS is difficult. Recently deep learning (DL) has been used for metabolite quantification of MRS signals in the frequency domain. In another study, it was shown that DL in combination with time-frequency analysis could be used for artifact detection in MRS. In this study, we verify the hypothesis that DL in combination with time-frequency analysis can also be used for metabolite quantification and yields results more robust than DL trained with MR signals in the frequency domain. We used the complex matrix of absolute wavelet coefficients (WC) for the time-frequency representation of the signal, and convolutional neural network (CNN) implementation for DL. The comparison with DL used for quantification of data in the frequency domain is presented.

**Keywords:** magnetic resonance spectroscopy; quantification; deep learning; machine learning;

## 1 INTRODUCTION

Magnetic Resonance Spectroscopy (MRS) has attracted the MR community over the past 7 decades [1]. A significant part of the interest in biomedical MRS stems from the possibility of noninvasive measurements of metabolites. Information about tissue metabolites can help in clinical diagnostics. For example, detection of metabolic pathway changes may facilitate diagnosing disease in earlier stages before anatomy changes can be observed [1], [2], and thus enable more efficient treatment. E.g., in glioma, a decrease of N-acetylaspartate (NAA) and creatine concentrations of NAA and creatine and an increase of choline, lipids, and lactate predicts an increase of the glioma grade. To reach such a goal, at first, we need to quantify metabolic concentrations. Because there are many obstacles to reaching an accurate estimate of the metabolite concentrations, the use of MRS in daily clinical practice is still not common. The existing MRS quantitation methods are based on model fitting of a signal either in the time or the frequency domain [3]. Even though, in theory there is no difference in which domain is used for fitting, the reality in practice could be different.

Deep learning has achieved many accomplishments in a wide range of tasks, including the MRI field [4]. Due to the poor signal-to-noise ratio (SNR), chemical shift displacement, and overlapping of signal components of the MRS signal, deep learning can be a useful tool. Recently, Hatami et al. showed the first step in this area by using the deep learning approach for MRS signal quantification [5]. Kim et al. conducted a comprehensive study on brain metabolite quantification using deep learning [6]. The input of both studies is a signal in the frequency domain (metabolite spectra), and their network is a 1D convolutional neural network (CNN). As we mentioned earlier, there are differences between time and frequency domain quantification in practice. Be a case in point, elimination of the first few distorted data points of a signal in the time domain does not significantly dis-

turb the time-domain analysis, whereas the missing time-domain data points can result in complicated modulations throughout the entire spectrum [2]. To overcome the difficulties of the signal analysis in a single domain, time-frequency analysis has been carried out for decades in other areas [4]. Nevertheless, finding an accurate tool for the time-frequency analysis is fraught with difficulty. Here is where deep learning comes to play. Thomas et al. constructed time-frequency images of a speech signal and used them as an input to a CNN for classification [7]. Kyathanahally et al. learned a CNN with time-frequency data to detect and remove ghosting artifacts in clinical magnetic resonance spectra of human brain [8]. Given the mentioned accomplishments of deep learning and time-frequency analysis in a variety of different areas, in particular in MRS for signal artifacts detection, this paper describes to our knowledge the first attempt to use this state-of-the-art technique to quantify MRS signal by deep learning and time-frequency analysis. First, we generate simulated MRS signals. Second, we transform the signals to the time-frequency representation. Third, we train a CNN with the new time-frequency representation. Finally, the result is compared with the previous study.

## 2 METHODS

A framework is created to generate MRS signals with different amplitudes, damping factors, and frequency shifts. Second, these one-dimensional signals are transformed into their two-dimensional time-frequency representation using wavelet transformation (WT). Finally, the data are split into two datasets, the training and testing datasets. The input of the CNN is the time-frequency representation of signals, and the output is 21 values, which are the concentration-related amplitudes of 20 metabolites and the amplitude of the background signal. The CNN is trained with a training dataset of signals of known amplitudes. Then, the trained CNN is used to estimate the metabolite amplitudes of the test dataset. Finally, the techniques for accuracy evaluation are used.

### 2.1 SIGNAL GENERATION

Deep learning approaches need a considerable amount of data. For this purpose, we need a basis set (metabolite signals with known concentrations) either simulated or acquired. To be able to compare our results with the previous studies [5], [9], we used the same simulated basis set as used in those studies, i.e., the basis set provided for the ISMRM challenge 2016 [10]. The MRS signal is defined as a combination of amplitude-scaled phase-shifted metabolite basis set signals, the baseline and noise (in this study we use a noiseless signal). The mathematical model for the parametric part of the MRS signal is given by:

$$S[n] = \left[ \sum_{m=1}^M A_m \cdot X_m[n] \cdot e^{(\Delta\alpha_m + 2i\pi\Delta f_m n\Delta T)} \right] + A_{MM} \cdot MM[n] \cdot e^{(\Delta\alpha_{MM} + 2i\pi\Delta f_{MM} n\Delta T)} \quad (1)$$

where  $X_m[n]$  is the  $n$ -th sample of the  $m$ -th simulated metabolite,  $\Delta T$  is a sampling period,  $A_m$  is the scaling factor of the metabolite ( $A_m \cdot X_m[0]$  is an indication of the metabolite concentration),  $\Delta\alpha_m$  is the damping factor,  $\Delta f_m$  is the frequency shift of the  $m$ -th metabolite, and  $M$  is the number of metabolites. For our signal simulation the values of the amplitude, damping, and frequency shift are chosen randomly from a defined range with a uniform distribution ( $A = [0, 1]$ ,  $\Delta\alpha = [-10, 10]$  and  $\Delta f = [-10, 10]$ ). The known background signal  $MM$  is considered as another metabolite, then is added to  $S[n]$  with a random scaling factor, damping, and frequency shift ( $A_{MM}$ ,  $\Delta\alpha_{MM}$  and  $\Delta f_{MM}$ ). Ten thousand signals are generated, in which the process of value selection is entirely random, thus preventing any bias to our train dataset. The basis set used was simulated for sequence PRESS, magnetic field 3T, echo time  $TE = 30$  ms, spectrum width  $SW = 4000$  Hz, and 2048 time-domain samples.

## 2.2 SIGNAL PROCESSING

The time-frequency representation of the 1D signal shows a signal in both the time and frequency domain simultaneously. One of the forms of the time-frequency representation of the signal is a scalogram (a matrix of absolute values of the continuous wavelet coefficients (CWC) of a signal ) that can be plot as a function of time and frequency. The scalogram is calculated using the Matlab Wavelet Toolbox (R2019a, Mathworks Inc.,Natick, MA, USA). We use Morse wavelet to compute the CWC. The last 512 points of the time signals are cut off to reduce the amount of computation for the CWC calculation. The selection of the number of points was decided by visual inspection of the signals to ensure that no significant information will be lost. The wavelet coefficients are computed. The minimum and maximum scales are determined automatically based on the energy spread of the wavelet in frequency and time by the toolbox. The coefficients matrix is a matrix where each row corresponds to one scale, and its column size is equal to the length of signal. Scalogram with 340 frequency bins and 1536 time points ( $340 \times 1536$  matrix) is created. Finally, the real and imaginary parts of 10000 matrices are stored in two channels.

## 2.3 CNN

A convolutional neural network is developed using the Matlab Deep Learning Toolbox (R2019a, Mathworks Inc.,Natick, MA, USA) on NVIDIA GTX 1050Ti graphics processing units. The architecture of the CNN is shown in Fig. 1 . This network includes one input layer with two channels, six convolutional layers, five max pool layers, and one regression layer. Rectified linear unit (ReLU) activation functions are used between CL and MP layers. The mean square error is implemented as the loss function. The output of regression layer is 21 parameters which correspond to twenty metabolites and one background MM. Using these parameters and Eq (1), the estimated signal is reconstructed.

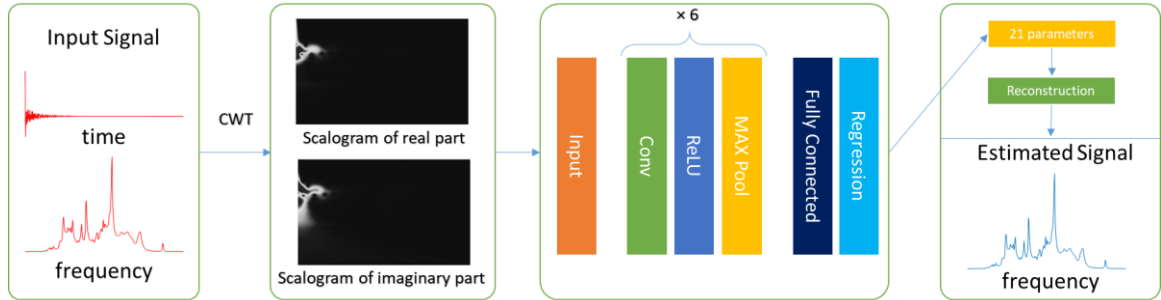


**Figure 1:** A schematic of the proposed approach. The generated signal based on a linear combination of metabolites basis sets is converted to two gray Scalogram images (real and imaginary). These images feed to CNN as inputs. The CNN includes 6 blocks, which comprise a Convolutional, Rectifier and Max-pooling layer. The last layers are a fully connected and a regression layer (which has 21 outputs). The estimated signal is reconstructed with the estimated parameters.

## 2.4 ACCURACY EVALUATION

Two methods are used to measure the accuracy of the model. First, the mean absolute error, which is the most straightforward regression error metric. MAE is defined as below for each metabolite:

$$MAE[m] = \frac{1}{N} \sum_{n=1}^N |A_{mn} - A'_{mn}| \quad (2)$$

where  $m$ ,  $N$ ,  $A$ , and  $A'$  are the metabolite index, the number of test datasets, the ground truth, and the estimated amplitude, respectively. The second method is the Symmetric mean absolute percentage error (SMAPE) which is given by:

$$\text{SMAPE}[m] = \frac{\sum_{n=1}^N |A_{mn} - A'_{mn}|}{\sum_{n=1}^N |A_{mn} + A'_{mn}|} \quad (3)$$

## 2.5 RESULTS

The dataset is separated into two datasets, namely a training dataset and a test dataset. The training dataset contains 80% of the data and the remaining 20% are the test dataset. CNNs with different hyperparameters such as minimum batch size, initial learning rate, and validation frequency are tested, and the CNN with the best result is chosen. The minimum batch size, initial learning rate, and validation frequency are 30, 1e-5, and 10, respectively. It has been shown that increasing the training sample would decrease the value of loss function [5]. Nonetheless, to be able to compare results obtained with our new approach (DL with time-frequency domain input) with the results of the Hatami et al approach (DL with frequency domain input) in a reasonable time, we decided to use only 10000 samples for CNN training and testing. Training and validation loss for the given dataset are 0.18 and 0.23, respectively.

Fig. 2 shows one of the tested (ground truth) signal, its estimate, and residual. The following conclusions may be drawn from this figure. First, the method used is able to estimate the tested signal. Second, residuals mainly occur when the signal shows rapid fluctuation.

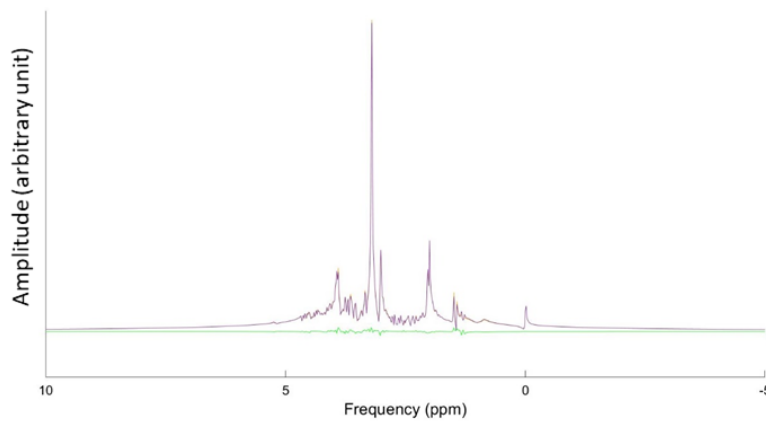


**Figure 2:** Example of the signal estimation – ground truth signal (orange), estimated signal (violet) and residual signal (green).

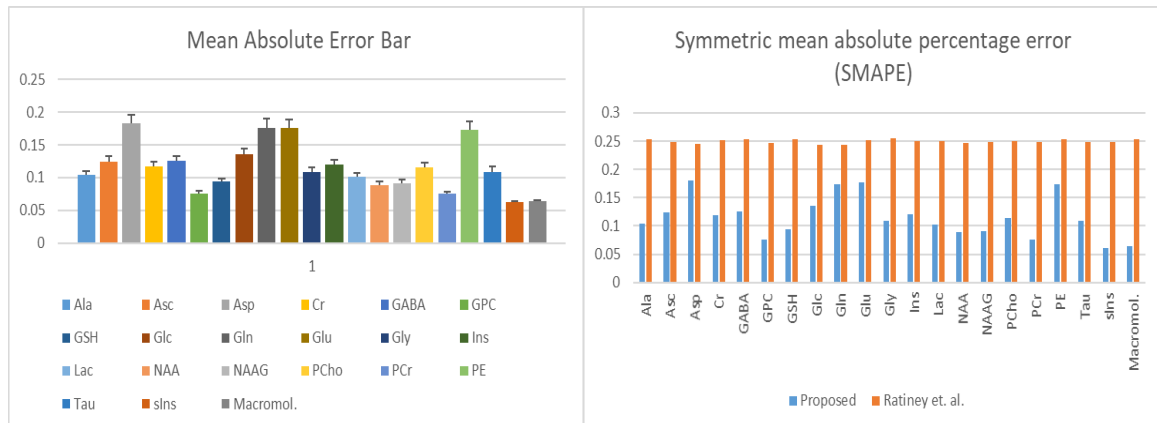


**Figure 3:** (left) Mean absolute error bar of every metabolite and its variance. (right) The symmetric mean absolute percentage error of each metabolite for (blue) our study (orange) Hatami et al.[5]

The mean absolute errors (MAE) of metabolites are shown in Fig. 3 (left). Even though the amount of error is not too low compared to the amplitude range ([0, 1]), the variance of the error is small. Fig. 3 (right) shows the comparison of the Symmetric mean absolute percentage error (SMAPE) between our approach and Hatami et al. approach. To avoid any bias in comparison, we used

the CNN described in this study and train it with our training set but in one case in the form of scalogram and in the other case (Hatami et al.) with the data in the frequency domain. The proposed approach shows less amount of error compared to their method.

### 3 CONCLUSION

Quantification of MRS is an important topic where a robust and universal panacea approach to quantify signals is needed. It was shown in this study that time-frequency deep learning quantification could outperform single domain quantification used in the previous studies [2, 5] and hopefully as a method using information from both MRS domains be successfully used also for quantification of signals with artifact patterns [8]. The next steps may be to verify the tested approach on 1) the simulated noisy MRS with different signal-to-noise-ratios and for different pulse sequences 2) on real MRS acquired from a phantom, 3) on MRS acquired from a rat, and 4) to implement this approach as a plugin in the jMRUI software package [11].

### ACKNOWLEDGEMENT

This research was supported by European Union's Horizon 2020 research and innovation program under the Marie Skłodowska-Curie grant agreement No 813120 (INSPIRE-MED).

### REFERENCES

- [1] M. Van Der Graaf, "In vivo magnetic resonance spectroscopy: Basic methodology and clinical applications," *Eur. Biophys. J.*, vol. 39, no. 4, pp. 527–540, 2010.
- [2] Robin A. de Graaf, "In Vivo NMR Spectroscopy," *In Vivo NMR Spectroscopy*. pp. 1–42, 13-Feb-2019.
- [3] J. B. Poulet, D. M. Sima, and S. Van Huffel, "MRS signal quantitation: A review of time- and frequency-domain methods," *J. Magn. Reson.*, vol. 195, no. 2, pp. 134–144, 2008.
- [4] H. Alaskar, "Deep Learning-Based Model Architecture for Time-Frequency Images Analysis," no. January 2018, 2019.
- [5] N. Hatami, B. Lyon, and U. Etienne, "Magnetic Resonance Spectroscopy Quantification using Deep Learning," 2018.
- [6] H. H. Lee, "Intact metabolite spectrum mining by deep learning in proton magnetic resonance spectroscopy of the brain," no. January, pp. 33–48, 2019.
- [7] S. Thomas, S. Ganapathy, G. Saon, and H. Soltau, "Analyzing convolutional neural networks for speech activity detection in mismatched acoustic conditions," in *ICASSP, IEEE International Conference on Acoustics, Speech and Signal Processing - Proceedings*, 2014, pp. 2519–2523.
- [8] R. Kreis and S. P. Kyathanahally, "Deep Learning Approaches for Detection and Removal of Ghosting Artifacts in MR Spectroscopy," vol. 863, pp. 851–863, 2018.
- [9] D. Das, E. Coello, R. F. Schulte, and B. H. Menze, "Quantification of Metabolites in Magnetic Resonance Spectroscopic Imaging Using Machine Learning," vol. 3, pp. 462–469, 2017.
- [10] ISMRM, "MRS Fitting Challenge (ismrm.org/workshops/Spectroscopy16/mrs\_fitting\_challenge/)," 2016. [Online]. Available: [ismrm.org/workshops/Spectroscopy16/mrs\\_fitting\\_challenge/](http://ismrm.org/workshops/Spectroscopy16/mrs_fitting_challenge/).
- [11] D. Stefan *et al.*, "Quantitation of magnetic resonance spectroscopy signals: The jMRUI software package," *Meas. Sci. Technol.*, vol. 20, no. 10, 2009.

# RECONSTRUCTION OF NON-UNIFORMLY SAMPLED SIGNALS USING GERCHBERG-PAPOULIS METHOD

**Ondrej Mihálik**

Doctoral Degree Programme (1), FEEC BUT

E-mail: xmihal06@stud.feec.vutbr.cz

Supervised by: Petr Fiedler

E-mail: fiedlerp@feec.vutbr.cz

**Abstract:** Analysis of non-uniformly sampled signals is often severely limited, since most signal processing methods rely on constant sampling period. If we still want to apply these methods, the signal must be resampled. Gerchberg-Papoulis algorithm is a method of signal reconstruction. It is commonly used for band-limited extrapolation of uniformly sampled data. We show that it is suitable for reconstruction of non-uniformly sampled signals as well. Our target application is reconstruction of time series measured by a car driving simulator. To demonstrate the benefits of band-limited reconstruction, we compare it with standard interpolation methods. The main advantage of the proposed algorithm is its ability to deal with noise and sampling jitter.

**Keywords:** Gerchberg-Papoulis, non-uniform sampling, jitter, band-limited signal, one-step reconstruction.

## 1 INTRODUCTION

Signals cannot be sampled perfectly. During sampling, we are restricted by time, physical or financial constraints. Sometimes the acquired signal is not sampled as uniformly, or densely, as we require. If the quality of sampling cannot be improved, we have to use mathematical post-processing methods to reconstruct the original signal.

An example of such situation occurs in a car-driving simulator [1]. Non-uniform sampling rates are caused by non-real time properties of the operating system. The simulator uses input devices (a steering wheel and pedals) which measure driver's reactions. Sampling of such signals can be greatly improved by adding custom-made digital sensors with built-in microcontroller to assure real-time sampling; there is no need for signal reconstruction. However, many other signals are simulated—e.g., the position of the car. Their samples are generated by a computer. Therefore, their sampling cannot be improved by mounting additional actuators; we are forced to reconstruct the signal by mathematical methods.

The paper presents a solution to the problem of non-uniform sampling. It is divided as follows. In Section 2, we recall some fundamental facts concerning the sampling theory. We focus on the peculiarities of non-uniform sampling and reconstruction. In Section 3 we discuss the computational complexity. Section 4 is devoted to numerical experiments. At first, we reconstruct a theoretical signal to support full understanding of the method. Then we show reconstruction of a signal from the vehicle driving simulator. This demonstrates that the method is fully suitable for practical data processing.

## 2 THEORY

### 2.1 UNIFORMLY SAMPLED BAND-LIMITED SIGNALS

A signal  $f(t)$  is related to its spectrum  $F(\omega)$  by the Fourier transform

$$F(\omega) = \int_{-\infty}^{\infty} f(t)e^{-j\omega t} dt. \quad (1)$$

Here  $t$  denotes time and  $\omega$  stands for angular frequency. Signals which satisfy

$$F(\omega) = 0, \quad \text{for } |\omega| > \Omega, \quad (2)$$

are called band-limited with band-limit  $\Omega$ . They possess some very useful properties—engineers are well acquainted with the famous Shannon-Nyquist sampling theorem. It states that band-limited signal  $f(t)$  can be fully represented by its samples. There is no loss of information and it can be perfectly reconstructed by means of sinc interpolation:

$$f(t) = \sum_{k=-\infty}^{\infty} f(kT_s) \frac{\sin \pi(t/T_s - k)}{\pi(t/T_s - k)}, \quad \text{for } 0 < T_s < \frac{\pi}{\Omega}. \quad (3)$$

## 2.2 NON-UNIFORMLY SAMPLED BAND-LIMITED SIGNALS

It is not so widely known that the sampling density requirement also holds for non-uniformly sampled signals. Henry Landau had shown that non-uniformly sampled band-limited signals can be perfectly reconstructed, if the average sampling frequency is at least two times higher than the maximal frequency in the original signal's spectrum [2].

Of course, the reconstruction can no longer be achieved via the well-known sinc interpolation. Still, it can be solved using Gerchberg-Papoulis (GP) method—a method which is normally used for extrapolation of uniformly sampled data [3]. In [4] GP method was used for reconstruction of non-uniformly sampled data. The authors probably did not realise that they had, in fact, implemented GP method.

## 2.3 GERCHBERG-PAPOULIS METHOD

Let  $D$  denote a time-limiting operator

$$Df(t) = \begin{cases} f(t) & \text{for } |t| \leq 1, \\ 0 & \text{for } |t| > 1. \end{cases} \quad (4)$$

Similarly, let  $B$  denote a band-limiting operator

$$Bf(t) = \frac{1}{2\pi} \int_{-\Omega}^{\Omega} F(\omega) e^{j\omega t} d\omega. \quad (5)$$

If we measure a signal  $f(t)$ , and the measurement is of finite length, we get a time-limited signal  $g_0(t) = Df(t)$ . If the original signal  $f(t)$  is band-limited—i.e.,  $f(t) = Bf(t)$ —then it can be reconstructed using GP method. The method consists of time-limiting and band-limiting operations. The result of  $m$ 'th iteration  $g_m(t)$  is given by the equation

$$g_m(t) = \bar{D}B g_{m-1}(t) + g_0(t), \quad (6)$$

where  $\bar{D}$  is the complement of  $D$ , so that for any signal

$$f(t) = Df(t) + \bar{D}f(t). \quad (7)$$

The following figure illustrates the first GP iteration.

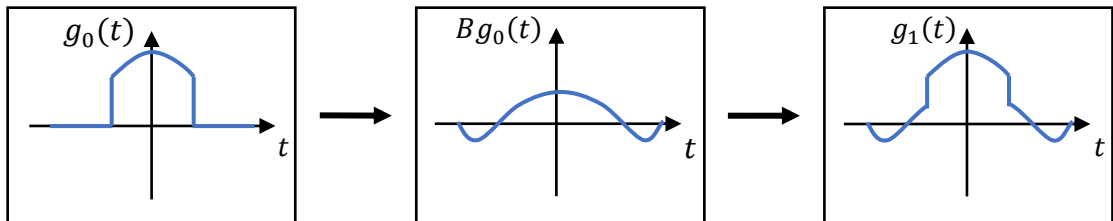


**Figure 1:** The first iteration of GP method.

We start with the known signal  $g_0(t)$ . The operator  $B$  smoothens the signal so that it spreads out (Figure 1, middle). But it also changes its values in the observed interval, so the following step is

time-limiting by  $\bar{D}$  and adding  $g_0(t)$ . This way we correct all known values (Figure 1, right). Then another iteration may follow.

Now we can take the last step towards the reconstruction of non-uniformly sampled signals. We make a generalization, that sole sample may be regarded as an infinitely small observation interval. Then Figure 1 shows what happens to individual sample. It widens, but its central point stays unaltered. So, at non-uniform sampling,  $D$  is not a rectangular window; it is a union of many infinitely small intervals.

### 3 COMPUTATIONAL EFFICIENCY

The iterative algorithm requires large computational efforts. In each cycle, it uses Fast Fourier Transform (FFT) and inverse FFT for long sequences of data. As we get closer to the solution, the convergence slows down. The problem can be bypassed via accelerated GP algorithm [5] or one-step GP algorithm [6]. We choose the latter. Then, the reconstruction can be computed using single matrix inverse and four matrix multiplications.

The last problem is that the calculations become numerically unstable as the band-limit and the length of the data increase. To make the inverse computationally feasible, we had to apply Tikhonov regularization. The approach is similar to [7]; however, we do not use Prolate Spheroidal Wave Functions. They would pose a heavy computational burden, which can only be bypassed by storing a large number of their samples to cover all possible positions of signal's non-uniform samples.

## 4 NUMERICAL EXPERIMENTS

### 4.1 RECONSTRUCTION OF A SINE WAVE

To demonstrate the importance of band-limit, we show reconstruction of a sine wave with angular frequency of  $16\pi$  rad/s. The chosen signal is intentionally as simple as possible. This way we can fully concentrate on the proposed method.

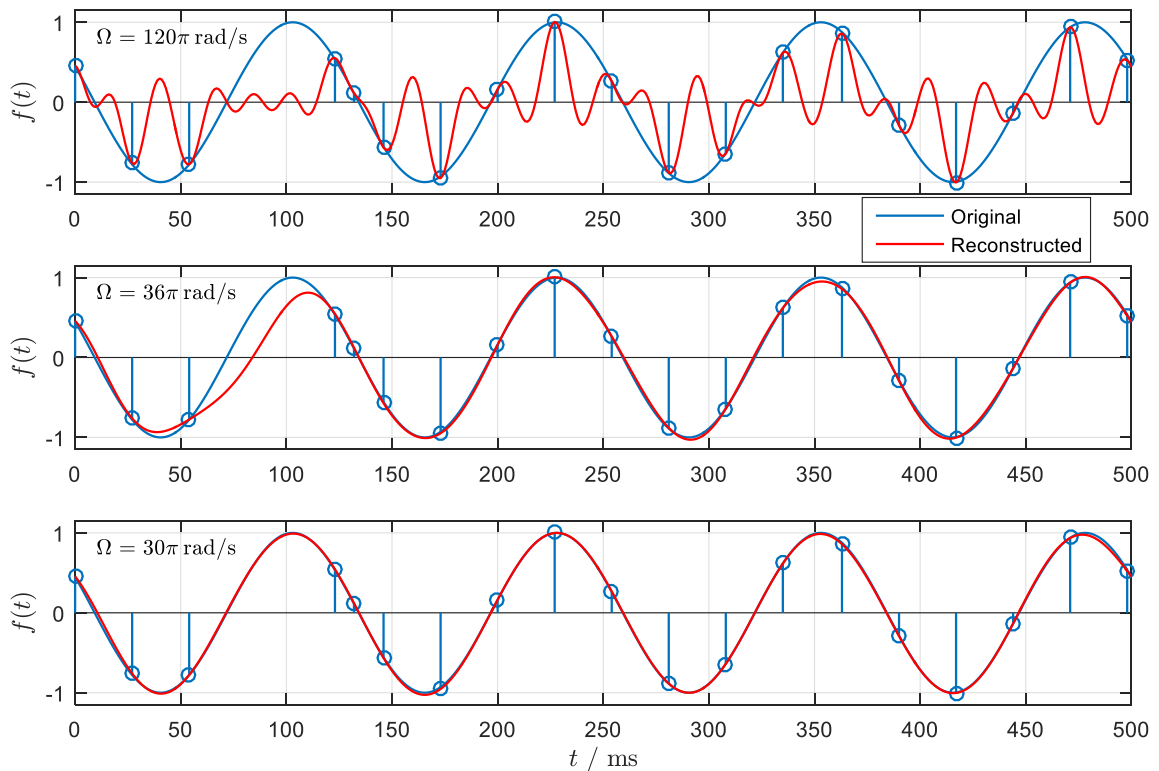


**Figure 2:** Sampled sine signal and its reconstruction for different band-limiting values  $\Omega$ .

At first, the sine signal is sampled. We use real non-uniform time stamps as they were recorded by the car driving simulator. Then, in order to make the signal more realistic, we add Gaussian noise with SNR of 40 dB. This way we simulate sampling of a real noisy signal. Continuous sine signal  $f(t)$  with its noisy samples  $f_s(t)$  is shown in Figure 2 (blue).

Sampled signal  $f_s(t)$  can be understood as a sequence of Dirac pulses multiplied by the original signal's amplitude.

$$f_s(t) = \sum_{k=-\infty}^{\infty} f(t_k) \cdot \delta(t - t_k). \quad (8)$$

For large band-limit  $\Omega$ , the reconstructed signal still resembles closely to the sequence of Dirac pulses (Figure 2, top, red).

By decreasing the band-limit  $\Omega$ , pulses are widened and smoothed. We set  $\Omega = \pi/T$ , where  $T$  is the average sampling period. This yields relatively good reconstruction (Figure 2, middle, red).

Finally, we reduce the band-limit, so that  $\Omega = \pi/(1.2 \cdot T)$ . When the  $\Omega$  is small enough, we get the desired reconstruction (Figure 2, bottom, red). A severe sampling non-uniformity is visible in the time interval  $60 \text{ ms} < t < 120 \text{ ms}$ . Clearly, the method is capable of solving the problem. The reconstructed signal is nearly indistinguishable from the original. The small discrepancies are mainly due to the added Gaussian noise.

## 4.2 RECONSTRUCTION OF MEASURED DATA

The car driving simulator collects data from a simulated vehicle. An example of frequently used scenario is a long motorway drive. The simulator records car's distance from the centre of the lane (measured in metres) and stores it for further analysis. Obtained samples can be seen in Figure 3 (blue).

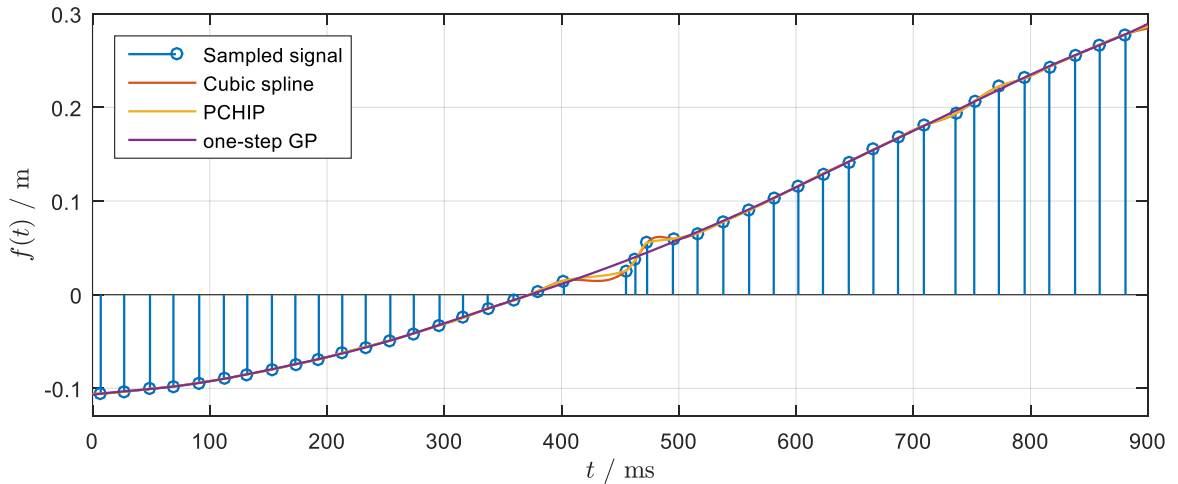


**Figure 3:** Sampled and reconstructed signal (position of the simulated car).

The figure shows that the car moves from the right edge of the lane to the left. The driver tries to perform rather slow changes, as the car has relatively high speed. Thus, the signal varies slowly. Nevertheless, three samples after  $t = 400 \text{ ms}$  are visibly delayed (see Figure 3 in the middle). The anomaly is physically improbable; it should be regarded as a sampling error.

Figure 3 compares one-step GP method with interpolation by cubic spline and Piecewise Cubic Hermite Interpolation Polynomial (PCHIP). If a sample is corrupted, interpolation creates undesirable oscillations. On the other hand, GP method simply ignores all corrupted samples and the signal remains smooth. This is the method's main advantage in practical applications. If the interpolation was

used in practice, the spurious changes would complicate further data processing—e.g., the derivative of the signal would be severely distorted.

## 5 CONCLUSION

We have proposed a method for reconstruction of non-uniformly sampled signals based on GP method. The method has simple interpretation—it yields a band-limited reconstruction of sampled signal. In contrast with interpolation methods, it is capable of dealing with noise and corrupted samples. This is an important advantage, if the processed samples contain noise.

The requirement of iterative computation was bypassed by computing matrix inverse. To avoid the ‘blow-up’ problem, we have applied Tikhonov regularization. The proposed algorithm was tested with simple sine-wave signal and with the data from vehicle driving simulator. Our results suggest that the reconstruction is fully suitable for practical applications.

We realise that there are other methods, which work for noisy signals—an example is fitting the samples with polynomials [8]—but these methods are rather heuristic. They require more parameters, most of which do not seem to have any meaningful physical interpretation. In contrast, the band-limit  $\Omega$  is well understood by the engineers and it can be selected easily. It has the same interpretation as for uniformly sampled signals.

The sole disadvantage of the proposed method is the requirement of correctly chosen regularization parameter. We are currently conducting further research to design an algorithm to select it adaptively.

## ACKNOWLEDGEMENT

The completion of this paper was made possible by the grant No. FEKT-S-20-6205 – "Research in Automation, Cybernetics and Artificial Intelligence within Industry 4.0" financially supported by the Internal science fund of Brno University of Technology.

## REFERENCES

- [1] D. Michalik, O. Mihalik, M. Jirgl, and P. Fiedler, ‘Driver Behaviour Modeling With Vehicle Driving Simulator’, *IFAC-PapersOnLine*, vol. 52, no. 27, pp. 180–185, Jan. 2019, doi: 10.1016/j.ifacol.2019.12.753.
- [2] H. J. Landau, ‘Necessary density conditions for sampling and interpolation of certain entire functions’, *Acta Math.*, vol. 117, pp. 37–52, 1967, doi: 10.1007/BF02395039.
- [3] A. Papoulis, ‘A new algorithm in spectral analysis and band-limited extrapolation’, *IEEE Transactions on Circuits and Systems*, vol. 22, no. 9, pp. 735–742, Sep. 1975, doi: 10.1109/TCS.1975.1084118.
- [4] F. Marvasti, M. Analoui, and M. Gamshadzahi, ‘Recovery of signals from nonuniform samples using iterative methods’, *IEEE Transactions on Signal Processing*, vol. 39, no. 4, pp. 872–878, Apr. 1991, doi: 10.1109/78.80909.
- [5] B. G. Salomon and H. Ur, ‘Accelerated iterative band-limited extrapolation algorithms’, *IEEE Signal Processing Letters*, vol. 11, no. 11, pp. 871–874, Nov. 2004, doi: 10.1109/LSP.2004.836950.
- [6] ‘An approach to band-limited signal extrapolation: The extrapolation matrix - IEEE Journals & Magazine’. [Online]. Available: <https://ieeexplore.ieee.org/document/1084442>. [Accessed: 12-Mar-2020].
- [7] S. Senay, L. F. Chaparro, and L. Durak, ‘Reconstruction of nonuniformly sampled time-limited signals using prolate spheroidal wave functions’, *Signal Processing*, vol. 89, no. 12, pp. 2585–2595, Dec. 2009, doi: 10.1016/j.sigpro.2009.04.020.
- [8] S. V. Porshnev, D. V. Kusaykin, and M. A. Klevakin, ‘On increasing the sample rate of the irregularly sampled jittered discrete-time signal. Algorithms based on correction of sampled values’, in *2017 Dynamics of Systems, Mechanisms and Machines (Dynamics)*, 2017, pp. 1–5, doi: 10.1109/Dynamics.2017.8239493.

# AUTOMATED FOVEA CENTER ESTIMATION IN ADAPTIVE OPTICS IMAGES

**Eva Valterova**

Doctoral Degree Programme (2.), FEEC BUT

E-mail: valterova@vutbr.cz

Supervised by: Radim Kolar

E-mail: kolarr@feec.vutbr.cz

**Abstract:** The adaptive optics (AO) is an insightful tool with high potential. Since the first demonstration in ophthalmology has undergone immense growth in its diagnostic application, mainly because the AO enables to capture retina in vivo with resolution on the cellular level. In the center of the retina is macula, containing the fovea. The fovea detection is possible with utilizing the knowledge of its characteristic properties. We developed and applied two methods for fovea center estimation. The first method is based on image maximum detection. The second is based on the 2D Gaussian curve fitting. The first method has proved better results in comparison with manual grading. The measured difference was  $32 \pm 27$  pixels. The second approach has in comparison with manual grading slightly higher difference equal to  $108 \pm 64$  pixels. Both of the methods estimated the foveal center within the expected foveal area.

**Keywords:** retina, adaptive optics, macula, fovea center

## 1 INTRODUCTION

The adaptive optics (AO) ophthalmoscope was demonstrated already in 1997 [1] and since then has undergone great development and growth in its application. The AO consists of three major components: the wavefront sensor, the wavefront corrector, and the control system linking those two parts [2]. The wavefront sensor measures in real-time the optical aberrations present in the optic path of human eye. Subsequently, the control system interprets the measured aberrations to the wavefront corrector to compensate them.

The compensation enables to reach image spatial resolution on cellular level [1, 3, 4]. Thus, individual photoreceptors and their properties are observable and new insight into the monitoring and detection of retina diseases in its very first beginning is possible. Such a resolution enables to determine retina conditions connected not only with photoreceptors but also with retinal blood vessels. Thanks to AO imaging the inherited retinal diseases, age-related macular degeneration and vascular diseases can be detected [5, 6].

The novel biomarkers related to photoreceptor's properties (size, positions, and mainly density) can be extracted from these high resolution images [7, 8]. These cones-related properties show spatial variations within the retina, which has been also confirmed by histological research [9]. Near the center of the retina is placed macula, a pigmented oval-shaped spot, where the vision is the sharpest within the retina. The sharp vision is caused by higher density of cones. The fovea, a small pit in the center of the macula, is typical by especially closely packed cones of smaller size.

Foveal detection in retinal images is a well-known problem. It is the main objective of many researchers groups but mostly in colour fundus images without adaptive optics. One of the basic approaches is to identify the fovea using correlation-based approaches and typical foveal characteristics - for example, the darkest area in the neighbourhood of the optic disc [10, 11]. Welfer et al. de-

veloped a method based on known anatomical constraints (fovea location with respect to optic disc) and mathematical morphology. It's been proved to be robust against local illumination changes and disturbances [12]. Nevertheless, the methods usually provide low specificity results in pathological retinas.

## 2 MATERIALS AND METHODS

Retinal images from the macular region were acquired on both eyes of ten healthy subjects. In total twenty AO images of size  $1500 \times 1500$  pixels were captured by flood illuminated AO camera (rtx1, Imagine Eyes, Orsay, France); an example is shown in Figure 1 (a). The framed areas in part (a) are magnified in part (b) respectively. The red-framed area demonstrates, that the resolution enables to display individual photoreceptors. The cones are light reflective and therefore in this image are captured as small bright spots with size of 5-9 pixels (that roughly corresponds to  $3,6 \mu m$ ).

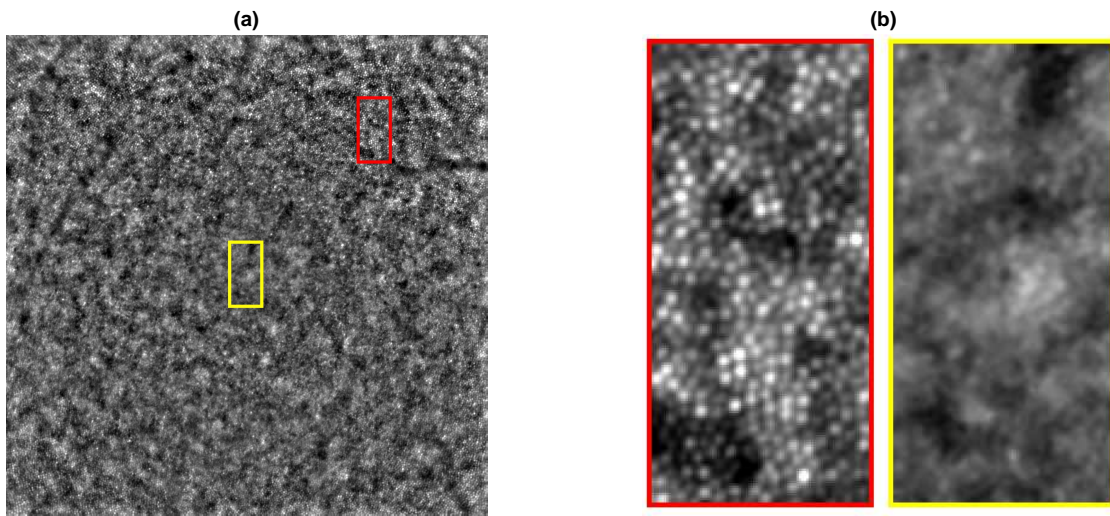


**Figure 1:** (a) The acquired AO image with marked parts zoomed in (b). (b) Red framed zoomed part of retina, where the cones are visible and yellow framed part of retina, where the size of cones is below resolution.

Our method, similar to [10, 11], is based on foveal image properties - the cone size in the foveal area is below AO system resolution and therefore the image is blurred within this area. An example is shown in the zoomed yellow framed part in Figure 1 (b). Nevertheless, the image contains also blurriness on edges interfering almost to the center.

### 2.1 METHODOLOGY

The simple methods of how to assess image blur can be based on local standard deviation. However, normalization with respect to the image brightness is needed. Therefore a simple measure of image blur can be defined as:

$$I_{std}(i, j) = \frac{I_S(i, j)}{I_m(i, j)}, \quad (1)$$

where the  $I_S$  denotes the estimation of local standard deviation in window of size  $15 \times 15$  pixels and  $I_m$  denotes the image filtered by mean filter of the same size.

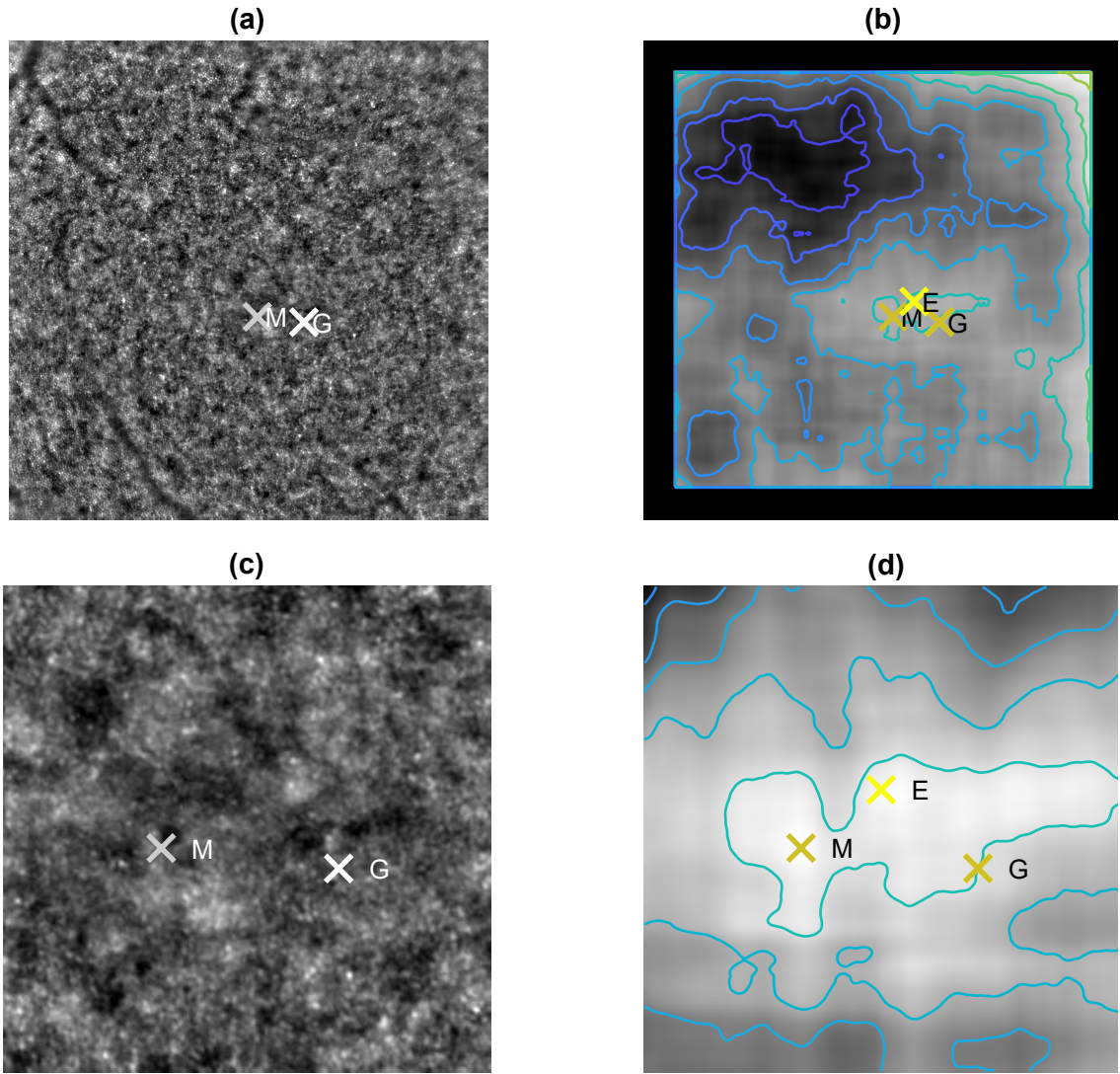


**Figure 2:** (a) The AO image with estimated fovea centers by method based on image maximum  $M$  and 2D Gaussian fitting  $G$ . (b) The computed image  $I_{std}$  with estimated fovea centers -  $E$  denotes the manual evaluator and contours highlighting the gray-scale differences. (c) The center region magnification of image (a), (d) The center region magnification of image (b).

The fovea center is afterward automatically estimated by two different approaches. In the first approach (labeled as  $M$ ) maximum value in image  $I_{std}$  is detected with the constraint that the maximum is detected only within the image center, because the fovea position is not expected close to the edges, due to eye fixation during measurement.

The second approach (labeled as  $G$ ) is based on 2D Gaussian curve fitting applied on the cropped image  $I_{std}$ , where the 2D Gaussian function is defined as

$$f(x, y) = Ae^{-\left(\frac{(x-x_0)^2}{2\sigma_x^2} + \frac{(y-y_0)^2}{2\sigma_y^2}\right)}, \quad (2)$$

where  $A$  is the curve amplitude,  $x_0$  and  $y_0$  are the curve center coordinates and  $\sigma_x^2$ ,  $\sigma_y^2$  define the curve

width. The fovea center is then defined by the positions of 2D fitted Gaussian curve.

The foveal positions have been also determined manually in order to receive a set of ground-truth data for reliable comparison.

### 3 RESULTS AND DISCUSSION

The computed image  $I_{std}$  is shown in Figure 2 (b) in comparison with its original version shown in Figure 2 (a). The central part magnification of image (a) and (b) is shown in (c) and (d) respectively. The contours in (b) and (d) highlight the gray-scale difference. The brightness level in these images corresponds directly to the blurriness.

The result of the first approach for fovea detection, based on the maximum value of the center image region, is denoted as  $M$  in Figure 2 and  $E$  is assigned to manual evaluator. The mean distance is defined by Euclidean distance

$$D(x,y) = \sqrt{(x_m - x_e)^2 + (y_m - y_e)^2}, \quad (3)$$

where  $x_m$  and  $y_m$  denotes coordinates of  $M$  and  $x_e$  and  $y_e$  are the coordinates of  $E$  and is equal to  $32 \pm 27$  pixels.

Sign  $G$  in Figure 2 is assigned to the fovea center detected by the 2D Gaussian curve fitting. The mean distance between  $G$  and  $M$  is  $108 \pm 64$  pixels. It is clearly seen, that the foveal center  $G$  is shifted against the  $M$  away from the upper left blurry area. This phenomenon of shift further from the interfering edge blurriness was observable across several images and can cause the higher value of displacement in the comparison with the manual grading.

To summarize, the method based on image maximum detection has proved better results in comparison with manual grading. Nevertheless is limited by correct eye fixation because the maximum is detected only in the center area of the image. The Gaussian fitting method is robust to the eye fixation, but is strongly involved by interfering blurriness caused by minor eye movements and retina curvature.

### 4 CONCLUSION

Twenty images of both eyes of ten healthy subjects were captured. Two methods for fovea center estimation were developed. The first one is based on image maximum detection in the image center and the second one is based on 2D Gaussian curve fitting. Both of them were compared with manual grading. The first method has proved better results in comparison with manual grading. The mean Euclidean distance was  $32 \pm 27$  pixels. The second approach has in comparison with manual grading slightly higher difference equal to  $108 \pm 64$  pixels. The defacement was probably caused by interfering image blurriness. Both of the methods determined successfully the center of the fovea within expected fovea area.

### ACKNOWLEDGEMENT

We thank Franziska G. Rauscher from IMISE, Leipzig University, Germany and Nadace “Nadani Josefa, Marie a Zdenky Hlavkovich”, Prague, Czech Republic for their support.

### REFERENCES

- [1] J. Liang, D. R. Williams, and D. T. Miller, “Supernormal vision and high-resolution retinal imaging through adaptive optics,” *JOSA A*, vol. 14, no. 11, pp. 2884–2892, 1997.

- [2] J. S. Gill, M. Moosajee, and A. M. Dubis, “Cellular imaging of inherited retinal diseases using adaptive optics,” *Eye*, vol. 33, no. 11, pp. 1683–1698, 2019.
- [3] M. Prasse, F. G. Rauscher, P. Wiedemann, A. Reichenbach, and M. Francke, “Optical properties of retinal tissue and the potential of adaptive optics to visualize retinal ganglion cells in vivo,” *Cell and tissue research*, vol. 353, no. 2, pp. 269–278, 2013.
- [4] D. R. Williams, “Imaging single cells in the living retina,” *Vision research*, vol. 51, no. 13, pp. 1379–1396, 2011.
- [5] M. Georgiou, A. Kalitzeos, E. J. Patterson, A. Dubra, J. Carroll, and M. Michaelides, “Adaptive optics imaging of inherited retinal diseases,” *British Journal of Ophthalmology*, vol. 102, no. 8, pp. 1028–1035, 2018.
- [6] M. Paques, S. Meimon, F. Rossant, D. Rosenbaum, S. Mrejen, F. Sennlaub, and K. Grieve, “Adaptive optics ophthalmoscopy: Application to age-related macular degeneration and vascular diseases,” *Progress in retinal and eye research*, vol. 66, pp. 1–16, 2018.
- [7] A. M. Dubis, R. F. Cooper, J. Aboshiha, C. S. Langlo, V. Sundaram, B. Liu, F. Collison, G. A. Fishman, A. T. Moore, A. R. Webster *et al.*, “Genotype-dependent variability in residual cone structure in achromatopsia: toward developing metrics for assessing cone health,” *Investigative ophthalmology & visual science*, vol. 55, no. 11, pp. 7303–7311, 2014.
- [8] K. M. Litts, R. F. Cooper, J. L. Duncan, and J. Carroll, “Photoreceptor-based biomarkers in aoslo retinal imaging,” *Investigative ophthalmology & visual science*, vol. 58, no. 6, pp. BIO255–BIO267, 2017.
- [9] C. A. Curcio, K. R. Sloan, R. E. Kalina, and A. E. Hendrickson, “Human photoreceptor topography,” *Journal of comparative neurology*, vol. 292, no. 4, pp. 497–523, 1990.
- [10] M. Mubbashar, A. Usman, and M. U. Akram, “Automated system for macula detection in digital retinal images,” in *2011 International Conference on Information and Communication Technologies*. IEEE, 2011, pp. 1–5.
- [11] C. Sinthanayothin, J. F. Boyce, H. L. Cook, and T. H. Williamson, “Automated localisation of the optic disc, fovea, and retinal blood vessels from digital colour fundus images,” *British journal of ophthalmology*, vol. 83, no. 8, pp. 902–910, 1999.
- [12] D. Welfer, J. Scharcanski, and D. R. Marinho, “Fovea center detection based on the retina anatomy and mathematical morphology,” *Computer methods and programs in biomedicine*, vol. 104, no. 3, pp. 397–409, 2011.

# SIMULATIONS AND MEASUREMENT OF ACOUSTIC EMISSION EFFECTS

**Jakub Krejčí**

Doctoral Degree Programme (3), FEEC BUT

E-mail: xkrejc44@stud.feec.vutbr.cz

Supervised by: Petr Beneš

E-mail: benesp@feec.vutbr.cz

**Abstract:** This paper deals with issue of method of acoustic emission and performed measurements of acoustic emission signals and simulation of this phenomenon. Main interest is given into measurement of acoustic emission transducer displacement to verify homogeneity on its surface in time and simulations by finite element method. Performed simulations deal with displacement calculation of calibration block after a capillary break, calculation of impedance characteristics of piezoelectric sensing element and their comparison with analytic solution or measurement.

**Keywords:** acoustic emission, simulation, COMSOL, impedance characteristic

## 1 INTRODUCTION

The systematic development of non-destructive testing methods has been apparent since the beginning of the last century and is related to the development of a technique where the purpose is to test the product without affecting its applicability.[1][2] This discipline involves many methods, such as chemical, infrared, mechanical or electromagnetic, each with its advantages and disadvantages, and often complement each other.

One method of non-destructive testing is acoustic emission (AE), which dates back to the middle of the last century. Acoustic emission is related to elastic stress waves, which arise after release of mechanical stress in the material. The frequency of propagating waves reaches high values (of the order of tens of kHz to units of MHz). The occurrence of the AE signal is usually the first signal to prevent irreversible deformation of the loaded object. Frequent use of AE is monitoring and localization of plastic deformation, leak testing (hissing), corrosion, welds and other tests of products.

AE sensors are based on various principles, such as piezoelectric, piezoresistive, capacitive or magnetostrictive. The most common type is piezoelectric, whose basic characteristic is the ripple of the frequency response at resonant frequencies. For discontinuous AE events, where event detection time is important, this phenomenon is irrelevant. In continuous AE measurements, where signal amplitude over a wide range of frequencies is essential, this is a parasitic phenomenon that needs to be suppressed. At present, the design of the AE broadband sensor is a frequently discussed topic. One of the wideband transducer solutions is the use of a thin disk that is supplemented with a damping compound to reduce resonance overshoot. Other solution is to design another shape of the piezoelectric element, which has more resonant frequencies with lower amplitude.

## 2 MEASUREMENT OF TRANSDUCER DISPLACEMENT

In one of the first experiments I focused on measuring displacement of the AE transducer by means of an interferometer, similarly as presented by Monnier. [3] Unlike this paper, I did not measure the displacement across the entire sensor surface, but only on the trajectory of its diameter. Due to circular

symmetry, the displacement should be the same at all points on the individual circles. Another goal for this simple measurement was to gain practical experience with available laboratory equipment.

Since the sensor is matt and its surface is slightly rough, it was necessary to ensure better reflection of the laser beam. The use of self-adhesive reflective pads used in conventional vibro-diagnostic applications is not appropriate. This reflective surface could affect the deflection of the sensor by its inertial mass, the adhesive tape on the underside of the reflector may affect the surface stiffness. All these influences are difficult to quantify, so I used a method that raises less doubt. In the measuring line, a silver marker was applied to the surface of the sensor (Fig. 1a). The influence of the surface is minimal and the reflected signal has reached a sufficient intensity.

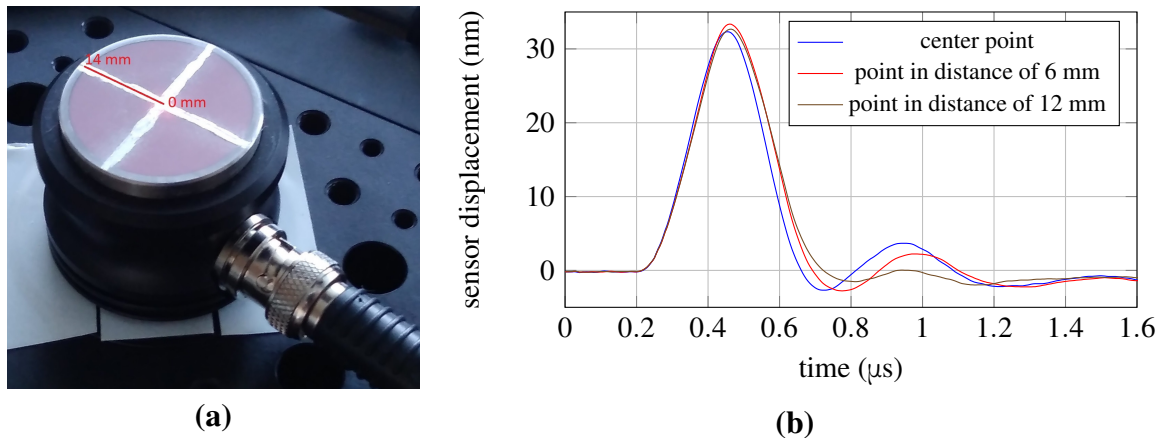


**Figure 1:** (a) Measured sensor, (b) Comparison of sensor displacement for different distances from center

Radius of the sensor is 14 mm and a motorized linear stage was used for positioning of the sensor, I proceeded from the center to the edge with a step of 1 mm. The transducer was excited by a pulse of 400 V amplitude and a duration of approximately 0.1 μs. The start of the measurement was synchronized with this excitation pulse. Results of three selected points are shown in Fig.1b. From the start of the measurement up to 0.2 μs, the displacement of the sensor was zero, then it began to increase. The peak was reached at time 0.45 μs and then decreased. In general, the displacement of the sensor during pulse excitation can be evaluated as uniform with a short and low oscillations, highest oscillation was measured in the center.

### 3 SIMULATION OF CAPILLARY FRACTURE

The next step in the performed simulations is to calculate the deformation of the material after the capillary fracture, i.e. after the release of the applied force. This is the method defined by the standard for the primary calibration of AE sensors. [4] The results can be verified because there exist an analytical calculation of this phenomenon. [5][6]

As a test object I chose a calibration cylinder in our laboratories. In the simulation, a step release of force was achieved by a two-step solution - static and time dependent, and used Solid Mechanics physics to define boundary conditions. The static part dealt with loading of the center of the upper side of the cylinder with a force of 10 N, time dependent assumed to applied force. Bottom part of the object was fixed and remaining were in free settings. The deflection was detected at a distance of 14 cm, in which the calibration takes place. These values are based on experiments performed in the dissertation of Ing. Jiří Kepřt, PhD. [7]

The computation in the time domain was made in range 0 to 100 μs with step 0.1 μs and it brought

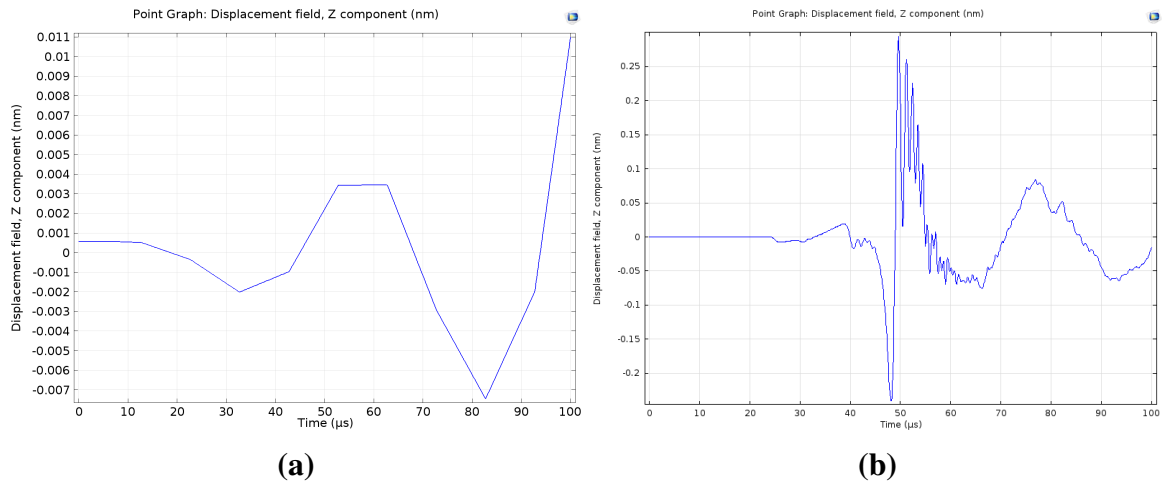


**Figure 2:** Progression of cylinder surface deflection calculated by COMSOL software: (a) One of the first versions, (b) Current state of simulation

several complications, because many factors affect the results and time of the calculation. One of them is the time step. At first the results did not differ or only slightly differed for many mesh settings. The investigation revealed that the setting of the solver needs to be changed. By default, the option that the time step size is set automatically. Therefore, in some simulations, changing the time step did not affect the results. After changing the settings the results are more stable, the simulation reacts to the configuration changes, which is evident from the comparison in Fig. 2. The calculation time can be influenced by other elements, such as tolerance or solver. Currently, the simulation lasts approximately 8 hours on a regular desktop PC and cannot be significantly improved due to hardware limitations. In last weeks I requested a computing time on supercomputer at IT4Innovations [8] and this request was approved as a project DD-19-46-*Simulation of wideband acoustic emission sensor*. Thanks to this step the results of the simulation can be improved.

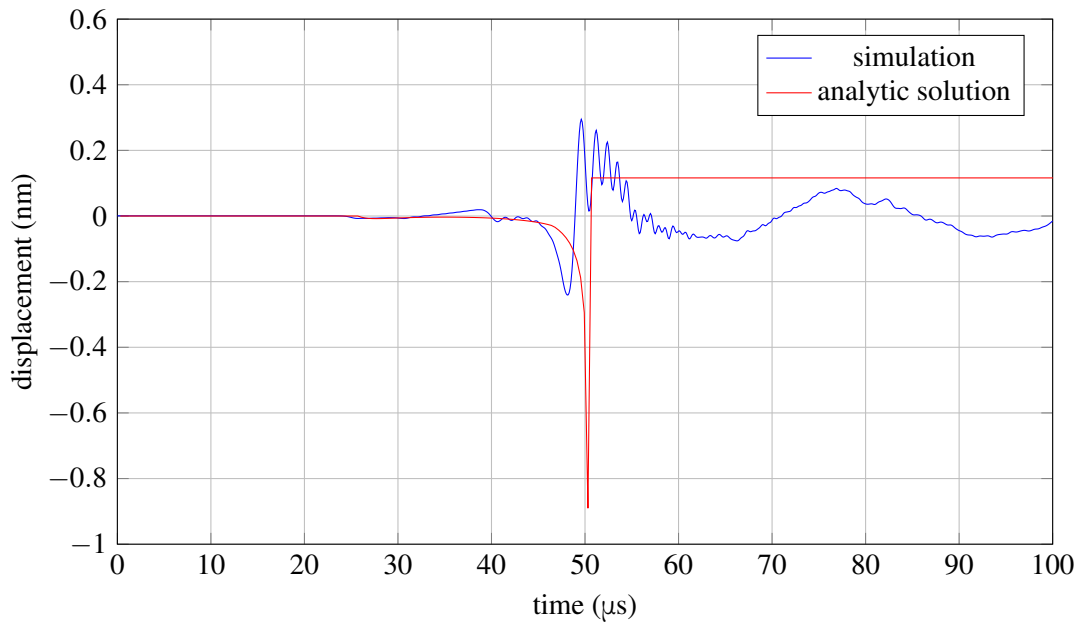


**Figure 3:** Comparison of analytical solution and simulation of displacement on the surface of calibration cylinder for capillary fracture

Furthermore, I compared the deflection with the analytical solution, which was considered in Ing. Jiri Kepřt, PhD. dissertation and whose source code I followed. However, it is apparent from Fig. 3, the time of main peak and its amplitude are different for same material constants. Biggest difference is evident from stabilized displacement after capillary fracture event, which oscillates around zero value in simulation, but for analytic solution is at certain value. This difference will be more investigated with higher computing resources for different solver settings to obtain suitable setup.

#### 4 SIMULATION OF IMPEDANCE CHARACTERISTIC

Achieving an impedance characteristics of sensing elements in sensors is one of the key part in acoustic emission simulations. One of them was performed for the same element dimensions as are used in manufactured sensors, namely a thin disk with height 0.426 mm and diameter 4.50 mm (Fig. 4). The disc is made from material PZT-5H, which is also used in simulation. Simulation was carried out in frequency domain in range from 20 to 2 000 kHz with step 20 kHz, when a periodic voltage was applied to the upper and lower sides (electrodes) of the element (AC/DC Module). Piezoelectric element was not fixed by any condition, it was in a free state (Solid Mechanics Module). Results were compared with measurement performed by impedance analyzer HP 4294, which applies voltage 500 mV to the tested object, therefore the same voltage was set-up in the simulation. The only difference between the experiment is that during the measurement the sample is placed between the measuring tongs, however the simulation assumes a free state.

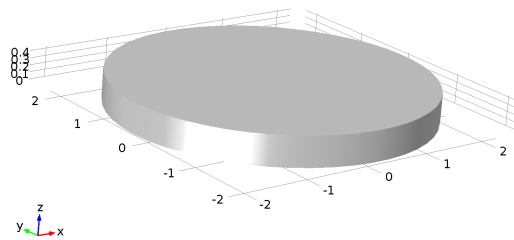


**Figure 4:** Examined piezoelectric element

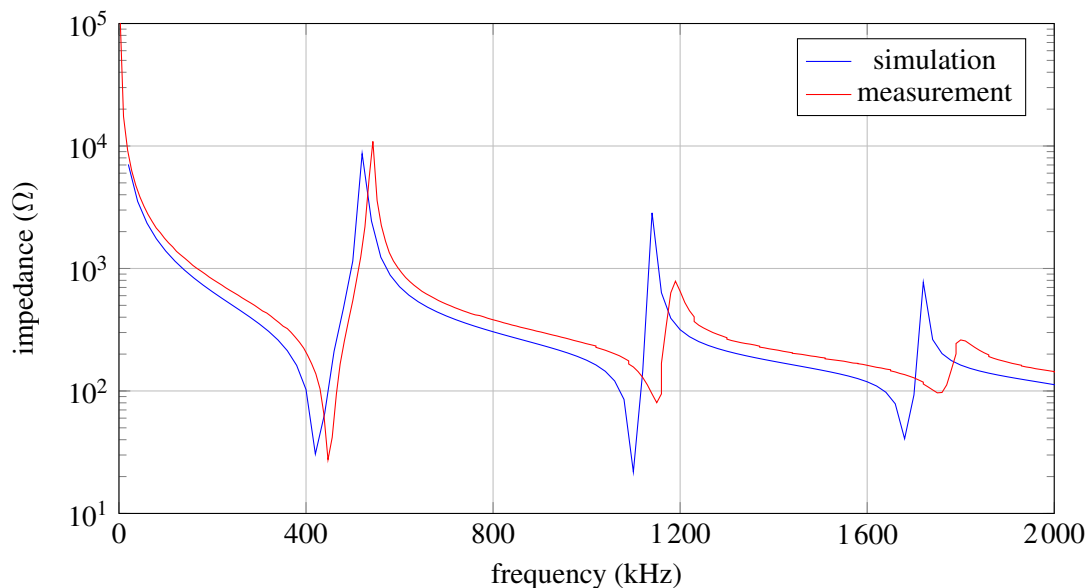


**Figure 5:** Impedance characteristic of thin piezoelectric disc

As can be seen in Fig 5, the results generally correspond, but their difference is increasing for higher frequencies. This can be caused by material differences (material in COMSOL library has different properties than produced one), in geometrical difference or some undefined features in simulation. At this stage these results are sufficient for our purposes and more complex simulation of whole sensors will be performed.

## 5 CONCLUSION

Presented paper dealt with the issue of acoustic emission sensors, performed experiments and simulations. Measurement aimed at transducer displacement after pulse excitation showed the displacement is uniform on the surface, but sufficient signal reflection must be ensured. One of simulations examined surface displacement after capillary fracture with similar peak arrival time and amplitude as analytic solution, but different damping. Result achieved by simulation had a tendency to oscillate, this difference will be more researched thanks to obtained computing time on supercomputer.

Another simulation was focused on impedance characteristic of piezoelectric element, which was compared to measurement with impedance analyzer. The results differed only to a lesser extent and they will be used as a step for further progress. That will contain more complex model of a sensor and it should cover whole calibration process. Thanks to these steps it will be possible to optimize sensor parameters by simulations.

## ACKNOWLEDGEMENT

The completion of this paper was made possible by the grant No. FEKT-S-20-6205 - "Research in Automation, Cybernetics and Artificial Intelligence within Industry 4.0" financially supported by the Internal science fund of Brno University of Technology.

## REFERENCES

- [1] KOPEC, B. Nedeštruktivní zkoušení materiálů a konstrukcí : nauka o materiálu IV. 1. ed. Brno: Akademické nakladatelství CERM, 2008. 571 s. ISBN 978-80-7204-591-4
- [2] MILLER, R. K.; HILL, E. v. K.; MOORE, P. O. *Acoustic Emission Testing*, American Society for Nondestructive Testing: Nondestructive Testing Handbook
- [3] MONNIER, T.; SEYDOU, D.; GODIN, N.; ZHANG, F. *Primary Calibration of Acoustic Emission Sensors by the Method of Reciprocity, Theoretical and Experimental Considerations*. Journal of Acoustic Emission, 2012, vol. 30, s. 152-166.
- [4] ISO 12713:1998 (E) Non-destructive testing - Acoustic emission inspection - Primary calibration of transducers
- [5] HORA, P. *Calibration of Transducers for Acoustic Emission*. Acta technica ČSAV. 1991, no. 2, p. 190 - 220.
- [6] PEKERIS, C. L. *The seismic surface pulse* Proceedings of the National Academy of Sciences of the United States of America, 1955, vol. 41, s. 469-80.
- [7] KEPRT, J. *Primární kalibrace snímačů akustické emise* Brno: Vysoké učení technické v Brně, Fakulta elektrotechniky a komunikačních technologií, 2018. 171 s. Vedoucí dizertační práce doc. Ing. Petr Beneš, PhD.
- [8] National supercomputing center. *IT4Innovations* [online]. Ostrava [accessed 2020-03-11]. Available from: <https://www.it4i.cz/?lang=en>

# THE TWO-MASS SYSTEM PARAMETER IDENTIFICATION WITH LEVENBERG-MARQUARDT ALGORITHM

Ondřej Bartík

Doctoral Degree Programme (3), FEEC BUT

E-mail: xbarti07@stud.feec.vutbr.cz

Supervised by: Petr Blaha

E-mail: blahap@feec.vutbr.cz

**Abstract:** This paper is focused on the parameter identification of the Two-Mass mechanical flexible system for motor drive applications. The whole methodology is based on the amplitude frequency characteristic given by the Welch spectrum analysis method. Then, an initial estimate of the plant parameters is extracted from the amplitude frequency characteristic and it is used as the starting point for the Levenberg-Marquardt algorithm to enhance the parameter estimation.

**Keywords:** Two-mass flexible system, Welch method, Spectral analysis, Levenberg-Marquardt method

## 1 INTRODUCTION

Plenty of mechanical rotary systems with any flexible coupling can be modeled as the two-mass system. As the examples; the toothed belt, axial rotary flexible connection, and long torque shaft connection can be given. Work [1] can be used as a good knowledge background for the physical based modeling of the multi-mass systems. These types of systems (plants) show resonant behavior on certain frequencies. This means that there are (anti)resonant peaks on the plant frequency response. Such a behavior causes many problems in closed-loop system design and hence, it is necessary to identify this behavior as best as possible. For the satisfying parameter estimate, an appropriate identification method has to be chosen. Right beside this, an appropriate input signal has to be chosen as well. This means that the signal must be rich enough to ensure sufficient plant excitation. Widely used methods for identification of the electric drive systems are methods based on the frequency analysis or the spectral analysis. The method used in this paper is based on the spectral analysis using power spectral densities (periodograms) estimates according to:[2]. The main goal of the identification experiment presented in this paper is to obtain the plant parameters estimate, which allows successful reconstruction of the resonant and anti-resonant peaks values and their positions on the plant frequency response.

## 2 TWO-MASS SYSTEM MODELLING

The Two-Mass mechanical flexible system can be understood as the system with the single input and with two outputs and can be described by the following set of the differential equations.

$$\frac{d\omega_m}{dt} = -\frac{b}{J_m}\omega_m - \frac{k}{J_m}\theta_m + \frac{b}{J_m}\omega_l + \frac{k}{J_m}\theta_l + \frac{T_i}{J_m} \quad (1)$$

$$\frac{d\theta_m}{dt} = \omega_m \quad (2)$$

$$\frac{d\omega_l}{dt} = \frac{b}{J_l}\omega_m + \frac{k}{J_l}\theta_m - \frac{b}{J_l}\omega_l - \frac{k}{J_l}\theta_l \quad (3)$$

$$\frac{d\theta_l}{dt} = \omega_l \quad (4)$$

Where  $J_m$  and  $J_l$  are the inertias of the shaft and load, respectively. Parameter  $b$  is the dumping coefficient and the parameter  $k$  is the flexible coefficient. Variables  $\omega_m$  and  $\omega_l$  stand for the motor shaft and the load angular velocities, respectively. The variables  $\theta_m$  and  $\theta_l$  are shaft and load angular positions. Finally, the  $T_i$  variable stands for the input torque generated by the electric part of the machine. The typical frequency response of the plant with  $T_i$  as the input and  $\omega_m$  as the output is shown in Figure 1.

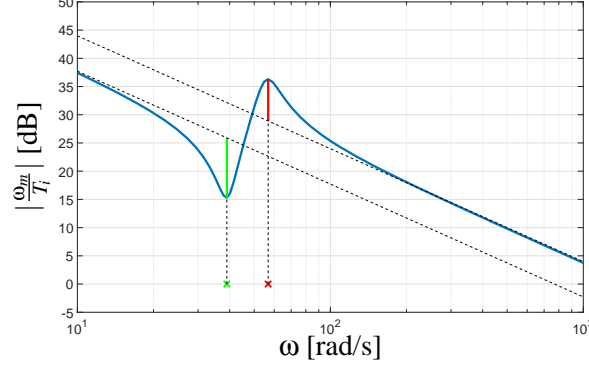


**Figure 1:** Flexible system frequency response (example)

The blue line represents the magnitude of the mechanical part of the drive systems with a flexible mechanical part. Red and green lines represent resonance and anti-resonance overshoots, respectively. Red and green crosses then represent their positions in the frequency. The mentioned transfer function of the examined plant is as follows:

$$G_p(s) = \frac{\omega_m(s)}{T_i(s)} = \frac{1}{J_m + J_l} \frac{1}{s} \frac{J_l s^2 + bs + k}{J_m J_l s^2 + bs + k} \quad (5)$$

where the  $s$  stands for Laplace operator. The bi-quadratic member creates the flexible element of the system. The main goal of this paper is to show the procedure of the  $J_m$ ,  $J_l$ ,  $k$ , and  $b$  parameters estimation. The resonant angular frequency  $\omega_r$  and anti-resonant angular frequency  $\omega_a$  are described by the following relations [3], [4]:

$$\omega_r = \sqrt{k \frac{J_m + J_l}{J_m J_l}} \quad (6)$$

$$\omega_a = \sqrt{\frac{k}{J_l}} \quad (7)$$

The analytical form of the amplitude frequency characteristic can be easily derived by replacing  $s$  with the  $j\omega$  in (5) and evaluating the absolute value to gain the following relation:

$$|G_p(\omega)|_{dB} = 20 \log_{10} \sqrt{\frac{(k - J_l \omega^2)^2 + b^2 \omega^2}{(k(J_m + J_l) - J_m J_l \omega^2)^2 + b^2 (J_m + J_l)^2 \omega^2}} \quad (8)$$

Now, the values of the resonant and anti-resonant peaks can be easily derived by substituting (6) and (7) into (8) respectively. Then, the following relations are obtained:

$$R_{dB} = 20 \log_{10} \frac{1}{J_m + J_l} \sqrt{1 + \frac{k \frac{J_l^3}{J_m}}{b^2 (J_m + J_l)}} \quad (9)$$

$$A_{dB} = 20 \log_{10} \sqrt{\frac{b^2}{b^2(J_m + J_l)^2 + kJ_l^3}} \quad (10)$$

The model was widely discussed in the previous work: [5] Relations (6), (7), (9), and (10) are used to examine the accuracy of the identified parameters in the final part of this paper.

### 3 DATA PROCESSING

The used Welch method of the spectral analysis can be described by the following formula:

$$|\hat{G}_p(\omega)| = \frac{\mathcal{F} \frac{1}{N} \sum_{i=0}^N R_{wy_i}(\tau) w_i(\tau)}{\mathcal{F} \frac{1}{N} \sum_{i=0}^N R_{uu_i}(\tau) w_i(\tau)} \quad (11)$$

The method is based on the averaging of  $N$  periodograms. Where periodograms are given as the Fourier images of the cross-correlation and auto-correlation functions, respectively. For accuracy increase, there is a window function applied on each periodogram. The window function is defined as follows:

$$w(\tau) = 0.5 - 0.5 \cos\left(\frac{2\pi}{L-1}\tau\right) \quad (12)$$

where  $L$  is the length of the data block (periodogram). As mentioned in the Introduction section, the spectral analysis serves only as the initial estimate for the Levenberg-Marquardt algorithm. This algorithm minimizes the nonlinear least-squares problem:

$$\|\mathbf{f}(x, B) - \mathbf{y}_m\|_2^2 = (\mathbf{f}(x, B) - \mathbf{y}_m)^T (\mathbf{f}(x, B) - \mathbf{y}_m) = (\mathbf{r})^T (\mathbf{r}) \quad (13)$$

where  $\mathbf{f}(x, B)$  is a set of nonlinear equations and  $B$  is a set of function parameters. The  $\mathbf{y}_m$  is a set of measurements. For the optimum solutions, it is necessary that following partial derivatives are equal to zero:

$$\frac{\partial \mathbf{r}^T}{\partial B} \mathbf{r} = \mathbf{J}^T \mathbf{r} = \mathbf{v} \quad (14)$$

where  $\mathbf{J}$  is Jacobian matrix. The vector  $\mathbf{v}$  should be equal to zero for the optimal solution. Levenberg-Marquardt method presents the solution of this problem as:

$$(\mathbf{A}^{(k)} + \lambda \mathbf{D}^{(k)}) \mathbf{B}_d^{(k)} = -\mathbf{v}^{(k)} \quad (15)$$

where  $\mathbf{A}^{(k)}$  is  $k$ -th estimate of Hessian defined as the  $\mathbf{A} = \mathbf{J}^T \mathbf{J}$ . Parameter  $\lambda$  is the value of a scale factor and diagonal matrix  $\mathbf{D}^{(k)}$  is an additional scale matrix. Finally,  $\mathbf{v}^{(k)}$  is a gradient in  $k$ -th step. According to: [6] the  $\mathbf{D}$  is set as  $\mathbf{D}^{(k)} = \mathbf{J}^{T(k)} \mathbf{J}^{(k)}$ . The estimate of the Jacobian matrix in each step of the algorithm is calculated as follows:

$$\mathbf{J}_{*,i}^{(k)} = \frac{\mathbf{f}(x, B_i + \Delta) - \mathbf{f}(x, B_i)}{\Delta} \quad (16)$$

where  $\Delta$  is a user-defined tolerance value.

#### 3.1 PARAMETERS EXTRACTION

For the initial parameter estimate, the values of resonance frequency  $\omega_r$  and anti-resonance frequency  $\omega_{ar}$  are used. An additional point at low frequencies ( $\omega_{low}$ ) is used as well. See Figure ?? (a). The point is half of decade distant from the anti-resonance frequency. Now, from (6), (7), (9), (10) and with the additional point and with  $J_{c,0} = \frac{J_{m,0}J_{l,0}}{J_{m,0}+J_{l,0}}$  one can derive:

$$\frac{1}{J_{m,0} + J_{l,0}} = J_s = |G_p(\omega_{low})| \quad (17)$$

$$J_{m,0} = \frac{\omega_{ar}^2}{\omega_r^2} J_s \quad (18)$$

$$J_{l,0} = J_s^{-1} - J_{m,0} \quad (19)$$

$$k_0 = \omega_r^2 J_{c,0} \quad (20)$$

$$b_0 = \sqrt{\frac{k_0 J_{l,0}^3}{R^2 J_{l,0}^3 J_{c,0}^{-3} - J_{l,0} J_{c,0}^{-1}}} \quad (21)$$

#### 4 EXPERIMENT DESCRIPTION

The experimental testbench is formed by the long torque shaft connected to the Permanent magnet synchronous motor (PMSM) and the flywheel (1 kg and 10 cm diametral) placed at the other end of the shaft. The electrical part of the PMSM is considered to be controlled by the Field-oriented control strategy and its design is omitted in this paper. And the whole electrical part of the PMSM is abbreviated into a simple torque generator following:  $T_i = i_q K_i$ . Where  $i_q$  is the current applied on the q-axis and  $K_i$  is the torque-current constant of the PMSM. The sampling frequency for the measurement was set to 2 kHz. The q-axis current and the shaft velocity were measured and used for the spectral analysis. As the input signal, a Pseudo Random Binary Sequence (PRBS) was used. There were 65536 samples acquired and the length of the data block (length of the periodogram) for the Welch analysis was set to 8192 samples. The complete algorithm was implemented at the dSPACE DS1103 platform. In the Figure 2 (a) there are two estimates of the (5). The first one (red solid line)

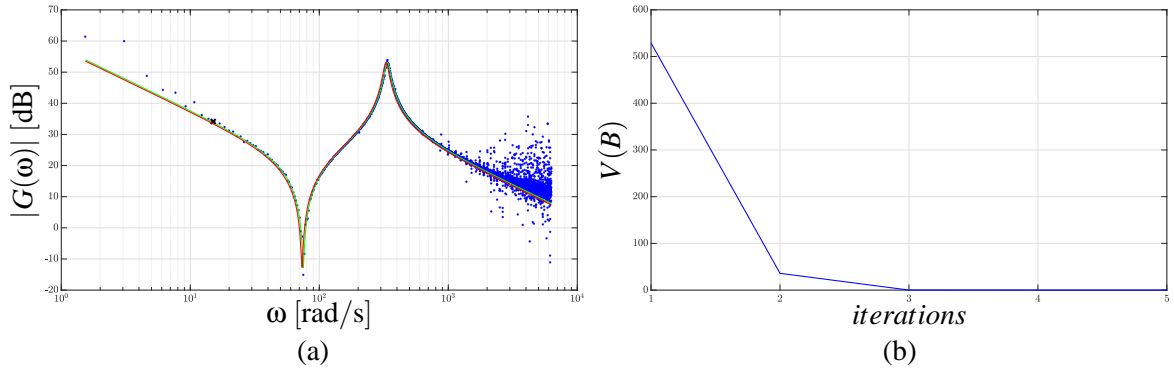


**Figure 2:** (a) - Blue dots represent curve obtained by the Welch method, red solid line stands for the model with the initial estimate and the green line is the model given by the Levenberg-Marquardt algorithm. The black cross is an additional point. (b) - Value of normalized cost function over the iterations

is obtained with the initial parameter estimate based on the Welch method. The second one (green) is obtained as the final value of the parameters estimate by the Levenberg-Marquardt algorithm. In Figure 2 (b), there is the normalized value of the cost function with which the algorithm is optimized. The cost function formula can be obtained from (13) as follows:

$$V(B) = \frac{1}{N} (|G_p(\omega, B)| - |\hat{G}_p(\omega)|)^T (|G_p(\omega, B)| - |\hat{G}_p(\omega)|) \quad (22)$$

where  $N$  is the number of the curve data points obtained by the Welch method (blue points in Figure 2 (a)). One can see, that the convergence of the cost function is fast. The minimum of (22) is found within the 5 iterations. The value of  $\lambda$  was set to  $\lambda = 0.75$  and the value of  $\Delta$  was set to  $\Delta = 1 \cdot 10^{-1}$ . The ending condition of the algorithm is given by the maximum number of iterations and the minimum change of the  $B$  parameters and minimum change of the cost function  $V(B)$ . Both are given by the value of  $\Delta$ .

Parameter	Welch	Levenberg-Marquardt	theoretical
$J_m$	$6.45 \cdot 10^{-5} \text{ kg} \cdot \text{m}^2$	$6.76 \cdot 10^{-5} \text{ kg} \cdot \text{m}^2$	$6.5 \cdot 10^{-5} \text{ kg} \cdot \text{m}^2$
$l$	$1.31 \cdot 10^{-3} \text{ kg} \cdot \text{m}^2$	$1.33 \cdot 10^{-3} \text{ kg} \cdot \text{m}^2$	$1.3 \cdot 10^{-3} \text{ kg} \cdot \text{m}^2$
$k$	$6.75 \text{ kg} \cdot \text{m}^2 \cdot \text{s}^{-2}$	$6.95 \text{ kg} \cdot \text{m}^2 \cdot \text{s}^{-2}$	$7 \text{ kg} \cdot \text{m}^2 \cdot \text{s}^{-2}$
$b$	$2 \cdot 10^{-3} \text{ kg} \cdot \text{m}^2 \cdot \text{s}^{-1}$	$3 \cdot 10^{-3} \text{ kg} \cdot \text{m}^2 \cdot \text{s}^{-1}$	$3 \cdot 10^{-3} \text{ kg} \cdot \text{m}^2 \cdot \text{s}^{-1}$

**Table 1:** Parameters comparison

In Table 1, there are results compared with the theoretical values. Theoretical values are obtained from the geometric attributes of the testbench (flywheel diameter, shaft length, shaft diameter, and shaft shear modulus). The inertia higher values are caused by the omitted additional connections in the testbench (flexible couplings etc.).

## 5 CONCLUSION

The main goal of this paper was to demonstrate the possible use of Welch spectrum analysis with the Levenberg-Marquardt algorithm for the motor drive plants with the two-mass mechanical load parameter estimation. The Welch method was used to create an initial estimate for the Levenberg-Marquardt algorithm. This algorithm found the minimum of (22) within the 5 iterations. Obtained results are presented and briefly discussed.

## ACKNOWLEDGEMENT

The completion of this paper was made possible by the grant No. FEKT-S-20-6205 - “Research in Automation, Cybernetics and Artificial Intelligence within Industry 4.0” financially supported by the Internal science fund of Brno University of Technology.

## REFERENCES

- [1] Antoine Boutros, Philippe El-Jurdi, Hadi Y. Kanaan, and Kamal Al-Haddad. Modeling and simulation of a complex mechanical load using the multi-mass approach. *Proceedings of the Mediterranean Electrotechnical Conference - MELECON*, (April):373–379, 2014.
- [2] Peter D. Welch. The Use of Fast Fourier Transform for the Estimation of Power Spectra: A Method Based on Time Averaging Over Short, Modified Periodograms. *IEEE Transactions on Audio and Electroacoustics*, 15(2):70–73, 1967.
- [3] Ming Yang, Weilong Zheng, Kaixuan Yang, and Dianguo Xu. Suppression of mechanical resonance using torque disturbance observer for two-inertia system with backlash. *9th International Conference on Power Electronics - ECCE Asia: “Green World with Power Electronics”, ICPE 2015-ECCE Asia*, pages 1860–1866, 2015.
- [4] George Ellis and Robert D. Lorenz. Resonant load control methods for industrial servo drives. *Conference Record - IAS Annual Meeting (IEEE Industry Applications Society)*, 3:1438–1445, 2000.
- [5] Ondrej Bartik. PARAMETER IDENTIFICATION OF THE TWO-MASS MECHANICAL FLEXIBLE SYSTEM USING WELCH METHOD. *Proceedings of the 25th Conference STU-DENT EEICT 2019*, (1):561–565, 2019.
- [6] Roger Fletcher. A Modified Marquardt subroutine for non-linear least squares. *H. M. Stationery Office, Harwell, Berkshire*, pages 1–28, 1971.

# FIR FILTER RESONANCE COMPENSATION FOR RANDOM VIBRATION GENERATION

**Jan Kunz**

Doctoral Degree Programme (4), FEEC BUT

E-mail: xkunzj00@stud.feec.vutbr.cz

Supervised by: Petr Beneš

E-mail: benesp@feec.vutbr.cz

**Abstract:** This paper deals with a random vibration generation on vibration shakers using a FIR filter. Every shaker has its resonances and anti-resonances which causes troubles in random vibration generation, for instance in presented shaker the difference between maximum and minimum in frequency characteristic is nearly 50 dB. Therefore, we decided to create a FIR filter with inverse characteristic with respect to the shaker to minimize those differences. To design such a filter a frequency characteristic of the shaker has to be measured, then the characteristic is simplified using Ramer–Douglas–Peucker algorithm. Finally, the characteristic is inverted and FIR filter is designed using Remez algorithm. Using this FIR filter the difference in frequency characteristic drops from 50 dB to less 2 dB.

**Keywords:** Mechanical vibration, random vibration, FIR filter, resonance

## 1 INTRODUCTION

Mechanical vibrations are essential part of environmental testing procedure, because everything is, during its lifetime, exposed to vibration. Different equipment are exposed to different types of vibration based on their purpose and destination. For this reason, there exist many different testing procedures, for instance for industrial equipment, cars, aerospace, etc. However all these procedures are using sine, sweep sine, or random vibration to test the devices. Therefore generation of such a signal is necessary for the testing. Moreover, mechanical vibrations are also used in other areas, such as modal analysis, energy harvesters characterization, and mechanical sensor testing.

The vibrations are usually performed on electrodynamic shakers, which can be easily driven by electrical signal. On the other hand, the description of electrical and mechanical parameters and their mutual influence is complex and can be found in [1]. In general, the parameters and their mutual influence results in resonances and anti-resonances, which has to be taken into account when driving these shakers.

Traditional approach to control random vibrations is based on narrowband filters and control of the effective value (rms) of the vibrations [1]. Nowadays, with increased computational power new algorithms and methods have been developed, for instance robust methods [2], precision methods [3], or energy efficient methods [4]. Unfortunately, these methods are not suitable for low computational power systems.

Commercially available vibration driving software firstly identifies the system to find their main resonances and anti-resonances and then uses sophisticated control algorithms to keep the amplitude of the vibration within specified range. Therefore, these control systems are expensive and does not allow further modifications. So, this solution is not suitable for occasional testing and research. For this reason we decided to develop our own vibration control system.

We have already developed a control system capable of sine and sweep sine vibration control, where

signal effective value is controlled via PID controller [5]. This system is working quite well if the resonances and anti-resonances have lower quality factor and are sparsely distributed. Otherwise, the system is not able to control the amplitude properly.

Nevertheless, the resonances can have a high quality factor and especially resonance and anti-resonance can be very close to each other. Moreover, the need for simple vibration noise control system still lasts. For these reasons, we have decided to develop a new control system.

## 2 RANDOM VIBRATION CONTROL

Random vibrations are usually defined as a vibration with constant power spectral density on specified frequency range, the maximal amplitude error is usually  $\pm 3$  dB. This is quite challenging to achieve, due to resonances and anti-resonances in the system.

A recommended way how to achieve a white noise on vibration shakers, is to divide the frequencies spectrum to several narrower ones, where the amplitude is controlled independently [6]. This attitude is versatile, but require a lot of computational power to filter input and output data. Therefore, this algorithm is not suitable for distributed systems like NI CompactRIO.

For this reason, we decided to create a FIR filter with inverse characteristic of the vibration system and using it to filter the input data for the shaker so, the system should have a constant frequency characteristic. Then, a PID controller can easily control the amplitude of the vibration. This system is less computational demanding than the aforementioned method, so it can be used on NI CompactRIO. Moreover, this filter can be also used in our current sine control system to improve its properties. On the other hand, for a different shakers, or load on shaker a new filter needs to be created.

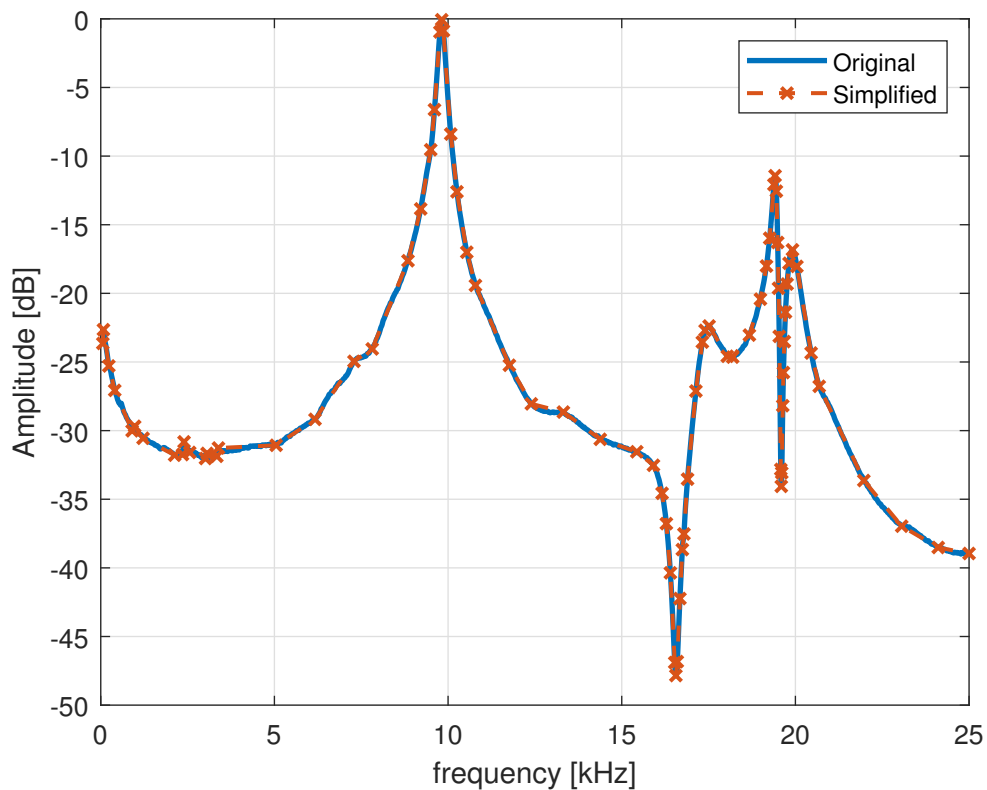


**Figure 1:** Frequency characteristic of vibration shaker - measured and after simplification using Ramer–Douglas–Peucker algorithm

## 2.1 INVERSE FILTER

The frequency characteristic of the shaker is created using ratio of frequency spectra of the output and input signal with 1 Hz resolution. The data are generated and measured using NI PXI 6363 card. To minimize the error, the characteristic is created by averaging 1000 measurement. Nevertheless, the resulted spectrum were still quite noisy therefore, a spline filter was used. The filtered frequency characteristic is visible in the figure 1.

To create a FIR filter according to specific frequency characteristic a Remez exchange method was selected [7]. There has to be enough input data to interpret the shape properly, however there cannot be too much of the data due to numerical stability. In our case, the algorithm is stable if the input data are a few hundreds samples long. And the maximum distance between samples is 100 Hz, otherwise the algorithm creates peaks or notches between those points. For this reason, it is necessary to process the data to describe the shape properly, but contain only a few hundreds of samples.

For this reason, the frequency characteristic was simplified using Ramer–Douglas–Peucker algorithm [8]. This algorithm remove points which can be replaced by line segment within a specified tolerance. This method simplified the frequency characteristic to 84 points (figure 1). However, this method keeps some wide areas without any point. Therefore, if there is an area larger than 100 Hz without a point, one is added. The resulted characteristic is described by 298 points.

Then, the data are inverted to create the inverse filter and the FIR filter is created using aforementioned Remez algorithm. The length of the filter was determined experimentally to 2001 samples. The frequency characteristic of the filter is visible in the figure 2.

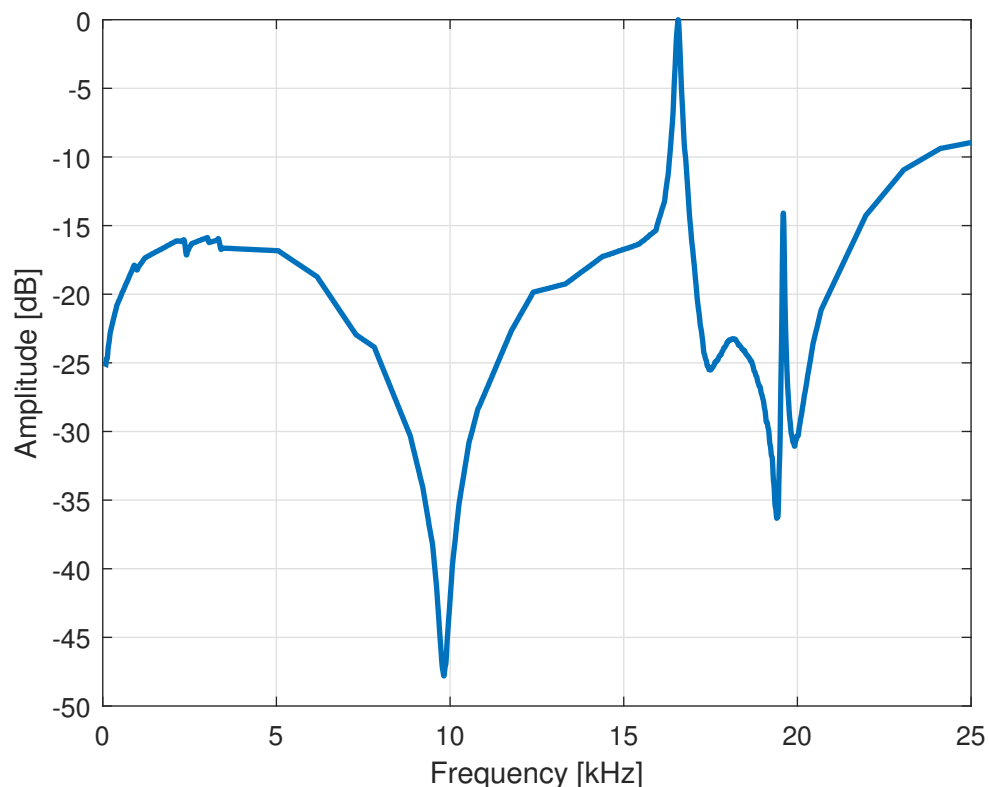


**Figure 2:** Frequency characteristic of the FIR filter

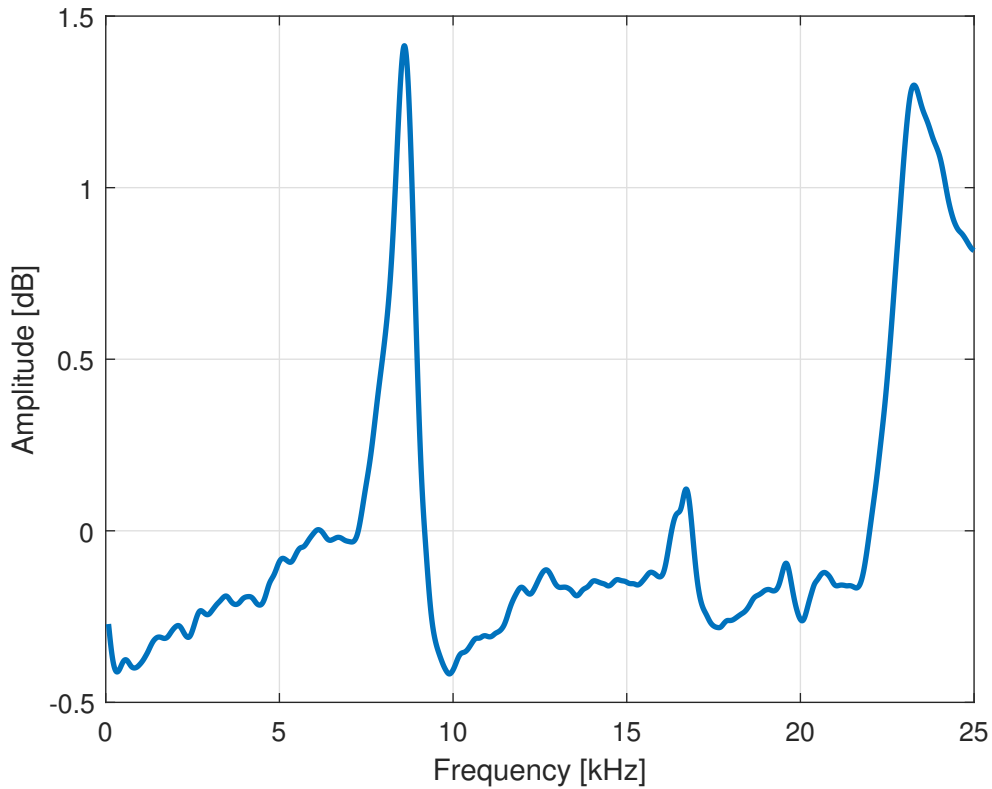


**Figure 3:** Resulted spectrum of the vibration

## 2.2 VIBRATION GENERATION

The FIR filter is used to filter the input white noise data to the vibration shaker to minimize its resonances. The amplitude of the vibration is controlled using simple PI controller. The spectrum of the vibration signal on the vibration shaker is visible in the figure 3. In the resulted spectrum are still visible some traces of the original resonances, however the overall error is smaller than 2 dB, which is within the limits described by [6]. Therefore, this method can be used to generate random vibration.

## 3 CONCLUSION

In this paper we describe a method of generation a random vibration with constant power spectral density. To do that a shaker resonances has to be suppressed. In our case, we do this using FIR filter. To design such a filter we need the frequency characteristic of the shaker, which can be easily measured using the input and output signal spectrum ratio. Then, from the spectrum are using Ramer–Douglas–Peucker algorithm extracted important points, which are then inverted and used to design FIR filter using Remez exchange method.

The resulted FIR filter is then used to filter the input signal to the shaker. The resulted system has more or less constant frequency characteristic. The differences in the resulted spectrum are smaller than 2 dB, which is great improvement because the in the original spectrum were nearly 50 dB. The effective value of the vibration is then controlled by simple PID controller.

Moreover, this method can be used also in sweep sine vibration to overcome the resonances and anti-resonances. On the other hand, The FIR filter has to be designed for different vibration shakers and loads, as it can change the resonances. However, the FIR filter can be easily created, so this constrains

does not cause much difficulties.

Unlike the standard approach, this method is not able to reflect runtime changes in the frequency characteristic of the vibration system, which can be caused for instance by temperature. On the other hand, it is possible to update the inverse filter during vibration generation, however this will largely increase needed lot of computational power, so in that case a standard approach seems to be a better option. Nevertheless, in applications with minor runtime frequency characteristic changes this method can be used.

## ACKNOWLEDGEMENT

The completion of this paper was made possible by the grant No. FEKT-S-20-6205 - “Research in Automation, Cybernetics and Artificial Intelligence within Industry 4.0” financially supported by the Internal science fund of Brno University of Technology.

## REFERENCES

- [1] Cyril M Harris and Allan G Piersol. *Harris' shock and vibration handbook*, volume 5. McGraw-Hill New York, 2002.
- [2] Y. Uchiyama and M. Fujita. Robust acceleration and displacement control of electrodynamic shaker. In *2006 IEEE Conference on Computer Aided Control System Design, 2006 IEEE International Conference on Control Applications, 2006 IEEE International Symposium on Intelligent Control*, pages 746–751, 2006.
- [3] G. Guan, W. Xiong, and H. Wang. Random vibration control based on adaptive filter. In *2010 IEEE International Conference on Mechatronics and Automation*, pages 1825–1830, 2010.
- [4] Chang-Ming Liaw, Wen-Chin Yu, and Thin-Huo Chen. Random vibration test control of inverter-fed electrodynamic shaker. *IEEE Transactions on Industrial Electronics*, 49(3):587–594, 2002.
- [5] Čala Martin. Few issues related to an electrodynamic exciter control. In *Proceedings of the 21st Conference STUDENT EEICT 2015*, pages 450–454, april 2015.
- [6] IEC:60068-2-64. *Environmental testing - Part 2-64: Tests - Test Fh: Vibration, broadband random and guidance*, 2 edition, 2008.
- [7] James McClellan and T Parks. A unified approach to the design of optimum fir linear-phase digital filters. *IEEE Transactions on Circuit Theory*, 20(6):697–701, 1973.
- [8] David H Douglas and Thomas K Peucker. Algorithms for the reduction of the number of points required to represent a digitized line or its caricature. *Cartographica: the international journal for geographic information and geovisualization*, 10(2):112–122, 1973.

# MEASUREMENT SYSTEM FOR DETERMINING FORCES ACTING ON LOOSE CONCRETE ROOF PAVER

**Vlastimil Mancl**

Doctoral Degree Programme 1, FEEC BUT

E-mail: xmancl00@stud.feec.vutbr.cz

Supervised by: Petr Beneš

E-mail: benesp@feec.vutbr.cz

**Abstract:** This paper introduces the topic of measuring the wind-induced forces on a concrete roof pavers. It describes the creation of a system, allowing such measurements and it also proposes two methods. First discussed method is measuring differential pressure. The second is measuring the weight of a roof paver. This article proved, that those methods can give meaningful results and that the future research should continue to use and improve this measurement system.

**Keywords:** CompactRio, Differential pressure measurement, Gust induced forces, LabVIEW, Load cell, Loose concrete roof paver, Pressure, Scale, Wind, Wind induced forces.

## 1 INTRODUCTION

The influence of wind has been a subject of research for ages. One of its aspects is its ability to demolish land objects such as buildings. Hurricanes, for example, are on a par with earthquakes in terms of environmental loads for buildings. [1, 2] For that reason construction industry is constantly trying to reinvent building procedures to build structures, which can withstand the forces of strong winds. On the contrary every time a building is being constructed, there is also a significant focus on price. Stronger constructions are more expensive than the less robust. With this in mind we can say, that it is important to know where is the border when forces, caused by wind, becomes dangerous to people or buildings. Because when we know the border, then we can build construction durable enough to withstand strong winds, but not overly strong which would be unnecessarily expensive.

The most stressed part of a building during strong winds such as hurricane is the roof. Most of the industrial structures, offices or commercial buildings etc. uses flat roofs, which are constantly under the influence of flow of wind. More stronger winds can cause significant uplifting forces, which then leads to damage of the roof or in a worse scenario, to separation of a roof from the rest of the building.

Flat roofs are usually covered with loose concrete roof pavers. Pavers are not only used on roofs, but they are commonly used in construction of podiums or small city squares etc.. Loose concrete pavers are heavy, relatively thin concrete blocks, which are resting on a pads, made usually from plastic. That means, that only the gravity force is holding them in place. The flow of wind creates difference between external (over the paver) and internal (under the paver) pressure and that creates an uplifting force. If the uplifting force is larger than the gravity force, then the concrete pavers dislodge and can transform into an airborne missiles. So its important to know, how the pavers are influenced by the wind flow.

The main focus of this research is to measure and determine pressures acting on loose concrete roof pavers. First necessary step was to decide what method to use for measuring those forces. The measurement of differential pressure method was selected as one of the first methods. This method is comparing pressure over and under the paver and determines difference between them. To determine if the data from differential method are meaningful, the measurement of paver weight was used.

After the sensors were chosen, the measurement system could be made. This article is about that measurement system, its components, properties and future plans for making this system better.

## 2 DEVICES

Sensor DLH-L05D-E1BD-C-NAV8 from company Amphenol All Sensors was chosen for measuring differential pressure. This sensor has two pressure inputs. The measuring range of this sensor is  $\pm 1.250$  kPa with typical precision of  $\pm 0.20\%$  from fullscale[3]. This range was estimated based on the measurement made by Aly Mousaad Aly et al.[4]. They measured maximum of 1.419 kPa during their test with wind speed up to 28.48 m/s with simulation of turbulence and wind gusts [4]. Test of Aly Mousaad Aly et al. was slightly different in nature so we decided to use measurement range mentioned above. The sampling frequency is up to 230 Hz. This sensor communicate through I<sub>2</sub>C interface.

The reason was also because wind, with velocity of 28.48 m/s is declared as violent storm in Beauforts scale [5]. We do not expect stronger winds in the place of the measuring.

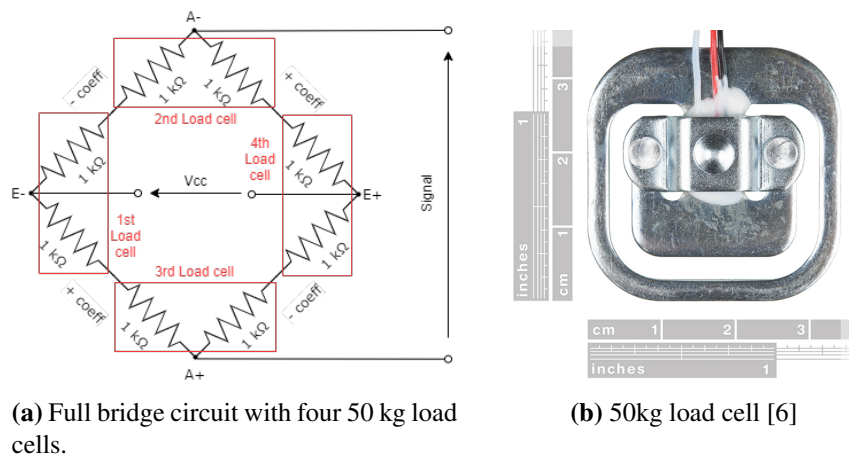


**Figure 1:** 50 kg load cell and its usage in making full bridge circuit.

The second sensor, was the load cell, used to measure weight of the concrete paver this sensor can be seen in figure 1b. This load cell is simply called “Load Sensor - 50kg” by the manufacturer Sparkfun. The four of this load cells were used for supporting each corner of the paver, which weighs 27 kg. The load cells measurable weight range is up to 50 kg. Manufacturer states, that if you use 4 of them, then the range is up to 200 kg[6]. This load cells were used, because they were already available in our department. They are sufficient for proofing pressure measuring, but load cell with smaller range should be used in future for more precise measuring.

The load cell is made out of metal beam and two strain gauges, which are glued to the metal beam made for transition of forces. Two 1 kΩ strain gauges are connected to the half-bridge. This half bridge has 3 outputs. The strain gauges has opposite resistance coefficients in the same direction of deformation. This property is utilized for building full bridge with four load cells. The four load cells are put under plate to create a scale. The circuit of a full bridge can be seen in figure 1a.

The opposite coefficient ensures that measured load can be anywhere on the plate and still be measured correctly. So the measured weight is not dependent on load position on a plate. In case of this experiment the plate is the paver and simultaneously the load.

The full bridge is powered and measured by circuit board HX711, which contains 22-bit AD converter. This converter then communicates through proprietary interface. Creation of a special software, to communicate with this interface, was needed. The sampling frequency is up to 12 Hz.

The data from the sensors are being gathered by measurement cards for CompactRIO from the National Instruments. This device is placed in nearby wiring closet, where it is connected to the WAN network, from where the data flow is redirected to the PC through TCP/IP interface. All of the measured data are being saved on the PC. All software for communication and data management had to be created for the purpose of this research. Also the calibration of the weight had to be performed. All of this was a significant part of the research, but this article doesn't focus on that.

### 3 METHODOLOGY AND CONFIGURATION

As mentioned before, the differential pressure is being determined from pressure under and over a concrete paver, which is placed on a roof of a building of Faculty of electrical engineering and communication in Brno. The placement of the paver is half meter from a ledge which is 40 cm high parapet. The other ledges are more than 2 meter distant.

The paver is in lee of that parapet. We can presume that the parapet is causing turbulence and thus slowing the wind speed. That is the reason why the  $\pm 1.250$  kPa range for pressure sensor was chosen. Placement of the paver on the roof can be seen in figure 2a.

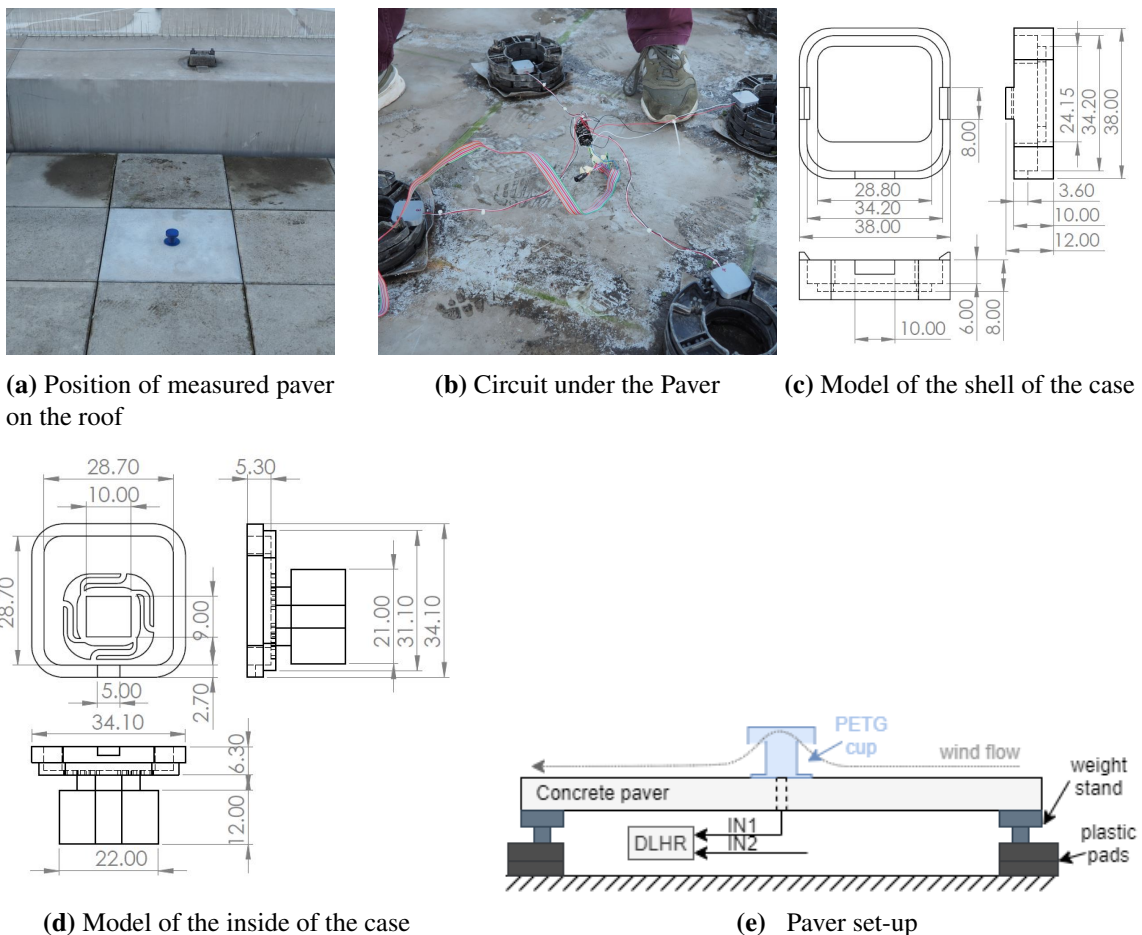


**Figure 2:** Placement of the paver. Circuit underneath the paver and model of the load cell case

The load cells are placed in custom made cases. Those cases were designed in SolidWorks 2017 and printed from PETG material on a 3D printer. This material should be durable enough to withstand at least a half of a year in harsh conditions. Case is made from two parts, the inside and the shell. The shell is made to be in contact with the paver. It is designed to keep the load cell in place and to allow flex of the inner beam with strain gauges. The inside part of the case is made for fixing the load cell

in place. Its another purpose is to transmit the stress trough stand and little metallic sheet to the inner beam to cause flex of the strain gauges. Whole case is high enough to sit in the plastic pads and still elevate the paver to the level of the rest of the pavers, so the measured paver doesn't stick out. The cases and their placement can be seen in figure 2b. The models and dimensions of the case parts are shown in figure 2c and 2d.

The reason for measuring weight is, that without the wind flow the weight of the paver would be stable over time. But when the wind start flowing, the uplifting forces will act against the gravitational force. Resulting force of the paver against the roof (or the scale) will be lower, so will be the measured weight. Weight can be transformed directly into force and then into a pressure. This principle is used in section 4. Resulting paver setup is shown in the figure 2e.

#### 4 MEASURED DATA AND RESULTS

The measuring was running all day from 10. 2. 2020 to 17. 2. 2020. During this time span the Sabina storm hit most of the Europe. The data were stored in files, which were saved every hour. The wind speed that day in Brno, was up to 11 m/s and the gust speed was up to 25 m/s [7].

The data from that day were put trough algorithm for signal processing, created in LabVIEW 2017. This algorithm removes DC part from both signals and uses Furrier transform for re-sampling the signal from weight sensors. The re-sampling was needed for making correlation possible. A slow drift of a signal from weight sensors could be seen. This drift was caused by temperature changes.

The pressure sensor is compensated, in terms of temperature changes, but not the weight sensors. Fortunately we can presume that variation of the signal in dependency on temperature is much slower than the variation caused by wind. So the filtration of low frequencies was performed to remove temperature dependency.

Correlation followed after the filtration and re-sampling process. The results of correlation showed that those two signal are very similar to each other, but also showed that the signal from weight sensors is delayed. The results of correlation made possible do determine how much should be the slower signal shifted in time so we could see the overlap. The signal processing section is also a very significant part of the research, but its not the focus of this article.

In the figure 3a we can see data after signal processing but before the time shift. The resulting overlap can be seen in figure 3b. This similarity is proving, that both sensors are measuring similar signals.

The area around 2045th second in figure 3 shows significant variation in measured weight and differential pressure. This was caused by strong gust. The difference of the pressure is 151.9 Pa. The difference in weight is 1602 g. That is 15.71 N. If we use pressure equation, where F is the uplifting force and the S is the surface area of a paver:

$$p = \frac{F}{S} = \frac{15.71}{0.5^2} = 62.84 Pa \quad (1)$$

Then we get the pressure of 62.84 Pa. This is significantly different. The possible reasons will be discussed in conclusion.

#### 5 CONCLUSION

In this research the measurement system for measuring forces acting on a roof paver, was created and proved to be functional. The research also showed, that the data from weight scale and from pressure sensor are similar and meaningful. Several tools were utilized in creation of this system, such as 3D printing, virtual instrumentation or signal processing in LabVIEW.

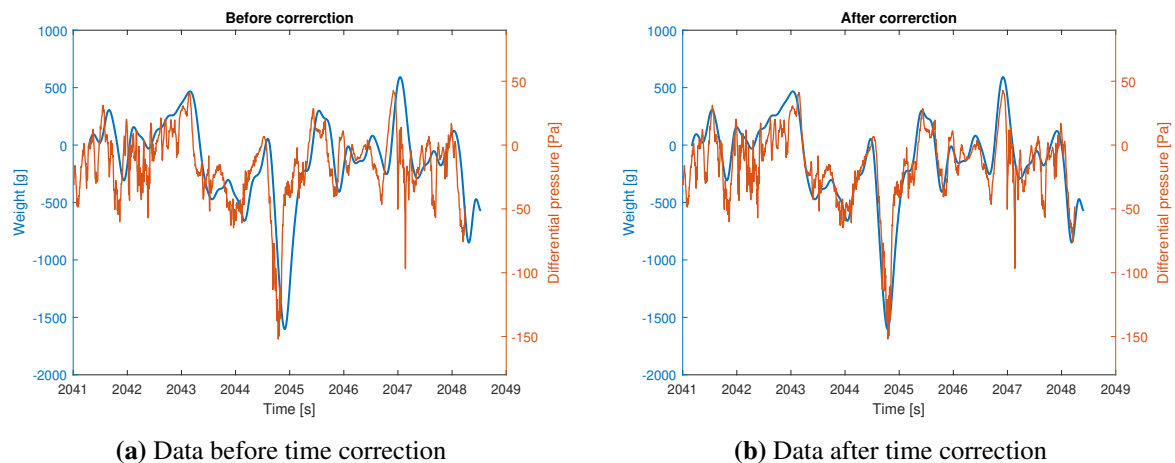


**Figure 3:** Part of the data measured on 10th of February 2020 at 17:00, showing the strong gust.

The final pressure values are different, but that could be caused by the plastic cap, protecting pressure sensor from the water. It is possible that it disturbs the flow of the wind and causes turbulence. The dependency of a cup shape on a pressure should be object of the future study.

Another future step should be determining the uncertainties and to extend the measurement to the adjacent pavers to create a measurement matrix. That would mean that we could measure the distribution of pressure in larger area and possibly determine the direction or the speed of the wind. In addition, the next iteration of this system should include directional anemometer.

## ACKNOWLEDGEMENT

The completion of this paper was made possible by the grant No. FEKT-S-20-6205 - “Research in Automation, Cybernetics and Artificial Intelligence within Industry 4.0” financially supported by the Internal science fund of Brno University of Technology.

## REFERENCES

- [1] Holmes DJ. *Wind loading of structures*. London: Spon Press; 2001.
- [2] Simiu E, Scanlan RH. *Wind effects on structures, fundamentals, and applications to design*. 3rd ed. New York: Wiley-Interscience; 1996.
- [3] All Sensors. *DLHR - Low Voltage Digital Pressure Sensors Series*. DS-0350 Rev C. 16035 Vineyard Blvd. Morgan Hill, CA 95037.
- [4] ALY, Aly Mousaad, Girma T BITSUAMLAK a Arindam Gan CHOWDHURY. *Full-scale aerodynamic testing of a loose concrete roof paver system*. *Engineering Structures* [online]. Elsevier, 2012, 44(C), 260-270 [cit. 2020-03-15]. DOI: 10.1016/j.engstruct.2012.05.008. ISSN 0141-0296.
- [5] Met Office. *National Meteorological Library and Archive Fact sheet 6 — The Beaufort Scale*. ver 01. National Portrait Gallery, London. 2010. United Kingdom.
- [6] SparkFun Electronics. *Load Sensor - 50kg*. [website] USA. Available from URL: <<https://www.sparkfun.com/products/10245>>. [cit. 2020-3-15]
- [7] InMeteo. *In-pocasi - Brno - Turany*. [website]. Czechia, Pilsen. Available from URL: <[https://www.in-pocasi.cz/archiv/brno/detailed?\\_typ=vitr&historie=202002-10&detailed\\_usek=24#daily\\_graph](https://www.in-pocasi.cz/archiv/brno/detailed?_typ=vitr&historie=202002-10&detailed_usek=24#daily_graph)>. [cit. 2020-3-15]

# SEMI-SUPERVISED DEEP LEARNING APPROACH FOR BREAKING GEOCACHING CAPTCHAS

**Ondrej Bostik**

Doctoral Degree Programme (4), FEEC BUT

E-mail: bostik@feec.vutbr.cz

Supervised by: Karel Horak

E-mail: horak@feec.vutbr.cz

## **Abstract:**

For nearly two decades, a substantial part of developed anti-abuse and anti-spam systems for web applications called CAPTCHA is based on imperfections in OCR (Optical Character Recognition) algorithms. But with improvements in Deep Learning in OCR, these systems are now obsolete. More and more systems can now break various text Captchas with great accuracy. Now with sufficient training dataset, almost every text-based Captcha scheme can be broken.

The focus of this work is to present an idea of a semi-supervised method for reading text-based Captcha which needs only a small initial dataset. The main part of this article is dealing with the problem of training a deep learning system with only a small sample of target Captcha scheme via transfer learning.

**Keywords:** OCR, CAPTCHA, Deep learning, semi-supervised learning, MATLAB

## **1 INTRODUCTION**

Common most used approach to Captcha (Completely Automated Public Turing Test to tell Computers and Humans Apart) implementation for web services is based on OCR (Optical Character Recognition) problem. Current OCR algorithms can be very robust, but they have some weaknesses. This imperfection limits the usage of these algorithms but can be utilized for Captcha purposes with great advantage. The server sends an image with a sequence of characters to the client-side. This image is prepared in a way that uses known OCR issues against the artificial solver (computer). At the same time, as the Captchas become more and more robust, people who try algorithmically solve this kind of Captcha challenge helps to improve the OCR algorithm [1].

This kind an iteration process helps both sides, but development advanced so far, that current Captcha schemes are very complex for humans and the computers have a significantly higher success rate than humans. Many current Captcha challenges are so complicated, that humans cannot solve them, but machines can. Automated versatile systems for cracking Captcha can beat many schemes without any kind of human interaction. Some of these systems can be tweaked to learn new unknown Captcha challenge. As previous research has shown, this kind of system can overcome almost any possible Captcha scheme with a high success rate [2, 3, 4].

Most recent attacks use convolutional neural networks (CNN) in combination with other techniques. For example in [5] Gao et al utilized CNNs in the first phase for feature extraction and Long short-term memory for actual recognition. Another similar work was presented in [6], where 2 deep nets were used, one estimating the length of the text, the other using this information to get the supposed correct answer. The disadvantage in both works are in the need to build a large annotated dataset for initial system learning.

This disadvantage is bypassed by the system in [7]. The system use a small annotated sample (about 500pcs) to learn the generator of synthetic Captcha codes of the same style. The generator is based on a Generative adversarial network. The generated data is then used to train the basic version of CNN and the original data is used to fine-tune the network.

## 2 PROPOSED SOLUTION

The main idea of this paper is to use the target web-page for generating sufficient enough dataset without annotation a huge number of data. The process benefits from the fact, that the target web-page uses the Captcha to validate the input data. The target web-page needs to generate a Captcha image for every request and validate data received from the user. The attacker can easily make an autonomous system, which downloads the Captcha image, tries to guess the answer (with a random answer or with a Captcha breaking system) and send it to the server. The attacker is automatically notified by the server, whether the sent answer is correct or not. With the use of distributed attacks and the great number of attempts, the attacker can obtain a great number of testing samples without annotating a single Captcha image.

In this paper, the method will be tested on the annotated dataset, rather than the online test to lower the network traffic. To speed the initial phase up, the small sample of 30 images was used to pre-train the classification network as a starting point for this experiment.

### 2.1 INPUT DATASET

The dataset used in this experiment was created by downloading 16731 Captcha images from the page <http://geocheck.org> via Selenium Webdriver. This Captcha scheme used on this page consists only of numbers of the constant length of 5 digits. The implementation has a great weakness. The verification process is located at the client-side, e.g. the correct answer is present on the web page send to a user computer. The only security measure used is insecure MD5 hash. The automated Python script can download the Captcha image and break MD5 hash to obtain the right answer in less than 0.25s. This makes this Captcha scheme perfect for rapid dataset creation. The sample image from the dataset is presented in figure 1.



**Figure 1:** Sample of input dataset used for the experiments

### 2.2 IMPLEMENTATION

The entire experiment was done in MATLAB computational environment using Deep Learning Toolbox and Computer Vision Toolbox. Experiment setup and data flow is described on figure 2.

In the first stage, the 30 Captcha images was labeled via *Image Labeler* to create precise annotation of character location. Extracted regions was then used to train segmentation deep neural network [8] with layers shown on table 1. Training used algorithm called stochastic gradient descent with momentum [9], initial learning rate set to 0.001 and mini batch size of 10 for total number of 100 epochs. The class weights were set according the ratio of the classes in training data.

With this segmentation network, the initial batch of learning images was created. This RGB image contains one letter each and each was resized to 28x28px size and saved to disk with the correct label.

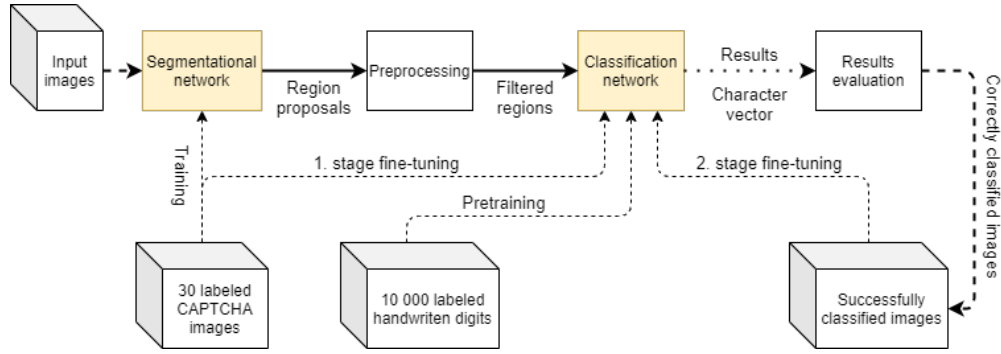


**Figure 2:** Experiment setup diagram

	Layer type	Layer description
1	Image Input	60x213x3 images with 'zerocenter' normalization
2	Convolution	32pcs 3x3x3 convolutions with stride 1 and padding 1
3	ReLU	ReLU
4	Max Pooling	2x2 max pooling with stride 2 and padding 0
5	Convolution	32pcs 3x3x32 convolutions with stride 1 and padding 1
6	ReLU	ReLU
7	Max Pooling	2x2 max pooling with stride 2 and padding 0
8	Transposed Convolution	32pcs 4x4x32 transposed convolutions with stride 2 and cropping 1
9	ReLU	ReLU
10	Transposed Convolution	32pcs 4x4x32 transposed convolutions with stride 2 and cropping 1
11	ReLU	ReLU
12	Convolution	2pcs 1x1x32 convolutions with stride 1 and padding 0
13	Softmax	Soft-max
14	Pixel Classification Layer	Class weighted cross-entropy loss with 2 classes

**Table 1:** Segmentation deep network used to classify pixels between background and foreground

The classification network was pre-train on 10000 handwritten digits dataset (1000 per digit) from Matlab demo datasets, 7500 images were used for training, 2500 for validation. The original dataset contains binary images, but for the test purposes, random color for character and background was selected and every image was colored. The structure of the network is shown in table 2. Training also uses an algorithm called stochastic gradient descent with momentum [9], an initial learning rate set to 0.01 for the total number of 4 epochs. This pre-trained network was saved as a starting point for further fine-tuning.

The pre-trained classification network was then fine-tuned using a labeled segment from the segmentation network. During the first stage of fine-tuning, 100 segments (10 per digit) were used for training, 50 for validation. The training uses the same parameters, but the number of epochs was set to 20 to make more emphasis on real data.

With both deep neural networks learned, the whole system was tested on the dataset of 16731 images. As can be seen in figure 2, every input image was segmented using the first network, preprocessed and every segment was classified. The resulted digits were compared with the ground truth. To make proper simulation of server response, the simulation only outputs true or false for the entire response, not for each digit. The correctly answered Captchas are then used to create a new dataset for next stage fine-tuning. The classification network fine-tuned on the new data and the process is repeated.

	Layer type	Layer description
1	Image Input	28x28x3 images with 'zerocenter' normalization
2	Convolution	8pcs 3x3x3 convolutions with stride 1 and padding 'same'
3	Batch Normalization	Batch normalization with 8 channels
4	ReLU	ReLU
5	Max Pooling	2x2 max pooling with stride 2 and padding 0
6	Convolution	16pcs 3x3x8 convolutions with stride 1 and padding 'same'
7	Batch Normalization	Batch normalization with 16 channels
8	ReLU	ReLU
9	Max Pooling	2x2 max pooling with stride 2 and padding 1
10	Convolution	32pcs 3x3x16 convolutions with stride 1 and padding 'same'
11	Batch Normalization	Batch normalization with 32 channels
12	ReLU	ReLU
13	Fully Connected	10 fully connected layer
14	Softmax	Soft-max
15	Classification Output	crossentropyex with '0' and 9 other classes

**Table 2:** Classification deep network used to translate image regions into corresponding characters

### 3 RESULTS OF EXPERIMENT

All experiments was realised on a laptop computer with Intel Core i5-6300HQ with 4 cores and 2.3GHz frequency. The graphic card used was NVIDIA GeForce GTX 950M. The segmentation network was trained on 30 images for 300 iterations divided into 100 epochs. The entire training time was 1 minute and 50 seconds and resulted accuracy was 94.61%.

Training of the classification net was done in iterations. The statistics of the whole process is in table 3. In the pre-training phase, the dataset was trained on a different dataset to prepare the network working on similar image data. Then the pre-trained network was saved and then the learning continues on a tiny sample of annotated data (Iteration 1). Then the correctly classified images were used to enlarge the training data and were fine-tuned the network again twice. It is depicted in the table 3, that the number of epochs was updated in every iteration to prevent over-learning.

Iteration	Training count	Test count	Test accuracy	Total epochs	Total time
Pre-training	7 500	2 500	92.16	4	1m 26s
Iteration 1	100	50	78.00	20	5s
Iteration 2	1 190	1380	95.93	10	35s
Iteration 3	15 530	5 635	99.61	4	2m 55s

**Table 3:** Training results per iteration

After each training iteration, the validation accuracy was evaluated to see the progress and to enlarge the training dataset. The main parameter in the table 4 is image accuracy. With every phase (and with more train data) the success rate per image rises significantly.

### 4 CONCLUSION

This paper presents an idea of a semi-supervised method for text-based Captcha which needs only a very small initial dataset. Previous works need thousands of samples to learn the target scheme and break it. The presented experiment presents a semi-supervised method for training the Captcha

Iteration	Image count	Segment accuracy	Image accuracy	Successfully classified images	Total time
Iteration 1	16 731	48.62%	3.07%	514	15m 40s
Iteration 2	16 731	74.58%	25.30%	4 233	20m 21s
Iteration 3	16 731	83.15%	43.71%	7 313	25m 12s

**Table 4:** Validation results per iteration

breaking algorithm with only 30 annotated images.

The following work will focus on a more general method to break Captcha schemes with more security measures, like a wider character set and various lengths.

## ACKNOWLEDGEMENT

The completion of this paper was made possible by the grant No. FEKT-S-20-6205 - “Research in Automation, Cybernetics and Artificial Intelligence within Industry 4.0” financially supported by the Internal science fund of Brno University of Technology.

## REFERENCES

- [1] K. Kaur and S. Behal, “Designing a Secure Text-based CAPTCHA,” in *Procedia Comput. Sci.*, vol. 57, pp. 122–125, Elsevier, 2015.
- [2] E. Bursztein, J. Aigrain, A. Moscicki, and J. C. Mitchell, “The End is Nigh: Generic Solving of Text-based CAPTCHAs,” 2014.
- [3] H. Gao, J. Yan, F. Cao, Z. Zhang, L. Lei, M. Tang, P. Zhang, X. Zhou, X. Wang, and J. Li, “A Simple Generic Attack on Text Captchas,” in *Netw. Distrib. Syst. Secur. Symp. (NDSS 2016)*, 2016.
- [4] O. Bostik and J. Klecka, “Recognition of CAPTCHA Characters by Supervised Machine Learning Algorithms,” in *15th IFAC Conf. Program. Devices Embed. Syst. PDES 2018*, (Ostrava), p. 6, IFAC-PapersOnLine, 2018.
- [5] Y. Zi, H. Gao, Z. Cheng, and Y. Liu, “An End-to-End Attack on Text CAPTCHAs,” *IEEE Trans. Inf. Forensics Secur.*, vol. 15, pp. 753–766, 2020.
- [6] M. Tang, H. Gao, Y. Zhang, Y. Liu, P. Zhang, and P. Wang, “Research on Deep Learning Techniques in Breaking Text-Based Captchas and Designing Image-Based Captcha,” *IEEE Trans. Inf. Forensics Secur.*, vol. 13, pp. 2522–2537, oct 2018.
- [7] G. Ye, Z. Tang, D. Fang, Z. Zhu, Y. Feng, P. Xu, X. Chen, and Z. Wang, “Yet Another Text Captcha Solver: A Generative Adversarial Network Based Approach,” in *Proc. 2018 ACM SIGSAC Conf. Comput. Commun. Secur., CCS ’18*, (New York, NY, USA), pp. 332–348, Association for Computing Machinery, 2018.
- [8] K. Horak and R. Sablatnig, “Deep learning concepts and datasets for image recognition: overview 2019,” No. March 2016, p. 100, 2019.
- [9] K. P. Murphy, *Machine Learning: A Probabilistic Perspective*, vol. 27. Cambridge, MA: The MIT Press, 1. edition ed., 2012.

# COMPUTING PLATFORMS FOR DEEP LEARNING TASK IN COMPUTER VISION

**Lukas Kratochvila**

Doctoral Degree Programme (1), FEEC BUT

E-mail: kratochvila@feec.vutbr.cz

Supervised by: Karel Horak

E-mail: horak@feec.vutbr.cz

**Abstract:** The recent progress in machine learning in computer vision guides to enormous hardware requirements. This paper discovers new innovative hardware capable of dealing with immense demands. The important decision is concentrating on task learning or the final classification. The main concern is on five domains: single-board computers, hardware accelerators, graphics cards, workstations, and cloud computing. These devices have several key features for detection that are discussed. Cloud computing is another presented approach. Furthermore, different delivery models of cloud computing are addressed.

**Keywords:** Deep learning, Hardware, Cloud computing

## 1 INTRODUCTION

The recent development in machine learning leads to the use of large data sets and time-consuming algorithms. A deep learning field especially needs immense resources as it is mentioned in [1]. The progress creates huge demand on hardware. The most time-consuming part is learning a model because we have to work with large data sets. On the other hand, the final classification could be done with less computing and resource demands, therefore, it can be used as hardware solution with limited resources.

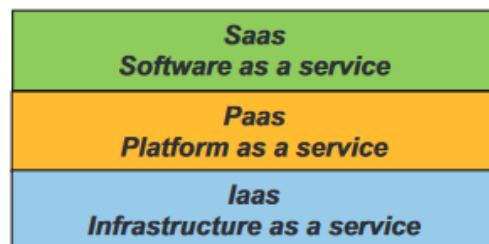


**Figure 1:** Cloud delivery models [2]

The hardware advances and we can see a new device development, e. g. Graphical Processing Units (GPU) or Tensor Processing Unit (TPU). Or we can use specific graphic cards to learn a model. These tools are employed mainly with rendering a 2D view from a 3D object. Another devices are workstations specialized in deep learning and hardware accelerators. Beside the presented devices, new equipment with limited resources, has been developed. An example can be a single-board device capable of running an operating system. This kind of device still can be used for computer vision [3].

Another option is the use of cloud service. Then we can use the advantages of the cloud. Kapil and all [2] suggest these advantages: efficient use of hardware, better and cheaper backup and disaster recovery, better management, ability to set up and test new machines, fewer network infrastructures, lower power and cooling costs, lower co-location costs and better security.

In this task it is essential to make a decision, if we will use the hardware for learning a new model or for computing the final classification. The most common arrangement is to apply cloud computing, workstations or GPU graphic cards for learning and embedded devices for the final classification.

National Institute of Standards and Technology defines standard cloud services, which can be divided into three delivery models. The first option is infrastructure as service (IaaS), the second option is

platform as a service (Paas), and the third option is software as a service (Saas). This division could be seen in Fig 1. We can distinguish the hierarchy of the models. Each level integrates levels below. The IaaS offers only virtualized hardware resources, like storage, or server. The Paas delivery model proposes a platform for the client to develop, debug and build. The Saas providers are e.g. BigML, BitYota, Precog, Google prediction API, EigenDog, Metamarkets, Myrrix, PriorKnowledge Veritable API or Predictobot [4]. Another view is in Fig. 3. The conceptual model of the cloud is in Fig 2. We can see that the delivery models are just a part of the whole conceptual model.

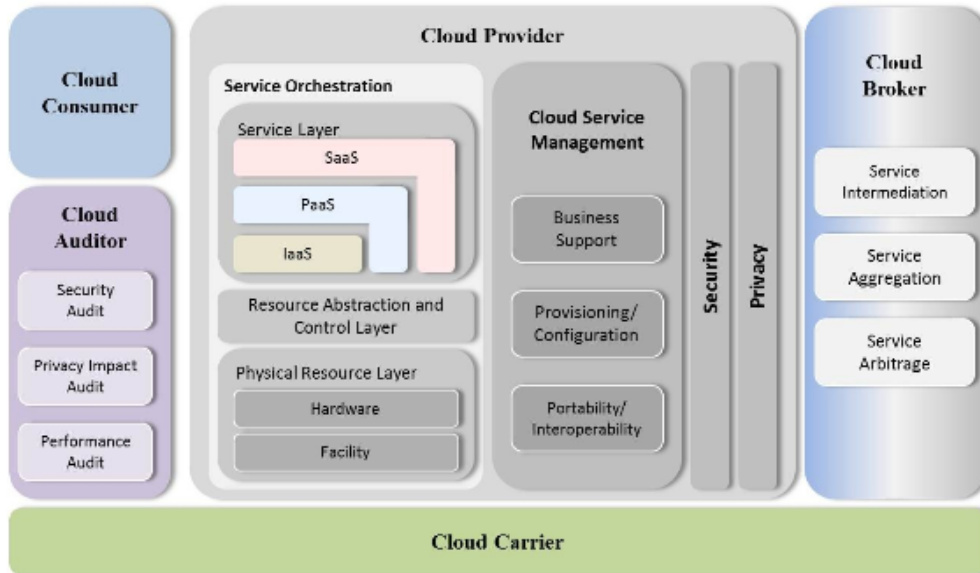


**Figure 2:** Cloud conceptual reference model [5]

Peteiro-Barral[6] presents three main approaches on how to speed up the learning process: development of faster algorithms, use of a relative data representation, or data partition. In our case, we can use a faster algorithm, but our main concern will be the partition of the data. Pop [4] describes in detail distributed learning options and classifies five distinguished categories: Machine Learning environments, Plugins for Machine Learning tools, Distributed Machine Learning libraries, Complex Machine Learning systems, and Software as a Service providers for Machine Learning.

## 2 POSSIBILITIES FOR DEEP LEARNING

### 2.1 HARDWARE

We begin our survey on hardware solutions. In this case, We will go through 4 categories: single-boards, accelerators, graphic cards, and workstations developed mainly for this task. The first and second instances could be mixed and used for the learning model, but it will be unreasonable because we can use other solutions to learning and achieve better results.

The first category concerns single-board devices. Though limited in resources, they have remarkable computational power. Examples are presented in Tab. 1. When we want to apply them for our calculation, we may need some variety of cluster structure or use of a specific library. Notable device in this category is Jetson TX2 from the NVIDIA company.

The price of this kind of device is in the tens or hundreds of US Dollar(USD). The key features are computational units: the CPU, GPU, or TPU. Significant property is also the amount of memory. Also, an important parameter for access to memory is the type that is in the brackets.

Name	CPU	GPU	Memory[GB]
Rpi4B [7]	4x1,5GHz	VideoCore IV 500MHz	4 (LPDDR4)
ODROID-N2 [8]	4x1,8GHz	Mali-G52	4 (DDR4)
Beagleboard X15 [9]	2xCortex-A15	2xSGX544	2 (DDR3)
Tinker Edge R [10]	8xCortex-A72 + 4xCortex A53	Mali-T860	4 (LPDDR4)
Jetson TX2 [11]	2xDenver 1.5 + 4xCortex-A57	256xNVIDIAPascal	8 (LPDDR4)
Coral DevBoard [12]	4xCortex-A53 + Cortex-M4F	GC7000+TPU coprocessor	1 (LPDDR4)

**Table 1:** Table with examples of single-board computers.

The second category focuses on accelerators. In this area, we have two options. The first one is a video processing unit (VPU) developed by the Intel company. The mentioned TPU is produced by the Google company. The cost of these devices moves around tens of USD.

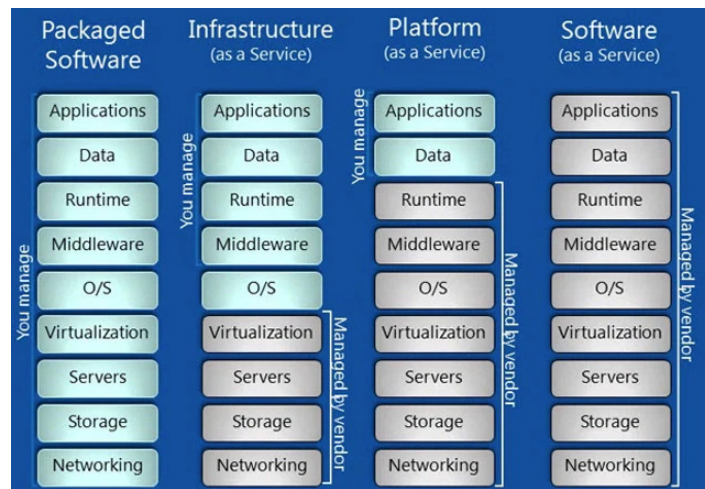


**Figure 3:** Cloud service definition.<sup>1</sup>

The third part is about the graphic card. These cards are developed mainly for computer games or rendering programs. Their power is being presented in GPU. GPU is focused on multiplication, therefore, can be used efficiently for deep learning. The Tab. 2 contains comparison of the graphic-card attributes from two leading producers. Notable advantage of the CUDA library from NVIDIA, in contrast to the library from AMD, is it's open character. Another advantage of NVIDIA is the library cuDNN specialized in deep learning. Other producers of the graphic cards are ASUS, ATI, Leadtek, or S3 Graphics.

Name	Producer	Clock Rate[MHz]	Memory[GB]	FP64 [GFLOPS]	TDP[W]
Pro WX7100	AMD	1243	8 (GDDR5)	358	130
RX 5700 XT	AMD	1605	8 (GDDR6)	609,6	225
M4000	NVIDIA	773	8 (GDDR5)	80,39	120
RTX 2070	NVIDIA	1620	8 (GDDR5)	233,3	175
RTX 4000	NVIDIA	1545	8 (GDDR6)	222,5	160
RTX 2080Ti	NVIDIA	1545	11 (GDDR5)	420,2	250

**Table 2:** Table with examples of graphic card for PC [13].

The price of these devices is in thousands of USD. The key features, in this area, are listed in the

<sup>1</sup>Source: <<https://venturebeat.com/2011/11/14/cloud-iaas-paas-saas/>>

Tab. 2. The clock rate indicates how many operations the processor can do in one second. Again the memory is significant, especially for working with files, e. g. computer vision operates with large images thus this operation requires more memory space. Floating Point Operations Per Second (FLOPS) is a theoretical value that shows how many operations (in our case with a 64-bit number) are possible to process. Thermal design power (TDP) is a value of maximal heat, which can be produced in order of a safe performance of the device.

The last category of the listed hardware solution are workstations. In Tab. 3 are two examples of workstations specially developed for machine learning. Key features are two. The first one are devices, from which the workstation is composed. The second are interfaces. As we can see, they are composed from the above mentioned categories of hardware solutions. These workstations can be applied e. g. in autonomous cars.

Name	Hardware	Interfaces
NVIDIA Data Science Workstation	3XS DSW Q116X, Intel Xeon W-2145, 128GB RAM, 24GB NVIDIA Quadro RTX6000, 1TB M.2 SSD, 4TB HDD	2x RJ-45, 6x USB 3.0, 1x USB 3.1 Gen2 Type-A, 1x USB 3.1 Gen2 Type-C
Puget Systems	2 or 4 RTX 2080Ti, RTX 2070 or Titan V, Intel Xeon-W 2145 8-core or Intel Xeon-W 2195 18-core, 128 or 256GB memory, 1TB system SSD, 2TB data SSD, 4GB storage HD	2x RJ-45, 4x USB 3.0, 1x USB 3.1 Gen2 Type-A, 1x USB 3.1 Gen2 Type-C

**Table 3:** Table with examples of workstations.

## 2.2 CLOUD COMPUTING

Remarkable approach to development of a deep learning model is usage of cloud computing. When we use Iaas, we gain cloud advantages and acquire a new model. The cloud services should be working all the time, so we can learn the model continuously. In Tab. 4 are shown some representatives of various delivery models with examples and content.

Type	Examples	Content
Iaas	Salesforce, NetSuite, Zoho, Zimbra, Office Live, Concur, Taleo	Computer, Block Storage, Network
Paas	Google app engine, Force.com, Azure	Object Storage, Identify, Runtime, Queue, Database
Saas	Amazon EC2 & S3, Rackspace, EMC, Sun, BlueCloud	Monitoring, Content, Colaboration, Communication

**Table 4:** Table with examples of cloud services [14].

## 3 EXPERIMENTAL SETUP

In the context of this article an experimental setup was build. For the learning part, was chosen graphic card RTX2080Ti from NVIDIA company. This card can be also used for the final classification, but for the experiment were chosen single-board computer RaspberryPi 4B.

## 4 CONCLUSION AND FUTURE WORK

This article discusses hardware possibilities for deep learning computing. In section 2, were presented tables with key features in each category of devices. We studied four main categories. Cloud computing was presented and several examples were given. In section 3 were given laboratory setup.

The following work could be focused on hybrid systems. Interesting idea of these systems is to create a server constructed of powerful graphic cards and clients constituted from embedded devices.

## 5 ACKNOWLEDGEMENT

The completion of this paper was made possible by the grant No. FEKT-S-20-6205 - "Research in Automation, Cybernetics and Artificial Intelligence within Industry 4.0" financially supported by the Internal science fund of Brno University of Technology.

## REFERENCES

- [1] K. Horak and R. Sablatnig, "Deep learning concepts and datasets for image recognition: overview 2019," in *Eleventh International Conference on Digital Image Processing (ICDIP 2019)*, vol. 11179, p. 111791S, International Society for Optics and Photonics, 2019.
- [2] D. Kapil, P. Tyagi, S. Kumar, and V. P. Tamta, "Cloud computing: Overview and research issues," in *Proceedings - 2017 International Conference on Green Informatics, ICGI 2017*, pp. 71–76, Institute of Electrical and Electronics Engineers Inc., nov 2017.
- [3] K. Horak and L. Zalud, "Image processing on raspberry pi for mobile robotics," *International Journal of Signal Processing Systems*, vol. 4, no. 2, pp. 1–5, 2016.
- [4] D. Pop, "Machine learning and cloud computing: Survey of distributed and saas solutions," *CoRR*, vol. abs/1603.08767, 2016.
- [5] L. Badger, D. Bernstein, R. Bohn, F. de Vault, M. Hogan, M. Iorga, J. Mao, J. Messina, K. Mills, E. Simmon, A. Sokol, J. Tong, F. Whiteside, and D. Leaf, "US Government Cloud Computing Technology Roadmap," *Nist Special Publication*, 2014.
- [6] D. Peteiro-Barral and B. Guijarro-Berdiñas, "A survey of methods for distributed machine learning," nov 2013.
- [7] "Raspberry Pi 4 vs Pi 3 - What are the differences?," [website]. <<https://www.cnx-software.com/2019/06/24/raspberry-pi-4-vs-pi-3-what-are-the-differences/>>, cite:[2020-03-14].
- [8] "ODROID-N2 | ODROID," [website]. <<https://www.hardkernel.com/blog-2/odroid-n2/>>, cite:[2020-03-14].
- [9] "BeagleBoard.org - x15," [website]. <<https://beagleboard.org/x15>>, cite:[2020-03-14].
- [10] "ASUS Tinker Edge R Pico-ITX Board to Feature Rockchip RK3399Pro SoC," [website]. <<https://www.cnx-software.com/2019/05/31/asus-tinker-edge-r-pico-itx-rk3399pro-soc/>>, cite:[2020-03-14].
- [11] "Jetson TX2 Module | NVIDIA Developer," [website]. <<https://developer.nvidia.com/embedded/jetson-tx2>>, cite:[2020-03-14].
- [12] "Dev Board datasheet | Coral," [website]. <<https://coral.ai/docs/dev-board/datasheet/>>, cite:[2020-03-14].
- [13] "GPU Database | TechPowerUp," [website]. <<https://www.techpowerup.com/gpu-specs/>>, cite: [2020-03-14].
- [14] M. D. Shah and C. Dhiman, "Cloud computing architecture & services," 2015.

# INFLUENCE OF REACTIVE POWER COMPENSATION IN TRANSFORMER STATION ON VOLT-VAR REGULATION OF DISTRIBUTED ENERGY SOURCES

**Viktor Jurák**

Doctoral Degree Programme (1), FEEC BUT

E-mail: xjurak04@stud.feec.vutbr.cz

Supervised by: Jaroslava Orságová

E-mail: orsagova@feec.vutbr.cz

**Abstract:** This article is focused on the influence of reactive power compensation on the secondary side of the distribution transformer on the Volt-Var regulation of distributed power sources in LV networks. The paper shows the mutual effects of compensation and Volt-Var control on a simple simulation in PSS<sup>®</sup> Sincal. The first part of the paper is dedicated to the description of the simulated scheme and parameterization of individual components. In the second part the results of the simulation are summarized, the contraindications identified, and recommendations are given.

**Keywords:** distributed energy sources, reactive power compensation, Volt-Var regulation

## 1 INTRODUCTION

The power system is currently undergoing many changes. Share of distributed power sources is increasing, the character of appliances is changing and the number of cable lines is rising. These changes must be adapted to the way the electricity system operates. Reactive power flows are one of the problems to be addressed. Distributed power sources use reactive power to stabilize the voltage at the connection point, which then passes to the networks of higher voltage levels. Other sources of reactive power are consumers of electricity themselves, where due to the increasing numbers of appliances with inverters, it is possible to expect an increase in consumption of capacitive character. Network elements themselves are also a significant source of reactive power. For the above reasons, distributors are starting to consider compensation at the low voltage (LV) level.

The transfer of active power is accompanied by reactive power, which does not do any active work. However, reactive power transmission on the network elements causes active losses and voltage drops. Reactive power also blocks the transmission capacity of network elements that could be used to transmit active power.

## 2 LOW VOLTAGE NETWORK SIMULATION

The main subject of the simulation is to assess the effect of compensation and implementation of  $Q(U)$  (Volt-Var) regulation of distributed sources at LV level during selected operating conditions. At the same time, the contraindication of compensation on the secondary side of the DT (Distribution Transformer) to  $Q(U)$  source control in terms of stable and economical operation of the whole network is also assessed. For better demonstration of interconnections between  $Q(U)$  regulation and compensation, a model of only one medium voltage (MV) branch formed by cable, at the end of which is one distribution transformer 22 / 0.4 kV, is used first. The scheme of the simulated network including the monitored parameters is in Figure 1.

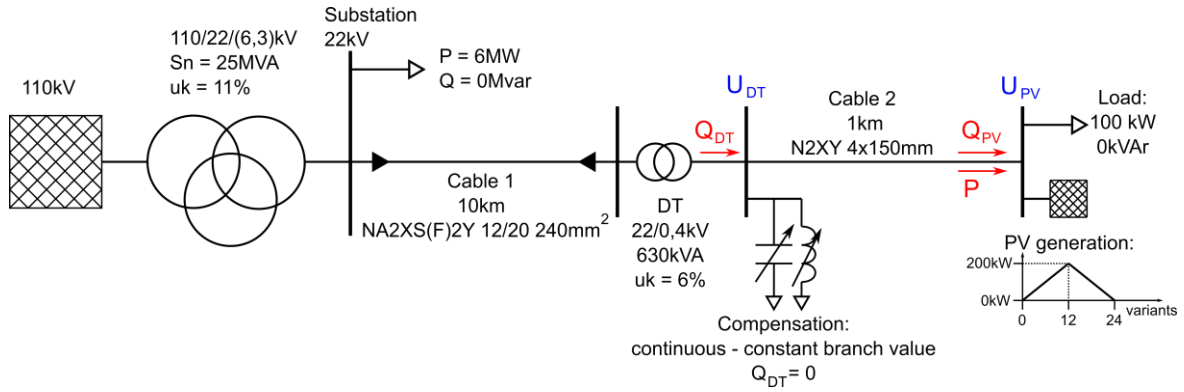


**Figure 1:** Schematics of simulated network with  $Q(U)$  regulation of PV power source and compensation on LV side of DT

The simulation was performed in the PSS® Sincal 14.5 software. The load profile mode was used for the simulations. This mode enables the calculation of steady-state sets in which the  $P$  (active power) and  $Q$  (reactive power) of the source and load changes. In the computational program, these individual steady state sets are seen as the behaviour of source and load over time. The calculation was set on a daily basis in steps of 1h. With this setting, it was possible to create 24 separate steady-states. Since the simulation did not model the daily load curves, these individual steady-state runs with respect to the parameterization of the source and load powers are referred below as states.

The LV network that is the subject of this simulation is fed from a 22 / 0.4 kV distribution transformer with a nominal apparent power 630 kVA. The transformer is parameterized according to [1]. On its secondary side, there is a compensation, which allows continuous regulation to zero  $Q$  flow through DT ( $Q_{DT} = 0$ ). The compensation means being the ideal compensator. The secondary side of the transformer is connected with a 1 km long LV cable N2XY 150 mm<sup>2</sup>. The LV line was selected from the element library available in PSS® Sincal. The specific impedance of this line is:  $\bar{Z}_k = R_k + jX_k = 0,124 + j0,078 \Omega/\text{km}$ . The cable was chosen intentionally because it has a low specific reactance compared to the specific resistance. This should lead to higher  $Q$  values provided by  $Q(U)$  regulation of power supply. The use of cable in the simulation also takes into account the trend of expansion of low-voltage cabling.

At the end of the LV line is considered a node to which a constant load with a  $P$  of 100 kW and a  $\cos\phi = 1$  is connected, as well as a power source with a maximum  $P_{\max} = 200$  kW. The power supply is parameterized as a linear ramp where the  $P$  rises linearly from 0 kW to 200 kW in steps of 0 to 12 and decreases from 200 kW to 0 kW in steps of 12 to 24. This setting of the power source and load ensures the transmitted  $P$  profile over LV line in the range of 100 kW (direction of  $P$  flow from MV to LV) to -100 kW.

The simulation is a set of 24 steady-state runs. The input parameter that changes in these individual steady-state runs is only the  $P$  produced by the PV. The load remains constant. The monitored parameters are the voltage in the DT and PV nodes and the  $Q$  provided by the PV within the  $Q(U)$  control (its setting is described in section 2.1). Three variants are then tested with respect to compensation in DT and  $Q(U)$  source control. These variants are as follows:

- without compensation and  $Q(U)$  control,
- without compensation, with  $Q(U)$  control,
- with compensation and  $Q(U)$  control.

## 2.1 Q (U) SOURCE CONTROL

The  $Q(U)$  control is primarily used to compensate the  $\Delta U$  (voltage drop) caused by the  $P$  by  $Q$ . Ideally, the voltage increase due to  $P$  supply should be suppressed by  $Q$  consumption. In a simplified form, the  $\Delta U$  across the series impedance, which forms resistance and reactance (e.g. line or transformer), can be expressed by equation (1).

$$\Delta U \approx \frac{P}{U_{L-N}} \cdot R + \frac{Q}{U_{L-N}} \cdot X \quad (\text{V}) \quad (1)$$

Where  $R$  ( $\Omega$ ) is the series resistance,  $X$  ( $\Omega$ ) is the series reactance,  $P$  (W) is the single-phase transmitted active power,  $Q$  (VAr) is the single-phase transmitted reactive power, and  $U_{L-N}$  (V) is the line-to-neutral value of the voltage. The reactive power of inductive character is considered in this paper.

The equation (1) applies when we consider both  $P$  and  $Q$  consumption. Then just this voltage drop decreases the voltage in the PV node. It can be seen from the equation (1) that while the part of the  $\Delta U$  caused by the transmission of  $P$  through the line is dependent on the  $R$ , the part of the  $\Delta U$  caused by the transmission of  $Q$  is proportional to the  $X$ . If the direction of  $P$  or  $Q$  is reversed, it is necessary to respect this fact and change the sign of  $P$  or  $Q$  in equation (1).

It follows from the above equation that the efficiency of voltage regulation by  $Q$  injection is strongly dependent on the  $X$ , respectively the principle of compensating the  $\Delta U$  caused by the transfer of  $P$  by  $Q$  depends on the  $R/X$  (ratio of resistance to reactance). From [2] it follows that while overhead LV lines have the  $R/X \sim 2.3$ , LV cable lines have the  $R/X \sim 5.4$ . Voltage regulation is the more efficient, the lower the  $R/X$  is. Therefore, the regulation is more effective in overhead LV networks than in cable networks. For comparison, the overhead MV lines have the  $R/X \sim 1.2$ .

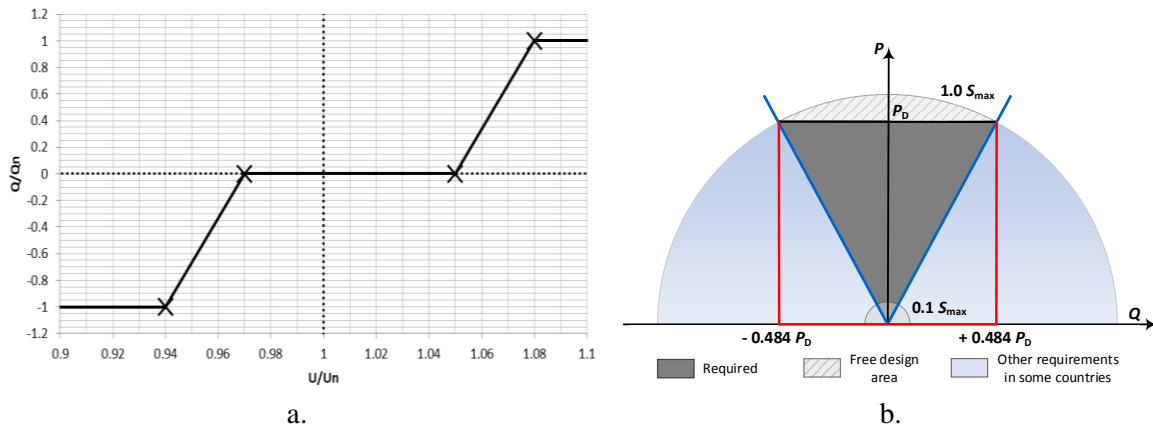


**Figure 2:** a. Setting the  $Q(U)$  source control, b. Requirements for reactive power supply / consumption

The parameterization of the  $Q(U)$  characteristics of the PV control is set according to the setting example given in the valid Annex No. 4 PPDS (Czech rules for the operation of distribution networks) [3]. The setting of the characteristics is shown in Figure 2 a.

In addition to the application of the  $Q(U)$  characteristics, amount of  $Q$  support is also affected by PQ diagram which is also defined in [3]. The duty to enable voltage support by  $Q$  is within the  $\cos\varphi = 0.9$  (blue area of Figure 2 b.). Conventional inverters are usually designed to a maximum  $Q$  value that corresponds to the  $Q$  value at rated  $P$  and a  $\cos\varphi = 0.9$  (red area of Figure 2 b.).

In the simulation, the source is set according to the red area of Figure 2 b. The  $Q(U)$  control is allowed even though  $P$  provided by PV is zero. This has the advantage that the power supply can

compensate (or at least reduce) the  $\Delta U$  due to  $P$  consumption by supplying  $Q$ . In these load-dominant conditions, this behaviour can emulate e.g. an electric vehicle charging station equipped with  $Q(U)$  control.

The combination of the type and length of the LV line and the nominal  $P$  of the source and the load was intentionally chosen so that the voltage is within the permissible limits even when the  $Q(U)$  control is switched off. To demonstrate the effect of compensation on  $Q(U)$  control, the line cross-section was selected so that the power supply did not deliver its maximum  $Q$  when the  $Q(U)$  was switched on, i.e. the voltage was between  $0.94U_n$  and  $1.08U_n$ .

### 3 SIMULATION RESULTS

The simulation results are shown in Figure 3. In the first part of the figure, the active power is at the end of the LV line. This power is a set parameter and is the same for all three variants. In the second part of the graph, there is the  $Q$  at the end of the LV line  $Q_{PV}$ . Since there is no power source / consumption of  $Q$  other than PV, this value can be considered as a value provided by the  $Q(U)$  control. It can be seen from this that if the  $Q(U)$  control is switched off, the PV does not produce or consume any  $Q$ . When the control is switched on, the PV supplies / consumes  $Q$  that corresponds to the  $U_{PV}$  voltage according to the set control curve  $Q(U)$  (Figure 2 a.). The  $Q$  supply / consumption will then cause a voltage drop (in positive / negative direction). If the transmitted  $P$  is low and the voltage at the PV is within the dead band of  $Q(U)$  control, the PV does not supply or consume any  $Q$ .

If both the  $Q(U)$  control and the compensation are switched on, it can be seen from the  $Q_{PV}$  that this value is greater than when the compensation is switched off. In a condition where 100 kW is transferred to the load through the line, the difference in  $Q$  is approximately 10 kVAr. This increase occurs only if the power supply PV is not at the maximum  $Q$ , i.e. the voltage  $U_{PV}$  is within the limits  $0.94U_n - 0.97U_n$  and  $1.05U_n - 1.08U_n$  according to Figure 2 a. This  $Q_{PV}$  increase is caused by the fact that  $Q$  does not pass through DT and therefore does not cause the  $\Delta U$  on the MV line and especially on the distribution transformer. In equation (1), the part of  $\Delta U$  in which the  $Q$  appears, is only relevant for the  $X$  of the LV line.

In Figure 3, the voltage in the DT node is also plotted. It can be seen from this curve that when the compensation is switched on, the voltage is slightly higher than the value when the compensation is switched off (both states without  $Q(U)$  control). This is due to the fact, that even though the load is only active, the transmission of this power over the LV line produces  $Q$  on the LV line  $X$ . This  $Q$  with off compensation is not compensated and causes  $\Delta U$  in negative direction. On the other hand, when  $Q(U)$  control is on and compensation is off, the supply of  $Q$  through the distribution transformer causes a positive  $\Delta U$  and increases the voltage in the DT when the  $P$  is consumed (variants 1-4 and 20-24). Conversely, the  $Q$  consumption at an increased voltage at the PV node causes a negative  $\Delta U$  at the secondary side of the DT (variants 10-14).

### 4 CONCLUSION

The results shows that when the compensation is switched on, the section of the grid on which the controlled  $\Delta U$  occurs by regulating the  $Q$  is reduced. The control is then limited only to the LV line, which usually has a larger  $R/X$  and thus the control is less efficient. This results in a greater amount of  $Q$  provided by the  $Q(U)$  control.

Under the conditions of the simulation, an extreme increase of approximately 10kVAr occurred. If the PV were closer to DT, it could be expected that the amount of  $Q$  would be even greater and this  $Q$  could not affect the voltage due to the small value of  $X$  between PV node and DT node.

Compensation in LV networks with a high proportion of distributed generation sources should therefore be avoided.

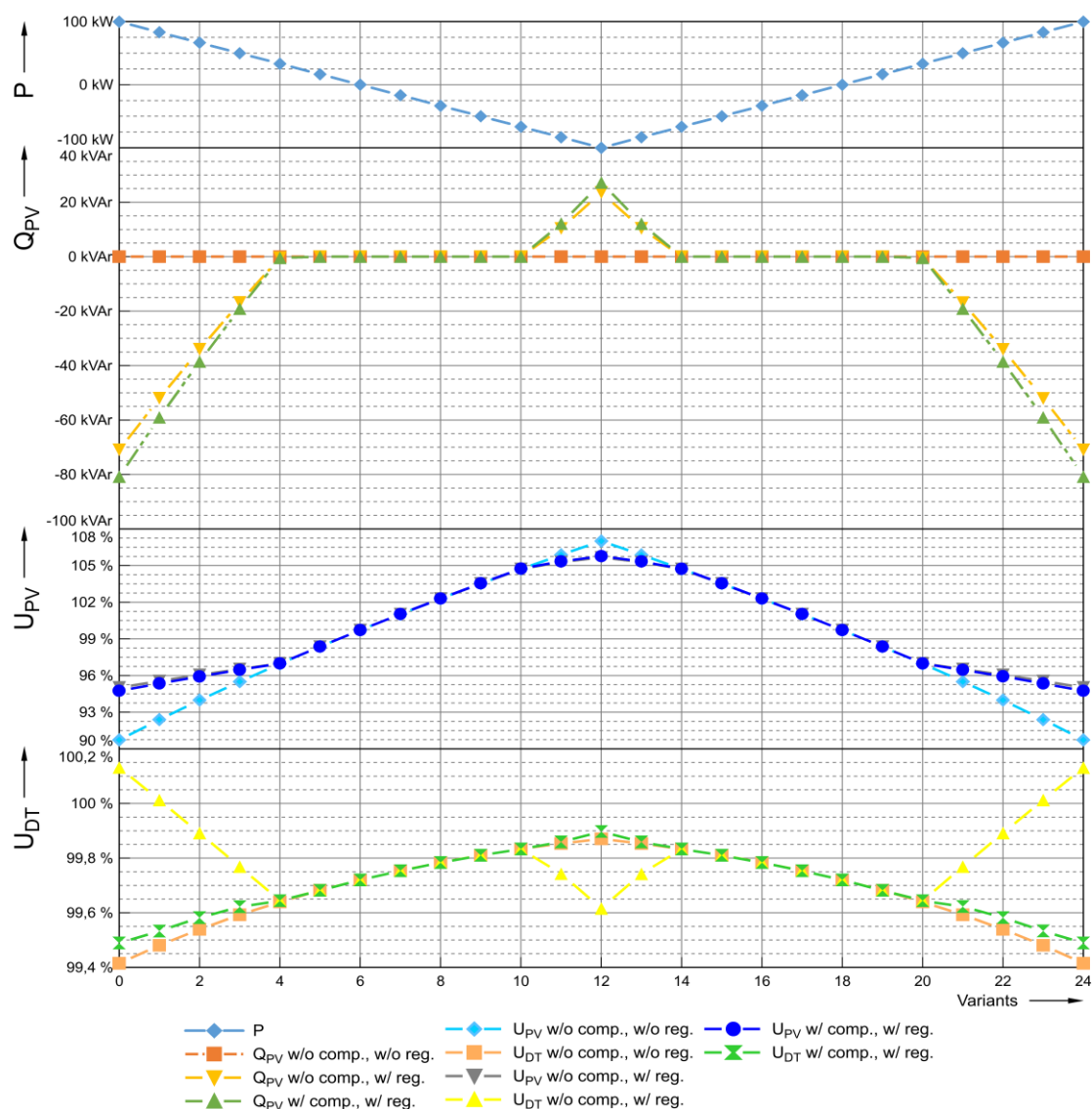


**Figure 3:** Voltage and reactive power profiles depending on the active power transmitted through LV cable

## REFERENCES

- [1] Trojfázové olejové hermetizované transformátory 50 - 2 500 kVA, 7.2 - 24 kV, straty CoCk , Al vinutie [online]. [cit. 2019-01-21]. Available from: <http://www.bez.sk/subor/103.pdf>
- [2] PNE 33 3430-0: Výpočetní hodnocení zpětných vlivů odběratelů a zdrojů distribučních soustav. Páté vydání. 2015.
- [3] Pravidla provozování distribučních soustav: Příloha 4 - Pravidla pro paralelní provoz výroben a akumulacních zařízení se sítí provozovatele distribuční soustavy [online]. 2017 [cit. 2020-03-05]. Available from: [https://www.eon-distribuce.cz/sites/default/files/2018-09/Priloha\\_c\\_4\\_Pravidla\\_pro\\_paralelni\\_provoz\\_vyroben\\_a\\_akumulacnich\\_zarizeni\\_se\\_siti\\_PDS\\_new.pdf](https://www.eon-distribuce.cz/sites/default/files/2018-09/Priloha_c_4_Pravidla_pro_paralelni_provoz_vyroben_a_akumulacnich_zarizeni_se_siti_PDS_new.pdf)

# POWER CONVERTERS FOR CELL ELECTROPORATION

**Martin Folprecht**

Doctoral Degree Programme (3), FEEC BUT

E-mail: xfolpr01@stud.feec.vutbr.cz

Supervised by: Dalibor Cervinka

E-mail: cervinka@feec.vutbr.cz

**Abstract:** This contribution refers about some topologies of power converters, which are used for medical purposes. The use of power converters in treatment of a cancer or an arrhythmia is a modern medical technique, which is still in development. The aim of the contribution is to compare current samples of power converters for medical purposes and briefly describe a design of a high-frequency power generator for AC electroporation.

**Keywords:** power supply, DC-DC converter, DC-AC converter, high frequency, MOSFET, IGBT

## 1 INTRODUCTION

A cell electroporation is a modern non-invasive method, which is suitable for treatment of some diseases. For example, the cancer and the arrhythmia. It is also used in genetic engineering, biotechnologies and food processing. Impacts on patient's body are minimalized, so it leads to shortening the period of the treatment. The method requires rectangular high-voltage pulses with very short length. These pulses are generated by power converters, whose topologies are described in following statements. Two samples are from the USA and two have been developed at FEEC BUT.

## 2 CELL ELECTROPORATION

The cell electroporation is based on very short high-voltage pulses. These pulses are applied to a treated tissue by special electrodes. Pulses lead to an increase of the permeability of the cell membrane. Ions, molecules and other chemical compounds can flow through nanopores created in the membrane. There are two ways of electroporation: reversible electroporation and irreversible electroporation. The difference between these two ways consists in a lifetime of nanopores. Temporary nanopores are created during reversible electroporation (RE), whereas irreversible electroporation (IRE) causes permanent nanopores, which lead to the death of the cell. The lifetime of nanopores depends on electrical properties of pulses (voltage, shape, frequency) and on biological properties of tissue and cells (dimensions, shape, density, temperature). Reversible electroporation is used in genetic engineering, irreversible electroporation is suitable for treatment of diseases. Electroporation can be also divided according to polarity of pulses: DC electroporation uses unipolar pulses and AC electroporation is based on bursts of high-frequency bipolar pulses. The length of the burst is similar to the length of one DC pulse. AC electroporation is suitable especially for the treatment of arrhythmia, because it does not cause muscular contractions [1].

## 3 TOPOLOGIES OF POWER CONVERTERS FOR CELL ELECTROPORATION

Power converters are usually divided into four groups: AC-DC (rectifiers), DC-DC (pulse converters), DC-AC (inverters) and AC-AC (triac regulators). These groups can be further classified according to different criteria. DC electroporation requires unipolar pulses, which are generated by DC-DC converters, whereas DC-AC inverters are suitable for high-frequency AC electroporation. Required output voltage reaches units of kilovolts with current about tens of amperes in both cases, so it is

advantageous to use a pulse transformer to increase the voltage. The transformer also provides a galvanic isolation between AC mains and patient's body. There are two different topologies, where the transformer is used. In the first case, the transformer is a part of the converter, which generates electroporating pulses. This topology is more advantageous, because there is not a risk of high-voltage pulse with uncontrollable length in the case of failure in the control or power circuits. One disadvantage can be seen in possible deformation of the pulse shape due to parasitic capacitance of the transformer. The second solution is a combination of DC-DC converter and high-voltage capacitors. These capacitors are charged from DC-DC converter with transformer. Electroporating pulses are generated by a high-voltage switch, which connects the capacitors with application electrodes. When the high-voltage switch fails, capacitors are discharged into the patient's body. This the main disadvantage of this topology. On the other hand, high-voltage pulses are purely rectangular without any deformation. High-voltage supplies with capacitors must be equipped with safety transistor switches, which provide discharge of the capacitors. Some current high-voltage supplies are described in following paragraphs [2].

### 3.1 NANOKNIFE DEVICE FOR DC IRE

Nowadays, NanoKnife is the one and only commercial device, which is approved for DC electroporation. It is the topology with battery of high-voltage capacitors. A block diagram of this device is in Figure 1. The device is powered from AC mains. AC voltage is rectified by bridge rectifier with capacitor. The second stage is the DC-DC converter with pulse transformer, which charges the battery of high-voltage film capacitors. The output voltage of the converter can be regulated from 100 V to 3 kV. Electroporating pulses are generated by IGBT transistor. The device is equipped with 6 output terminals for 6 application electrodes, which are chosen by relay switch [3].

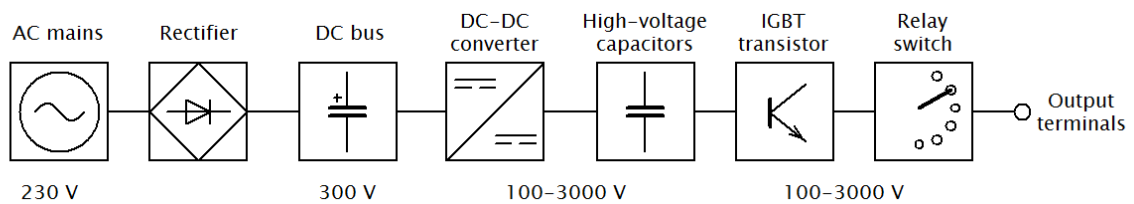


**Figure 1:** Block diagram of the NanoKnife device

The length of the pulse is variable from 20 to 100  $\mu$ s. An operator can also adjust the count of the pulses from 10 to 100. Maximal value of the output current is 50 A. Pulses can be synchronized with EKG. The device contains safety circuit, which discharges high-voltage capacitors in the case of fault [3].

### 3.2 FEEC BUT HIGH-VOLTAGE SOURCE FOR DC IRE

This high-voltage source has been developed for experimental purposes, because NanoKnife device is very expensive. Block diagram of the source is in Figure 2 [1].

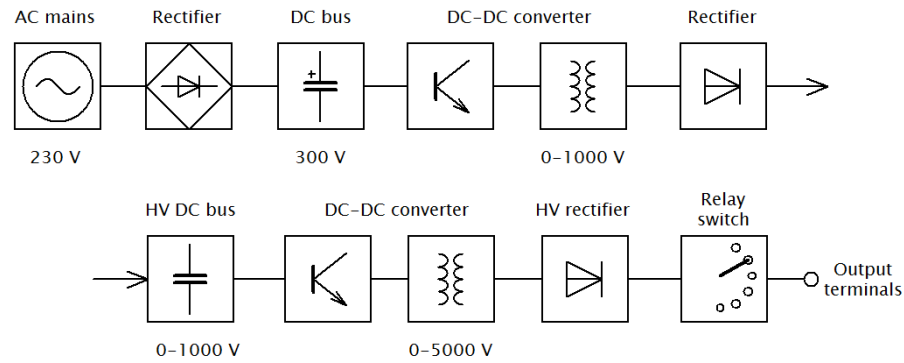


**Figure 2:** Block diagram of high-voltage source from FEEC BUT

It is a cascade of two DC-DC converters with pulse transformers. The first one is a two-switch forward converter, which is powered from AC mains. AC mains is rectified by bridge rectifier. The output voltage of this converter can be regulated from 0 to 1000 V. Output voltage is used for charging of the second DC bus, which is constructed from film capacitors. Total capacity of these capacitors is 110  $\mu\text{F}$ . Electroporating pulses are generated by the second DC-DC converter. It is also the two-switch converter topology. The height of electroporating pulses can be set from 0 up to 5000 V. Maximal value of the output current is 100 A. These maximal values are higher than output parameters of NanoKnife device. Application electrodes are connected by relay switch. High-voltage pulses are rectified by HV rectifier created from 10 SiC diodes C4D20120D manufactured by CREE. Reverse voltage of each diode is 1200 V, so the total reverse voltage is 12 kV. The power part of the converter contains two IGBT modules FF1000R17IE4 by Infineon. Maximal collector to emitter voltage is 1700 V and maximal collector current is 1000 A. Modules are driven from integrated drivers 2ED300C17-S. Voltage and current are sensed by LEM sensors. The whole device is controlled by signal processor. Besides the height of the pulse, the operator is also able to adjust the pulse width from 20 to 150  $\mu\text{s}$  and the time space between pulses from 0.2 to 2 s. Adjusted values are viewed on alphanumeric display [1].

### 3.3 HIGH-FREQUENCY GENERATOR FOR AC IRE

High-frequency generator for AC electroporation was patented in 2019, but commercial device is not available. The block scheme of the generator is in Figure 3.

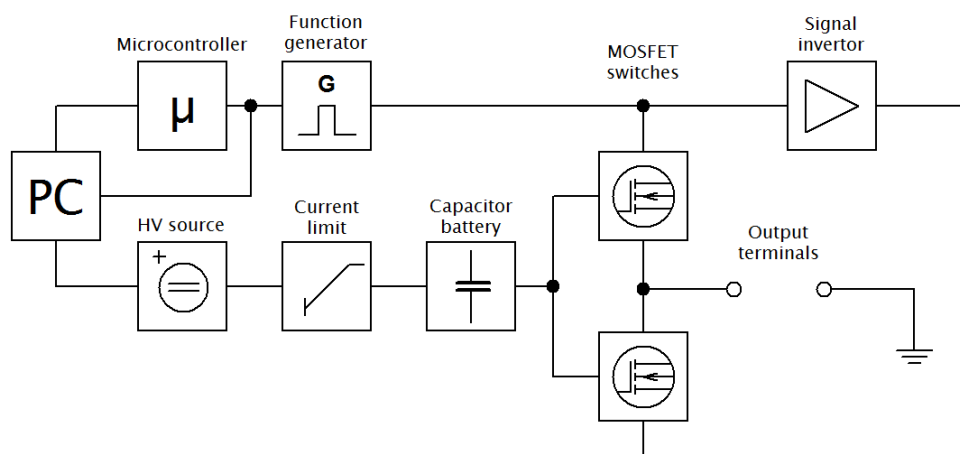


**Figure 3:** High-frequency generator for AC electroporation

A source of rectangular pulses is the function generator (Tektronix AFG 3011). The length of the burst, the space between bursts and the count of bursts is controlled by microcontroller (Arduino). Programmable laboratory supply LabSmith HVS448 works as a high-voltage source, which charges the battery of capacitors. Current limit is provided by resistors. Bursts of high-voltage pulses are generated by two MOSFET modules HV 1000 by DEI. The first module is driven from Tektronix generator directly, the second one through signal inverter (LM7171). Maximal input voltage of each module is 950 V and maximal output voltage is  $\pm 850$  V. Maximal output current into  $50 \Omega$  load is 17 A. A control part of each module is powered from AC mains. Output frequency can be varied from 250 kHz to 2 MHz, the length of each burst is  $100 \mu\text{s}$  and the space between bursts is 1 s. Described high-frequency generator is created from connected laboratory appliances and does not contain pulse transformer. Application electrodes are connected directly to high-voltage capacitors by MOSFET switches. When the switch is damaged, capacitors are discharged into electroporated tissue [4].

#### 4 FEED BACK POWER CONVERTER FOR AC ELECTROPORATION

This converter was developed at FEED BACK UNIVERSITY for experimental purposes. It is a compact device powered from AC mains. Two changeable pulse transformers allow to choose maximal output voltage value (2.5 kV or 1.3 kV). Maximal output current is 11 A (or 21 A with the second transformer), output peak power 27.5 kW is the same for both transformers. The operator can set the frequency of pulses from 65 to 470 kHz, the length of the burst from 40 to  $120 \mu\text{s}$  and the space between following bursts from 0.5 to 1.5 s. Output values are adjusted by potentiometers. Output voltage value and the count of bursts is viewed on displays. Circuit diagram of the power part is in Figure 4 [2].

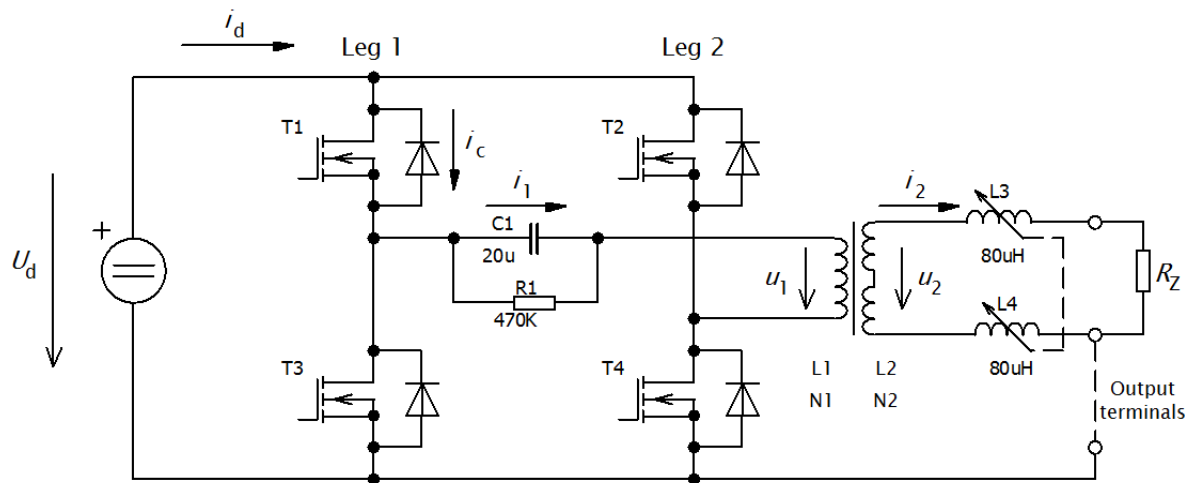


**Figure 4:** Circuit diagram of power part of the converter

Power part of DC-AC converter consists of four MOSFET transistors  $T_1$ - $T_4$ . These transistors are switched in diagonals. It means that two transistors,  $T_1$  and  $T_4$  or  $T_2$  and  $T_3$  are switched together. Capacitor  $C_1$  is used for elimination of DC magnetization of pulse transformer. Primary voltage  $u_1$  and secondary voltage  $u_2$  have rectangular shape and the height of secondary pulses is different with transfer ratio  $N_2/N_1$  of the transformer. Primary current  $i_1$  consists of magnetizing current  $i_\mu$  and secondary current  $i_2$  transferred to the primary winding. The shape of secondary current  $i_2$  is rectangular and the shape of magnetizing current  $i_\mu$  is triangular. The transformer is constructed on ferrite core Lj U 7020 CF 297. Ferrite material is used for its high resistivity, which eliminates eddy currents. The core does not contain air gap, which is useless here. Effective area of the core  $S_{Fe}$  is  $400 \text{ mm}^2$ , effective magnetic length  $l_{Fe}$  is 269.8 mm and relative magnetic permeability  $\mu_{rFe} = 2100$ . The number of primary turns  $N_1$  is given by equation (1) and it is calculated for the lowest frequency  $f = 65 \text{ kHz}$ :

$$N_1 = \frac{U_d}{4 \cdot f \cdot B_{\max} \cdot S_{Fe}} \quad (1)$$

Maximal flux density value  $B_{\max} = 0.35$  T is chosen.  $U_d$  is voltage in DC bus. For maximal value  $U_d = 320$  V, the number of primary turns  $N_1 = 9$  is obtained. This number is valid for both transformers. The number of secondary turns  $N_2$  can be calculated from equation (2):

$$N_2 = \frac{U_2}{U_1} \cdot N_1 \quad (2)$$

$U_1$  is chosen voltage value in DC bus and  $U_2$  are required maximal values of the output voltage. For  $U_1 = 300$  V,  $N_1 = 9$  and  $U_2 = 2500$  V,  $N_2 = 75$  is obtained. The second transformer with  $U_2 = 1300$  V has  $N_2 = 39$  secondary turns. Maximal drain current of transistors IXFK100N65X2 is 100 A. An over-current protection turns the driving circuits off, when primary current  $I_{1\max}$  exceeds 96 A. Maximal value of magnetizing current  $I_{\mu\max}$  is given by equation (3):

$$I_{\mu\max} = \frac{B_{\max} \cdot l_{Fe}}{N_1 \cdot \mu_0 \cdot \mu_{rFe}} \quad (3)$$

For  $B_{\max} = 0,35$  T,  $l_{Fe} = 269.8$  mm,  $N_1 = 9$ ,  $\mu_0 = 4 \cdot \pi \cdot 10^{-7}$  and  $\mu_{rFe} = 2100$ ,  $I_{\mu\max} = 4$  A is calculated. Maximal value of the output current  $I_2$  can be calculated now (4):

$$I_2 = \frac{U_1 \cdot (I_{1\max} - I_{\mu\max})}{U_2} \quad (4)$$

For  $U_1 = 300$  V,  $I_{1\max} = 96$  A,  $I_{\mu\max} = 4$  A and  $U_2 = 2500$  V,  $I_2 = 11$  A is obtained. When the second transformer with  $U_2 = 1300$  V is mounted, secondary current reaches  $I_2 = 21$  A. Magnetizing current decreases, when working frequency  $f$  rises. For that reason, maximal output current  $I_2$  can exceed calculated values (4), when the operator sets higher working frequency. The cross-section area of the primary and secondary conductor must be divided into many thin insulated conductors because of skin effect. Variable inductors  $L_3$  and  $L_4$  (Figure 4) are used for elimination of high-frequency capacitive currents, which flow through the parasitic capacity of the transformer into patient's body and then into the ground. These currents can affect measuring devices [2].

## 5 CONCLUSION

This contribution was focused on power converters used for medical purposes, especially for cell electroporation. DC electroporation uses unipolar pulses, that can be generated by DC-DC converters. AC electroporation is based on bursts of high-frequency bipolar pulses, which can be generated by DC-AC converters. In topologies with pulse transformers, electroporating pulses are transmitted by the transformer, which provides the galvanic isolation of patient's body from AC mains. Different topologies are based on high-voltage capacitors, which are connected to application electrodes by solid-state switches with MOSFET or IGBT transistors. Both topologies have their advantages and disadvantages, that are mentioned in relevant paragraphs. Two described converters are from the USA and two have been designed and developed at FEEC BUT.

## ACKNOWLEDGEMENT

This research work has been carried out in the Centre for Research and Utilization of Renewable Energy (CVVOZE). Authors gratefully acknowledge financial support from the Ministry of Education, Youth and Sports under institutional support and BUT specific research program (project No. FEKT-S-20-6379).

## REFERENCES

- [1] Novotná, V. Analýza elektrických a tepelných dějů při elektroporaci. Dizertační práce. Brno: Vysoké učení technické v Brně, Fakulta elektrotechniky a komunikačních technologií, Ústav výkonové elektrotechniky a elektroniky, 2019. Vedoucí práce Ing. Dalibor Červinka, Ph.D. Dostupné z: <https://www.vutbr.cz/studenti/zav-prace/detail/122349>
- [2] Patočka, M. Magnetické jevy a obvody ve výkonové elektronice, měřicí technice a silnoproudé elektrotechnice. 1. vyd. V Brně: VUTIUM, 2011, 564 s. ISBN 978-80-214-4003-6
- [3] NanoKnife. 2020. Dostupné z: <https://nanoknife.com>
- [4] Arena, C.; Davalos, R.; Sano, M. High Frequency Electroporation For Cancer Therapy. US2019/10292755B2.USA: 2019. Dostupné z: [www.freepatentsonline.com/10292755.pdf](http://www.freepatentsonline.com/10292755.pdf)

# ZERO CURRENT SWITCHING QUASI-RESONANT BUCK CONVERTERS

**Radek Tománek**

Doctoral Degree Programme (1), FEEC BUT

E-mail: xtoman30@stud.feec.vutbr.cz

Supervised by: Pavel Vorel

E-mail: vorel@feec.vutbr.cz

**Abstract:** This paper reviews the basic topologies of zero current switching quasi-resonant buck DC-DC converters and describes their basic properties. Further, there is an analysis of half-wave and full-wave zero current switching quasi-resonant DC-DC converters.

**Keywords:** quasi-resonant buck DC-DC converter, zero current switching, zero voltage switching, ZCS QRC, ZVS QRC

## 1 INTRODUCTION

Switching converters are used today in almost every electrical or electronic device. Switching converters enable to reduce dimensions and weight of used transformers, coils and capacitors in conventional power sources and allow to reduce losses and thus increase efficiency, even with the possibility of electronic regulation of output quantities.

However, conventional hard-switched converters cause considerable electromagnetic interference due to the fast switching of semiconductor elements.

During the switching events, switching losses are on the semiconductor elements, which negatively affect the resulting efficiency of the converter. E.g. during the switching-on or switching-off process of the switching transistor in a buck-converter, a state occurs in which the supply voltage is on the semiconductor element and simultaneously through which the output current flows. The instantaneous value of the power losses on the switch  $p_{sw}(t)$  is then given by the relation 1.

$$p_{sw}(t) = v_{DS}(t) \cdot i_D(t) \quad (1)$$

Resonant and quasi-resonant converters are removing these shortcomings. They switch the semiconductor elements either when zero voltage  $v_{DS}$  is on the switching element or no current  $i_D$  flows through it. Surrounding elements ensure that this condition is approximately fulfilled during the entire duration of the switching event.

Resonant and quasi-resonant converters can generally use various types of half controllable semiconductor elements or fully controllable elements as controllable switches. In this article I will limit myself to transistor switches, namely MOS-FET. However, the basic properties described will not differ significantly even when using some other semiconductor switching elements.

## 2 QUASI-RESONANT CONVERTERS (QRC)

The basic topologies of the quasi-resonant converters can be divided according to the switching method into zero current switching (ZCS) and zero voltage switching (ZVS).

## 2.1 ZERO VOLTAGE SWITCHING (ZVS)

The principle is based on the fact that a capacitor is connected in parallel to the switching transistor. This ensures that when the switching event occurs at zero voltage, the voltage does not manage to increase too much during the short time of switch on or switch off events of the transistor so that the voltage can typically be considered to be zero during the entire duration of the switching event. [1] Basic topology of half-wave zero voltage switching quasi-resonant DC-DC converters is in the Fig. 1.

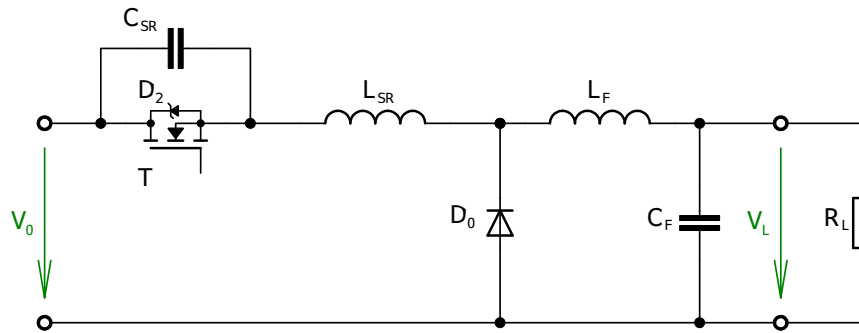


**Figure 1:** Basic topology of half-wave zero voltage switching quasi-resonant DC-DC converters

## 2.2 ZERO CURRENT SWITCHING (ZCS)

Analogously, the principle is that an inductor is connected in series with the switching transistor. This ensures that when the switching event starts at zero current, the current does not manage to increase too much during the short time of switch on or switch off events of the transistor so that the current can typically be considered to be zero during the entire duration of the switching event. This type of converter is further divided into two types: half-wave ZCS QRC and full-wave ZCS QRC. [2]

### 2.2.1 HALF-WAVE ZCS QRC

Basic topology of half-wave zero current switching quasi-resonant DC-DC converters is in the Fig. 2. Important waveforms are in the Fig. 3.

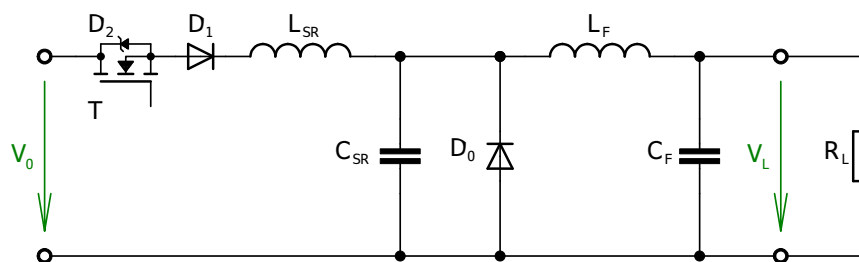


**Figure 2:** Basic topology of half-wave zero current switching quasi-resonant DC-DC converters

Transistor T is switched on when the capacitor  $C_{SR}$  is completely discharged and a free-wheeling diode  $D_0$  is flowed by current  $I_{LF}$  (time  $t_1$ ). Thus, the inductance  $L_{SR}$  is applied to the entire input voltage  $V_0$ . The current inductance  $L_{SR}$  will start to grow linearly (until  $t_2$ ). When  $I_{LSR}$  reaches  $I_{LF}$ , the free-wheeling diode  $D_0$  closes and the capacitor  $C_{SR}$  starts charging.

This decreases the voltage at the inductance  $V_{L_{SR}}$  and thus the steepness of the current increase by the inductance  $I_{L_{SR}}$  begins to decrease. As soon as the voltage at the capacitor  $V_{C_{SR}}$  reaches the supply voltage  $V_0$ , the current by the inductance  $I_{L_{SR}}$  stops rising and then starts to drop ( $t_3$ ). However, the capacitor  $C_{SR}$  is still charging, so the voltage on it increases (until  $t_4$ ).

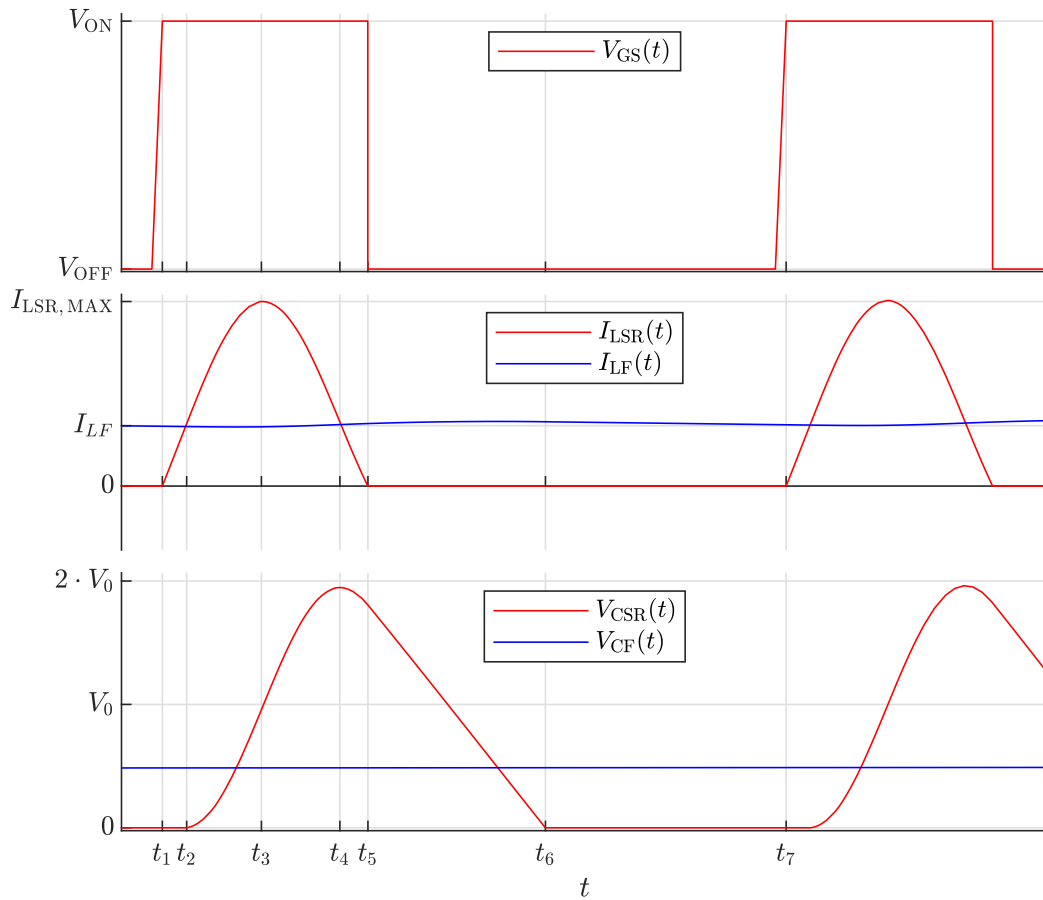


**Figure 3:** Simulation time courses of half-wave zero current switching quasi-resonant DC-DC converters

After the current  $I_{L_{SR}}$  drops of inductance to zero, no current flows through it because the diode  $D_1$  closes ( $t_5$ ). Furthermore, the capacitor  $C_{SR}$  is discharged only by the current drawn  $I_{L_F}$ . When it is completely discharged, the diode  $D_0$  will open and the current  $I_{L_F}$  will only flow through this diode ( $t_6$ ).

### 2.2.2 CONTROL OF HALF-WAVE ZCS QRC

The inverter can be continuously controlled by changing the turn-off time. After the capacitor  $C_{SR}$  is discharged ( $t_6$ ), the next period can be started immediately, thus achieving the maximum output voltage. In case the no-load, output voltage  $V_L$  will be equal to the input voltage  $V_0$ .

If the transistor  $T$  does not switch on immediately after the capacitor  $C_{SR}$  has been discharged, but the switch on is delayed, the mean value of the output voltage will drop. The LC filter smooths the pulsating voltage on the  $V_{C_{SR}}$  capacitor so that the output voltage  $V_{CF}$  can be almost constant.

The basic condition of the function of this circuit is that an amplitude of a resonant current  $I_{RES,MAX}$

will be higher than the current drawn by the load  $I_{LF}$ .

$$I_{RES,MAX} = I_{LSR,MAX} - I_{LF} \quad (2)$$

$$I_{RES,MAX} > I_{LF} \quad (3)$$

$$I_{LSR,MAX} > 2 \cdot I_{LF} \quad (4)$$

If this condition were not met, the inductance current  $I_{LSR}(t)$  would not drop to zero and the transistor  $T$  would not be able to be switched off at zero current. [3]

### 2.2.3 FULL-WAVE ZCS QRC

Basic topology of full-wave zero current switching quasi-resonant DC-DC converters is in the Fig. 5. Important waveforms are in the Fig. 4.

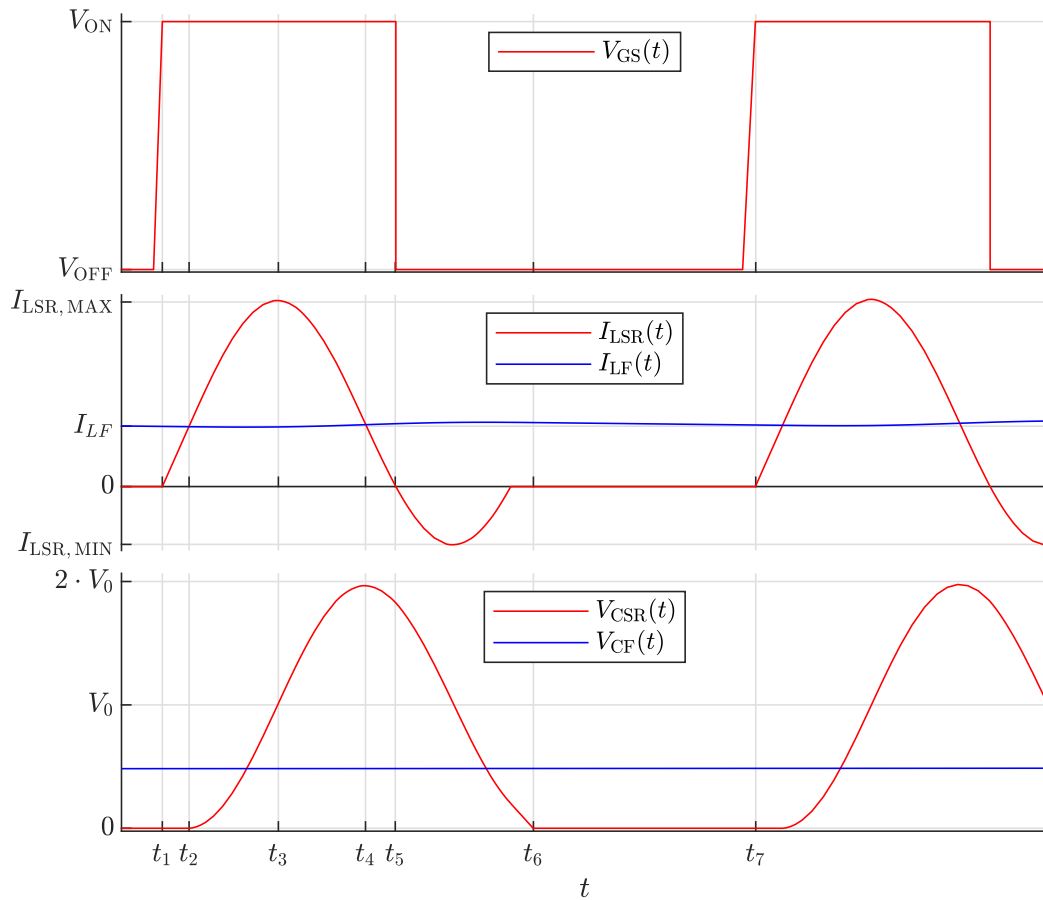


**Figure 4:** Simulation time courses of full-wave zero current switching quasi-resonant DC-DC converters

Until time  $t_5$  this inverter behaves exactly the same way as the half-wave ZCS QRC described in the 2.2.1 section. Then, the current flows through the inductor  $I_{LSR}$  in the opposite direction – to the power supply via diode  $D_2$ . This will eliminate the losses caused by the diode  $D_1$  compared to the previous solution.

Diode losses of  $D_2$  are considerably smaller with  $I_{LF}$  compared to  $I_{RES,MAX}$ , as the  $I_{LSR}$  current in the positive direction is significantly greater than the current  $I_{LSR}$  in the negative direction, as can be seen from the time course in the Fig. 4.

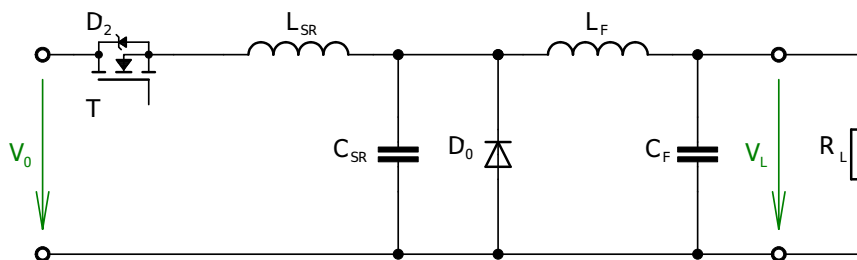


**Figure 5:** Basic topology of full-wave zero current switching quasi-resonant DC-DC converters

Another advantage of this converter can be the significantly lower dependence of the switching period on the current consumption  $I_{LF}$ . The disadvantage, however, is that part of the period returns part of the energy stored in the resonant circuit to the power supply, which unnecessarily increases line losses. [3]

### 3 CONCLUSION

Zero current switching quasi-resonant buck DC-DC converters combine the advantages of conventional converters in the form of relatively simple control and resonant inverters in the form of soft transistor switching, eliminating transistor switching losses and the absence of steep edges causing broadband interference.

The above-mentioned ZCS QRCs are very simple wiring with the minimum necessary components to ensure reliable operation. The only limitation for proper operation is not to exceed the maximum load current.

### ACKNOWLEDGEMENT

This research work has been carried out in the Centre for Research and Utilization of Renewable Energy (CVVOZE). Authors gratefully acknowledge financial support from the Ministry of Education, Youth and Sports under institutional support and BUT specific research programme (project No. FEKT-S-20-6379).

### REFERENCES

- [1] S. Chauhan and A. K. Pandey. *Simulation of ZVS buck converter for charging application using PSIM simulator* In *2017 International Conference on Computation of Power, Energy Information and Commuincation (ICCPEIC)*. Melmaruvathur. 2017. pp. 809-814. doi: 10.1109/IC-CPEIC.2017.8290478
- [2] J. Sun, X. Wang and X. Han. *Averaged modelling and analysis of buck ZCS-QRC*. In *Proceedings of the IEEE International Symposium on Industrial Electronics*. Xian. China. 1992. pp. 680-684 vol.2. doi: 10.1109/ISIE.1992.279689.
- [3] P. VOREL. *Nové koncepce rezonančních měničů pro velké výkony*. Brno, 1999. Dissertation thesis. Brno University of Technology, Faculty of Electrical Engineering and Computer Science, Department of Radioelectronics. Thesis supervisor V. Novotný.

# FIELD ELECTRON EMISSION PERFORMANCE AND ORTHODOXY TEST OF TUNGSTEN EMITTERS WITH AND WITHOUT THIN TUNGSTEN TRIOXIDE BARRIER

**Daniel Burda**

Doctoral Degree Programme (1), FEEC BUT

E-mail: xburda14@stud.feec.vutbr.cz

Supervised by: Dinara Sobola

E-mail: sobola@feec.vutbr.cz

**Abstract:** This initial study aims to explore the topic of thin barrier layers for single tip cold field emitters. The experiment and measurements have been conducted in ultra-high vacuum field electron microscope. Additionally, micrographs of the emitter were obtained using scanning electron microscope. The performance of the emitter was evaluated using orthodoxy test and Murphy-Good plots, which can give more complete picture of emitter changes during field emission.

**Keywords:** Cold field emission, single tip field emitters, tungsten tip, self-heating of electron emitter, tungsten trioxide, dielectric barrier, Murphy-Good plot

## 1 INTRODUCTION

The research on the topic of field electron emission sources is motivated by many practical applications, which ranges from electron guns operating at room temperature, compact X-ray sources to novel field emission displays. Two main categories have emerged over the years, single tip field emitters (STFEs) and large area field emitters (LAFEs), usually consisting of many emission sites, for example arrays or clusters of nanorods or nanotubes. This paper deals with the former group of field emitters. The material mainly used for STFEs is tungsten due to its durability, high melting point, low sputtering ratio, the main applied research goals are to increase stability, emission current density, brightness, while also improve the longevity.

In cold field electron (CFE) emission regime, most of the electrons escape by tunneling from electron states below the Fermi level. An equation describing CFE from ideal planar metallic surfaces was published in 1956 by Good et al. [1], which since then has been modified and extended and used for analysis of CFE current–voltage ( $I$ – $V$ ) characteristics of various emitters not only the metallic. This approach may not be always phenomenological or mathematically correct but may still be “good enough” approximation. Recently, an orthodox CFE emitter test [2] for measured  $I$ – $V$  characteristics to indicate, whether CFE theory can be used to describe an emitter properly and orthodox conditions [3] was developed.

The family of equations starting with the one in 1956 is called *Fowler-Nordheim equations*. Tunneling is assumed through *Schottky-Nordheim* (SN) barrier, which is illustrated in the Figure 1. Directly measured  $I$ – $V$  characteristics from field electron microscope (FEM) can be used under specific *orthodox* conditions to extract emitter performance related properties. In this paper, *extended Murphy-Good equation* (EMG) is employed (more details on the subject in [2,3,4,5]):

$$I(V) = \{A^{\text{SN}}(\theta \exp \eta)V_{\text{R}}^{-\kappa}\}V^{\kappa} \exp(-\eta V_{\text{R}}/V) \quad (1)$$

where  $A^{\text{SN}}$  is the formal emission area assuming SN barrier tunneling,  $V_{\text{R}}$  is a (constant) reference measured voltage [4] needed to pull the top of a characteristic SN barrier, of zero-field height  $\phi$ , down to the emitter Fermi level [2],  $\theta$  and  $\eta$  are work function dependent scaling parameters defined

in [4],  $\eta \sim 9.836239 (eV/\phi)^{1/2}$ , parameter  $\kappa(\eta)$  is also related:  $\kappa = 2 - \eta/6$ . By applying natural logarithm to (1), the equation becomes:

$$\ln \{I/V^\kappa\} = \ln\{A^{SN}(\theta \exp \eta)V_R^{-\kappa}\}V^\kappa - \eta V_R/V \quad (2)$$

The equation (2), called *theoretical Murphy-Good plot*, is linear as every parameter on its right side is constant except for  $I/V$ . For orthodox field emitters, it is possible to extract the emitter characteristic voltage conversion length (VCL)  $\zeta_C$  and related [4] field enhancement factor  $\gamma$  and formal emission area  $A^{SN}$  by transforming measured characteristics into  $\ln\{I/V^\kappa\}$  vs.  $(1/V)$  and fitting it with a linear function [3]. When the transformed  $I-V$  characteristics cannot be fitted with linear function, it is an indicator of non-orthodox behavior and field emission related parameters cannot be extracted. The *electron emission convention* is used, which omits negative signs in electric fields, voltages, currents, and current densities and treats them as positive.

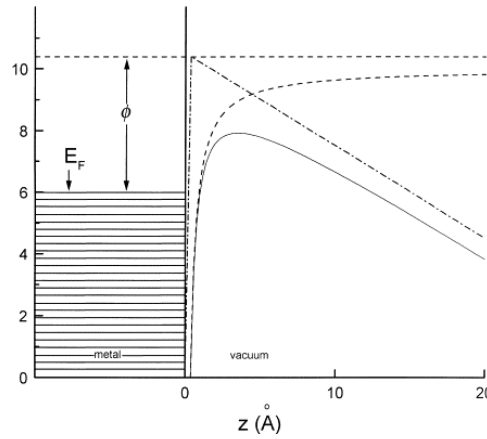


**Figure 1:** Representation of a metal-vacuum interface,  $E_f$  Fermi level,  $\phi$  work function, dot-dash – triangular barrier, dashed line – image potential, full line – *Schottky-Nordheim barrier*. From [6].

## 2 EXPERIMENTAL CONDITIONS

The preparation and characterization of the electron emitter can be described in three phases. In the first phase, tungsten wire (GoodFellow no. 7440-33-7, 99.9+%) with diameter of 0.3 mm was electrochemically etched in in-house setup described elsewhere [7], which was configured for simple one-step lamellae drop-off technique. The etching of tungsten wire takes place in a thin lamella of 2M NaOH solution stretched out on a Pt ring, where the tungsten wire acts as the anode, and Pt ring acts as the cathode, detailed description can be found in [8,9]. With this etching technique, sharp tungsten tips with tip radius of 50 nm and less can be prepared, which makes them suitable for field electron emission applications. After the etching in NaOH solution the produced tungsten tip is inevitably covered with thin layers of  $WO_x$  and ternary-phase oxides [10].

In the second phase, the tungsten tip was loaded into in-house FEM for subsequent cleaning of the tungsten tip by self-sputtering and then the measurement of field electron emission characteristics and field emission pattern of the clean tungsten tip. During these steps, FEM was continuously pumped down to ultra-high vacuum (UHV) levels up to  $10^{-7}$  Pa. The applied cathode voltage was set by DeLong Instruments high voltage supply. The emission current between the tungsten emitter and Al coated Nd:YAG scintillator was measured by Keithley 485 Pico ammeter.

In the third phase, high cathode voltage was applied to the tungsten tip, which resulted in heating up of the tip by high current density. The temperature of the apex may reach up to over 1300 K, the emission shifts from field to field-thermal. After 5 minutes, the applied voltage, also the emission was switched off, and oxygen from a small attached cylinder was introduced into the FEM chamber through a precise needle valve, effectively increasing the pressure from  $3.7 \cdot 10^{-7}$  Pa to  $1 \cdot 10^{-5}$  Pa. After 2 minutes, the oxygen flow was stopped and the chamber was left to pump down for 4 hours until the initial pressure was restored. The formation of nanometer thin layer of high quality  $WO_3$  on

the clean surface is assumed. The measured  $I$ - $V$  characteristics of clean emitter and oxidized tungsten emitter are presented in the Figure 2.

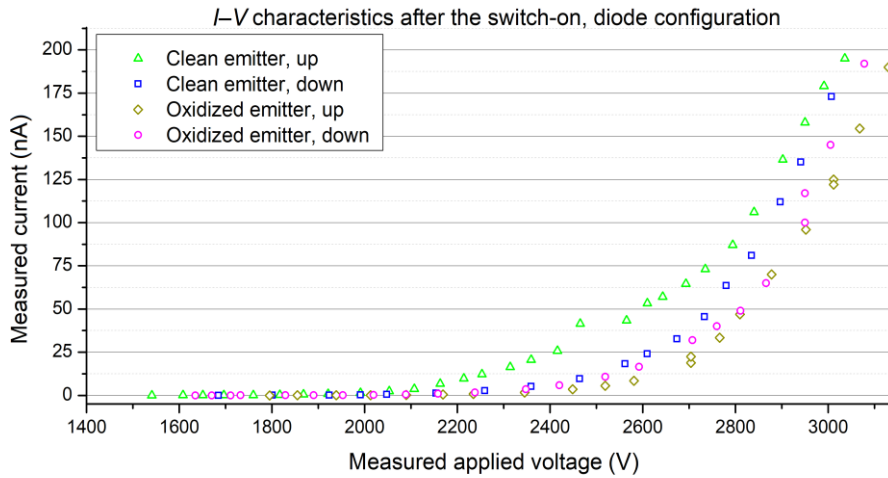


**Figure 2:** The emission characteristics of clean and oxidized tungsten emitter, forward (up) and backward (down) voltage scanning.

### 3 RESULTS

The work function of tungsten and  $\text{WO}_3$  is assumed to be 4.5 eV and 5.6 eV respectively. Although the formation of  $\text{WO}_3$  could not be observed directly, after the supposed oxidation of the apex of the emitter, the threshold voltage needed for stable emission current  $> 2$  nA shifted significantly from the value of 2030 V for clean emitter to 2350 V, when the forward voltage scanning was performed (up). But during backward voltage scanning (down), the threshold voltage of oxidized emitter decreased and was of similar value: 2050 V (clean) and 2070 V (oxidized). This behavior indicates the surface changes on the apex of oxidized emitter during measurement steps. Recorded emission patterns are illustrated in the Figure 3, the main observable difference is in the brightness of the patterns, the change of emission centers is not noticeable. Accurate evaluation of changes over time in emission centers would require setup adjustments and is considered in the future.

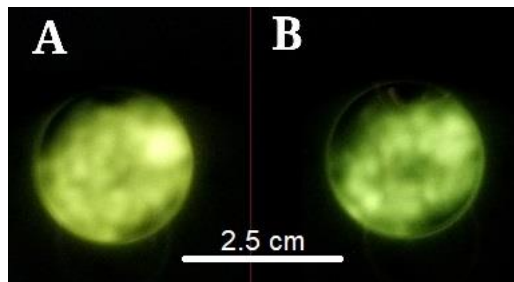


**Figure 3:** Comparison of the electron pattern projected at the backside of the scintillator. Applied cathode voltage of 3 kV (maximum measurement value). A) clean emitter, higher intensity/higher current observed B) supposedly oxidized emitter.

From the Murphy-Good plots presented in the Figure 4, the clean emitter shows clearly non-orthodox behavior in the left upper part of M-G plot for upward voltage increase, there may be several causes [3] including field-dependent geometry, heating-dependent changes in work function, adsorbate removal and the tip can no longer be described by *Fowler-Nordheim theory*. The extracted data of interest are in Table 1, note the significant difference in  $A^{\text{SN}}$  by the factor of 7 between the spurious and the correct values. The non-spurious values are in good agreement with those of a conventional

< 100 nm radius tungsten tip. In the first three steps (excluding spurious part), the extracted parameters show a small progress, which may be attributed to the gradual tip blunting. The thickness of tungsten trioxide deposited during the third step is assumed to be several nanometers, because the difference between the values of  $A^{SN}$ ,  $\zeta_C$ ,  $\gamma$  before and after the oxidization would be more significant otherwise.

Emitter, Step	Orthodoxy test	$A^{SN}$ (nm <sup>2</sup> )	$\zeta_C$ (m)	$\gamma$ (-)
Clean, Up (spurious)	Undecided/Fail	1.01	$4.32 \cdot 10^{-7}$	$2.32 \cdot 10^4$
Clean, Up,	Pass	7.44	$4.89 \cdot 10^{-7}$	$2.05 \cdot 10^4$
Clean, Down	Pass	7.98	$5.39 \cdot 10^{-7}$	$1.85 \cdot 10^4$
Oxidized, Up	Pass	9.41	$5.51 \cdot 10^{-7}$	$1.81 \cdot 10^4$
Oxidized, Down	Pass	24.29	$6.002 \cdot 10^{-7}$	$1.665 \cdot 10^4$

**Table 1:** Emitter orthodoxy test results and field emission values: formal emission area  $A^{SN}$ , voltage conversion length  $\zeta_C$ , field enhancement factor  $\gamma$ , calculated from plots in Figure 4.

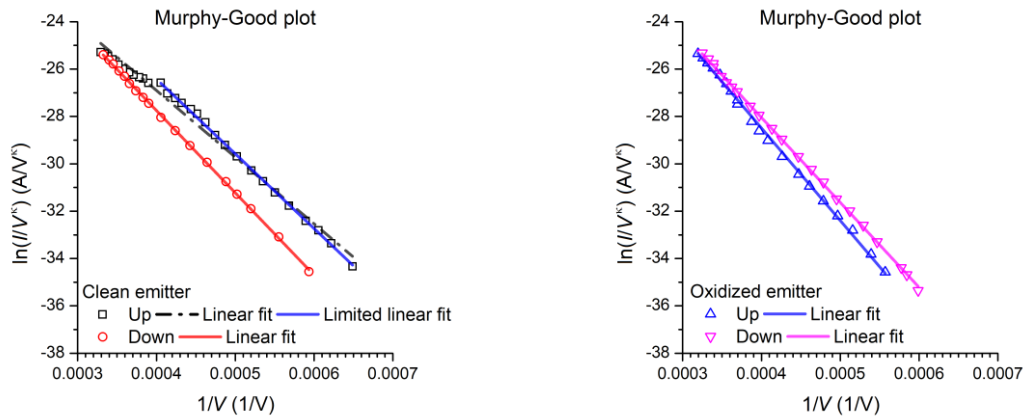


**Figure 4:** Murphy-Good plots and linear fits. Note the dash-dot black line – the example of improper fit leading to spurious results.

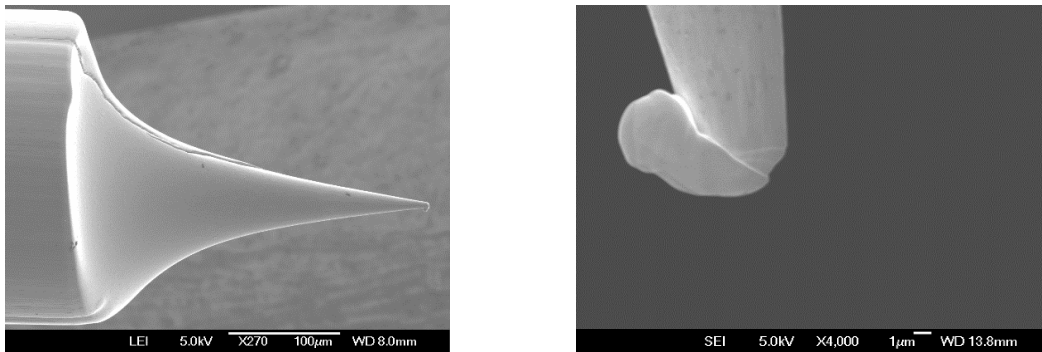


**Figure 5:** SEM micrographs of the examined emitter. The detail shows destruction of the apex.

After the FEM experiment, analysis using SEM revealed the destruction of the emitter apex, which is shown in the Figure 5. This phenomenon is common when the cold field emission regime changes towards thermal regime, which drains electrons even more towards the anode, resulting in rapid heating and melting.

Counterintuitively, it may not result in a significant change of the emission current. It is largely controlled by applied cathode voltage but also the setup conditions and the occurrence cannot be completely predicted. The values extracted from the M-G plots also give information, when the apex

of the emitter started to melt. It was most probably at the maximum applied voltage of 3 kV, between forward and backward voltage screening of the oxidized emitter. Then, during the backward voltage screening, the formal emission area increased by the factor of 2.5 and the tip became more blunter as indicated by the larger further decrease of extracted field enhancement factor.

#### 4 SUMMARY

During the FEM measurements, several changes indicating modifications of the field emitter were observed. The method of oxidation was proposed and demonstrated. The thickness of prepared tungsten trioxide barrier on top of the tungsten emitter tip was assumed to be of several nanometers thick only. More experiments aimed towards preparation of tungsten trioxide barriers with a thickness larger than 10 nm are to be carried out in the future.

After the oxidization, at applied cathode voltage of 3 kV, the emitter started to melt, which became evident only after the subsequent SEM imaging. During this event, the formal emission area increased by the factor of 2.5. Whether the tungsten trioxide layer have survived the melting is unclear and superfluous, it can no longer be analyzed for field emission. In the follow-up experiments detailed element analysis with TEM to clarify the formation of tungsten trioxide layer is planned.

#### ACKNOWLEDGEMENT

The author would like to thank to EBL group at Institute of Scientific Instruments of the Czech Academy of Sciences, where the presented research was conducted, the infrastructure was supported by RVO:68081731. The work was also supported by FEKT-S-20-6352.

#### REFERENCES

- [1] GOOD, R H. and Erwin W. MÜLLER. 1956. Field Emission. *J Vac Sci Technol B* [online]. Berlin, Heidelberg: Springer Berlin Heidelberg, 176–231.
- [2] ALLHAM, Mohammad, Richard FORBES, Alexandr KNÁPEK, Marwan MOUSSA. 2020. Implementation of the Orthodoxy Test as a Validity Check on Experimental Field Emission Data. *J Elect Eng Technol* [online]. **71**.
- [3] FORBES, Richard G. 2018. Tutorial lecture, April 2018: Field electron emission and the interpretation of Fowler-Nordheim plots. [online]. DOI: 10.13140/RG.2.2.13535.15526/
- [4] FORBES, Richard G. 2019. The Murphy–Good plot: a better method of analysing field emission data. *Roy Soc Open Sci* [online]. **6**(12).
- [5] FORBES, Richard G and Jonathan H.B DEANE. 2007. Reformulation of the standard theory of Fowler–Nordheim tunnelling and cold field electron emission. *P Roy Soc A-Math Phy* [online]. **463**(2087), 2907–2927.
- [6] MODINOS, A. 2001. Theoretical analysis of field emission data. *Solid State Electron* [online]. **45**(6), 809–816.
- [7] KNÁPEK, Alexandr, Jiří SÝKORA, Jana CHLUMSKÁ and Dinara SOBOLA. 2017. Programmable set-up for electrochemical preparation of STM tips and ultra-sharp field emission cathodes. *Microelectron Eng* [online]. **173**, 42–47.
- [8] MELMED, Allan J. 1998. The art and science and other aspects of making sharp tips [online]. *J Vac Sci Technol B* [online]. **9**(2).
- [9] KLEIN, M. and G. SCHWITZGEBEL. 1997. An improved lamellae drop-off technique for sharp tip preparation in scanning tunneling microscopy. *Rev Sci Instrum.* **68**(8), 3099–3103.
- [10] KNÁPEK, Alexandr. 2013. Methods of preparation and characterization of experimental field-emission cathodes. Brno. Doctoral thesis. Brno University of technology.

# STRUCTURAL CHARACTERIZATION OF ALN THIN FILMS OBTAINED ON SILICON SURFACE BY PE-ALD

**Rashid Dallaev**

Doctoral Degree Programme (3rd year), FEEC BUT

E-mail: [xdalla03@vutbr.cz](mailto:xdalla03@vutbr.cz)

Supervised by: Petr Sedlák

E-mail: [sedlakp@feec.vutbr.cz](mailto:sedlakp@feec.vutbr.cz)

**Abstract:** The aim of this study is to investigate the hydrogen impregnations in AlN thin films deposited using plasma-enhanced atomic layer deposition technique. As of date, there is an apparent gap in the literature regarding the matter of hydrogen impregnation within the AlN layers. Hydrogen is a frequent contaminant and its content has detrimental effect on the quality of resulted layer, which is why it is relevant to investigate this particular contaminant and try to eliminate or at least minimize its quantity. Within the films hydrogen commonly forms amino or imide types of bonds ( $-\text{NH}_2$ ,  $-\text{NH}$ ). There is only a handful of analytical methods enabling the detection of hydrogen. This particular study comprises two of them – Fourier-transform infrared spectroscopy (FTIR) and second ion-mass spectrometry (SIMS). XPS analysis has also been included to examine the surface nature and structural imperfections of the grown layer.

**Keywords:** atomic layer deposition, aluminum nitride, thin films, fourier-transform infrared spectroscopy, hydrogen impregnations, x-ray photoelectron spectroscopy.

## INTRODUCTION

Aluminum nitride is a semi-conductive material with wide band gap (6,2 eV), its crystalline structure forms a hexagon akin to the mineral known as wurtzite (zinc sulfide), thus AlN is often called a wurtzite-phased material. This material can boast high thermal resistance in inert atmospheres [1].

Thin films of aluminum nitride (AlN) have seen an increase in popularity lately, due to the promising characteristics and properties of this material such as already mentioned wide band gap, excellent mechanical properties, high electrical resistance, high chemical stability, high breakdown voltage, low temperature for deposition and a potential for piezoelectricity [2]. A low deposition temperature of AlN renders it advantageous over other materials with piezoelectric properties as zinc oxide or zirconate titanate since it allows it to be utilized in conventional silicon monolithic systems where low temperature process is a requirement [3]. A low deposition temperature (under 400 °C) of AlN is also a reason why this material is a suitable option for post-processing of the integrated circuits. There are also records of AlN being implemented in surface acoustic wave filters and bulk acoustic wave [4].

Atomic layer deposition (ALD) is a subtype of CVD methods for obtaining thin films in vapor phase. Certain advantages of ALD over its analogues make it a more attractive choice for thin film fabrication process. Those advantages include the possibility of the precise control over the film growth and staged process with purging session between each stage allows to keep the chamber clean from waste components which occur after each precursor introduction. ALD also shows a lot of promise in energy conversion technologies and semiconductor manufacturing process [5]. Atomic precision of ALD is essential for application in nanoelectronics. For the last several years ALD has been proving itself to be a relatively cheap method with great scalability and precision necessary for high-quality thin film fabrication at the nanoscale level.

However, there still seems to be a lack of adequate and comprehensive studies when it comes to impurities in AlN thin films obtained by ALD and other methods [7, 8]. This particular papers attempts to bring some contribution to filling the gap in that area.

## PREPARATION OF THE SAMPLES

In this work we obtained AlN thin films using plasma enhanced atomic layer deposition (PE-ALD) on silicon substrates. Deposited films then have been analyzed using FTIR, XPS and SIMS instruments.

Prior to deposition silicon substrates with dimensions of 1x1x0,1cm and (100) orientation were cleaned in isopropanol. Each individual ALD cycle comprised of the next steps: 1) injection of TMA (0,06sec), 2) purge 10sec, 3) flow of N<sub>2</sub>/H<sub>2</sub> (20 sccm) and activate plasma (40 sec), 4) purge 5sec

The total amount of such ALD cycles was 1100 and this converts into resulting thickness of approximately 70 nm. The temperature of deposition was chosen to be 250 °C which is within the AlN ALD window. The energy of plasma was 300W. The annealing was implemented at 1000 °C for duration of 1 hour, however, for 10 minutes of this hour the temperature was increased to 1250 °C.

## RESULTS AND DISCUSSION

### 3.1 FOURIER-TRANSFORM INFRARED SPECTROSCOPY DATA

Infrared reflectance is a spectroscopic non-destructive analysis allowing to study the nature of the chemical bonds. We used FTIR in the reflectance mode in which the intensity of the dispersed light from the sample is presented on the graph as a function of the wavelength. By evaluation the peaks and dips of the intensity we can make draw some conclusion on the type of chemical bonds existing in the sample. FTIR reflectance spectrum of AlN on silicon is given in fig 1.

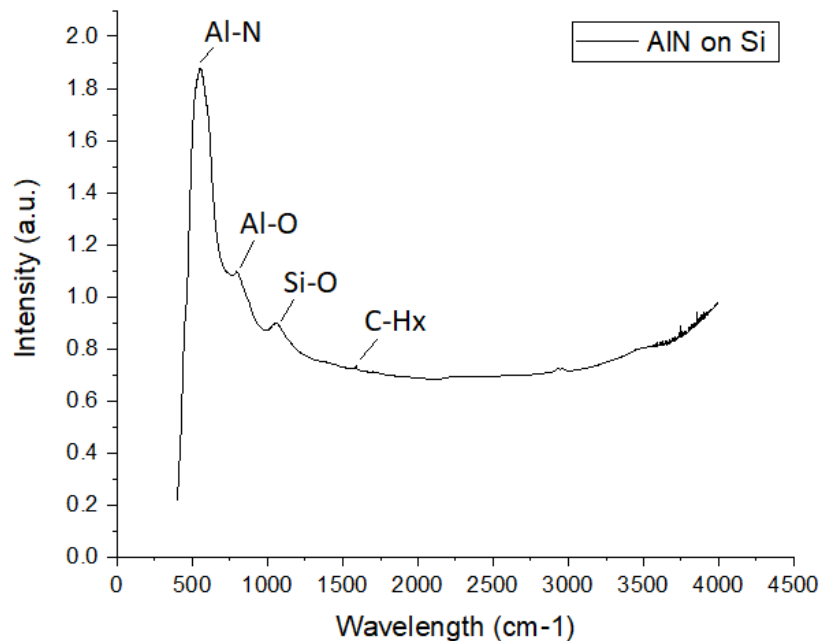


**Figure 1:** Raman spectra of AlN on Si substrate

The most intensive peak at ~615 cm<sup>-1</sup> is attributed to Al–N, vibration mode A<sub>1</sub>(TO); less intensive peaks at 735 cm<sup>-1</sup> and ~1100 cm<sup>-1</sup> are assigned to  $\nu$ (Al–O), vibration mode Al–O and to Si–O vibration mode  $\nu$ (Si–O) correspondingly [9, 10]. There is also a barely visible peak at ~1500eV

which is according to [11] corresponds to C-H bonds. Given our initial goal to detect hydrogen within the AlN films, this peak is of particular interest.

### 3.2 SECONDARY ION-MASS SPECTROMETRY

Unlike FTIR and XPS, SIMS is a destructive technique and relies on sputtering a crater on the sample with high energy ions, after which by collecting the ejected (secondary) ions distribution profiles of the elements in the depth of the sample are created. SIMS is extremely sensitive method and allows detecting all elements (including hydrogen). However, quantization in SIMS is complicated and requires the use of the standards which are not always available especially for less common materials. The quantization of hydrogen is further complicated by the fact that it is picked up by analyzer not only from the sample but also from atmosphere, even under high-vacuum. In this study SIMS was used in time-of-flight mode, the sputtering of the film was conducted using oxygen gun. 3D profile distribution for chosen elements in the bulk of the film are given in the Figure 2. The depth of the cratered  $\sim 200\text{nm}$  (the density of the AlN film is around  $70\text{ nm}$ ).

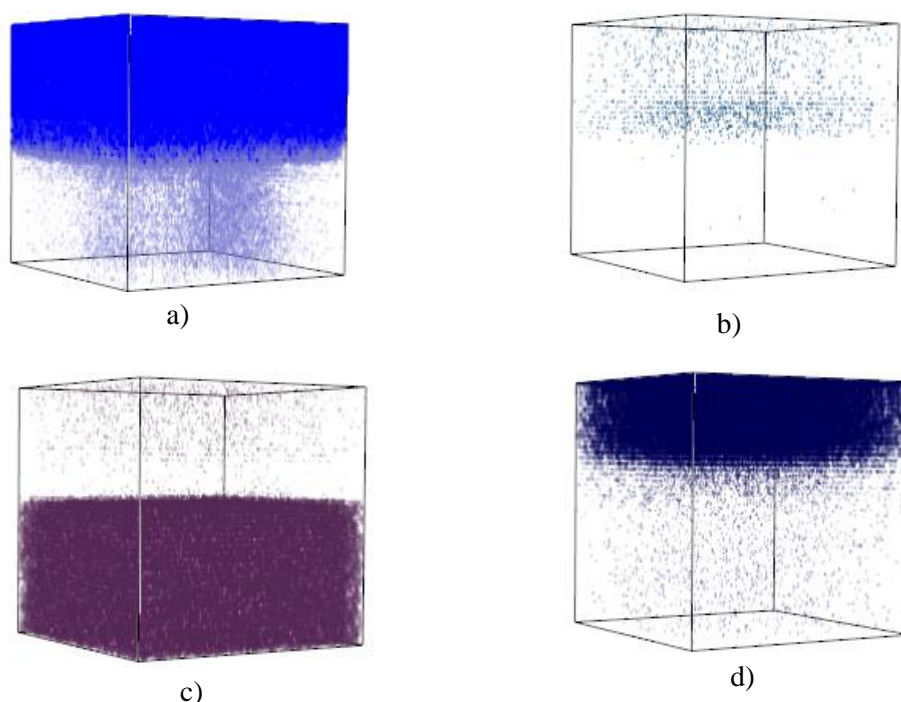


**Figure 2:** SIMS 3D profiling images of: a) Aluminum, b) Nitrogen, c) Silicon, d) Hydrogen.

As was expected we have a dense distribution of aluminum atoms and less so of nitrogen in the AlN layer (fig 2a and fig. 2b). Low intensity of nitrogen atoms is due to the fact that measurement was performed in a positive mode, whereas the bulk of nitrogen secondary ions are negative by nature. In addition, D. Cao et al. [16] claim that annealing of AlN in the nitrogen atmosphere might improve the quality of the layer and thereby increase the amount of nitrogen atoms.

Once the sputtering beam has breached the AlN layer, no more aluminum is picked up, instead we can observe the dense distribution of Si atoms belonging to the substrate (fig 2c). The hydrogen 3D profile is presented in fig 2d. Since SIMS detector collects not only atoms emitted from the surface but also from the atmosphere it is next to impossible to tell how much of the hydrogen exactly belongs to the AlN layer. However, at the very least we can reasonably presume that main part of it exists in the AlN layer and not in the substrate, given the drastic decline in its concentration once the AlN layer is breached.

### 3.3 X-RAY PHOTOELECTRON SPECTROSCOPY (XPS) DATA

XPS analysis is given here to provide additional information on the nature of the chemical bonds, mostly on the surface since x-ray penetrates first 7-10 nm of the layer, no sputtering was used. The fitting was done in CasaXPS software. The whole spectrum was shifted to center C1s (C-C bond) at 284.8 eV.

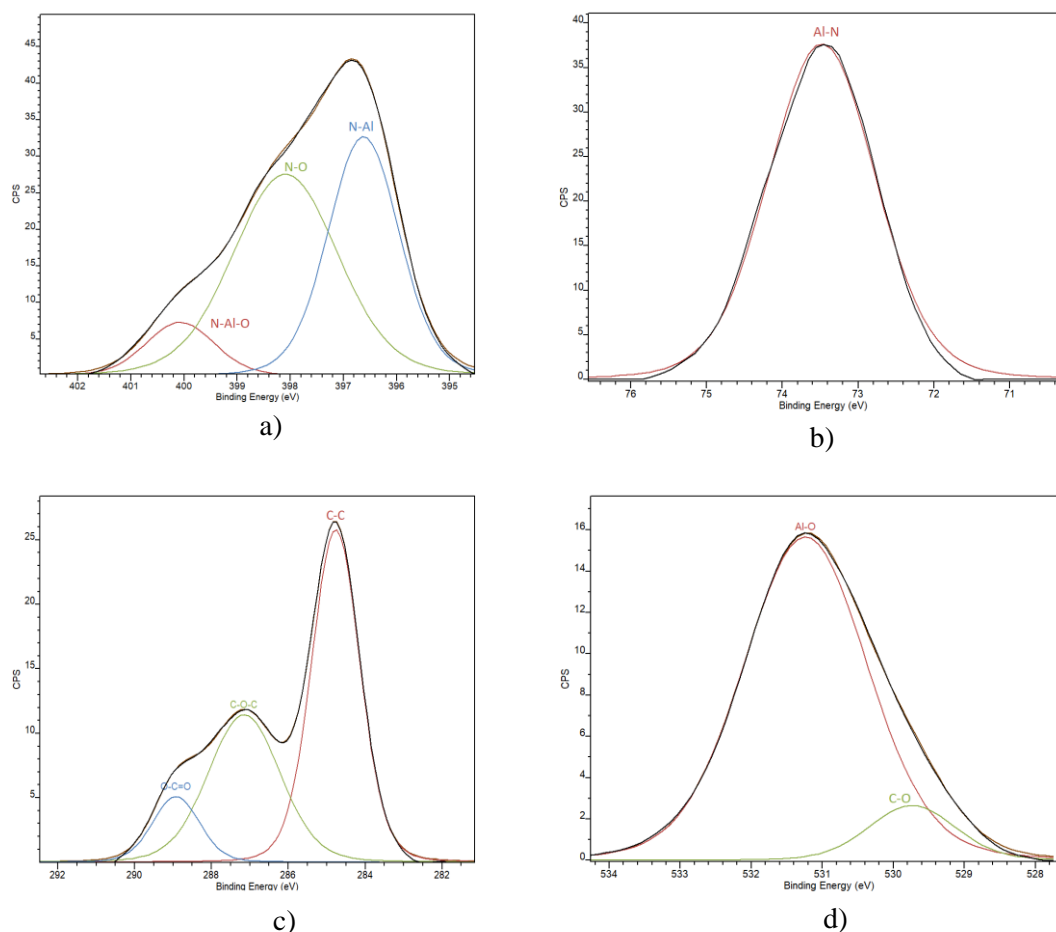


**Figure 3:** XPS elemental spectra for AlN on Si: a) N1s, b) Al2p, c) C1s, d) O1s

The nitrogen peak (fig. 3a) can be deconvoluted into three subpeaks with binding energies of 396,6eV, 398eV and 400 eV. The tallest of them at 396,6 eV refers to N-Al bond and the other two are ascribed to N-O and N-Al-O correspondingly [12].

Aluminum exhibits just one high-intensity peak (fig.3b) at ~73,5 eV which is precisely the binding energy of Al-N according to literature [13, 17], which goes along well with the data of the nitrogen peak.

Carbon is an inevitable contaminant in form of carbon (fig.3c) and oxygen (fig.3d) are also presented. Carbon forms a triplet of peaks at 284,8eV; 286,5eV and 288,5 eV which are attributed to C-C; C-O-C and O-C=O correspondingly. Oxygen doublet consists of peaks at 529,8 eV (C-O) and 531eV (Al-O) [14, 15].

### CONCLUSION

This paper's aim was to study chemical structure of AlN thin films obtained by ALD on silicon substrates. To achieve this goal such analytical methods as FTIR, SIMS and XPS were utilized. FTIR

analysis detected C-Hx bond proving the hydrogen presence in the AlN layer, the hydrogen contamination has further been confirmed by the SIMS method in the 3D distribution hydrogen profile. XPS method showed the presence of oxygen and carbon impregnations. However, when it comes to the AlN structure, all three methods showed rather promising results - Al-N bond was detected by FTIR and XPS whereas SIMS analysis provided a dense concentration of aluminium atoms in the film. In summary, it can be said that the overall quality of the deposited layer is reasonable and contaminations level are within the norm for AlN layers obtained using ALD. However, impurities should be further investigated and the methods for their elimination should be developed. High-temperature annealing is reportedly a good tool for improving the crystallinity of the films and removing undesired and defective bonds by the process of diffusion and atomic rearrangement.

## ACKNOWLEDGEMENT

This work was supported by the Internal Grant Agency of Brno University of Technology, grant No. FEKT-S-20-6352. CzechNanoLab project LM2018110 funded by MEYS CR is gratefully acknowledged for the financial support of the measurements/sample fabrication at CEITEC Nano Research Infrastructure.

## REFERENCES

- [1] V. A. Tarala, A. S. Altakhov, V. Ya. Martens, S. V. Lisitsyn, Growing aluminum nitride films by Plasma-Enhanced Atomic. (2015). doi:10.1088/1742-6596/757/1/012003
- [2] Y. Bian, M. Liu, G. Ke, Y. Chen, J. DiBattista, E. Chan, Y. Yang, Aluminum nitride thin film growth and applications for heat dissipation, *Surf. Coatings Technol.* 267 (2015) 65–69. doi:10.1016/j.surfcoat.2014.11.060
- [3] C. Giordano, I. Ingrosso, M.T. Todaro, G. Maruccio, S. De Guido, R. Cingolani, A. Passaseo, M. De Vittorio, AlN on polysilicon piezoelectric cantilevers for sensors/actuators, *Microelectron. Eng.* 86 (2009) 1204–1207. doi:10.1016/j.mee.2008.12.075
- [4] A. Andrei, K. Krupa, M. Jozwik, P. Delobelle, L. Hirsinger, C. Gorecki, L. Nieradko, C. Meunier, AlN as an actuation material for MEMS applications. The case of AlN driven multilayered cantilevers, *Sensors Actuators, A Phys.* 141 (2008) 565–576. doi:10.1016/j.sna.2007.10.041.
- [5] R.W. Johnson, A. Hultqvist, S.F. Bent, A brief review of atomic layer deposition: From fundamentals to applications, *Mater. Today.* 17 (2014) 236–246. doi:10.1016/j.mattod.2014.04.026
- [6] M. Schlesinger, M. Paunovic, Electroless deposition of copper, *Mod. Electroplat.* 1 (2010) 433–446. doi:10.1002/9780470602638.
- [7] M. Reusch, K. Holc, L. Kirste, P. Katus, L. Reindl, O. Ambacher, V. Lebedev, Piezoelectric AlN films for FPW sensors with improved device performance, *Procedia Eng.* 168 (2016) 1040–1043. doi:10.1016/j.proeng.2016.11.335.
- [8] A.I. Abdulagatov, Sh. M. Ramazanov, R.S. Dallaev, E.K. Murliev, D. K. Palchaev, M. Kh. Rabadanov and I.M. Abdulagatov, Atomic Layer Deposition of Aluminum Nitride Using Tris(diethylamido)aluminum and Hydrazine or Ammonia. *Russian Microelectronics* (2008), Vol. 47, No. 2, 118–130 doi: 10.1134/s1063739718020026
- [9] C. John, Interpretation of Infrared Spectra, A Practical Approach, *Encycl. Anal. Chem.* (2000).

- [10] M. Broas, P. Sippola, T. Sajavaara, V. Vuorinen, A. Pyymaki Perros, H. Lipsanen, M. Paulasto-Kröckel, Structural and chemical analysis of annealed plasma-enhanced atomic layer deposition aluminum nitride films, *J. Vac. Sci. Technol. A Vacuum, Surfaces, Film*. (2016). doi:10.1116/1.4953029.
- [11] P. Motamedi, K. Cadien, Structural and optical characterization of low-temperature ALD crystalline AlN, *J. Cryst. Growth*. (2015). doi:10.1016/j.jcrysro.2015.04.009.
- [12] H. Kim, H. Ju, B. Joon, Optic Investigation of fast and slow traps in atomic layer deposited AlN on 4H-SiC, *Opt. - Int. J. Light Electron Opt.* 184 (2019) 527–532. doi:10.1016/j.ijleo.2019.05.002.
- [13] Y. Li, C. Zhang, X. Luo, Y. Liang, D. Wu, C. Tin, X. Lu, Applied Surface Science Surface , structural and optical properties of AlN thin films grown on different face sapphire substrates by metalorganic chemical vapor deposition, *Appl. Surf. Sci.* 458 (2018) 972–977. doi:10.1016/j.apsusc.2018.07.138.
- [14] Z. Tseng, L. Chen, W. Li, S. Chu, Resistive switching characteristics of sputtered AlN thin films, *Ceram. Int.* 42 (2016) 9496–9503. doi:10.1016/j.ceramint.2016.03.022.
- [15] D. Rashid, S. Stach, Ş. Țălu, D. Sobola, A. Méndez-Albores, G.T. Córdova, L. Grmela, Stereometric Analysis of Effects of Heat Stressing on Micromorphology of Si Single Crystals, *Silicon*. (2019). doi:10.1007/s12633-019-0085-4.
- [16] D. Cao, X. Cheng, Y.H. Xie, L. Zheng, Z. Wang, X. Yu, J. Wang, D. Shen, Y. Yu, Effects of rapid thermal annealing on the properties of AlN films deposited by PEALD on AlGaIn/GaN heterostructures, *RSC Adv.* 5 (2015) 37881–37886. doi:10.1039/c5ra04728e.
- [17] L. Rosenberger, R. Baird, E. McCullen, G. Auner, G. Shreve, XPS analysis of aluminum nitride films deposited by plasma source molecular beam epitaxy, *Surf. Interface Anal.* 40 (2008) 1254–1261. doi:10.1002/sia.2874.

# STRUCTURAL ANALYSIS OF GAAS-BASED PV CELLS AFTER IONIZING IRRADIATION

**Nikola Papež**

Doctoral Degree Program (4), FEEC BUT

E-mail: Nikola.Papez@vutbr.cz

Supervised by: Dinara Sobola

E-mail: sobola@vutbr.cz

**Abstract:** Morphology and structural analysis of photovoltaic cells based on GaAs before and after high dose gamma radiation of 500 kGy was investigated. Cobalt-60 emitter was used as the synthetic radioactive isotope. This radioactive form of cobalt is commonly used for space instruments and devices testing. Atomic force microscopy (AFM) was used to study the morphology and roughness differences. Cross-sectional investigation using transmission detector to thin layers observing was performed. Also, with use of sputtering system of Secondary Ion Mass Spectroscopy (SIMS) a detailed molecular and elemental information about the surface top layers was showed. Another molecular and structural changes in the top layers using two optical methods of Raman spectroscopy and spectrophotometry were also identified.

**Keywords:** GaAs, gamma radiation, AFM, STEM, SIMS, spectrophotometry

## 1 INTRODUCTION

It is known that Earth's atmosphere is capable of absorbing the gamma radiation. Electromagnetic radiation, such as gamma rays  $\gamma$ , is high penetration radiation that comes from the spontaneous decay of radionuclides. The most commonly used radiation source for testing is  $^{60}\text{Co}$  or otherwise called cobalt-60. It is widely used in sterilization and radiotherapy, but its use can also be found in the testing of space equipment installed on various space objects. Cobalt-60 has a half-life of 5.27 years and generates two photons with energy of 1.17 MeV and 1.33 MeV. It decomposes into a stable isotope of nickel-60 ( $^{60}\text{Ni}$ ) [1].

Because of the assumption that equipment operating in space, such as solar cells, will no longer be serviced or changed, it is highly desirable to ensure and verify radiation hardnesses as many as possible methods for their smooth operation. The radiation hardness for devices of this type is normally tested with Cobalt-60 [2].

## 2 MATERIALS AND METHODS

In this work, several dozen GaAs-based solar cells were irradiated using gamma rays. Irradiation took place in the irradiation center Roztoky u Prahy in the Czech Republic at standard temperature and air conditions. No shielding was used and the measurement was at a direct distance. Cobalt-60 was used as the emitter and the dose absorbed by the solar cells was 500 kGy. The irradiation time was 21 days. By this exposure was simulated accelerated aging, which under normal conditions in the solar system took several years. Several measurement methods have been used, which are described below, allowing a better understanding of the behavior of the material after such strong irradiation [3].

Measurement of surface topography at the nanometer scale was investigated using NTEGRA Prima microscope with semi-contact mode and scanning speed of  $8.04 \mu\text{m/s}$ . The monocrystalline probes

were used with a tip curvature of 10 nm, type NSG01. Morphological changes were examined before and after irradiation, and so were other measurement methods. To reduce the probability of random structures, the regions on the solar cell were scanned several times.

From the measured morphological data the roughness analysis and several informative surface parameters were performed. These parameters were calculated from the  $10 \times 10 \mu\text{m}$  scan area range. The average height of features was selected as a parameter describing surface morphology; average roughness  $S_a$  represents the total topology scale; kurtosis  $S_{ku}$  parameters and skewness  $S_{sk}$  describing a deviation from the normal distribution of the measured height points. In roughness analysis, features are called surface irregularities. The overall reading of the altitude points in the surface analysis of this PV cell was summarized in a histogram of features representing a typical bell-shaped curve.

Although the effects of such intense radiation that have been performed can have a severe and visible impact on the material, scanning electron microscopy with transmission detector has been preferred for detailed analysis and understanding. The lamellas with a thickness of 80 nm were prepared, and the GaAs layer was examined. For this purpose, the FEI Helios NanoLab 660 microscope was used. Bright-field (BF) mode has been selected for image generating. An unscattered electron beam is selected by objective aperture, and scattered electrons are excluded. Surface areas, where are electron absorbed, appears to be darker. Where are the electron transmitted from the area, appears to be brighter. During the observation, the high voltage was set to 30 kV and the current to 50 pA [5].

Elemental and molecular information about the sample was given by SIMS with reflectron Time-of-Flight mass analysis (TOF). The instrument system is called IONTOF TOF.SIMS 5. For this analytical technique, a solid surface is bombarded by primary ions. Collision cascade is generated after the primary ion energy is transferred to atoms through atomic collisions. Main investigated peaks are:  $\text{Ga}^+$ ,  $\text{Al}^+$ ,  $\text{Ti}^+$ ,  $\text{As}^+$ . As a primary beam, it was chosen ions of  $\text{Bi}_3^{++}$  with the energy of 60 keV. As a sputter beam, it was used reactive species of  $\text{O}_2$  with the energy of 2 keV and  $100 \times 100 \mu\text{m}$  crater size.

The spectrophotometry spectra were measured in the range of UVA, VIS and NIR regions – 200 nm to 1000 nm using the Optical Spectrometer Ocean optics JAZ 3-channel. The gold-coated wafer was used as a calibration sample.

Another optical method used, was confocal Raman imaging performed by WITec alpha300 R system. Where as a light source was set a 532 nm green laser with VIS spectrophotometer. Spectral information was collected with 5 mW laser power as one single spectrum.

### 3 RESULTS

Atomic force microscopy measurement of the morphology on the sample after exposure (Figure 1b) manifested itself in the form of higher surface segmentation. These surface changes described in Table 1 may affect the differences in the optical parameters, but it depends mainly on its extent. The most considerable differences against measurement in Figure 1a were observed in the case of higher kurtosis  $S_{ku}$  and skewness  $S_{sk}$  parameters. In histogram in Figure 1c can be seen a decrease in height on average after irradiation. In the order of nanometers this can be considered a slight decrease. It can be assumed that this change will not affect the optical properties on a large scale. It is important to realize that the changes in the surface are in the order of nanometer units [6].

**Table 1:** Photovoltaic cell surface roughness parameters.

	Average height [nm]	$S_a$ [nm]	$S_{ku}$ [-]	$S_{sk}$ [-]
Before irradiation	7.220	2.133	0.085	0.133
After irradiation	5.561	1.521	2,233	1.046

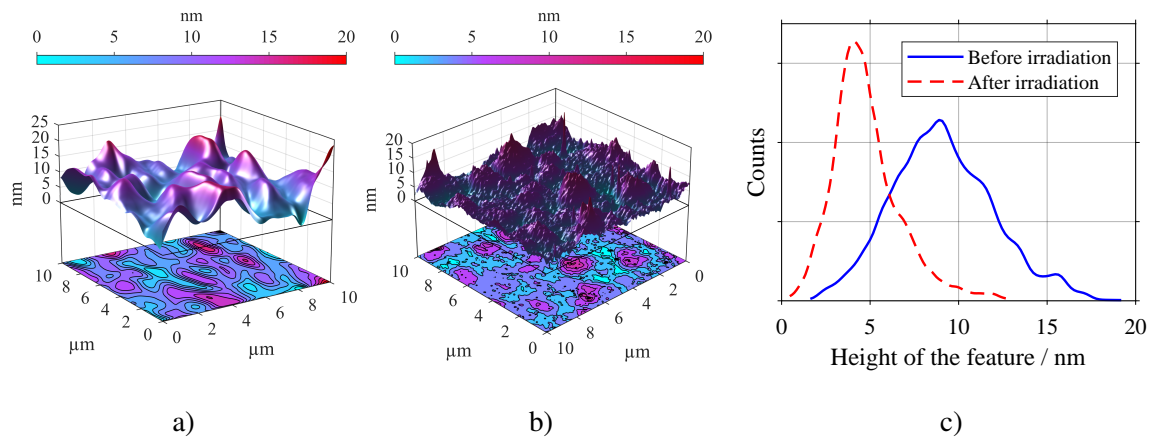


**Figure 1:** Surface morphology measured by AFM a) before and b) after irradiation; and the c) height histogram of features for both cases.

Both Figures 2a and 2b show a cross-section of a thin lamella over several layers. At the top of the sample – the colored layer – is carbon, which served only as a protective layer in the formation of the lamella. The several modes to observe the lamella were used. A dark field is commonly used to detect imperfections in a material, but in this case, it was best to observe using the bright field, thanks to which was captured the most details of the layers for this type of the sample. As can be seen, when measured by an electron microscope at a given scale, degradation does not manifest itself to this extent. This can be considered an excellent result that has been reported after irradiation.

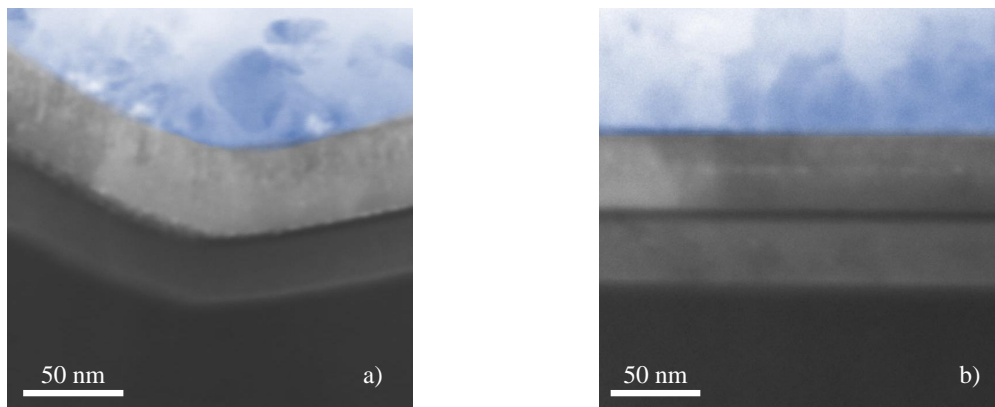


**Figure 2:** Cross-section visualised by STEM using bright field mode on thin lamella. The top metal layers of the sample are visible a) before and b) after irradiation. The bottom darkest layer is GaAs. The colored top layer serves as a protective carbon layer.

Figure 3 and 4 shows that a considerable amount of aluminium and titanium was found on the very surface. Thanks to this layer, the cell also maintains its stability and its degradation is slowed down.

In most cases did not undergo significant changes for gallium and arsenide after irradiation, and the solar cell thus retained its elemental composition for the most part. A slight difference can be seen in the loss of Ga and As in the top layer in Figure 3c and 4c before and after the irradiation. This can be confirmed by different distribution of thin layer of Al (Figure 4a) and especially Ti (Figure 4b) layer, where the difference is most noticeable and where after irradiation is a significant diffusion of the titanium layer into the material.

In roughness analysis, it was mentioned that when changing the surface parameter differences in Table 1, some optical properties may change. One of the essential properties of a solar cell is its

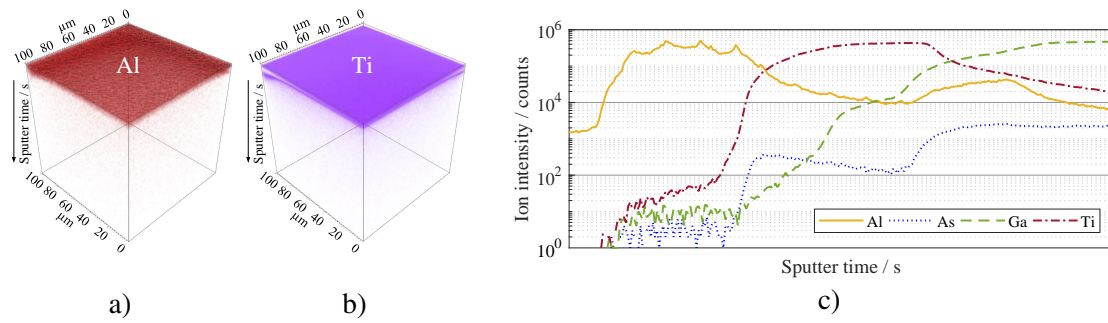


**Figure 3:** Three-dimensional view of protection layers of a) aluminum and b) titanium; and c) distribution of the most important elements during sputtering with use of SIMS before irradiation.

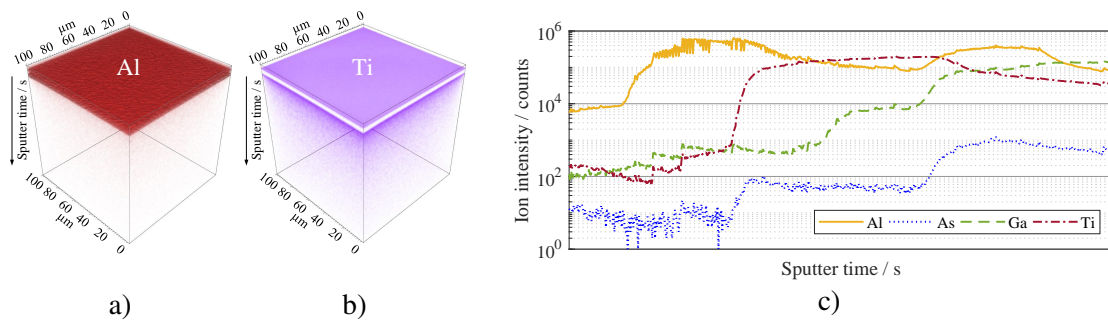


**Figure 4:** Visualisation of two protective layers of a) aluminum and b) titanium; and its c) distribution after irradiation.

reflectance. This reflectance is described by the light spectrum in Figure 5, which is composed of three parts. As can be seen, the two curves of the sample almost overlap both before and after irradiation. Thus, it can be stated that gamma radiation minimally affects the performance of the cell in terms of reflectance. The detected interference in the NIR region indicates the occurrence of the existing thin layers described in Figure 3a, b and 4a, b. Intensity change and curve shift occurs due to different thicknesses of the coating layers before and after irradiation. In the UVA light region is a visible shift. The difference is apparent within 5 nm to 10 nm. Shift of the curve results in a change in refractive index.

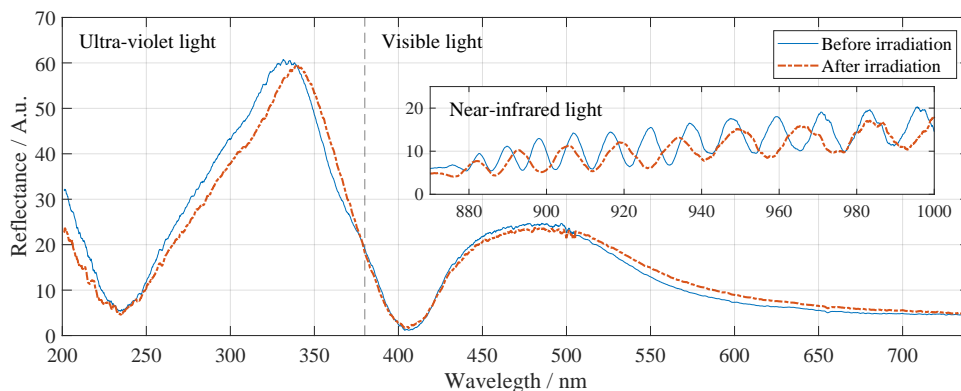


**Figure 5:** Electromagnetic spectrum divided into three areas of light – ultraviolet, visible and near-infrared. The reflectance of the solar cell before and after irradiation is shown in the spectrum.

Several significant differences were observed in Figure 6 after irradiation of the sample in Raman spectroscopy. For greater clarity, the spectra overlap to correctly compare differences between samples. The amount of material and atomic displacement from normal lattice positions are characterized by a characteristic peak at  $294\text{ cm}^{-1}$  of the GaAs longitudinal-optical mode, which rapidly lost its intensity after irradiation of the sample. The purity of the material may also indicate the different proportions and shape of the GaAs TO and AlAs LO modes, where less variation can be observed. However, the sharpness of the peak remains relatively unchanged. An important role is played by the ratio between GaAs TO and AlAs LO, which increased from 1:0.89 to 1:0.55 after irradiation. This ratio indicates a difference in the aluminum, which was also observed in previous measurements [7].

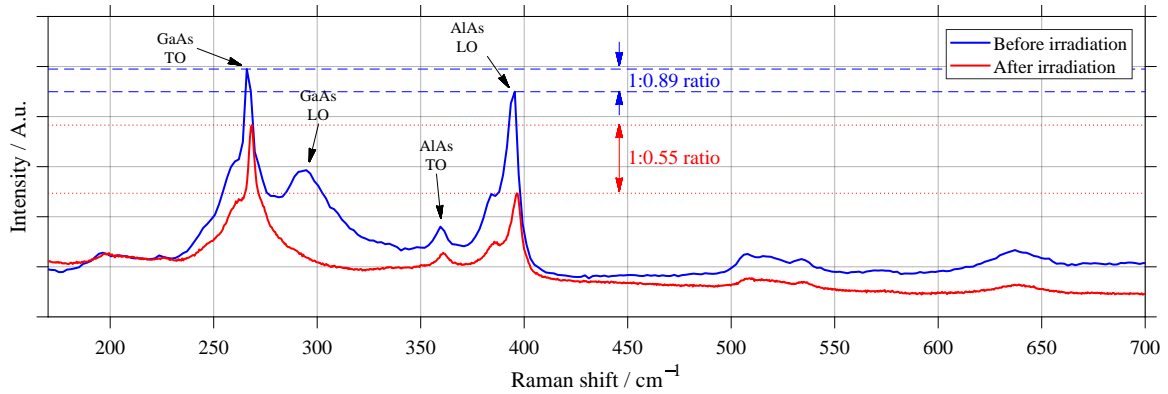


**Figure 6:** Two overlapping Raman spectra of the measured sample GaAs describing changes before and after irradiation of  $^{60}\text{Co}$ . Difference between GaAs transverse-optical (TO) and AlAs longitudinal-optical (LO) modes are marked by lines which indicates and measures their ratio.

#### 4 CONCLUSION

Using extensive analytical analysis, several changes were observed on samples exposed to irradiation with the radioactive isotope  $^{60}\text{Co}$  at a dose of 500 kGy. Such a high dose already reliably affects the operation of some electrical devices, and it was, therefore, advisable to ascertain the impact it would have on GaAs-based solar cells that are specifically designed for these purposes [8]. From the above measurements, it was proved after irradiation, especially the diffusion of Ti and Al protective metals deeper into the GaAs material. This phenomenon has been proven from SIMS measurements (Figure 3 and 4) and spectrophotometry (Figure 5) in the NIR region on the difference of shifted interferences. The changed refractive index mainly in the UVA region may then be affected by the difference in PV cell morphology, which was in the range of several nanometer units (Figure 1c and Table 1). Measured methods thus correlate with each other and confirm the results. It can be concluded from the above measurements that after irradiation with gamma rays, many complex processes take place which disrupts the atomic composition (Figure 6) and generally affects the entire structure of the solar cell. This measured knowledge may serve as a base of great importance for the future development of solar cells and their resistance to using in space conditions.

#### ACKNOWLEDGEMENT

Research described in the paper was financially supported by the Ministry of Education, Youth and Sports of the Czech Republic under the project CEITEC 2020 (LQ1601), by the Internal Grant Agency of Brno University of Technology, grant No. FEKT-S-20-6352. Part of the work was carried out with the support of CEITEC Nano Research Infrastructure supported by MEYS CR (LM2018110).

## REFERENCES

- [1] FETEHA, M. Gamma radiation effect on the GaAs solar cell performance. *Proceedings of the IEEE Twenty-Seventh International Symposium on Compound Semiconductors*, 2000, p. 91–96.
- [2] PAPEŽ, N.; GAJDOŠ, A.; DALLAEV, R.; SOBOLA, D.; SEDLÁK, P.; MOTÚZ, R.; NEBOJSA, A.; GRMELA, L. Performance analysis of GaAs based solar cells under gamma irradiation. *Applied Surface Science*, 2020, 510, issue 145329, p. 513–517. ISSN 0169-4332.
- [3] PAPEŽ, N.; DALLAEV, R.; SOBOLA, D.; MACKŮ, R.; ŠKARVADA, P. Microstructural investigation of defects in photovoltaic cells by the electron beam-induced current method. *Procedia Structural Integrity*, 2020, s. 595–600. ISSN: 2452-3216.
- [4] PAPEŽ, N.; SOBOLA, D.; ŠKVARENINA, L.; ŠKARVADA, P.; HEMZAL, D.; TOFEL, P.; GRMELA, L. Degradation analysis of GaAs solar cells at thermal stress. *Applied Surface Science*, 2018, issue 461, p. 212–220. ISSN: 0169-4332.
- [5] GAJDOŠ, A.; ŠKARVADA, P.; MACKŮ, R.; PAPEŽ, N.; ŠKVARENINA, L.; SOBOLA, D. Isolation and optoelectronic characterization of Si solar cells microstructure defects. *Journal of Physics: Conference Series*, 2018, 1124, issue 4, p. 1–6. ISSN: 1742-6596.
- [6] TĚLU, Š.; PAPEŽ, N.; SOBOLA, D.; ACHOUR, A.; SOLAYMANI, S. Micromorphology investigation of GaAs solar cells: case study on statistical surface roughness parameters. *JOURNAL OF MATERIALS SCIENCE MATERIALS IN ELECTRONICS*, 2017, 28, issue 15, p. 1–12. ISSN: 0957-4522.
- [7] NAYAK, J.; SAHU, S. N.; NOZAKI, S. GaAs nanocrystals: Structure and vibrational properties. *Applied Surface Science*, 2006, 252, issue 8, p. 2867–2874. ISSN: 0169-4332.
- [8] SAHIN, R.; KABACELIK, I. Effects of ionizing radiation on the properties of mono-crystalline Si solar cells. *Radiation Physics and Chemistry*, 2018, 150, p. 90–94. ISSN: 0969-806X.

# EFFECT OF ORGANIC ADDITIVES ON ELECTROCHEMICAL PROCESSES INFLUENCING ZINC-AIR BATTERY PARAMETERS

**Jan Smejkal**

Doctoral Degree Programme(1), FEEC BUT

E-mail: xsmej18@stud.feec.vutbr.cz

Supervised by: Ladislav Chladil

E-mail: chladil@feec.vutbr.cz

**Abstract:** This work is focused on the study of influence of selected organic additives on the properties and morphology of zinc deposit on the negative electrode when used in zinc-air accumulators. The deposition was made on the tin plate electrodes in a solutions of 6 mol/l KOH saturated with ZnO with added additives (Abeson Na 50, Flavol KDA, Span 85, Lugalvan G35 and Triton X-100). All chosen additives were studied with a focus on the morphology of zinc deposit, with regard to their ability to suppress dendritic growth and with focus on zinc corrosion. Changes in zinc morphology were studied by using a Tescan Vega 3 electron microscope and a Rigaku MiniFlex HR 600 X-ray diffractometer.

**Keywords:** Zinc-air, battery, morphology, dendritic growth, additives

## 1 INTRODUCTION

Energy storage with secondary cells can be used wherever there is no direct between electricity production and consumption. Long-term energy storage is a very important topic in the field of electrical equipment development. This is due to the need for long-term storage of excess electricity, to the increasing representation of alternative sources in electricity generation, and also to the increasing number of portable applications.

Zinc-air cells are promising in the future due to their low cost, low ecological footprint, and their other positive properties. Another advantage of these batteries is the high accumulated energy of up 1,65 V and the high density of accumulated energy [1]. However, Zn-air batteries are not as widely used as other types of batteries. This is due to the bigger amount of adverse effects occurring with these batteries. Dendritic growth is very undesirable. Dendritic growth is the growth of crystals in irregular shapes on the surface of the zinc electrode. Dendrites grow from negative to positive electrode. If dendritic growth is not suppressed, there may be a short circuit between the electrodes [2]. Another problem is the corrosion of zinc, which occurs in accumulator in the current state. Zinc corrosion is closely related to the evolution of hydrogen in the accumulator and causes partial consumption of the active mass or self-discharge [3].

In the cathodic polarization of the negative electrode (when charging zinc-air battery) the active mass (in the discharged state formed by ZnO crystals) begins to change to metallic zinc. In this process, zincates dissolved in the electrolyte are deposited in the current collector of the negative electrode. The reactants are contained both in solution as  $Zn(OH)_4^{2-}$  and as on the electrode such as zinc oxide. The structure of the deposit and the formation of dendritic growth is strongly dependent on the current density. At current densities lower than 15 mA/cm<sup>2</sup>, a deposit with moss structure is formed [4, 5]. The moss structure consists of tiny particles in cylindrical shapes [6]. At current densities between 15-30 mA/cm<sup>2</sup> a layered deposit structure is formed. The increase in this structure is controlled by both diffusion and the activation process. At current densities exceeding 30 mA/cm<sup>2</sup> dendrites increase in the direction perpendicular to the electrode. At the top of the dendrites, a

spherical diffusion layer is formed. When this layer is formed, ZnO moves to the top of the dendrites.

Adding additives can slow down or stop the formation of dendrites in the battery. The additives affect the displacement of zinc ions in the electrolyte. As the electron transfer rate changes, zinc deposition slows and active sites are blocked by surfactant particles. The hydrophobic part of the surfactants is pivoted towards the surface, thereby creating a barrier to the ion access to the electrode surface [7].

## 2 MEASUREMENT

The electrodes were made of rolled tin plate. The tin electrode was square with a side length of 1,5 cm (the active electrode area was 2,25 cm<sup>2</sup>) and thickness of 0,5 mm. To the working part of the electrode, a brass wire was soldered by means of which electrical quantities were brought. Before measurement, the electrode had to be cleaned in a 10% sulfuric acid solution.

The next step was to mix the 500 ml solution to which the organic additives were added. The basic solution contained 6 mol/l KOH solution, 37,35 g/l ZnO and was prepared at an elevated temperature of 200°C. To this solution the organic additives listed in Tab. 1 at a concentration of 1000 ppm were added.

Business name	Chemical description	Detailed information
<b>Abeson Na 50</b>	Sodium Dodecylbenzene-sulfonate	Anionic surfactant with good foaming and wetting properties. Used as a universal surfactant.
<b>Flavol KDA</b>	Coconutamidopropyl betaine based on coconut oil	A fine amorphous surfactant used as a wetting agent and foaming booster in industry.
<b>Span 85</b>	Nonionic oleic acid surfactant	Biodegradable nonionic surfactant used in the cosmetics industry.
<b>Lugalvan G35</b>	Aqueous polyethyleneimine solution	Used as polish in the galvanic industry.
<b>Triton X-100</b>	Polyethylen glycol-phenyl ether	Nonionic surfactant used in metal plating industry.

**Table 1:** Chemical composition and use of selected additives.

Zinc deposition was performed using potentiostatic deposition (at constant overvoltage). At potentiostatic deposition the constant overvoltage was set to 150 mV compared to the electrode equilibrium potential, i.e. transition Zn/ZnOH<sub>4</sub><sup>2-</sup>. At the overvoltage of 150 mV, we were in the range of high current densities exceeding 30 mA/cm<sup>2</sup>. At such high overvoltage, the influence of additives on the formation and growth of dendrites was very well observed. The measurement was carried out for 60 minutes due to the need to exceed the initiation time for the formation of dendrites. The reference electrode was zinc wire and the counter electrode was a nickel mesh.

The deposited structures were examined using a Tescan Vega 3 electron microscope (detailed photo of the surface of deposited structures) and a Rigaku MiniFlex 600 HR X-ray diffractometer (measured and evaluated diffractograms for individual samples). Diffractograms were measured over a range of 20-120° at step 0,02°, divergence slit of 0,01 and kβ filter of 0,03. The values from the diffractometer were related to the greatest zinc peak for a clearer evaluation.

## 3 RESULTS AND DISCUSSION

In Figure 1, the current response of the negative electrode at a periodic surge of 150 mV relative to the zinc electrode equilibrium potential can be seen to simulate a high current density mode.

The Flavol KDA additive stabilized after 15 minutes. Towards the end of the deposition, a sharp increase in current density was observed, which was caused by the sudden formation of hydrogen. The Span 85 additive had a very similar course to the KOH solution in the first half of the measurement. In the second half there was a greater increase in current density than in KOH, suggesting that larger dendrites were grown than in KOH. With the Triton X-100 additive, a constant increase in current density has been observed since the beginning of the deposition. The increase can again be associated with an increase in dendrites. Abeson Na 50 showed a significant increase in current density after 15 minutes of deposition. This increase in current density indicates the growth of large and sharp dendrites. As can be seen, the Lugalvan G35 additive had a steady state current after 5 minutes. This suggests that there was no increase in the active deposit area.

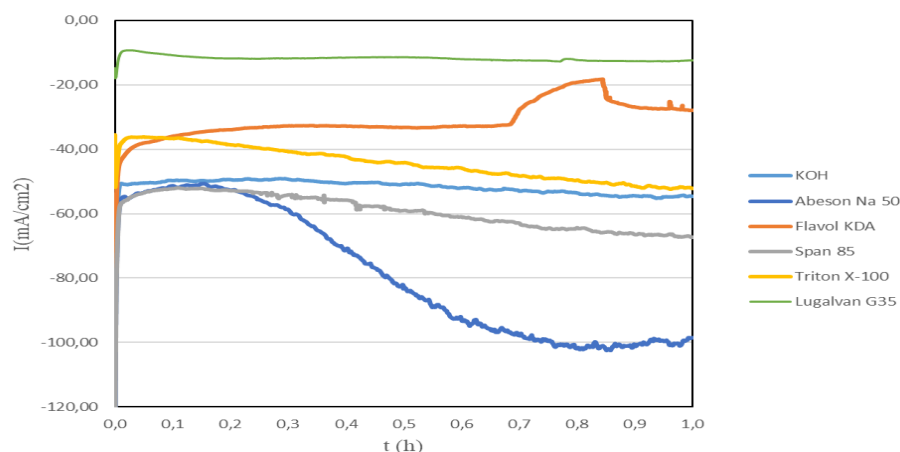


**Figure 1:** Current waveform for zinc deposition in a three-electrode circuit for solutions with added additives at a concentration of 1000 ppm and for a KOH solution without added additives at a constant overvoltage of 150 mV against the equilibrium potential of the zinc electrode.

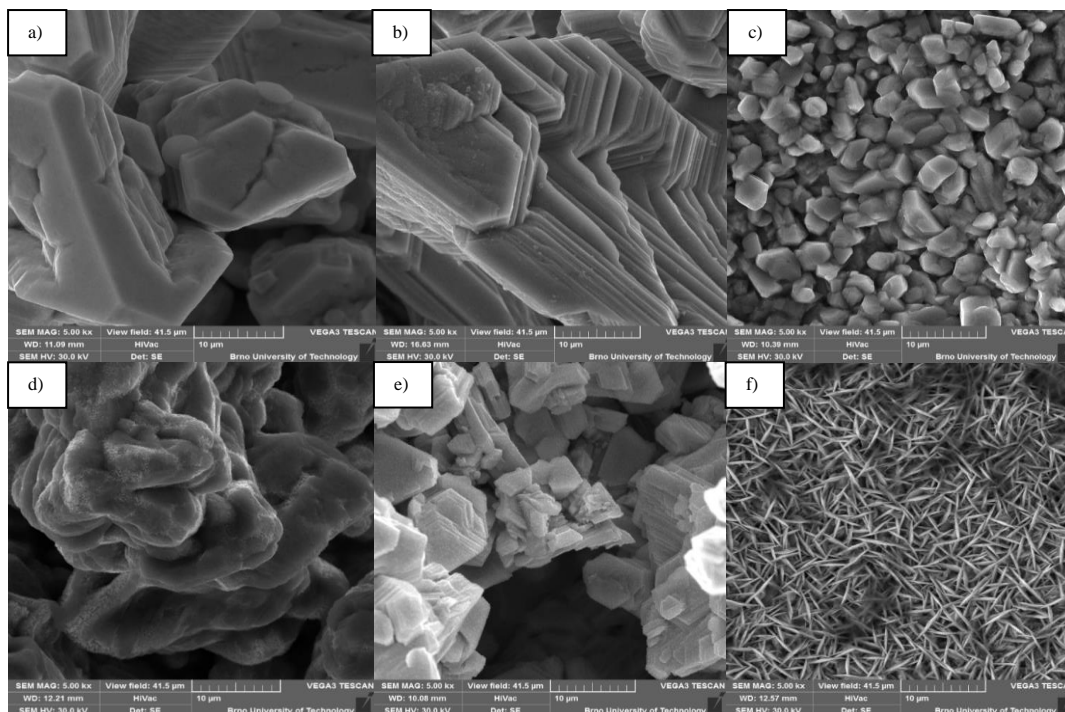


**Figure 2:** Detail of the structure of deposited particles at constant overvoltage. The additives were contained in a concentration of 1000 ppm in solution. Images at a magnification of 5000 $\times$ , field of view 41,5  $\mu\text{m}$  and accelerating voltage 30 kV. a) KOH, b) Abeson Na50, c) Flavol KDA, d) Span 85, e) Triton X-100 and f) Lugalvan G35.

In Figure 2, it can be observed that the additives used significantly influenced the shape, uniformity of growth and diffusion properties of the zinc deposit. The KOH solution showed uniform growth of the deposit across the electrode area. This deposit did not show good porous properties. Abeson Na 50 additive increased layered, non-porous deposit in the center of the electrode. Sharp long dendrites increased in the peripheral parts of the electrode. In the presence of the Flavol KDA additive, a porous structure formed by tiny crystals was formed. Dendrite growth occurred in the peripheral parts of the electrode, but the length of these dendrites was less than of the Abeson Na 50 additive. The additive Span 85 initiated the growth of a very pronounced deposited structure in the clusters. The clusters were not circular in shape but were grown perpendicular to the electrode surface. Very long crystals were grown at the electrode edges. The Lugalvan G35 additive has grown over the entire electrode area. The deposit consisted of thin long flakes that showed good porosity. Dendrite formation was completely suppressed at the electrode edges.

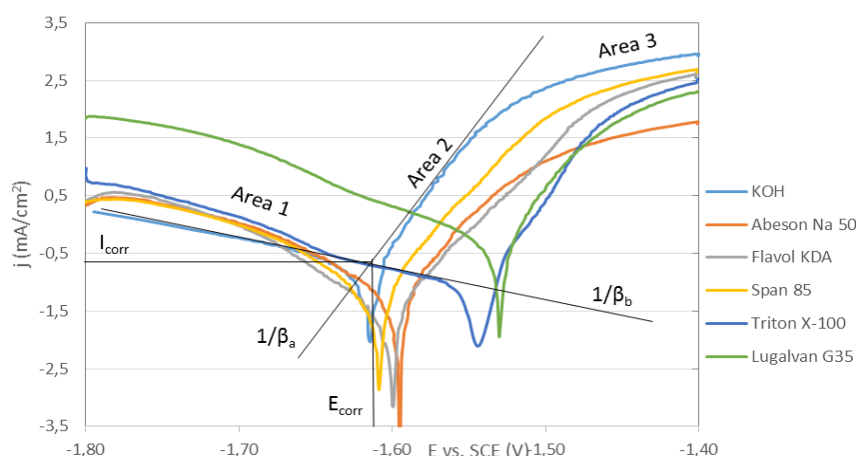


**Figure 3:** Potentiodynamic curves of zinc electrode in electrolyte 6 mol/l KOH and in electrolyte 6 mol/l KOH with added additives.

Figure 3 shows the individual potentiodynamic curves of the zinc electrode. In area 1, a current response occurs due to the formation of hydrogen on the Zn electrode. Dissolving of zinc starts with increasing potential (area 2). At the peak, at potential  $E_{corr}$ , the reaction rate formation of hydrogen and zinc dissolution is equal. In area 3, zinc dissolves.

Abeson Na 50, Span 85 and Flavol KDA additives have very similar course as solution of KOH. Lugalvan G35 and Triton X-100 additives accelerated hydrogen formation in area 1. These additives separated the hydrogen formation reaction from the equilibrium potential, the Triton X-100 additive by 60 mV and the Lugalvan G35 additive by 80 mV. These additives also significantly increased the corrosion potential to 6 mol/l KOH solution. This increase is negative for real use due to a drop in the Zn-air batteries equilibrium voltage.

In Figure 4, it is possible to observe the diffraction spectrum of the deposited structures in KOH without added additives and in KOH solutions with added additives.

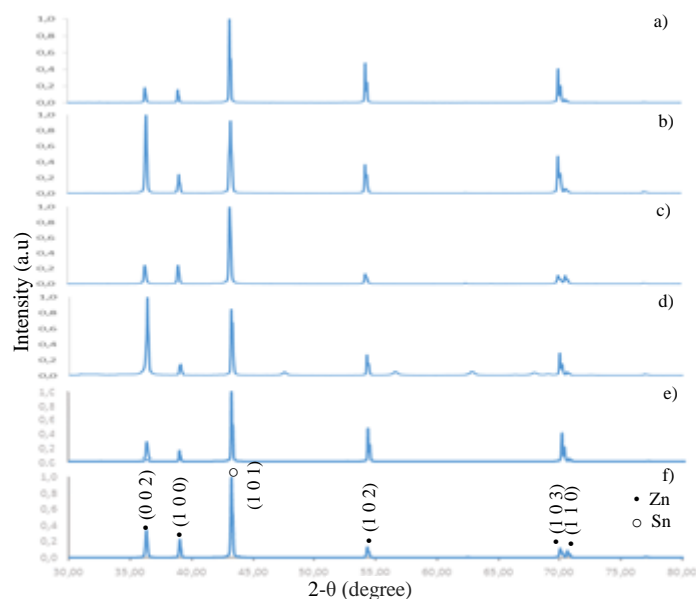


**Figure 4:** Diffraction spectrum of Zn deposits from a 6 mol/l KOH solution with added 1000 ppm additives at constant overvoltage. a) KOH, b) Abeson Na50, c) Flavol KDA, d) Span 85, e) Lugalvan G35 and f) Triton X-100.

#### 4 CONCLUSION

As can be seen from the measured results, the used additives influenced the deposit structure. The Abeson Na 50 additive showed the growth of long sharp dendrites primarily in the peripheral parts of the electrode. In the case of Flavol KDA, dendrite growth was partially suppressed. The dendrites were shorter than those of the Abeson Na 50 additive and were primarily grown in the peripheral parts of the electrode. Lugalvan G35 and Triton X-100 additives significantly suppressed dendritic growth over the entire electrode area, including the peripheral parts of the electrode. The additives also influenced the properties of the zinc deposit with respect to corrosion and hydrogen formation. Most of the selected additives had a positive effect on the amount of corrosion current, only the additive Lugalvan G35 showed a significantly higher corrosion current compared to an electrolyte of 6 mol/l KOH. From the above results it is evident that Triton X-100 and Lugalvan G35 appear to be the most suitable additives. Lugalvan G35 despite of its negative corrosion effect.

#### ACKNOWLEDGEMENT

This work was supported by the specific graduate research of the Brno University of Technology No. FEKT-S-20-6206.

#### REFERENCES

- [1] LI, Yanguang a Hongjie DAI. Recent advances in zinc–air batteries. *Chem. Soc. Rev* [online]. 2014, 12.1.2014, 43(15), 5257-5275. DOI: 10.1039/C4CS00015C. ISSN 0306-0012. Available from: <http://xlink.rsc.org/?DOI=C4CS00015C>.
- [2] CHANG, H. a C. LIM. Zinc deposition during charging nickel/zinc batteries. *Journal of Power Sources* [online]. 1997, 66(1-2), 115-119 [cit. 2020-03-07]. DOI: 10.1016/S0378-7753(96)02536-0. ISSN 03787753. Available from: <https://linkinghub.elsevier.com/retrieve/pii/S0378775396025360>
- [3] BEVERSKOG B., PUIGDOMENECH I. Revised pourbaix diagrams for zinc at 25– 300 °C. *Corrosion Science*, sv. 39, č. 1, s. 107-114, 1997.

- [4] CHLADIL, L., O. ČECH, J. SMEJKAL a P. VANÝSEK. Study of zinc deposited in the presence of organic additives for zinc-based secondary batteries. *Journal of Energy Storage* [online]. 2019, 21, 295-300. DOI: 10.1016/j.est.2018.12.001. ISSN 2352152X. Dostupné z: <https://linkinghub.elsevier.com/retrieve/pii/S2352152X18304481>.
- [5] CHLADIL, L., O. CECH a P. VANYSEK. Pulse Deposition of Zinc in Electrolytes with Reduced Zinc Oxide Solubility. *ECS Transactions* [online]. 2016, 74(1), 137-146. DOI: 10.1149/07401.0137ecst. ISSN 1938-6737. Dostupné z: <https://iopscience.iop.org/article/10.1149/07401.0137ecst>.
- [6] WANG R. Y., KIRK D. W., ZHANG X. G. Characterization and Growth Mechanism of Filamentous Zinc Electrodeposits. *ECS Transactions*. 2007, 2007:16, 19-27.
- [7] MANSFELD F., GILMAN S. The Effect of Lead Ions on the Dissolution and Deposition Characteristics of a Zinc Single Crystal in 6N KOH. *Journal of The Electrochemical Society*. 1970, 117:5, 588.

# VIBRATION AND IMPACT MEASUREMENT FOR COLLISION ANALYSIS

Tomáš Musil <sup>a</sup>, Martin Andruška <sup>b</sup>

<sup>a</sup> Doctoral Degree Programme (3), FEEC BUT

<sup>b</sup> Master Degree Programme (1), FEEC BUT

E-mail: xmusil54@vutbr.cz, xandru00@stud.feec.vutbr.cz

Supervised by: Jiří Háze

E-mail: haze@feec.vutbr.cz

**Abstract:** The aim of this work is to analyze a suitable method of High-Velocity Impact detection with space debris for CubeSats. In order to detect and analyze collisions of space debris with nanosatellites, it was necessary to run a series of experimental measurements to verify what types of sensors would be suitable for HVI collisions detection. This article presents some of the sensors examined by experimental testing, its properties, suitability. The article also shows how the testing was performed.

**Keywords:** CubeSat, collision, space debris, vibrations, piezoelectric actuator

## 1 INTRODUCTION

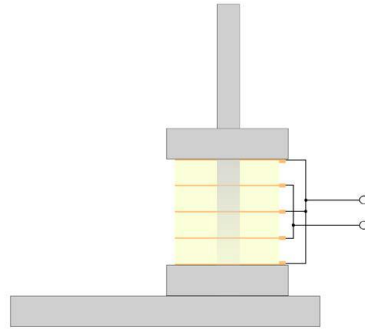
With increasing popularity and slightly lower costs of launching satellites into orbit, a CubeSat has become an interesting and relatively available option of exploring from space orbit even for smaller projects. But along with that, the space debris is becoming a frequently discussed topic and rising threat to every space object flying in orbit [1], [2]. This article deals with the design of a suitable detection method of high-velocity impacts (HVI) with space debris for nanosatellites [3]. A major problem with CubeSats is the available space, maximum weight and power consumption available for measuring apparatus, so it is sometimes useful to consider already integrated satellite sensors for HVI detection. An accelerometer is a typical example of standard nanosatellite sensor equipment. A low power consumption of the detection system is achieved by its inactivity, unless a situation requiring analysis occurred. When an adjustable input signal threshold is exceeded, the low-delay circuits are triggered to capture the event and analyze those data such as amplitude, spectral components, event time and potential criticality. In case of hardware damage, the values of known parameters such as a power consumption or temperature might suddenly or gradually change, also communication intermission of any system or complete loss of a communication may occur. Therefore, satellites are often equipped with diagnostic circuits that are capable of system diagnostic even while operating which might be helpful in case of the HVI detection.

## 2 TESTING APPARATUS

First, a vibration table was examined for the purpose of testing harmonic and long-term vibration exposure to the components. This method showed that the table with its high inertia and mass which also means only low frequency spectrum is not suitable for the purpose of the HVI detection. Therefore, a high frequency speaker was examined for this purpose, but when the tweeter was powered by pulse signal it exhibited an insufficient mechanical response to the signal due to its low membrane mass.

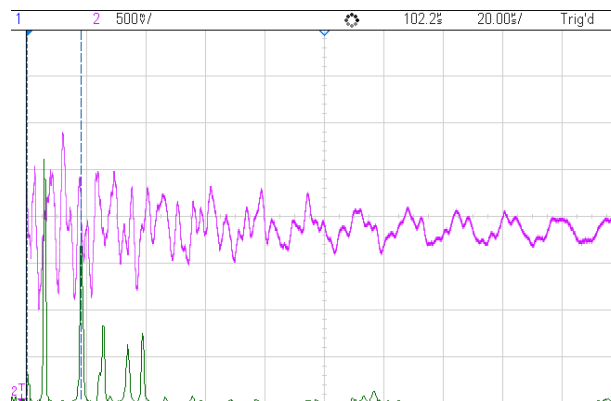
## 2.1 PIEZOELECTRIC ACTUATOR

Therefore, searching for a suitable vibration source led to usage of piezoelectric actuators which can generate high frequency vibrations and pulses. For this purpose, a 4-layer piezoelectric actuator with silver electrodes was used. Each of the 4 piezoelectric rings has a Cu-foil inserted in-between to connect power supply and as a whole it was pressed together with threaded rod (figure 1). The actuator was powered by a signal generator with maximum output voltage 20 V<sub>PP</sub>.



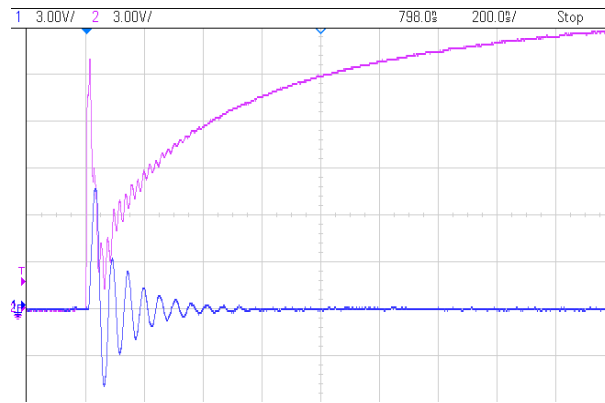
**Figure 1:** A 4-layer piezoelectric actuator

Figure 2 shows a detailed waveform of the 4-layer piezoelectric actuator with no pressure applied. Main frequency domain components correspond to commonly known frequencies of piezo-ceramic materials with maximal values of 60 kHz and 180 kHz [4]. This wave is also excited inside of a metal beam that is in mechanical contact with the actuator which together makes a source platform for measurement of various types of sensors.



**Figure 2:** Mechanical response of 4-layer piezoelectric actuator

It was found that the actuator's response can be measured in case when the piezo-ceramic material is free-mounted. Because the 4-layer piezo actuator has relatively high capacitance and unfavorable mechanical properties (weight, mounting method), it was no longer used. Instead of this a simple disc piezo actuator was used as the main mechanical generator. Before an experimental measurement of various sensors could be performed, it was necessary to explore properties of the disc piezo actuator in terms of vibration amplitudes and frequency bandwidth. It is common to use the Dirac-impulse waveform to determine the system response. When feeding the piezo actuator with very short nanosecond pulses a problem occurred because the piezo material reacts to the both rising and falling edges. The actuator also influences the feeding signal by its own capacitance which results in chaotic waveform. This leads to another mechanical deformation of the piezo material. The resulting behavior can be seen in figure 3. Waveform on channel 1 (blue) shows the piezo-element response and channel 2 (purple) represents the feeding signal. The piezo element reacts almost immediately with logarithmic attenuation as expected, oscillations have frequency at about 18 MHz.



**Figure 3:** Piezo element oscillations when rising edge signal applied

Based on the measurements, following waveform was set for further sensor measurements. The pulse width was determined to 35 ms with falling time 30 ms, rising time 120 ns with amplitude of 20 V. The figure 4 shows the final waveform that was used to drive the piezo actuator. The most significant advantage of this solution is the repeatability of the measurement.

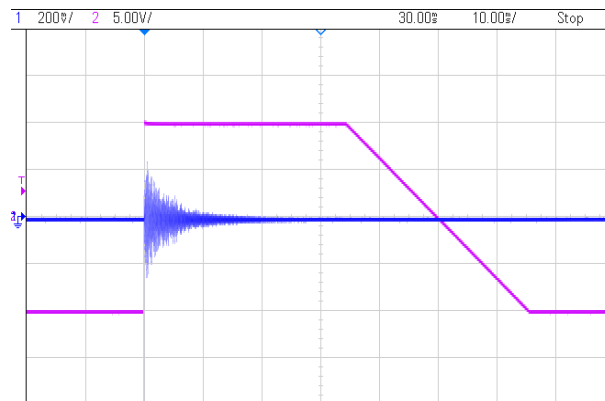


**Figure 4:** Final feeding waveform for piezo actuator

### 3 VIBRATION SENSORS

Accelerometers were excluded from the experiments after several measurements and considerations because they are designed to measure vibrations and oscillations with high amplitudes and they are not able to detect weak high-frequency surface waves caused by small dust particles. Because of very low-level output signal coming from sensors the signal had to be amplified. The amplifier consists of low-noise opamp OPA2134PA [5] used as a simple inverting amplifier with gain -10.

#### 3.1 PIEZO SENSING FILM PVDF

In this experiment, piezo sensing foils Parallax Vibra Tab and Pro-Wave Electronics FS-2513P were used. The piezoelectric material was applied to a substrate of excessively rigid material during manufacture process. The sensing foil when measuring surface vibrations generated a significantly weak signal compared to the other sensors and also insufficient frequency range, i.e. the sensor filtered higher frequency components probably by attenuating properties of the substrate.

#### 3.2 MEMS MICROPHONES

For the purpose of this measurement strictly analog condenser types of microphones were used, i.e. TDK InvenSense ICS-40730, TDK ICS-40212, Knowles SPH-0611LR5H-1, Vesper Technologies

VM1000R and their new model VM1010 [6]. This type of microphones was able to capture the frequency spectrum generated by mechanical pulses that was in area of ultrasound.

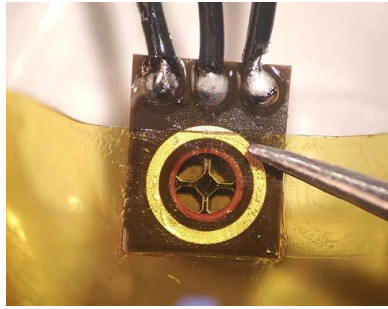


**Figure 5:** MEMS microphone TDK ICS-40730

The apparent success was rebutted by changing the pressure of the sensor attached to the beam. Increased contact resulted in closing the access to the MEMS hole for sound waves and so the mechanically transmitted vibrations did not produce a sufficient sensor response. Thus, the sensor output signal is significantly low and its level is around a noise level.

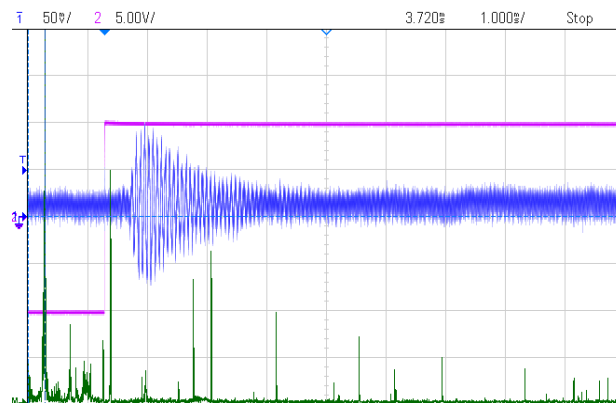


**Figure 6:** Waveform measurement of Vesper VM1010 along with spectral noise component

### 3.3 PIEZOELECTRIC DISCS

Piezoelectric disc shown in figure 7 has become the main reference sensor for any further experiments because of its high sensitivity and especially wide frequency range in comparison to the other samples. In figure 8 can be seen the piezoelectric disc response to the vibrations generated by the piezo actuator. The measured waveforms were slightly changing during the experiment due to changing the individual sensor and attaching them to the metal beam.

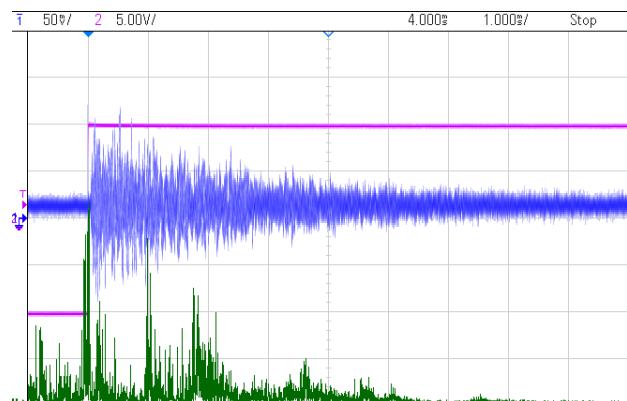
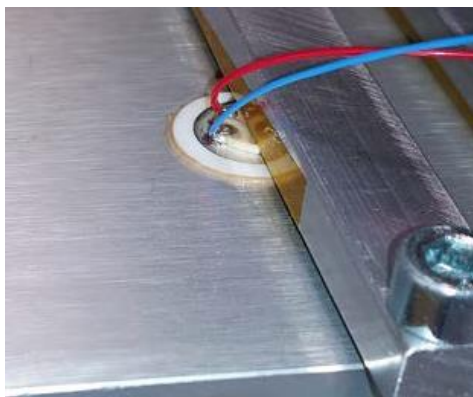


**Figure 7:** Piezoelectric disc and its response using piezo actuator as vibration source

## 4 CONCLUSION

This work is focused on exploring the possibilities of mechanical vibrations detection caused by HVI collisions with space debris. First, it was necessary to develop a suitable source of vibrations that might imitate real collisions. For this purpose, the vibrations table, high frequency speakers or any other electro-mechanic generator proved to be unusable. Further testing showed that the piezoelectric actuator meets the requirements, specifically the piezoelectric disc attached to metal beam proved to be an excellent option for upcoming experiments. The only drawback of this solution occurred when swapping between other types of sensors, therefore, changes in the attachment position and gripping force which significantly influenced amplitude and frequency spectrum of outgoing signal. The potentially new approach could be a usage of Vesper Technologies' s new piezoelectric MEMS microphones which were tested as well. Unfortunately, after series of experiments these failed to prove their usefulness for sensing vibrations or acoustic emissions in their original housing. In theory, piezoelectric microphone plates could achieve an enough sensibility if placed directly on a substrate. Piezoelectric films proved to be a potentially usable as a surface wave sensor if a suitable type is chosen. The main disadvantage is the low temperature resistance, the piezoelectric properties of PVDF sensors drop significantly at 70 °C or higher. As the best choice proved to be the piezoelectric disk. Appropriate combination of dimensions, substrate materials and other aspects of piezo element manufacturing can provide reliable HVI detection. After examining the appropriate piezo element mounting solutions on the CubeSat structure, deploying one or more sensors to a given configuration and after the final calibration, the amplitude of each satellite impact can be measured by reference. However, this approach requires calibration of the sensing apparatus of each CubeSat separately, as it was found that the measured values were significantly influenced by changes in the pressure and contact area of the sensor with the beam.

## ACKNOWLEDGEMENT

The article was supported by project no. FEKT-S-20-6215 – A novel approaches of modern micro- and nanoelectronics' utilization.

## REFERENCES

- [1] About space debris [online]. Available from: [https://www.esa.int/Safety\\_Security/Space\\_Debris/About\\_space\\_debris](https://www.esa.int/Safety_Security/Space_Debris/About_space_debris)
- [2] L.E., Iliescu & Lakis, A. & Oulmane. (2016). HYPERVELOCITY IMPACT (HVI) SIGNAL ANALYSIS. European Journal of Engineering and Technology.
- [3] ANDRUŠKA, Martin. VIBRATION AND IMPACT MEASUREMENT FOR COLLISION ANALYSIS [online]. 2019. Available from: <https://www.vutbr.cz/studenti/zav-prace/detail/119430>. Bachelor's Thesis. Brno University of Technology.
- [4] SERRIDGE, Mark a Torben R. LICHT. BRÜEL & KJÆR. Piezoelectric accelerometers and vibration preamplifiers: Theory and application handbook [online]. Nærum, Danish, 1987. Available from: <http://www.bksv.com/doc/bb0694.pdf>
- [5] OPAx134 SoundPlus™: High Performance Audio Operational Amplifiers [online]. 1997. Available from: <http://www.ti.com/lit/ds/symlink/opa2134.pdf>
- [6] VM1010: Wake-on-Sound Piezoelectric MEMS Microphone [online]. Available from: <https://vespermems.com/products/vm1010/>

# NUMERICAL MODELLING OF LI-S CHEMISTRY

**Martin Mačák**

Doctoral Degree Programme (2), FEEC BUT

E-mail: xmacak00@stud.feec.vutbr.cz

Supervised by: Petr Vyroubal

E-mail: vyroubal@feec.vutbr.cz

**Abstract:** This work presents a custom electrochemical model of a lithium-sulfur cell implemented into Ansys Fluent software. The model was used to analyse cyclic voltammetry at differently sized particles, which represented porous cathodes. The results indicate that the cyclic voltammetry response of the whole porous sulfur cathode could be solved as a response of a single particle, which might lead to a simplification of numerical simulations and in result, to accelerating their optimizing process.

**Keywords:** Li-S battery, electrochemistry, numerical modelling, Ansys Fluent, cyclic voltammetry

## 1 INTRODUCTION

Lithium-Sulfur batteries are seen as a candidate for the new generation of batteries because of their low cost, high theoretical capacity of  $1672 \text{ mAh} \cdot \text{g}^{-1}$  and associated energy density of  $2600 \text{ Wh} \cdot \text{kg}^{-1}$ . This means that practical Li-S battery system should allow for approximately twice the gravimetric energy density of conventional Li-ion batteries [1].

However, the practical application of Li-S batteries is inhibited by complex redox reactions of sulfur, which results in a large number of soluble intermediates with different properties. Furthermore, the poor electronic conductivity of both elemental sulfur  $\text{S}_8$  and  $\text{Li}_2\text{S}$ , as well as continuous dissolution and precipitation of solid species coupled with polysulfide shuttle leads to major challenges to the advancement of Li-S cells [2]. While there is an extensive focus on experimental research [3] on the general properties, the discharge/charge behaviour and microstructure of Li-S cells, the research on numerical models is quite limited [1,4].

This paper focuses on the numerical investigation of sulfur reactions by cyclic voltammetry as its results bring better information about the behaviour of electrochemical reactions and their properties. A custom electrochemical model based on the work of Kumaresan *et al.* [4] was implemented into commercially available software Ansys Fluent. The CV responses a porous electrode was investigated. The influence of the size of porous particles was studied more closely.

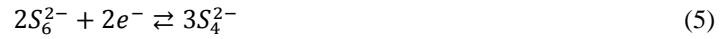
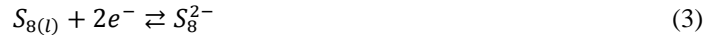
## 2 LI-S BATTERY

The usual Li-S cell is made of composite sulfur cathode based on solid elemental sulfur, conductive carbon and a binder, metallic lithium foil anode and an aprotic electrolyte such as 1,2-dimethoxyethane (DME):1,3-dioxolane (DOL) [4] with lithium salts usually consisting of  $\text{LiNO}_3$  or lithium bis-trifluoromethylsulfonfyl imide (LiTFSI) or their mixture. These salts decrease diffusion and migration of polysulfides into the electrolyte. Interestingly, it was found that lithium salts have no significant effect on the electrochemical performance of Li-S batteries as the behaviour strongly depends on the used solvent [5]. The course of electrochemical reactions is dependent the applied solvent and chemical properties of cathode. As stated in [6], the selection of the solvent strongly influences the stability of polysulfides, which consequently affect the chemical equilibrium between various polysulfides, which makes numerical simulations even more complicated [6]. The overall electrochemical reaction occurring in the Li-S cell can be described as [7]:



However, this reaction does not describe the complete mechanism of the creation of polysulfides during reduction and oxidation. These reactions are responsible for the characteristic two plateau discharge/charge curves. The high plateau is usually situated at 2.3 V – 2.4 V and is controlled by the reduction of longer chain polysulfides. The second plateau is situated at 2 V – 2.1 V and is controlled by the creation of  $Li_2S_2$  and  $Li_2S$  [8].

The model used in this work is based on the reaction mechanism presented by Kumaresan *et al.* [4] The cell at its initial state is fully charged and so the cathode consists of solid sulfur  $S_{8(s)}$ , which is being dissolved into liquid sulfur  $S_{8(l)}$ . During the discharge, the  $S_{8(l)}$  is gradually reduced into shorter chain polysulfides. The reverse process occurs during charging which results in longer chain polysulfides. These electrochemical reactions can be described as:



Depending on the concentration of  $Li^+$  ions and polysulfide chains several dissolution/precipitation reactions can be considered. These reactions are described in [4]. However, experimental studies have shown that all lithium sulfides except  $Li_2S_2$  and  $Li_2S$  are substantially soluble in the electrolyte, so they were not considered in this work, as they would not influence the results significantly [9].

## 2.1 CYCLIC VOLTAMMETRY

Cyclic voltammetry (CV) provides valuable information for initial electrochemical research on new systems. Fundamental studies on the electrochemical redox reactions of elemental sulfur on flat electrodes (e.g. glassy carbon, gold, platinum) in nonaqueous media have been extensively investigated. However, these studies do not capture the reaction behaviour in the batteries, as they differ in used electrodes and electrolytes. Additionally, studies of the fundamental mechanism rarely consider effects of the cathode, anode and structure, which greatly affect the redox process and battery performance. In such cases, the translation of the information between fundamental and application studies is difficult. Li-S batteries performance can be significantly influenced by electrode parameters such as sulfur loading and content, material of the current collector and the binder, battery parameter such as the electrolyte and its amount, separator and the amount of lithium, the assembling process and ultimately testing conditions [7, 10].

## 3 NUMERICAL MODEL

The numerical model used in this work is based on Nernst-Planck equations, which describe the flux of all ionic species and the Laplace equation describing the potential in the electrode as the potential in the electrolyte was considered to be 0 V. The reaction kinetics are defined by the concentration-

dependent Butler-Volmer equation. The numerical model is closely described in [9]. The final equations used are:

$$\frac{\partial c_i}{\partial t} - \nabla \cdot (D_i \nabla c_i) = 0 \quad (8)$$

$$\nabla \cdot (-\sigma_s \nabla \varphi_s) = 0 \quad (9)$$

$$\mathbf{j}_{far} = j_0 \left[ \left( \frac{c_A}{c_{ref}} \right)^\gamma e^{\left( \frac{\alpha_a F \eta}{RT} \right)} - \left( \frac{c_B}{c_{ref}} \right)^\gamma e^{\left( \frac{\alpha_c F \eta}{RT} \right)} \right] \quad (10)$$

$$\eta = \varphi_s - E_{eq} \quad (11)$$

Where  $c_i$  is the molar concentration [ $\text{mol} \cdot \text{m}^{-3}$ ],  $t$  is time [s],  $D_i$  is the diffusion coefficient [ $\text{m}^2 \cdot \text{s}^{-1}$ ],  $\varphi_s$  is the electrode potential [V],  $\sigma_s$  [ $\text{S} \cdot \text{m}^{-1}$ ] is the electrical conductivity,  $j_0$  is the exchange current density,  $c_A, c_b$  is the molar concentration of reduced and oxidized species [ $\text{mol} \cdot \text{m}^{-3}$ ],  $\alpha_a, \alpha_c$  is the anodic and the cathodic transfer parameter [-],  $\gamma$  is the dimensionless power of species [-],  $\eta$  is the overpotential, which is defined as a potential difference across electrode-electrolyte interface [V] and  $E_{eq}$  is the reduction potential [V].

Ansys Fluent offers a possibility of coupling with Microsoft Visual Studio, which can be used to create custom macros or models based on C++ language. The implementation is described more closely in [9].

#### 4 SIMULATION

The numerical model presented above was used to study CV of Li-S cells. As it is difficult to experimentally obtain the characteristic parameters of the reactions and polysulfides, they were taken from [4]. The dissolution/precipitation reaction of  $\text{Li}_2\text{S}$  was not considered as the reaction is a chemical and not an electrochemical one, it only depends on the concentration of species and the time. This means that in the CV study, there is only a short amount for the precipitation reaction to occur, as the  $\text{S}^{2-}$  is created only at the end of the cathodic scan [9]. Additionally, the cathode cannot be considered as a planar electrode which slightly increases the complexity of the problem. As described in [11], the porous cathode can be described by a single particle. Figure 1 shows the illustration of such geometry. Initially, the computational domain is uniformly filled with  $19 \text{ mol/m}^3$  of  $\text{S}_{8(0)}$ . CV responses of particles with different radii were modelled and investigated (50 nm, 5  $\mu\text{m}$  and 500  $\mu\text{m}$ ). The boundary condition for the electrode potential was set to a triangle sweeping signal with a scan rate of 0.1 mV/s, with a potential range of 1.8 V – 3 V, with a starting point at 3 V.

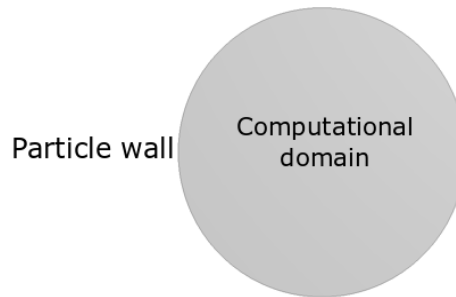


**Figure 1:** Illustration of the computational domain for a porous particle [9].

## 5 RESULTS

The numerical results were compared to an experimentally obtained CV of a Li-S cell (Figure 2 (a)). Its characteristics are described more closely in [9]. The results of simulations are also shown in Figure 2. General reaction mechanism is the same for all cases and corresponds with the measured voltammogram. The main difference lies in the amplitude and the position of the peaks. The simulations start with a cathodic scan, during which, two peaks are clearly noticeable. The first peak represents the reduction of the elemental sulfur  $S_{8(l)}$  to  $S_8^{2-}$  and  $S_8^{2-}$  to  $S_6^{2-}$ . The second prominent peak describes the simultaneous reductions of  $S_4^{2-}$  to  $S_2^{2-}$  and  $S_2^{2-}$  to  $S^{2-}$ . These peaks are corresponding with the two plateaus during the discharge process. The reduction of  $S_6^{2-}$  to  $S_4^{2-}$  is not visible in most cases. Similarly, during the anodic scan, two peaks are noticeable. However, their positions and shape are different as they consist of slightly different combination of reactions. The first peak at the lower potential consists of combination of oxidation of  $S^{2-}$  to  $S_2^{2-}$  and  $S_2^{2-}$  to  $S_4^{2-}$  and  $S_4^{2-}$  to  $S_6^{2-}$ , while the second peak consist of oxidation of  $S_6^{2-}$  to  $S_8^{2-}$  and  $S_8^{2-}$  to  $S_{8(l)}$ . As the radius of the particles decreased, the peaks of individual reactions were more separated and more noticeable. For the particle with the radius of 50 nm, the peak representing the reduction of  $S_6^{2-}$  to  $S_4^{2-}$  has become visible.

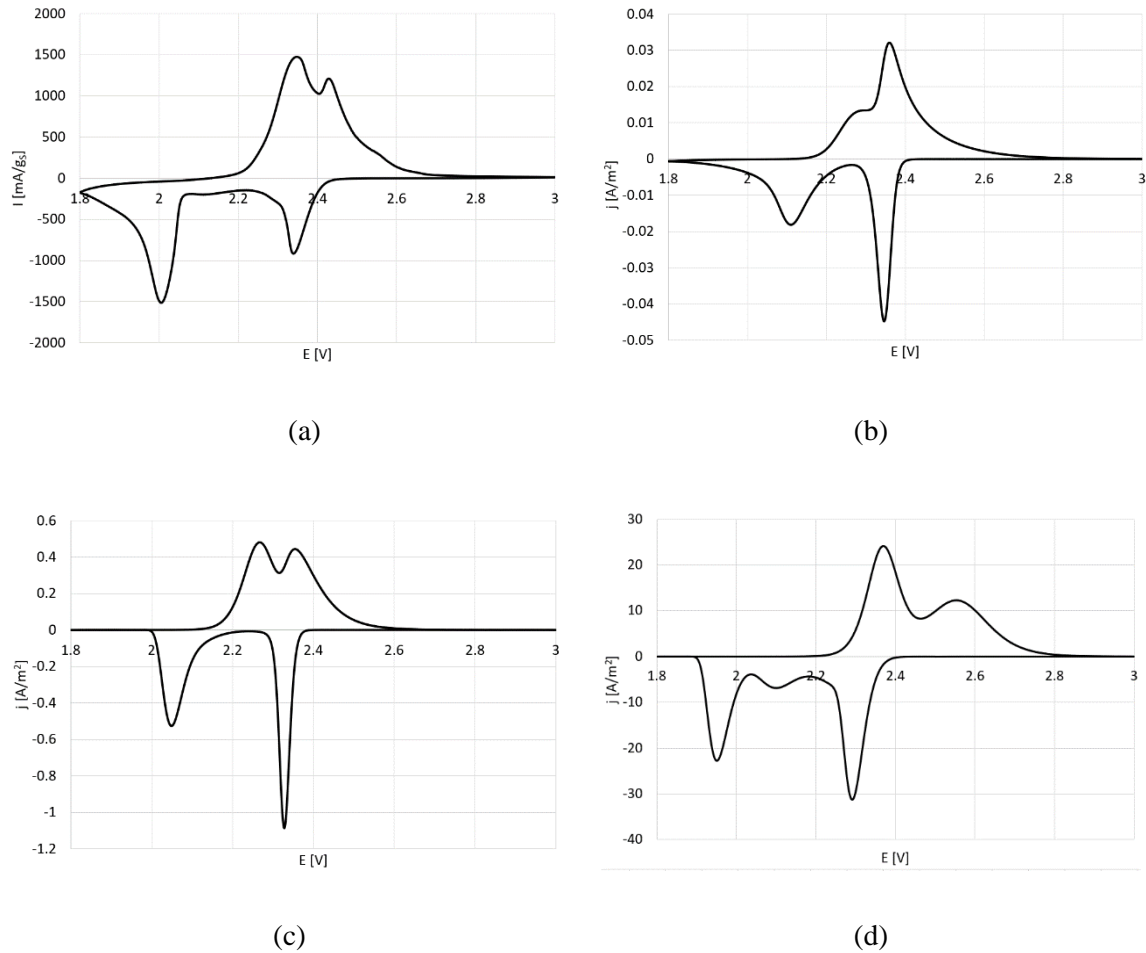


**Figure 2:** Resulting voltammograms – experimental (a) [9], numerical with a radius of 500  $\mu\text{m}$  (b), numerical with a radius of 5  $\mu\text{m}$  (c), numerical with a radius of 50 nm (d).

## 6 CONCLUSION

The presented results show that the custom electrochemical model is able to model CV of Li-S cells. By comparing the shapes of voltammograms, the modelling of the whole porous cathode might be

replaced by a single particle. This assumption leads to a significant simplification of the solution. Additionally, it might be possible to predict the size of the pores in the cathode. As the radius of particles decreased, the resulting CV has become more similar to the experimental measurement. The peaks of the individual reactions have become more separated and their position has been moved towards lower potentials during the reduction and towards higher potentials during the oxidation. From these simulations, it is possible to predict the size of the pores of the real cathode to be somewhere between 50 nm and 5  $\mu\text{m}$ , pointing towards radii of hundreds of nm as reported in [9]. Unfortunately, only qualitative comparison could be carried out, as the data was measured through the capacity, while the simulations were measured through the current density. In order to properly match the shape of voltammograms it would be necessary to measure the reaction rates and parameters of the exact cathode. Nevertheless, these simulations bring interesting insight to the reaction mechanism of Li-S cells, as it is possible to predict the influences of individual parameters.

## ACKNOWLEDGEMENT

This work was supported by the BUT specific research programme (project No. FEKT-S-20-6206).

## REFERENCES

- [1] A. F. Hofmann, D. N. Fronczek, and W. G. Bessler, "Mechanistic modeling of polysulfide shuttle and capacity loss in lithium-sulfur batteries", *Journal of Power Sources*, vol. 259, pp. 300-310, 2014.
- [2] R. Xu, I. Belharouak, X. Zhang, R. Chamoun, C. Yu, Y. Ren, A. Nie, R. Shahbazian-Yassar, J. Lu, J. C. M. Li, and K. Amine, "Insight into Sulfur Reactions in Li-S Batteries", *ACS Applied Materials & Interfaces*, vol. 6, no. 24, pp. 21938-21945, Dec. 2014.
- [3] R. Kumar, J. Liu, J. -Y. Hwang, and Y. -K. Sun, "Recent research trends in Li-S batteries", *Journal of Materials Chemistry A*, vol. 6, no. 25, pp. 11582-11605, 2018
- [4] K. Kumaresan, Y. Mikhaylik, and R. E. White, "A Mathematical Model for a Lithium-Sulfur Cell", *Journal of The Electrochemical Society*, vol. 155, no. 8, 2008.
- [5] A. Manthiram, Y. Fu, S. -H. Chung, C. Zu, and Y. -S. Su, "Rechargeable Lithium-Sulfur Batteries", *Chemical Reviews*, vol. 114, no. 23, pp. 11751-11787, Oct. 2014.
- [6] Q. He, Y. Gorlin, M. U. M. Patel, H. A. Gasteiger, and Y. -C. Lu, "Unraveling the Correlation between Solvent Properties and Sulfur Redox Behavior in Lithium-Sulfur Batteries", *Journal of The Electrochemical Society*, vol. 165, no. 16, pp. A4027-A4033, Dec. 2018.
- [7] X. Huang, Z. Wang, R. Knibbe, B. Luo, S. A. Ahad, D. Sun, and L. Wang, "Cyclic Voltammetry in Lithium-Sulfur Batteries—Challenges and Opportunities", *Energy Technology*, Apr. 2019.
- [8] K. Yoo, M. -K. Song, E. J. Cairns, and P. Dutta, "Numerical and Experimental Investigation of Performance Characteristics of Lithium/Sulfur Cells", *Electrochimica Acta*, vol. 213, pp. 174-185, 2016.
- [9] M. Mačák, P. Vyroubal, T. Kazda, and K. Jaššo, "Numerical investigation of lithium-sulfur batteries by cyclic voltammetry", *Journal of Energy Storage*, vol. 27, 2020.
- [10] M. Wild, L. O'Neill, T. Zhang, R. Purkayastha, G. Minton, M. Marinescu, and G. J. Offer, "Lithium sulfur batteries, a mechanistic review", *Energy & Environmental Science*, vol. 8, no. 12, pp. 3477-3494, 2015.
- [11] E. O. Barnes, X. Chen, P. Li, and R. G. Compton, "Voltammetry at porous electrodes: A theoretical study", *Journal of Electroanalytical Chemistry*, vol. 720-721, pp. 92-100, 2014.

# SIMULTANEOUS TRANSMISSION OF AMPLIFIED OPTICAL SIGNALS OF SELECTED PHOTONIC SERVICES

**Michal Látal**

Doctoral Degree Programme (1), FEEC BUT

E-mail: xlatal08@stud.feec.vutbr.cz

Supervised by: Petr Münster

E-mail: munster@feec.vutbr.cz

**Abstract:** This paper focuses on simultaneous transmission of selected photonic services by one single-mode optical fiber. The paper deals with the problem of simultaneous transmission of multiple photonic services by one optical fiber using the wavelength division multiplex technology and erbium-doped fiber amplifier (EDFA). Except common data transmission with a bitrate of 10 Gbps, a simultaneous high-speed data signal transmission with a bitrate of 200 Gbps and accurate time transmission are considered. During the simultaneous transmission of selected photonic services, the measurement of the transmission parameters was performed. In particular, the effect of possible mutual interference of individual transmission channels at 100 GHz spacing between individual signals was analyzed.

**Keywords:** accurate, data, dwdm, edfa, simultaneous, time

## 1 INTRODUCTION

Photonic services are a set of advanced optical network services that enable pure optical transmission without the need to convert optical to electrical signals. Photonic services are designed for the most demanding real-time communication applications. The most common real-time photonic services include accurate time and stable frequencies transmission [1].

Operation of these services is subject to the availability of dark fibers, unused optical fibres available for use in fibre-optic communication, and optical transmission networks beyond the capabilities normally available for transmission on, for example, the Internet. This can accommodate more demanding applications that have stricter requirements for accuracy. For some demanding applications, such as remote control of machines, medical operations or reproducible scientific experiments, it is necessary to achieve an extremely accurate and long-term stable transmission environment throughout the transmission path, as even small delay fluctuations can cause fatal consequences in these applications [2].

## 2 RELATED WORKS

Authors [3] performed simultaneous transmission of four photonic services with ITU DWDM 100 GHz grid spacing channels. Photonic services included 100G data signal, accurate time and stable frequency signal and sensing signal. Simultaneous transmission of all services was through two types of optical fibers, G.655 and G.653. FEC-BER and Q factor values were evaluated for the measurement results. The measurement results show that the G.653 fiber cause more interference of signal. Based on the results, 100 GHz channel spacing is not high enough and to eliminate possible interaction the higher spacing must be used.

However with utilizing frequency offset estimation before adaptive equalization enhances the performance capabilities of a digital coherent receiver in digital signal processing. This technique has

a great importance for long-haul DP-QPSK DWDM system with 50 GHz channel spacing. The considered system performs with minimum bit error rate over a wide range of launch power [4].

Another simulations for WDM system show using pulse-overlapping super-Nyquist (Pol-SN) to improve spectral efficiency of coherent optical transmission. The results of simulations indicate that the channel spacing of 224 Gbps can be reduced up to 20 GHz [5].

### 3 MEASUREMENT SETUP

The effect of amplification of optical amplifier on simultaneous transmission of three selected photonic services was verified in further measurements. Photonic time transfer services and two data signals were selected for this measurement. 10 Gbps data signal generated by the EXFO FTB-1 measurement platform and 200 Gbps data signal generated by optical coherent transmission system Coriant Groove™ G30. DWDM channels with 100 GHz spacing were assigned for each service, as shown in Table 1. Selected optical amplifier Keopsys KPS-BT-C-21-BO-FA is designed for wave multiplexes operating in the band 1530–1565 nm.

**Table 1:** Distribution of photonic services into DWDM channels with 100 GHz spacing

Channel	Frequency [THz]	Wavelength [nm]	Service
31	193.1	1552.52	Time signal
32	193.2	1551.72	Data 200 Gbps
33	193.3	1550.92	Data 10 Gbps

Figure 1 shows a detailed measurement diagram showing transmitted services and carrier wavelength settings for each.

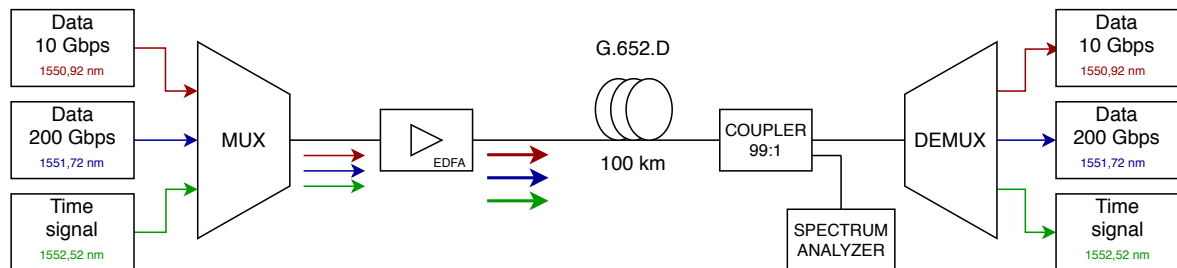


**Figure 1:** Scheme of simultaneous transmission amplified by EDFA

Optical signals for individual services were connected to neighboring DWDM channels. These signals were multiplexed together in a standard telecommunication multiplexer. The common optical signal was further amplified by an optical power amplifier, in the range of 10–15 dBm. The common optical signal was further coupled to an optical fiber of type G.652.D with a length of 100 km. A portion of the transmitted common optical signal was coupled at the end of the path using an optical power splitter with a 99:1 split ratio. The bound part of the transmitted common signal served as a source for the optical spectrum analyzer, by means of which individual optical signals were monitored for non-linear phenomena.

The common transmitted signal was further demultiplexed and the individual optical signals of the transmitted services were fed back to their source devices, where the transmission parameters of the received optical signals were evaluated.

#### 4 MEASUREMENT RESULTS

The main evaluated transmission parameter for data signals was bit error rate (BER), furthermore the parameters of chromatic dispersion, group delay, optical signal-to-noise ratio and Q-factor were monitored for data signal 200 Gbps. For the time signal, the time delay of the signal during optical fiber transmission was evaluated. The monitored transmission parameters and time delays depending on the amplification of the optical amplifier were evaluated by individual systems and recorded in the Table 2.

**Table 2:** Measured transmission parameters for amplified common signal

	Data 10 Gbps	Data 200 Gbps					Time signal
EDFA	BER	DGD	CD	OSNR	Q	BER	Delay
[dBm]	[Bit-ratio]	[ps]	[ps/nm]	[dB]	[dB]	[Bit-ratio]	[ns]
10	1.36E-09	2	1684	18.2	7.3	9.88E-03	495 986.118
11	7.06E-11	2	1686	18.7	7.3	9.69E-03	495 986.734
12	1.41E-12	2	1685	18.8	7.4	8.86E-03	495 987.628
13	3.49E-13	2	1687	19.1	7.5	8.34E-03	495 988.699
14	3.31E-13	2	1687	19.5	7.6	7.92E-03	495 989.771
15	<1.00E-14	3	1687	20.2	7.7	9.52E-03	495 992.371

The average bit error rate measured for the 10 Gbps data signal showed a clear proportion to the gradual amplification of the common signal by the optical amplifier. The lowest bit error rate was achieved by the 15 dBm optical amplifier data signal, when the bit error rate reached the minimum limit value of 1.00E-14, which the FTB-1 measuring platform can still detect.

Relatively the same bit error values were measured for the 200 Gbps data signal. Average measured values of bit error rate differed only very slightly in mantissa value, depending on amplification by optical amplifier, they were of the same order of magnitude. Similarly, the group delay (DGD) and chromatic dispersion (CD) values did not differ significantly depending on the amplification of the common signal. The dependence on common signal amplification was reflected in the average measured values of the optical signal-to-noise ratio (OSNR) and the Q-factor, which are closely related. From the measured average values we can see the improvement of these transmission parameters depending on the amplification of the common signal.

Accurate delay time values and deviations of successive delay values were monitored during time signal transmission. As the Table 2 shows, the deviation from the mean value was always in nanoseconds. The average delay value, for all gain values, was approximately the theoretical assumption for the optical signal propagation time over a given path. The increasing trend in the time delay values is caused by the gradual heating of the fiber; at a higher temperature of the optical fiber, the propagation time of the optical signal through the optical fiber is prolonged.

Figure 2 shows the spectrum of simultaneous transmission of time and data optical signals, indicating the corresponding DWDM channels for the three different gain values of the optical power amplifier. The optical spectral analyzer graph shows the amplification of individual optical signals after passing through an optical power amplifier.

#### 5 RESULTS

From the measured transmission parameters and especially from the graph of the optical spectral analyzer it can be deduced that the simultaneous transmission of time and data optical signals did not affect the transmission channels, which would significantly affect the stability of some of the transmitted photonic services. By gradually amplifying the power of the optical amplifier, some

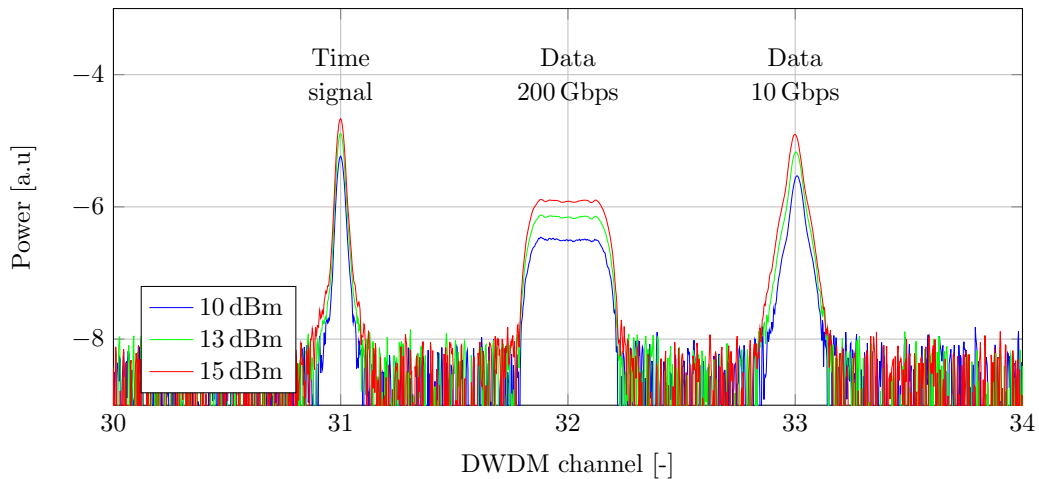


**Figure 2:** Spectrum of amplified common signal of selected services

transmission parameters for data signals were improved. In particular, it was the bit error rate for the 10 Gbps data signal and the optical-to-noise ratio and the Q-factor for the 200 Gbps data signal.

## 6 CONCLUSION

From the results of the measurements it can be deduced that, for DWDM transmission channels 100 GHz, there was no significant interaction between individual transmitted photonic services by one optical fiber, which would disrupt the successful transmission of these services.

Based on the measurements made, the selected bandwidth of 100 GHz for selected photonic services is sufficient for successful simultaneous transmission over one optical fiber. There were no non-linear phenomena interfering with the successful simultaneous transmission of photonic services.

## ACKNOWLEDGEMENT

The presented research was financed by the Ministry of Interior under grant no. VI20152020045.

## REFERENCES

- [1] P. O. Hedekvist, S.-Ch. Ebenhag, "Time and Frequency Transfer in Optical Fibers," in *Recent Progress in Optical Fiber Research* [online], Dr Moh. Yasin (Ed.), 2012, pp. 371-386 InTech, Available from: <https://www.intechopen.com/books/recent-progress-in-optical-fiber-research/time-and-frequency-transfer-in-optical-fibers>
- [2] P. Skoda, J. Radil, J. Vojtech, V. Smotlacha, P. Munster, S. Zvanovec, "Time transfer over 1900 km of DWDM network," *2017 40th International Conference on Telecommunications and Signal Processing (TSP)*, Barcelona, 2017, pp. 698-701.
- [3] T. Horvath, P. Munster, J. Vojtech, V. Smotlacha, "Simultaneous Transmission of Photonic Services over One Fiber with an ITU 100 GHz Grid," *Sensors*, vol. 19, no. 7, April 2019.
- [4] N. Sharma, S. Agrawal, V. Kapoor, "Estimation of frequency offset prior to adaptive equalization for improved performance of DP-QPSK DWDM system," *Optical Fiber Technology*, vol. 55, In progress (2020, March), Available: <http://www.sciencedirect.com/science/article/pii/S1068520019304791>
- [5] C. Xu, G. Gao, S. Chen, J. Zhang, "Pulse-overlapping super-nyquist WDM system," *Journal of Lightwave Technology*, vol. 36, no. 18, pp. 3941-3948, September 2018.

# ON THE LIMITS OF THE LORAWAN TECHNOLOGY: EVALUATION OF SPREADING FACTORS' PERFORMANCE

**Radek Možný**

Doctoral Degree Programme (first year) FEEC BUT

E-mail: xmozny03@stud.feec.vutbr.cz

Supervised by: Pavel Mašek

E-mail: masekpavel@vutbr.cz

**Abstract:** Over the course of the recent decade, the Low-Power Wide-Area (LPWA) technologies took their momentum and started to enable the reliable data transmissions in the Internet of Things (IoT) and Industry 4.0. In this paper, the LoRaWAN communication technology i.e., the license-exempt LPWA technology is described. The focus is given to the practical evaluation of different configurations of the Spreading Factor (SF) based on the signal level. The obtained results from the laboratory measurements confirm the suitability of lower SFs in case of decreased signal levels i.e. conditions close to the “deep indoor scenarios”.

**Keywords:** LoRaWAN, Spreading Factors, LPWA, Internet of Things, Industry 4.0

## 1 INTRODUCTION

As the vision of the Internet of Things (IoT) defined the concept of the Machine-type Communication (MTC) for the low-power end-devices i.e., sensors, servers, and data processing systems, it became clear the legacy wired/wireless communication technologies e.g., 2G/3G/4G cannot manage the data transmissions with required Quality of Service (QoS). The specific requirements are related more to the reliable communication with extended communication range than to the high-speed transmissions. Therefore, the narrow-group of technologies jointly known as Low-Power Wide-Area (LPWA) technologies has been defined in the last decade [1].

The goal of LPWA technologies is to provide scalable, low-cost, and energy-efficient enabler for the MTC or massive MTC (mMTC). The LPWA technologies of today can be divided into two main groups based on the utilization of the frequency spectrum: (i) license and (ii) license-exempt. The first group consists of the technologies defined by the 3rd Generation Partnership Project (3GPP) Narrow-Band IoT (NB-IoT) and Long-Term Evolution-Machine (LTE-M) technologies. The second group composes of multiple technologies operating in the non-licensed frequency bands – the two main representatives are LoRaWAN and Sigfox. As the license-exempt technologies do use the frequency spectrum with various systems that are not synchronized in time, the interference can occur [2].

In case of the non-licensed LPWA technologies in the Czech Republic, the LoRaWAN outperforms the remaining ones as it offers more flexible communication parameters with respect to the industry-driven scenarios, see the technology comparison in the Table 1. Therefore, the focus of the paper is to evaluate the communication parameters of LoRaWAN technology. Specifically, the intention is to give a clear representation of the relation between the Spreading Factor (SF) configuration and the signal level [3].

In line with the above-mentioned, the goal of this paper is to explore the communication capabilities of the private LoRaWAN network. For this, the LoRaWAN end-device was constructed. To be able to explicitly set the signal level, the laboratory setup was set using the shield-box and the attenuators together with the private LoRaWAN gateway.

**Table 1:** Technological overview for LPWA technologies for use in Europe: Sigfox, LoRa, LTE-M and NB-IoT [4, 5, 6].

	<b>Sigfox</b>	<b>LoRaWAN</b>	<b>LTE-M<sup>1</sup></b>	<b>NB-IoT<sup>1</sup></b>
<b>Coverage (MCL)</b>	159 dB	155 dB	155.7 dB	164 dB
<b>Spectrum</b>	Unlicensed	Unlicensed	Licensed	Licensed
<b>Bandwidth</b>	100 Hz	125, 250 kHz	1.08 MHz	180 kHz
<b>Max. ERP</b>	14 dBm	14 dBm	23 dBm	23 dBm
<b>Modulation</b>	DBPSK UL GFSK DL	LoRa FSK	QPSK, 16QAM	$\pi/2$ - BPSK, $\pi/4$ - QPSK, QPSK (DL + MT)
<b>Restrictions</b>	140 (UL), 4 (DL) Mess. per day	Duty Cycle	No limit	No limit
<b>UL datarate</b>	100 bps	0.3 – 50 kbps	1 Mbps	32 kbps
<b>DL datarate</b>	600 bps	0.3 – 50 kbps	1 Mbps	27 kbps
<b>Max. application payload size</b>	12 B (UL) 8 B (DL)	51 – 242 B	1600 B <sup>2</sup>	1600 B <sup>2</sup>

<sup>1</sup> According to Rel. 13 of the 3GPP standard.

<sup>2</sup> The maximum size of a Packet Data Convergence Protocol Service Data Unit (PDCP SDU) for NB-IoT.

## 2 LORAWAN TECHNOLOGICAL OVERVIEW

The LoRaWAN technology utilizes the license-exempt Industrial, Scientific and Medical (ISM) frequency spectrum as described above (868 MHz in EU) that is shared by multiple other technologies thus suffers from omnipresent interferences. Usage of ISM bands also brings other restrictions like limited Maximal Effective Radiated Power (Max. ERP) to 14 dBm and Time on Air (ToA) or in other words 1 % Duty Cycle (DC) limitation of LoRaWAN restricting this technology to maximal transmitting time of 36 s per hour. However, mentioned restrictions together with an absence of signaling (due to ALOHA access) are beneficial for the reduction of power consumption [6].

To overcome narrow-band interferences in the ISM band and to extend possible coverage area, LoRaWAN utilizes modulation based on frequency spreading, more precisely Chirp Spread Spectrum (CSS) LoRa modulation on the physical layer. To be more precise, LoRa spreads signal across 125 or 250 kHz band which ensures mentioned interference resilience and enhances receiver ability to decode a message from a distant transceiver. This is possible due to increased ToA from signal spreading. Also, LoRa permits to change slope and duration of spreading which allows to further increase possible coverage. On the other hand, this is the trade-off in data-rate reduction and ToA increase. These changes are divided into so-called Spreading Factors (SFs) in range of 7 – 12 where SF7 represents usage of highest data-rate and SF12 one with lowest data-rate but highest possible area coverage. It is important to mention that higher SF also reduces the maximal amount of transmitted data per hour due to DC limitations [7].

A notable advantage of LoRaWAN lies in its infrastructure, which allows utilizing either public networks (e.g. from the infrastructure of České Radiokomunikace (CRA)) or creating private networks consisting of Gateways (GWs) and possible MESH networks of End Devices (EDs). The downside can be initial costs for such infrastructure but later operational costs are reduced to a minimum due to the use of private networks in the ISM band. Thus private networks are suitable for large scale investors wanting to create their own network and thus protecting their valuable data. A private network scenario was also used in this work where private LoRaWAN Gateway was utilized [5].

### 3 MEASUREMENT SCENARIO AND RESULTS

Conducted measurement aimed to evaluate LoRaWAN performance in terms of communication limits for all SFs to not only verify a theoretical perspective for maximal Maximum Coupling Loss (MCL) with respect to receiver sensitivity. Also, the goal is to determine the success transmission rate at such a signal level and to find out how distant is this value from one enabling reliable communication with 100 % success rate for variable payload size. Another goal is to verify and evaluate the importance of Signal-to-Noise Ratio (SNR) thresholds for individual SFs. These observations could play an important role in terms of sufficient switching between SFs for achieving the best cost-effectiveness, power efficiency, and reliability for communication utilizing LoRaWAN.

#### 3.1 LABORATORY TEST BED

To ensure a stable environment for advanced measurements, the proper setup was assembled in the form of laboratory test-bed as depicted in Fig. 1. From the End-Device (ED) point of view, a universal communication device was constructed and utilized while using LoRaWAN module RN2483 from Microchip that was placed inside the RF shield box. By this, it was possible to achieve minimal ambient interferences and to assure connectivity of the device to laboratory LoRaWAN GW i.e., private GW. From the shield box, the device was connected directly to GW via coaxial cable with a step attenuator in the middle. Attenuator served for precise signal level setting with 1 dB step. As for GW, The Things Gateway<sup>1</sup> was utilized. All the procedures like LoRaWAN module control, power supply management and measurement data collecting from either module and GW provided controlling PC.

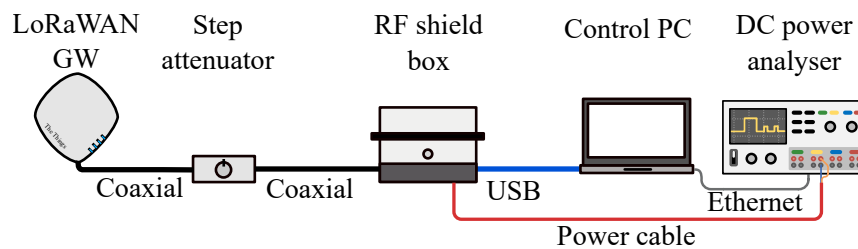


**Figure 1:** Schematic of the realized laboratory test-bed.

#### 3.2 MEASUREMENT METHODOLOGY

Measurement scenario was as follows: (i) turning on the power for the device, (ii) setting of SF, transmission power to 14 dBm and communication parameters according to The Things Network frequency plan<sup>2</sup>, (iii) message transmission to GW (iv) switching off the module power supply and measurement data storing. It is important to mention that non-acknowledged messages were being sent to GW and evaluated. Due to this, the SNR values must have been acquired from GW as the only receiving side. To properly evaluate the mentioned success rate, data obtained from GW served also for this purpose.

The measurements were done for conditions where each SF was able to reliably transfer all messages. Subsequently, the setup was also configured to find a threshold of the state where the device was able to successfully transfer at least one message. Each measurement was conducted for message sizes 2, 12 and 50 B. First payload sizes of 2 B and 12 B were chosen for possible comparison with Sigfox. Last payload size of 50 B was selected as near to max application payload size while utilizing SF12 (see Table 1). This enabled a comparison of all the SFs. Each measurement was repeated 50 times from which success rate and mean SNR value were calculated.

<sup>1</sup>See The Things Gateway: <https://www.thethingsnetwork.org/docs/gateways/gateway/>

<sup>2</sup>See The Things Network frequency plan:

<https://www.thethingsnetwork.org/docs/lorawan/frequency-plans.html>

All the results are as depicted in Table. 2 containing message transmission success rates and corresponding average SNR values with respect to setup attenuation. Nevertheless, it is good to keep in mind that Table. 2 contains only threshold values and to properly evaluate the whole experiment one must observe corresponding success rate dependencies between the threshold as depicted in Fig. 2.

**Table 2:** Success transmission rate and SNR with respect to signal attenuation for all SFs and message sizes 2, 12, and 50 B.

SF	Message Size [B]	Last transmission with 100% success rate		Last successful transmission	
		Attenuation [dB]	SNR [dB]	Attenuation [dB]	SNR [dB]
7	2	133	-4.12	138	-8.00
	12	132	-4.26	138	-8.40
	50	132	-4.60	137	-7.82
8	2	136	-8.13	141	-11.05
	12	137	-8.36	141	-10.00
	50	136	-8.48	140	-10.08
9	2	139	-10.71	143	-12.68
	12	140	-11.09	143	-13.36
	50	140	-11.20	143	-14.00
10	2	143	-13.29	146	-15.62
	12	142	-13.75	146	-16.23
	50	142	-14.19	145	-15.96
11	2	144	-14.34	149	-15.77
	12	144	-15.14	150	-17.75
	50	143	-14.76	148	-16.60
12	2	143	-11.71	151	-17.43
	12	143	-12.68	151	-19.10
	50	143	-13.81	150	-19.70

#### 4 CONCLUSIONS

In this paper, the real measurement of LoRaWAN technology is provided with respect to the evaluation of the spreading factors' performance and the resulting limits. Gathered results validated theoretical expectations about maximal coverage in terms of MCL for each SF. The findings are also supported by average SNR values. Each increase of SF resulted in an increase of MCL by roughly +3 dB which is also in line with theoretical expectations. On the other hand, the reliability of such transmission was under 10 %. To achieve 100 % reliable communication, attenuation must have been decreased by 5 dB which in most cases means more than doubling of received power. Moreover the increase of payload size from 2 to 50 B indicated link budget decrease by 2 dB. Observations also indicated predictability of SNR and confirmed its suitability (in comparison with Received Signal Strength Indicator (RSSI)) as a reliable indicator for proper SF selection leading to maximizing power efficiency, reliability of communication and overall LoRaWAN performance. During all measurements, RSSI indicated values in a range between -124 to -126 dBm across all SF, which would prevent any reliable assessment of SF switching.

Summarizing the above-mentioned, the evaluation of SF limits in this paper leads to the optimal SF switching. This is crucial for the improvement of the overall performance of LoRaWAN technology. Thus the obtained results could enable more reliable message transmission, improve EDs power efficiency and optimize DC usage. Therefore, there is a need for more intense research in this area. The next steps in this direction are repeating the same experiment as provided in this paper, but for acknowledged messages and subsequently, properly examine power efficiency and impact to battery life performance from measured results.

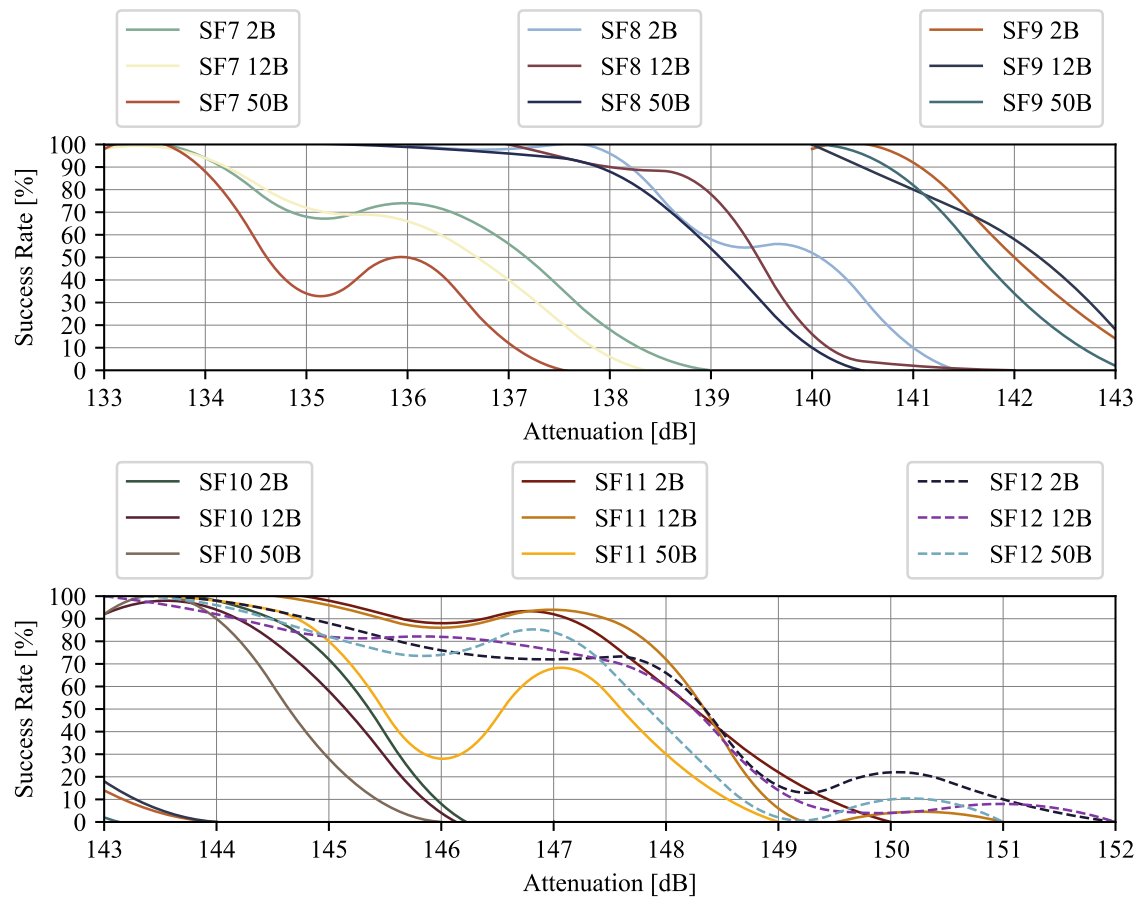


**Figure 2:** Success transmission rate with respect signal attenuation for all SFs and message sizes 2, 12 and 50B.

## ACKNOWLEDGMENT

For the research, the infrastructure of the SIX Center was used.

## REFERENCES

- [1] Z. Qin, F. Y. Li, G. Y. Li, J. A. McCann, and Q. Ni, "Low-power wide-area networks for sustainable IoT," *IEEE Wireless Communications*, vol. 26, no. 3, pp. 140–145, 2019.
- [2] F. Muteba, K. Djouani, and T. Olwal, "A comparative Survey Study on LPWA IoT Technologies: Design, considerations, challenges and solutions," *Procedia Computer Science*, vol. 155, pp. 636–641, 2019.
- [3] R. El Chall, S. Lahoud, and M. El Helou, "LoRaWAN network: radio propagation models and performance evaluation in various environments in Lebanon," *IEEE Internet of Things Journal*, vol. 6, no. 2, pp. 2366–2378, 2019.
- [4] P. Masek, M. Stusek, K. Zeman, J. Hosek, K. Mikhaylov, S. Andreev, Y. Koucheryavy, O. Zeman, J. Votapek, and M. Roubicek, "Tailoring NB-IoT for Mass Market Applications: A Mobile Operator's Perspective," in *2018 IEEE Globecom Workshops (GC Wkshps)*, pp. 1–7, IEEE, 2018.
- [5] K. Mekki, E. Bajic, F. Chaxel, and F. Meyer, "A Comparative Study of LPWAN Technologies for Large-scale IoT Deployment," vol. 5, pp. 1–7, 03 2019.
- [6] O. Liberg, M. Sundberg, E. Wang, J. Bergman, and J. Sachs, *Cellular Internet of Things: Technologies, Standards, and Performance*. Elsevier Science, 2017.
- [7] N. Sornin, "LoRaWAN Specification v1.1." *LoRa Alliance*, 2017.

# COMPARISON OF POWER QUALITY MONITOR DATA TRANSMISSION BETWEEN MODBUS TCP/IP AND IEC 60870-5-104

**Petr Musil**

Doctoral Degree Programme (2), FEEC BUT

E-mail: xmusil56@stud.feec.vutbr.cz

Supervised by: Petr Mlynek

E-mail: mlynek@feec.vutbr.cz

**Abstract:** With deployment of smart devices along the electrical grid key infrastructure points, communication process with regards to its volume and load on communication infrastructure needs to be described and evaluated. This article focuses on protocol Modbus TCP/IP and standard IEC 60870-5-104 with regard to their communication structure and principles within substation connected to network by broadband over power lines modems (BPL). This paper also offers two communication scenarios over BPL network by using real substation power quality monitor. Furthermore, performance of each solution is being summed up in the discussion. Conclusion offers a convenient solution for utilization of key values transmission on limited communication channel.

**Keywords:** broadband over power lines, IEC 60870-5-104, Modbus TCP/IP, Smart Grid, substation.

## 1 INTRODUCTION

Over the last years with growing demand for more solid electrical infrastructure, there is a significant effort from electric utility which focuses on deployment of smart devices. By implementing smart devices especially on low-voltage distribution substations, better overview about events and power quality values typical for this part of power grid would be obtained. Detailed information about real-time values also enables finer control for electrical grid operators and an increase in stability and efficiency of the whole electric power distribution process is expected [1].

The concept of Smart Grid takes into account vast field of communication technologies used for transmission of data from smart devices installed along the grid to controlling centers. For the primary distribution (extra high voltage and high voltage grid) and its key parts (power plants, etc.), communication technologies with low latency and high reliability are demanded. For this task, optical network is the most suitable choice. Excellent data throughput and low latency is being also outweighed by expensive and sometimes difficult installation process [2].

On the other hand for distribution grid, which is running on low voltage, smart devices are not already implemented at all grid key points. In this case more precise methods of both controlling and monitoring low voltage grid are required. Such solution is also deployment of power quality monitors into substations, which are smart devices with vast possibilities for grid management [3].

For sending data to grid operator, different technologies can be used. Since some of those substations are at distant locations, technologies such as LPWAN (Low Power Wide Area Network), PLC (Power Line Communication) or cellular networks are being used. These technologies are based on shared communication channel and its data throughput and latency is sometimes limiting [4]. This article mainly focuses on possible solutions of utilization and tries to find convenient communication protocol, which could be used for power quality monitors for its reliable and effective operation under non-ideal conditions.

## 2 MODBUS TCP/IP

Modbus TCP/IP (Modbus TCP) is a derived version of simple vendor-neutral Modbus protocol family, which was designed to fulfill needs in terms of control and supervision of equipment mostly in automation industry. In its original form Modbus was designed in 1970s to communicate on serial lines with programmable logic controllers. Communication is based on master-slave principle, where slave provides four object types to master: Coil (1 bit, read-write), Discrete input (1 bit, read-only), Input register (16 bits, read-only) and Holding register (16 bits, read-write).

With the growth of ethernet communication and rise of TCP/IP networks, Modbus was modified into Modbus TCP with regard to ethernet specifications, port 502 is being used. Each operation within this protocol are being recognized based on the Function code value. In general Modbus introduces the limit of maximum read/write registers that can be read at once. However in Modbus TCP only 123 registers can be read. To read higher number of registers, multiple reads have to be executed.

## 3 IEC 60870-5-104

IEC 60870-5-104 is an international standard introduced in the year 2000. Interoperability between devices which conform to this standard is being provided by interoperability list. Communication is of server-client type, based on principles of TCP/IP networks. Standard recognizes two directions: control and monitoring. The standard provides features such as: On-demand transmission, Spontaneous transmissions, Direct command transmission, Clock synchronization and File Transfer.

Communication in this standard is based on three types of units: APDU (Application Protocol Data Unit), APCI (Application Protocol Control Information) and ASDU (Application Service Data Unit). Basic unit APDU consists of APCI and can also consist of ASDU (used for carrying payload). Based on CF values, three formats of APCI are distinguished: I-format (controlling transfer and defying communication), S-format (supervisory functions, confirmations), U-format (Start, Stop and testing of communication line). The standard also specifies TypeID for identification of protocol structure. Under this identification various features are being recognized, such as those mentioned above.

## 4 MEASUREMENTS

Results in this paper are described by two different scenarios of using Modbus TCP/IP and IEC 60870-5-104 for the same transmission task. Network topology is shown in Fig. 1. BPL modems, PC and real substation device Meg44PAN with its PQ Meg software were used to simulate real conditions.

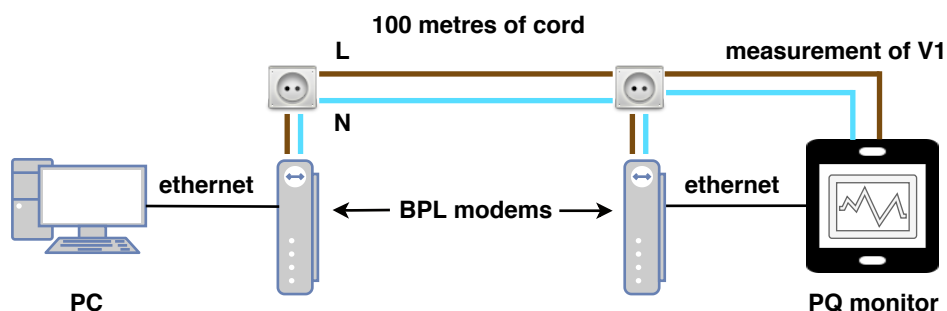


**Figure 1:** Measurement scheme - network topology.

#### 4.1 SCENARIO A: DOWNLOAD OF STORED MEASURED VALUES

Device Meg44PAN used for purposes of these measurements is equipped with a built-in memory and a possibility of using SD card. Meg44PAN is able to capture values defining various parameters of power grid. These values can be transmitted by network or can be stored in drive and then downloaded locally or remotely. Fig. 2 describes memory allocation with minimal measurement times by adjustable periods of capture.

In this scenario file containing values was downloaded through network topology as shown in Fig. 1. Both Modbus TCP and IEC 60870-5-104 were used to download .mdat file containing: values of quality of power grid, events due to specification, recorder of energy, rapid voltage changes, ripple control and signal of the ripple control.

For Modbus protocol, results are shown in Table 1, in total 9 475 packets were used to download 196 kB .mdat file. Average size of a packet was 153 B. On the other hand, when IEC 60870-5-104 was used, only 4 957 packets with average size of 235 B were transferred to download the file with the same size, see Table 2. Performance and efficiency of both protocols are summarized in Table 3, value of transmission efficiency is being calculated as a ratio of useful transmitted data to the overall data volume.

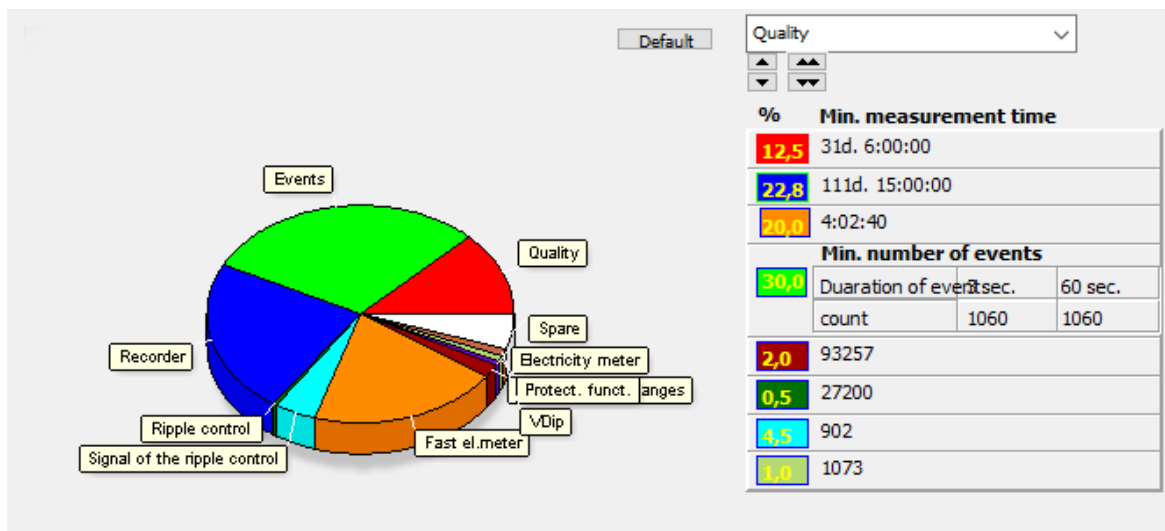


Figure 2: Memory allocation for different data values within Meg44PAN PQ monitor.

#### 4.2 SCENARIO B: REAL-TIME VALUE MONITORING

In this scenario simulation of operator monitoring voltage of single phase was used. Capture period was set to value of 5 seconds (option *Slow* on Fig. 3), device also offers options *Mid* (~1 sec) and *Quick* (~200 ms). Values were then being put into a plot, as shown in lower part of Fig. 3.

For protocol Modbus TCP, when 1 hour was used to monitor single phase voltage, 35 004 packets were used to transmit data from power quality monitor. its average size was about 149 B as Table 1 shows. For one data renewal 49 packets (986 packets per second, 7 316 B in total) had to be transmitted causing data flow of 150 kBytes/s for 0.050 of second.

Performance of standard IEC 60870-5-104 was significantly better, only 25 793 packets with average size of 184 B were used under the same 1 hour scenario, see Table 2. Within one data renewal 36 packets (193.7 packets per second, 6 613 B) were transferred with average flow of 35 kBytes/s for 0.186 of second.

**Table 1:** Results of Scenario A and B for Modbus TCP/IP.

Structure of Modbus TCP communication		Scenario A		Scenario B	
Function code	Transmitted type of data	packets	aver. size [B]	packets	aver. size [B]
4	Read File Record	10	66	1 440	66
20	Read Input Registers	9 450	153	32 844	155
71	Transmission init	8	72	0	0
-	TCP [ACK]	7	54	720	54
<b>TOTAL</b>		<b>9 475</b>	<b>153</b>	<b>35 004</b>	<b>149</b>

**Table 2:** Results of Scenario A and B for IEC 60870-5-104.

Structure of IEC 60870-5-104		Scenario A		Scenario B	
Type ID	Transmitted type of data	packets	aver. size [B]	packets	aver. size [B]
120	File ready	10	75	720	75
121	Section ready	10	76	720	76
122	Call dir,sel.file,call file,call sec.	30	73	21 60	73
123	Last section, last segment	20	74	1 440	74
124	Ack file, Ack section	20	73	1 440	73
125	Segment	2 840	368	9 363	359
-	Supervisory	606	60	2 880	60
-	TCP [ACK]	1 421	54	7 070	54
<b>TOTAL:</b>		<b>4 957</b>	<b>235</b>	<b>25 793</b>	<b>184</b>

**Table 3:** Comparison of effectiveness - Scenario A.

Size of transmitted .mdat file	Modbus TCP transmission	IEC 60870-5-104 transmission
196 kB	1 456.2 kB	1 165.3 kB
<b>Transmission efficiency:</b>	13.46 %	16.82 %
<b>Number of packets:</b>	9 475	4 957

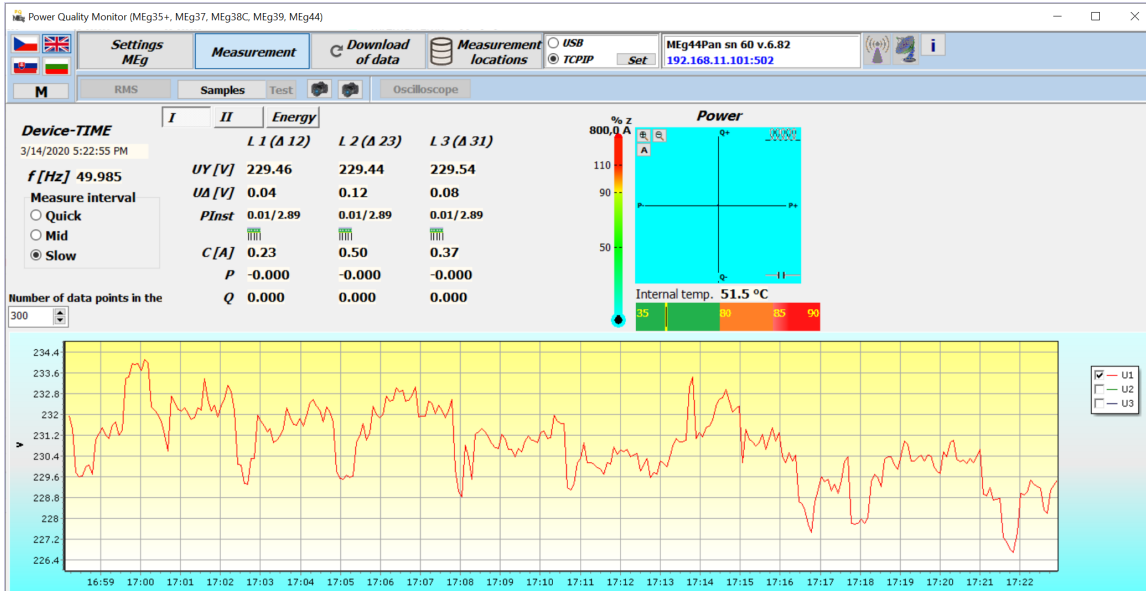


**Figure 3:** Real-time monitoring of phase V1 Voltage.

## 5 DISCUSSION

Based on the results presented in this paper, several outcomes can be observed. In comparison of both Modbus TCP and IEC 60870-5-104 used in these measurements, different structure of both determines the performance in different situations. Modbus TCP, based on original Modbus introduced several decades ago, is simple and does not provide very much options and possibilities of data structure definition within the protocol. Modbus TCP tends to use a higher number of packets, where payload which is carried in packets is significantly lower than payload carried by file transfer packets used in IEC 60870-5-104. Based on the results of Scenario B, it is significant that Modbus TCP tends to make bursts when power quality monitor is being interrogated which leads to extreme peaks in packets per second. This phenomenon and its impact might be emphasized especially when more monitors would be interrogated simultaneously at the same BPL line.

Design of standard IEC 60870-5-104 offers more possibilities of managing data transfer which leads to more effective transmission. Modbus which main purpose used to be communication with programmable logic controllers, where data types were limited only to those understood by such devices at that time. Large binary objects were not supported within Modbus.

## 6 CONCLUSION

This paper offers an insight into commonly discussed question about data volumes involved in controlling low voltage substations. Communication behaviour defines communication needs for further installation of new communication channels. The results of both scenarios described in this article are pointing out that design of standard IEC 60870-5-104 tends to outperform Modbus TCP/IP protocol in better data structure management and effectiveness. It also tends to use a lower number of packets and the overall load on the communication infrastructure is better balanced and spread over time. Nevertheless since IEC 60870-5-104 achieved higher average size of packets in all scenarios Modbus TCP/IP might be preferred in communication scenarios, where obsolete technologies with short frames are involved and fragmentation would be undesirable.

Since development of Smart Grids is being recognized with strong consensus, thorough understanding of communication needs and requirements leads to more convenient choices and faster progress in implementation phase. With massive deployment of such devices with its communication protocols, higher effectiveness of the whole controlled system should be achieved especially under worsened communication conditions.

## REFERENCES

- [1] THOMAS, Mini S and John D. (John Douglas) MCDONALD. 2015. *Power system SCADA and smart grids*. Boca Raton: CRC Press, xxii, 313 pages.
- [2] MA, Ruofei, Hsiao-hwa CHEN, Yu-ren HUANG and Weixiao MENG. 2013. Smart Grid Communication: Its Challenges and Opportunities. *IEEE Transactions on Smart Grid* [online]. IEEE, 4(1), 36-46. Available at: <https://ieeexplore.ieee.org/stamp/stamp.jsp?tp=&arnumber=6451177>
- [3] BOLLEN, Math H. J, Ratan DAS, Sasa DJOKIC, Phil CIUFO, Jan MEYER, Sarah K RONNBERG and Francisc ZAVODAM. 2017. Power Quality Concerns in Implementing Smart Distribution-Grid Applications. *IEEE Transactions on Smart Grid* [online]. IEEE, 8(1), 391-399. Available at: <http://ieeexplore.ieee.org/stamp/stamp.jsp?tp=&arnumber=7527692&isnumber=7792759>
- [4] FERREIRA, Hendrik. *Power line communications*. Chichester: John Wiley, 2010, xxvii, 507 s. : il. ISBN 978-0-470-74030-9.